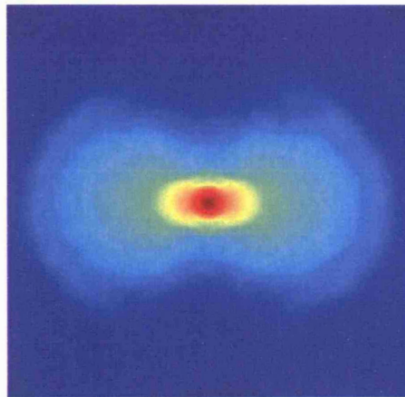


# **Three Dimensional Simulations of Rotating Core Collapse Supernovae**

A thesis submitted for the degree of  
Doctor of Philosophy  
at the University of Leicester.

by

**Rosie Telford**



Theoretical Astrophysics Group  
Department of Physics and Astronomy  
University of Leicester

September 2005

UMI Number: U206543

All rights reserved

INFORMATION TO ALL USERS

The quality of this reproduction is dependent upon the quality of the copy submitted.

In the unlikely event that the author did not send a complete manuscript and there are missing pages, these will be noted. Also, if material had to be removed, a note will indicate the deletion.



UMI U206543

Published by ProQuest LLC 2013. Copyright in the Dissertation held by the Author.  
Microform Edition © ProQuest LLC.

All rights reserved. This work is protected against  
unauthorized copying under Title 17, United States Code.



ProQuest LLC  
789 East Eisenhower Parkway  
P.O. Box 1346  
Ann Arbor, MI 48106-1346

© Rosie Telford 2005.

This thesis is copyright material and no quotation from it may be published without proper acknowledgement.

*To Mum and Dad*

# *Acknowledgements*

I would like to thank my supervisor, Graham Wynn, for his guidance over the past three years, for propping up my ego and for mopping up my tears when things got tough. I would also like to thank my erstwhile co-supervisor, Stephan Rosswog, for his superior knowledge and attention to detail.

Many thanks to everyone I've shared an office with during my time at Leicester for the camaraderie and for resisting the temptation to throw my mobile phone out of the window: Tim, Dave, Sam, Paul, Matthew and especially Owen for letting me steal his thesis design. Even greater thanks go to Skippy and Yohann for putting up with my control freak-ish tendencies not only in the office but also at home, and for their humour, kindness and happy-go-lucky influence.

Thanks also to the other inhabitants of Theory Cave, past and present: Dan and Martin for their help with IDL and Linux and for bigging me up in crises of confidence, James for being a True Friend, Lynnette for making me a pretty HR diagram, and Dean, Jim, Emma, Ralf, Roland and Klaus for being thoroughly nice people.

Thanks to Pam, Lucy, Lisa and the rest of the secretarial staff for their role in making the department such a friendly place.

For their endless patience and help when badgered with myriad questions about UKAFF, Hex and the theory group computers I am eternally grateful to Chris Rudge, Stuart Poulton and Richard West. The simulations in this thesis were run on these machines.

Thanks to Chris Fryer at LANL for helpful discussions and encouragement.

This thesis would not have been possible without the humour and support of my friends, especially Clare Bear, whose ability to clear the coffee room of physicists is astounding, and the rest of the jugglers. Thanks also to Magda and Alison for being great housemates and kindred spirits.

Finally, thanks to Mum and Dad, for their unconditional love and support in everything I have done throughout my life, and to my sister Ru and brother Rob for being as proud of me as I am of them.

# *Abstract*

A core collapse supernova is the dramatic death of a massive star by core implosion and subsequent explosion. Massive stars are known to rotate appreciably, yet the vast majority of supernova simulations over the years have not included rotation or its effects.

It is thought that moderate stellar rotation could assist the supernova explosion by lowering the effective gravitational potential in the core. More rapid rotation could give rise to jets and/or bipolar explosions. At the most extreme rotation rates it is thought that gamma ray bursts (GRB) are produced. These bursts may be delayed or revived at late times as a result of the collapsing core becoming rotationally unstable and fragmenting.

In this thesis the effects of rotation on core collapse are studied. Sophisticated progenitor models with rotation rates of up to a significant fraction of Keplerian are used as the starting points for three dimensional simulations. The computational method of Smoothed Particle Hydrodynamics is used to follow the collapse until core “bounce”, the point at which the collapse is halted.

It is shown that, before bounce, no instabilities occur even for the most rapid rotators. The maximum value obtained for the ratio of rotational to gravitational binding energy is around 0.13, just below the limit of 0.14 required for instability on a secular timescale. However, the more rapidly rotating models obtain interesting structures as they collapse. In these models the density distribution remains centrally peaked but is surrounded by a torus of centrifugally supported material, consistent with the collapsar model of GRB.

The gravitational wave signals emitted in collapse are also calculated. It is found that these are strongest for the slowly rotating models, in which the collapse is not slowed significantly. A supernova of this type in the Virgo galaxy cluster would be beyond the range of the current generation of gravitational wave detectors.

# *Contents*

<b>1</b>	<b>Introduction</b>	<b>1</b>
1.1	Motivation . . . . .	2
1.2	Going Out With A Bang: Core Collapse Supernovae . . . . .	2
1.3	Final Stages of Stellar Evolution . . . . .	6
1.3.1	Mass Loss . . . . .	8
1.4	Catastrophic Collapse . . . . .	9
1.5	Matter at High Densities . . . . .	10
1.5.1	Nuclear Pasta . . . . .	12
1.5.2	Effect of the Equation of State . . . . .	12
1.6	Shock Launch and Revival . . . . .	14
1.6.1	Supernova Energetics . . . . .	14
1.6.2	Shock Revival . . . . .	15
1.6.3	Fate of the Compact Remnant . . . . .	16
1.7	Importance of Three Dimensional Effects . . . . .	17
1.7.1	Convection . . . . .	19
1.7.2	Rotational effects . . . . .	20
1.8	Gamma Ray Bursts . . . . .	22
1.8.1	The Supernova–GRB Connection . . . . .	24
1.8.2	The Collapsar Model . . . . .	25

1.8.3	One Lump or Two? . . . . .	25
1.9	Supernovae in Binary Systems . . . . .	27
1.10	Summary . . . . .	29
<b>2</b>	<b>Numerical Method</b>	<b>30</b>
2.1	Introduction . . . . .	31
2.2	Equations of Fluid Dynamics . . . . .	31
2.3	Smoothed Particle Hydrodynamics . . . . .	33
2.3.1	SPH Representation of a Variable . . . . .	34
2.3.2	The Kernel . . . . .	36
2.4	SPH Equations Used in the Code . . . . .	37
2.4.1	The Continuity Equation . . . . .	37
2.4.2	Variable Smoothing Lengths . . . . .	37
2.4.3	The Momentum Equation . . . . .	38
2.4.4	Energy Conservation . . . . .	38
2.5	Treatment of Self Gravity . . . . .	39
2.5.1	The Tree . . . . .	39
2.5.2	Building the Tree . . . . .	40
2.5.3	Calculating the Forces . . . . .	42
2.6	Time Evolution of Smoothing Lengths . . . . .	42
2.7	Treatment of Viscosity . . . . .	44
2.8	Equation of State . . . . .	45
2.9	Time Evolution . . . . .	46
2.9.1	Timestepping . . . . .	47
2.10	Parallelization . . . . .	48

<b>3</b>	<b>Code Adaptations for Core Collapse</b>	<b>51</b>
3.1	Introduction . . . . .	52
3.2	Progenitor Models . . . . .	52
3.2.1	Distributing the particles . . . . .	54
3.2.2	Initial values for particles . . . . .	55
3.2.3	Setting the Smoothing Length . . . . .	57
3.3	Single Timestep Trials . . . . .	57
3.4	Multi-timestepping . . . . .	59
3.4.1	Runge-Kutta-Fehlberg integration . . . . .	59
3.4.2	Initialization . . . . .	62
3.4.3	The Outer Loop . . . . .	62
3.4.4	The Inner Loop . . . . .	63
3.4.5	Rearranging the Particles . . . . .	64
3.5	Including grad h terms . . . . .	64
3.5.1	Effects of individual h . . . . .	65
3.5.2	Altering the code . . . . .	67
3.6	Including shear viscosity . . . . .	69
3.7	Tests . . . . .	71
3.8	Summary . . . . .	72
<b>4</b>	<b>Collapse of the Woosley Progenitor</b>	<b>73</b>
4.1	Introduction . . . . .	74
4.2	Stellar Evolution Models . . . . .	74
4.3	Collapse of the 15 $M_{\odot}$ Progenitor . . . . .	75
4.4	The Effects of Adding Rotation . . . . .	82
4.4.1	Parametrization of Rotation . . . . .	84
4.4.2	Model Parameters . . . . .	85
4.5	Results and Discussion . . . . .	85

4.5.1	Effect of Rotation on Bounce Density and Rotation Parameter . . . . .	87
4.6	Summary . . . . .	91
<b>5</b>	<b>Collapse of the Rotating Progenitors</b>	<b>104</b>
5.1	Introduction . . . . .	105
5.2	Models and Parameters Used . . . . .	105
5.3	Models Without Rotation . . . . .	107
5.4	Slowly Rotating Models . . . . .	110
5.5	Rapidly Rotating Models . . . . .	115
5.5.1	Results . . . . .	117
5.6	“Binary” Models . . . . .	122
5.6.1	Results . . . . .	123
5.7	Models With Viscosity . . . . .	127
5.8	Models With Density Perturbations . . . . .	131
5.9	Summary . . . . .	132
<b>6</b>	<b>Gravitational Wave Signals</b>	<b>165</b>
6.1	Gravitational Wave Production . . . . .	166
6.2	The Weak-Field Quadrupole Approximation . . . . .	167
6.3	Results and Discussion . . . . .	169
6.3.1	Woosley Models . . . . .	170
6.3.2	Heger Models . . . . .	176
6.4	Summary . . . . .	180
<b>7</b>	<b>Concluding Remarks</b>	<b>187</b>
7.1	Summary and Discussion . . . . .	188
7.2	Future Avenues . . . . .	189

# Chapter 1

## *Introduction*

“He also made the stars.”

*Genesis 1*

## 1.1 Motivation

Approximately 10 billion years after the Universe sprang into existence, we ape-descended life forms find ourselves standing precariously on an insignificant blue-green planet, orbiting a small unregarded yellow sun far out in the uncharted backwaters of the unfashionable end of the Western Spiral arm of the Galaxy (Adams 1979), peering back at where we've come from.

Years of dogged observation, theory and debate have revealed to us that the blanket of stars stretched out above our heads, has, for the most part, formed from the remains of other stars before them.

The first stars in the Universe are thought to have had masses of hundreds of times solar. These stars fused hydrogen nuclei in their cores, then helium, carbon, oxygen and silicon. Most of them would have ended their lives by exploding as supernovae, showering the Universe with an abundance of elements. The next generation of stars, incorporating these elements, would not have been as massive, still many would have produced supernovae, strewing their contents about to become part of yet other stars.

The chemical enrichment of the Universe has grown mainly through the cycle of star formation, fusion in stellar cores and explosion. Almost all of the numerous elements that make up our bodies come from the dusty remnants of dead stars, the debris of countless supernovae. The compact objects left behind may have gravitational fields strong enough that even light can not escape from them, or magnetic fields that can accelerate particles to almost the speed of light. This is why we study them.

## 1.2 Going Out With A Bang: Core Collapse Supernovae

We observe supernovae as stars that suddenly appear in the sky or brighten by many orders of magnitude. Over the course of a week or so their intrinsic luminosity becomes comparable to that of a whole galaxy before slowly fading away in the following weeks or months.

Supernovae have been observed since ancient times when Chinese astronomers recorded the occasional appearance of "guest stars" (including novae). The brightest supernova since the advent of humankind occurred in 1006 and was observed in China, the Middle East and Europe. The Chinese also reported a supernova of 1054, whose remnant is still observed as the Crab Nebula, illuminated by emission from the neutron star that lies at its centre.

In 1572 Tycho Brahe discovered a “new” star in Cassiopeia which, aided by Kepler’s supernova in 1604, prompted a philosophical revolution as it became clear that the heavens were not, as previously thought, perfect and unchanging. Sometime between 1650 and 1680 another supernova occurred in Cassiopeia, whose remnant is now observed as the strong radio source Cas A. Since 1604, only one supernova has occurred close enough to us to be observed with the naked eye.

There are different types of supernovae, which are classified by their spectra. The principal division is between Type I, which show no hydrogen lines, and Type II, which have hydrogen. Observations of the locations of these types reveal that Type II supernovae are found only in regions of star formation, whilst Type I are found everywhere that there are stars.

The location and spectra of the main subgroup of Type I supernovae, known as Type Ia, are explained by them being thermonuclear. The sudden collapse of an accreting white dwarf when it reaches the Chandrasekhar mass (defined in Section 1.4) ignites carbon in a runaway nuclear reaction that explodes the star. White dwarfs are the end products of reasonably low mass and long-lived stars and are therefore found in older stellar populations.

Type IIs, which make up around 70% of all supernovae, are the result of the collapse of the cores of massive stars upon exhaustion of their nuclear fuel. Massive stars burn their fuel quickly, so Type II supernovae occur only in regions where stars are still forming. Two other subgroups of Type I supernovae, Type Ib and Ic, also originate in core collapse. They are distinguished from Type Ia by the absence of a strong absorption trough at  $\sim 6150 \text{ \AA}$  caused by blueshifted Si II at  $6355 \text{ \AA}$ . Type Ib show strong helium lines, especially He I at  $5876 \text{ \AA}$ , whilst Type Ic have little or no helium. Type Ib/c supernovae are thought to come from massive stars which have lost their envelopes in stellar winds.

As well as being classified by their spectra, supernovae can be grouped by the shape of their light curves. A typical light curve will rise to its peak value over the course of a week or two, as the luminous shell expands. In Type II supernovae, the peak may last for around 100 days, followed by a steady decline over roughly a year. This emission comes from the decay of nickel to cobalt, which itself decays to iron with a half life of 77 days. The main division in Type II supernovae is between II-P – “plateau” – which maintain their peak brightness for an extended period and II-L – “linear” – for which the brightness falls off steeply initially and then decays exponentially. A composite “typical” lightcurve for each of these types is shown in Figure 1.1. Further subdivisions are once more provided by the supernova spectrum, such as II-n – “narrow” – in which

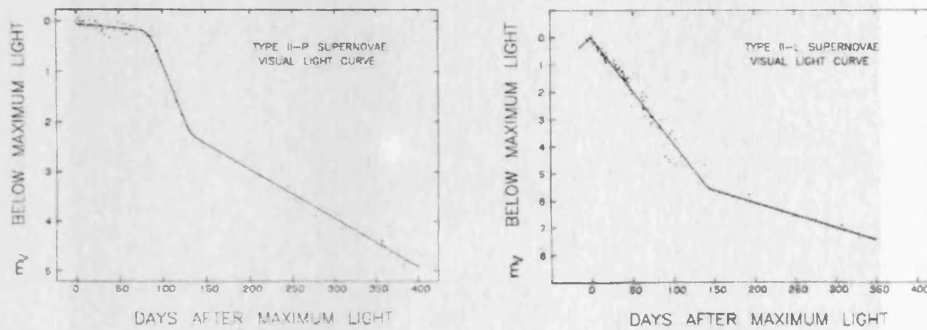


FIGURE 1.1. Composite visual lightcurves of Type II-P (“plateau”) and Type II-L (“linear”) supernovae, taken from Doggett & Branch (1985).

the ejecta is thought to be interacting with circumstellar material, II-d – “double” – and IIb, whose spectra begin as Type II and then change to Ib. Another class of supernovae – “hypernovae” – exhibit a strange, almost featureless continuum spectrum at maximum light. It is thought that in these cases the ejecta are moving at such extreme velocities that the spectral lines are broadened beyond recognition.

The explanation for these rare phenomena, observed since ancient times, took a long time in coming. It was Baade & Zwicky (Baade & Zwicky 1934*a*, Baade & Zwicky 1934*b*) who first postulated (correctly) that supernovae are transitions of ordinary stars to neutron stars. The concept of a star composed entirely of neutrons had been suggested by Landau in a private discussion soon after the discovery of the neutron in 1932. Early calculations gave the radius of such an object as about 10km, which is still the accepted value. Hoyle, in 1946, suggested that an instability associated with the photodisintegration of iron could be the trigger for collapse (Prialnik 2000). It is humbling to think that virtually all we know about supernovae has been discovered within the last couple of generations.

On 24th February 1987 a new star appeared in the Large Magellanic Cloud, the first supernova since 1604 visible to the naked eye, referred to as SN1987A. For the first time it became possible to make a detailed comparison of theory and observations. Once the remnant had faded it was observed that the star Sanduleak -69°202 had disappeared, revealing it to have been the progenitor. This was a surprise to astronomers as prior to explosion the star had been a fairly ordinary-looking blue supergiant – not the expected vast red supergiant. Also surprising was that the ejecta took the form of a bright ring rather than a spherical shell (Figure 1.2) and the overabundance of helium burning products observed in the ejecta, which implied that a great deal of mixing had taken place.

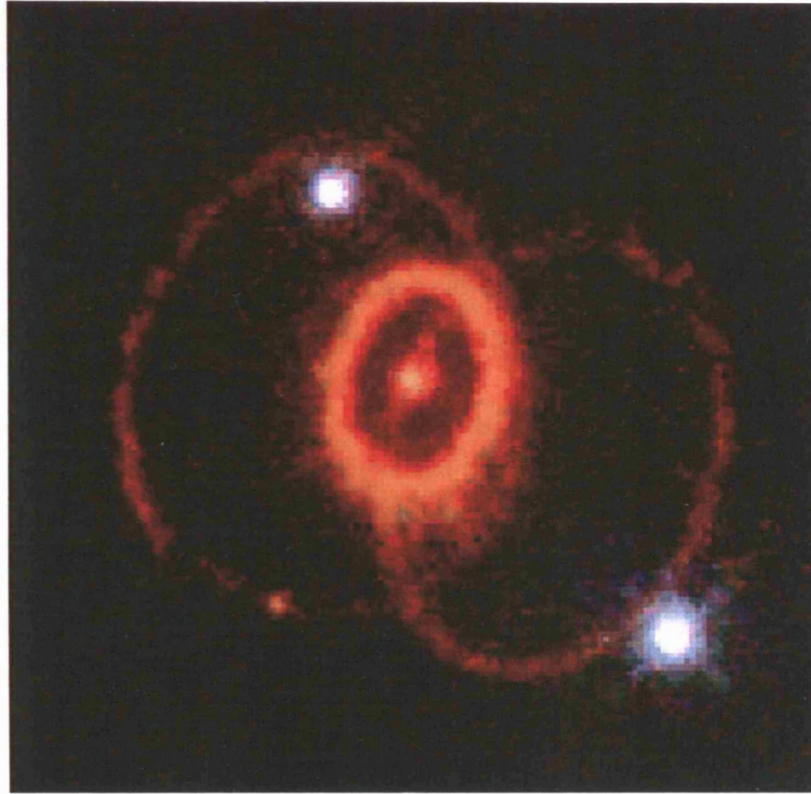


FIGURE 1.2. Hubble Space Telescope image of SN1987A, released in April 1994, showing the bright ring of ejecta and two off-centre rings of material illuminated by the supernova.

Less unexpected but just as exciting were observations of neutrinos from the supernova by Kamiokande II in Japan and IMB in Ohio – the first neutrinos ever detected from an extraterrestrial source other than sun.

A supernova is a big event in the life of a galaxy. Only a fraction of stars – those with masses  $\gtrsim 8 M_{\odot}$  – end their lives so dramatically. But the interactions of objects produced by core collapse – neutron stars and black holes – can be observed across the whole of the electromagnetic spectrum in many different environments. Supernovae are important in cosmology as probes of the star formation rate, galactic evolution due to the chemical enrichment they provide, neutrino physics, nuclear physics, gravitational wave astronomy and many other fields. Recently it has become clear that a subset of supernovae are connected to gamma ray bursts (GRB), powerful blasts of gamma rays that outshine the sky for their duration. (More about these in Section 1.8.) Few areas of astronomy cannot benefit from knowing more about supernovae.

## 1.3 Final Stages of Stellar Evolution

A supernova is the dramatic death of a star, the end point of an increasingly rapid sequence of events that takes place after it has exhausted its central store of hydrogen through fusion to helium. Hydrogen exhaustion marks the end of a star's main sequence lifetime and for stars more massive than  $\sim 8 M_{\odot}$  everything that takes place after this point is part of the process of demise. What follows is a summary of the stages a massive star passes through before the inevitable collapse of its core. A accessible description of these phases can be found in Prialnik (2000).

When the hydrogen in the core is used up hydrogen burning moves to a shell around it. Because there is no heat source within and therefore no heat flow through the core it becomes isothermal. There is a maximum mass for an isothermal core, above which it cannot support the stellar envelope, and it is exceeded for stars more massive than about  $2 M_{\odot}$ . In these stars the core is dynamically unstable and contracts, converting gravitational energy to thermal energy, until it restores the temperature gradient necessary to balance gravity. This temperature gradient causes heat loss so the core continues to contract on a thermal timescale. Because the dominant hydrogen burning process is the CNO cycle, which is proportional to a very high power of the temperature, during the first contraction the luminosity of the shell around the core increases and overshoots thermal equilibrium. The luminosity of the shell becomes greater than that of the star and the envelope must expand in order to radiate it away.

Helium burning is ignited in the core when the temperature reaches  $10^8$  K. Its products are carbon and oxygen. The rate of helium burning varies as  $\sim T^{40}$  so it takes place only at the centre of the core, where it is hottest. Helium is supplied to the centre by convection, which takes place in the inner core and ceases when the helium here is exhausted, leaving the outer layer of helium untouched. The helium burning lifetime of a star is less than one tenth that of the hydrogen burning lifetime. This is because the fusion of helium only supplies 1/10 of the energy per unit mass and also because the stellar luminosity is about an order of magnitude higher, due to the larger envelope.

While helium burning is taking place, the first “dredge up” occurs. This refers to the envelope becoming convective as a result of its increasing opacity combined with the need to transfer an increasing energy flux. Hydrogen burning products at the edge of the core are mixed into the envelope, increasing the metallicity observed at the surface of the star.

For stars with masses  $\gtrsim 10 M_{\odot}$  helium burning is followed by another phase of core contraction and envelope expansion. The second dredge up occurs, mixing mainly

helium and nitrogen into the envelope. Carbon burning is ignited, which in turn proceeds more quickly than helium burning.

As the stellar luminosity increases and approaches the Eddington limit, significant mass loss takes place by means of a strong stellar wind and affects the subsequent evolution. Energy is lost from the core through neutrino emission, which results in the nuclear fuel being consumed more quickly. Nuclear burning proceeds through heavier elements increasingly rapidly until eventually, after silicon burning, which lasts about a day, the inner core consists of iron group elements and no more fusion can take place.

At this stage the core of the star is made up of concentric shells burning different elements – iron-group elements in core surrounded by shells of silicon, oxygen, carbon, helium and hydrogen burning and the H-rich envelope. Figure 1.3 shows a schematic diagram of the structure of the star at the end of nuclear burning. In Figure 1.4 a Hertzsprung-Russell diagram shows the evolution of stars of 10, 15 and 20  $M_{\odot}$ .

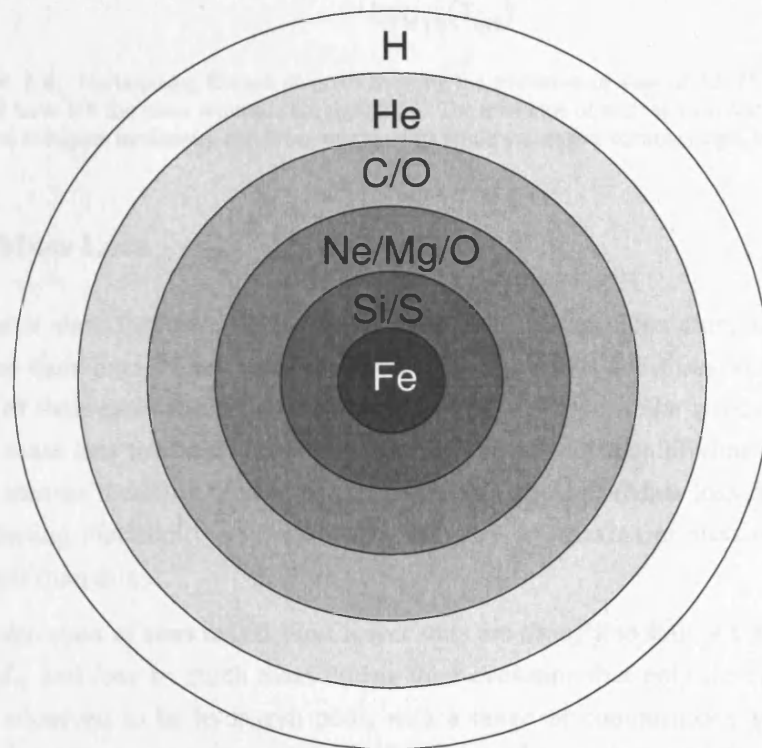


FIGURE 1.3. Schematic diagram of the composition of a massive star at the end of nuclear burning. A core consisting of iron-group elements is surrounded by concentric shells of increasingly lighter elements.

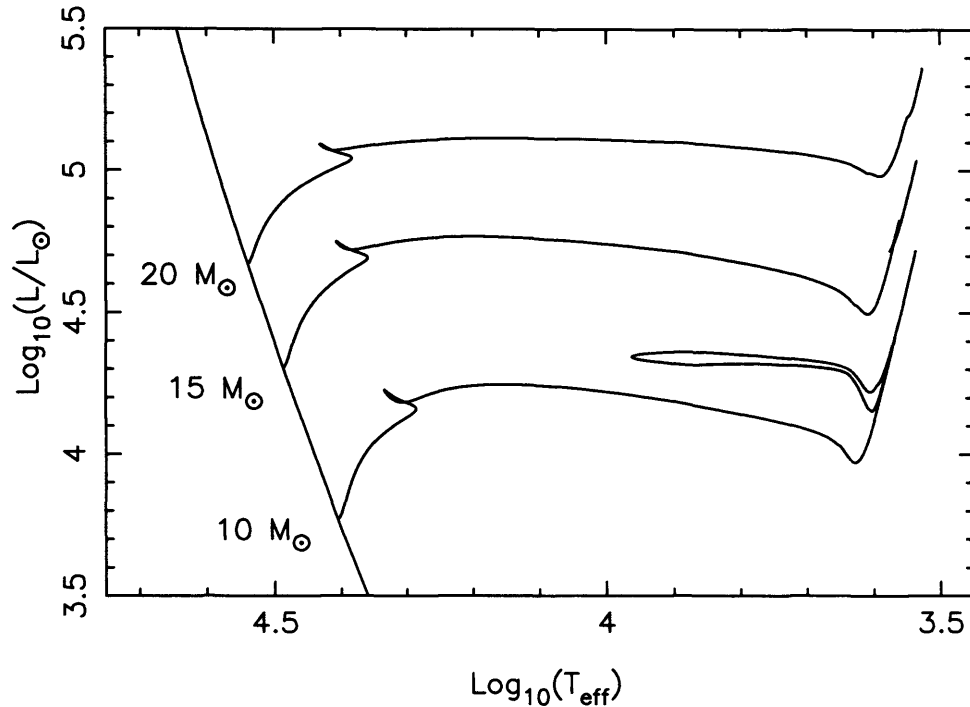


FIGURE 1.4. Hertzsprung-Russell diagram showing the evolution of stars of 10, 15 and  $20 M_{\odot}$  after they have left the main sequence (straight line). The envelope of each star expands, causing it to move to higher luminosity and lower temperature while successive burning stages take place.

### 1.3.1 Mass Loss

The massive stars that give rise to supernovae have luminosities close to Eddington throughout their lives. They therefore possess strong winds and mass loss affects every stage of their evolution. Stars greater than  $\sim 30 M_{\odot}$  have stellar winds so powerful that their mass loss timescale is shorter than their main sequence lifetime. Their main sequence masses therefore tend to converge towards  $30 M_{\odot}$ . (Mass loss rates increase with increasing metallicity, so in the early Universe the maximum mass of a star was much larger than this.)

A certain class of stars called Wolf Rayet stars are thought to start out more massive than  $30 M_{\odot}$  and lose so much mass during their evolution that only the core remains. They are observed to be hydrogen poor, with a range of compositions as a result of losing their envelopes at different stages of their evolution. (N.B. A stellar wind is not the only way to unbind an envelope – evolution in a binary can also produce a bare stellar core.) Wolf-Rayet stars are thought to give rise to Type Ib and Ic supernovae, which are core collapse supernovae with no hydrogen in their spectra. It is likely that Wolf-Rayet

stars are the progenitors of gamma ray bursts, which are described in detail in Section 1.8 below.

## 1.4 Catastrophic Collapse

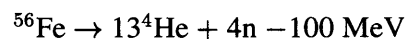
Once nuclear reactions in the core of a massive star have produced iron, no more reactions can take place, since both fission and fusion of iron group elements is endothermic. The core contracts once more and as the density rises the electrons become a relativistic, degenerate gas.

There is a maximum mass for which electron degeneracy can support the iron core against gravitational collapse. This is given by the Chandrasekhar limit

$$M_{Ch} \simeq 5.8Y_e^2 M_\odot \quad (1.1)$$

where  $Y_e$  is the ratio of electrons to baryons (Bethe 1990). When the mass of the degenerate core exceeds the Chandrasekhar limit self-gravity exceeds electron degeneracy pressure and the core cannot stop contracting. In the iron core at the onset of collapse  $Y_e$  is generally slightly below 0.5, giving a typical value for  $M_{Ch}$  of around  $1.4 M_\odot$ .

Once gravitational collapse has begun, instabilities arise that serve to accelerate the collapse to catastrophic proportions. As the density increases, electrons can be captured by heavy nuclei, thereby removing their contribution to the pressure. In addition, the pressure of a degenerate gas has a low sensitivity to temperature so that as the core contracts there is no increase in pressure to halt it. The temperature rises until it reaches the point where iron nuclei can photodisintegrate, by the reaction



which is endothermic, requiring  $100/56 \text{ MeV} \sim 2 \text{ MeV}$  per nucleon.

The energy absorbed by the photodisintegration of iron accelerates the collapse almost to free fall. Eventually the temperature becomes high enough to dissociate helium into protons and neutrons. Electron capture on free protons can then take place, causing yet more energy loss. During this time the inner core ( $\sim 0.8 M_\odot$ ) collapses homologically ( $v \propto r$ ), whilst the outer core collapse becomes supersonic and similar to free fall, with  $v \propto r^{-1/2}$ . At its maximum, the infall velocity reaches about half that of free fall. Figure 1.5 shows a schematic graph of the infall velocity. The only thing that is able to stop this runaway collapse is the pressure from the nucleons becoming greater than

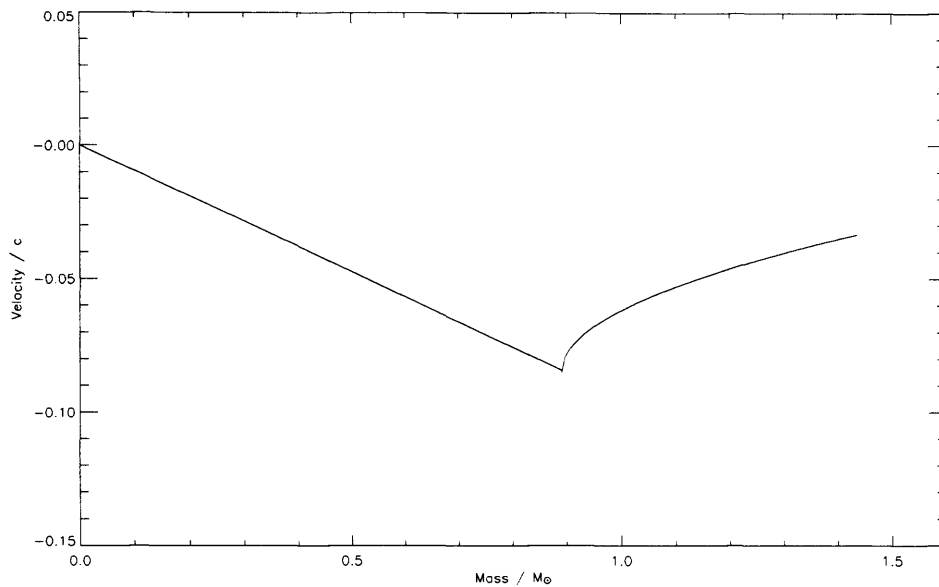


FIGURE 1.5. Schematic diagram of the infall velocity of material during core collapse as a function of enclosed mass, after Bruenn (1988).

the gravitational acceleration. This happens when the density is so high that the nucleons form a degenerate gas, around  $3 \times 10^{14} \text{ g cm}^{-3}$ .

The collapse of the core takes place on a dynamical timescale and it takes less than half a second for it to reach nuclear densities. It should be noted that, because the collapse happens so quickly, energy transport is negligible and each fluid element maintains essentially constant entropy. This is significant because it limits the effects of transport mechanisms to after collapse.

## 1.5 Matter at High Densities

As the density increases, the opacity of the matter to neutrinos rises and further electron capture is prevented by neutrino trapping. The discovery of the neutral weak current in the early 1970s meant that neutrinos could not only be absorbed by nucleons and scattered by electrons, but also scattered by neutrons (and protons too, to some degree) and hence nuclei. This insight led to the discovery of neutrino trapping (Freedman 1974, Mazurek 1975, Sato 1975), which occurs when the high density material in the core becomes opaque to neutrinos. A detailed theory was produced by Tubbs & Schramm (1975).

Trapping can be defined in a number of different ways. Cooperstein (1988) defines it as occurring when the neutrinos cannot escape from the star due to being dragged in with collapsing matter, which gives a trapping density of  $6 \times 10^{11} \text{ g cm}^{-3}$ . An alternative definition of the trapping density is that at which neutrinos can no longer diffuse significantly with respect to matter. This happens at a density of  $\simeq 10^{12} \text{ g cm}^{-3}$ . Bruenn (1988) found that the trapping density tends to be higher nearer the centre of the core, but generally in agreement with the figures cited above.

Once trapping has occurred, neutrinos attain thermodynamic equilibrium with themselves and can be described by a Fermi distribution. However, they are not in equilibrium with the electrons and so are described with their own temperature  $T_\nu$  and chemical potential  $\mu_\nu$ .

A “trapping radius” can be defined for the core as that within which neutrinos are trapped. We can also define the “neutrinosphere” as the radius at which the optical depth for neutrinos  $\tau = 2/3$ , outside which the neutrinos are assumed to stream freely to infinity. (A value of  $2/3$  rather than  $1$  is chosen because neutrinos emerge at an angle from the neutrinosphere rather than radially.) The neutrinosphere is distinct from the trapping sphere and is at a larger radius, meaning that neutrinos diffuse for a long time before emission. Since  $e$ ,  $\mu$  and  $\tau$  neutrinos have different rates of interaction with matter, the radius of the neutrinosphere is different for each species.

The mass of the inner core is very sensitive to neutrino reactions; for example, Bruenn (1988) found that including neutrino-electron scattering in simulations reduces the mass of the inner core from  $0.75 M_\odot$  to  $0.64 M_\odot$ . The difference between the inner (homologous) core mass and the total mass of the iron core is fundamentally important in determining how likely the shock produced at bounce is to successfully traverse the outer core and cause an explosion. The bigger the difference, the more material the shock has to travel through and the more energy it loses on the way.

The structure of the matter in the core changes dramatically during collapse. When collapse begins, the nucleons are in the form of a gas of heavy nuclei, surrounded by a lower density gas of alpha particles and nucleons. The lower density gas occupies most of the space but is made up of only a small fraction of the material. The electrons also form a gas, evenly distributed in space, which supply the pressure (as the nuclear pressure is often negative).

The adiabatic index given by this arrangement of matter is  $\Gamma < 4/3$ , meaning that once core collapse has begun it is unable to stop until the equation of state becomes “hard”. This occurs when the material reaches  $\sim$  saturation density, *i.e.* the density of

uniform nuclear matter,

$$\rho_s = 0.16 \text{ fm}^{-3}, \quad (1.2)$$

and the adiabatic index abruptly increases to  $> 1.6$ . At this point the collapse of the inner core is halted, sending a shock outwards into the infalling outer core, “core bounce”. At the “maximum scrunch” of the inner core, the central density is around 3 times the density of nuclear matter.

### 1.5.1 Nuclear Pasta

At the beginning of collapse, when the central density is comparatively low, the nuclei behave as a gas and are spherical. As the density increases and the transition to nuclear matter takes place, between  $\sim 0.1\rho_s$  and  $\rho_s$ , the nuclei minimize their energy by changing shape. This is known as the “nuclear pasta” phase (Ravenhall, Pethick & Wilson 1983, Bethe 1990). As the density increases, the spheres deform into prolate spheroids which align parallel to each other. These spheroids elongate into long cylinders, which then join together to give alternating flat plates of nuclear material and nucleon gas (which consists mainly of neutrons that have “dripped” out of nuclei). After this phase the stages invert, so that spaghetti-like gas spaces form between nuclear matter, which shorten into spheroids and finally produce spherical bubbles of gas in nuclear matter - “Swiss cheese”. The transition from Swiss cheese to uniform nuclear matter occurs when the density is around  $0.8\rho_s$ .

The nuclear pasta phases were originally ascertained from phase diagrams of the equilibrium state of nuclear material. The core collapse environment, with rapidly increasing density, is far from equilibrium. Recently, computational investigations into whether these phases can arise during core collapse have been carried out, which show that they do indeed occur (Watanabe et al. 2005). This is an important result, as pasta phases increase the neutrino opacity of matter (Horowitz, Pérez-García & Piekarewicz 2004), which in turn affects the mass of the inner core and the success of the shock.

### 1.5.2 Effect of the Equation of State

Investigations have taken place into the effect the equation of state (EOS) has on the formation of the shock and the mass and fate of the compact remnant. It is known that at a density of  $\sim 3 \times 10^{14} \text{ g cm}^{-3}$  neutron degeneracy pressure causes the polytropic index to increase suddenly from  $\Gamma < 4/3$  to  $\Gamma > 1.6$ . However, how large  $\Gamma$  actually becomes remains uncertain.

It has conventionally been accepted that a softer EOS (i.e. a lower  $\gamma$  above nuclear densities) is favourable for the shock as it leads to a “deeper” bounce (larger maximum density). This is true up to a limit above which the mass inside the shock becomes greater than the maximum mass of a neutron star and collapse to a black hole ensues. Some constraint on possible EOS is provided by the requirement that this critical mass must be at least as large as the observed maximum mass of neutron stars,  $\sim 1.44 M_{\odot}$  (but see the recent discovery of a neutron star of  $2 M_{\odot}$  claimed by Nice et al. (2005) and references therein).

Early investigations into the effect varying the EOS has on the prompt explosion showed that a soft equation of state did indeed facilitate explosion (Baron, Cooperstein & Kahana 1985, Takahara & Sato 1988). In contrast to these results, Swesty, Lattimer & Myra (1994) argue that, when constrained by observation and experiment, altering the compressibility parameters in a realistic equation of state has very little effect on the radius at which the shock stalls.

In realistic supernova simulations which require a sophisticated treatment for the EOS, that of Lattimer & Swesty (1991) is commonly used. This employs a compressible liquid drop model for nuclei with an adjustable nuclear force that can be varied to take into account the experimental uncertainties. A more up-to-date calculation is provided by Shen et al. (1998*a*), Shen et al. (1998*b*) who use relativistic mean field theory to calculate the interactions between nuclei, alpha particles, protons and neutrons up to densities exceeding nuclear. However, it is still reasonably common for modellers to parametrize the EOS as a polytrope before bounce with a polytrope of a higher index plus a thermal component after bounce (see *e.g.* Dimmelmeier, Font & Müller (2002)).

Sumiyoshi et al. (2005) recently ran simulations comparing the Lattimer-Swesty (LS) EOS to the Shen EOS. They found that the shock was not affected until more than 200 ms after bounce. However, with the LS EOS a more compact neutron star was formed, with the central density almost a factor of two higher.

There is much we do not know about the behaviour of matter at extremely high densities. Experiments with particle accelerators, determination of the mass-radius relation for compact objects and computer simulations will all help to constrain models. Until then the exact behaviour of the core during and after bounce will remain uncertain.

## 1.6 Shock Launch and Revival

The sudden stiffening of the equation of state at nuclear densities halts collapse and causes the inner core to rebound. A shock forms and travels outwards through the mantle, which is still infalling. Material passing through the shock is slowed drastically and subsequently settles onto the central object.

As the shock wave moves outwards it raises the temperature and entropy of the material – temperatures of  $5 \times 10^9$  K are obtained in the mantle, resulting in nuclear statistical equilibrium and the formation of heavy elements. Nickel rather than iron is produced because  $Z/A \approx 1/2$ . (It is the  $\beta$ -decay of this nickel that produces the exponentially decaying light curve of the supernova.)

Early theories of supernova production assumed that the shock would propagate through the whole star and in so doing would launch the envelope to infinity. More recently it has become clear that this is unlikely to be the case. As the shock travels through the iron core it loses energy by dissociating iron nuclei at a cost of  $\sim 9$  MeV per nucleon. As the shock slows, energy loss through the emission of neutrinos also becomes significant. The upshot of this is that the shock slows to a stop at a radius of a few hundred kilometres, becoming an accretion shock as material outside it continues to fall in. Computer simulations have shown that in most instances (generally those with the most realistic physics) the shock fails between 100 and 200km (Bowers & Wilson 1982, Wilson 1985, Bruenn 1989*b*, Bruenn 1989*a*, Baron & Cooperstein 1990).

### 1.6.1 Supernova Energetics

At this point it is timely to discuss supernova energetics. The huge luminosity of a supernova is only a tiny fraction of the energy released in core collapse. In collapsing from a “white dwarf” radius  $R_{wd} \sim 1000$  km to a proto-neutron star  $R_{pns} \sim 20$  km the roughly  $M_c \sim 1.5 M_\odot$  iron core releases

$$\Delta E_{grav} \simeq -GM_c^2 \left( \frac{1}{R_{pns}} - \frac{1}{R_{wd}} \right) \sim -\frac{GM_c^2}{R_{pns}} \sim 3 \times 10^{53} \text{ erg} \quad (1.3)$$

of gravitational energy.

The “explosion energy”, which is the luminosity of the supernova integrated over time, is observed to be of the order of a few  $\times 10^{51}$  erg. The kinetic energy of the supernova ejecta, from observations that give the typical expansion velocity  $v_{exp} \sim 10^4$  km s<sup>-1</sup>

and for a  $M_* \sim 10 M_\odot$  star, is

$$\frac{1}{2}(M_* - M_c)v_{env}^2 \sim 10^{52} \text{ erg} . \quad (1.4)$$

Another  $10^{52}$  erg is absorbed in nuclear reactions. It can be seen from these figures that there is a large difference between the gravitational energy released in collapse and the observed total energy of the explosion. Where has this energy gone? The answer is provided by neutrinos, which are emitted from the collapsed core and quietly carry off the majority of the gravitational energy.

### 1.6.2 Shock Revival

Because of the dominance of neutrinos in the energetics of the explosion, it was suggested that the absorption of neutrinos might revive the stalled shock by heating the material behind (downstream of) it, at a radius of 100-200 km. To produce the explosion energies observed the neutrinos need to deposit around 5-10% of their energy in this region. Colgate & White (1966) found in their simulations that this mechanism produced explosions where the prompt shock did not, although the significance of this was not immediately realised. Like the shock, the idea of neutrino heating took some time to be revived, the pioneer of the delayed shock hypothesis being Wilson (1985), who began to include the effects of neutrino energy deposition in his simulations.

The dominant mechanism for neutrino absorption is neutrino capture on free nucleons so absorption happens in the region where the shock has dissociated nuclei. This is within a radius  $r \sim 200$  km. Neutrino trapping helps by delaying the emission of neutrinos until the shock has formed. Neutrino diffusion in the mantle is also important. Its effect is to heat up the mantle—the temperature of a typical mass element rises from around 10 to 40 MeV. This helps to set up a negative entropy gradient that may drive convection currents, which also help transfer energy to the shock.

Once the shock begins moving again there is a certain cut-off in enclosed mass below which material will end up on the proto-neutron star and above which it will be expelled by the explosion. At the radius where this division happens the density has previously been decreasing due to the material falling in. Bethe (1990) gives the density as a function of time from the beginning of infall as

$$\rho = \frac{10^7 C}{\alpha t r_7^{3/2}} \quad (1.5)$$

where  $\alpha$  is a coefficient between 1/2 and 1,  $C$  is between 1 and 10 and  $r_7$  is the radius in units of  $10^7$  cm. This gives a density of around  $10^7$  g cm $^{-3}$  at  $r_7 = 1$  and  $t = 1$  s, very low compared to the core density of around  $10^{14}$  g cm $^{-3}$ . Once the shock has passed through and heated the material, most of the energy is held in radiation and electron-positron pairs. This cavity of radiation continues to drive the shock.

Since neutrinos are so important in mediating the energy transfer, it is important that they are modelled correctly in numerical simulations. This is the biggest challenge for the supernova community. There is a wealth of transport mechanisms for neutrinos, including absorption/emission from free nucleons, absorption/emission from nuclei, scattering,  $e^+e^-$  annihilation (pair and plasmon decay) and  $\nu\bar{\nu}$  annihilation. Even when the neutrino transport is handled by approximation, each of these must be taken into account and the rates calculated before a decision is made about whether or not to include its effects in the simulations. Full Boltzmann transport in one dimension is only just arriving (Liebendörfer et al. 2004, Liebendörfer et al. 2005, Rampp & Janka 2002). Its development is complemented by less sophisticated but improving methods in two dimensions (Livne et al. 2004, Buras et al. 2003). As I will discuss in the following sections, a full handling of neutrino transport is necessary but may not on its own even be sufficient for producing explosions.

### 1.6.3 Fate of the Compact Remnant

There is a critical stellar mass above which a black hole rather than a neutron star will be formed from core collapse. At present the location of this boundary is very poorly constrained. Fryer (1999) simulated the collapse of stars of different masses and identified three possible outcomes: formation of a neutron star by a strong explosion of a low mass star with little fallback; formation of a black hole by fallback after a successful explosion; and direct collapse of a massive star to a black hole, with no resultant explosion. He found that the transition region above which black holes were formed by fallback was around 18-25  $M_\odot$ . Stars greater than  $\sim 40 M_\odot$  were found to produce black holes by direct collapse. Assumptions about the initial mass function of the stars gave the ratio of black hole to neutron star formation in the Galaxy as 1.5%.

Metallicity affects mass loss rates and therefore the mass of the star at collapse. The effect of metallicity on the mass boundaries for different collapse outcomes was investigated by Heger et al. (2003). They found that if the metallicity is increased the boundaries can fall at significantly higher masses. Above solar metallicity mass loss may be high enough to prevent black hole formation completely.

It has been suggested that rotation may also be a determinant of the fate of the compact remnant (Akiyama & Wheeler 2005). In this scenario neutron stars are formed only in a transition region where rotation is strong enough for jets to form and assist explosion but not strong enough to cause the core to bounce “centrifugally”, producing a weak explosion with fallback. Predictions of the outcome of core collapse from initial stellar mass are evidently poorly constrained and uncertain.

## 1.7 Importance of Three Dimensional Effects

As neutrino transport in one dimensional simulations improved it became clear that the conditions therein were not sufficient to produce explosions. Even with neutrino heating the shock could not be imparted with enough energy to eject the envelope (Bruenn 1989a,b, Myra & Bludman 1989, Wilson 1985). A consensus is forming that higher dimensional effects are necessary to drive successful supernova explosions.

It is not unreasonable to expect that non-spherical effects should be important. Observations of core collapse supernovae have revealed that asymmetry is ubiquitous. Supernova remnants close enough to observe are rarely perfectly spherical, examples being the aptly-named guitar nebula or the off-centre rings around 1987A. Further evidence of asymmetry comes from measurements of the polarisation of supernova light, which is typically around 1% (Wang et al. 2003, Wang et al. 2001, Wang et al. 1996, Leonard et al. 2002, Leonard et al. 2001, Leonard et al. 2000). This gives the axial ratio of the ejecta as around 2:1. In addition, the degree of polarisation increases with decreasing envelope mass, implying that the asymmetry is stronger with increasing depth inside a star.

Observations of the proper motions of neutron stars give a distribution with a tail extending past  $\sim 500\text{-}1000 \text{ km s}^{-1}$ . It is possible that the distribution is actually bimodal with the second peak at  $\sim 500 \text{ km s}^{-1}$  (see Arzoumanian, Chernoff & Cordes (2002) and references therein). Velocities of this magnitude cannot arise from the orbital motion of a broken binary system and their explanation is presumed to lie in the supernova mechanism. Further evidence for NS “kick velocities” comes from the often off-centre positions of pulsars relative to their surrounding supernova remnants, for example the neutron star in Cas A (Thorstensen, Fesen & van den Bergh 2001).

A good review of the competing models for the production of neutron star kicks has been written by Lai (2003). These can be grouped into three categories:

- hydrodynamically driven by instabilities or oscillations in the core;



FIGURE 1.6. Hubble Space Telescope image of the highly aspherical supernova remnant N63A Menagerie.

- neutrino-magnetic field driven, in which neutrinos are emitted asymmetrically from the core due to magnetic fields;
- electromagnetically driven, where the kick is produced after explosion by a rotating, off-centred magnetic dipole.

In addition to direct observations of asymmetric systems, strong evidence for the occurrence of mixing before or during the explosion comes from observations of the gamma ray emission of SN1987A. Gamma rays are emitted from the decay of  $^{56}\text{Co}$ , itself a decay product of the  $^{56}\text{Ni}$  produced in the core. The gamma ray maximum was observed at around 350 days, much earlier than it would have had the nickel remained at the bottom of the envelope where it was produced.

With this evidence in mind, the following subsections discuss the most likely causes of asymmetry in supernovae.

### 1.7.1 Convection

As the shock expands into less dense regions the entropy gradient  $dS/dr$  just behind it becomes negative, enabling convection to set in. The Ledoux criterion for convection is (Bethe 1990):

$$\frac{dS}{dr} + \frac{(\partial\rho/\partial Y_e)_{p,S}}{(\partial\rho/\partial S)_{p,Y_e}} \frac{dY_e}{dr} < 0 \quad (1.6)$$

where  $\rho = \rho(p, S, Y_e)$ . Generally

$$\left(\frac{\partial\rho}{\partial S}\right)_{p,Y_e} < 0 \quad (1.7)$$

$$\left(\frac{\partial\rho}{\partial Y_e}\right)_{p,S} < 0 \quad (1.8)$$

so that Equation 1.6 becomes

$$\frac{dS}{dr} + a \frac{dY_e}{dr} < 0 \quad (1.9)$$

where  $a$  is positive.

In the prompt shock model, this criterion is generally satisfied. In the delayed shock model, after the shock has been revived  $dY_e/dr$  is negligible and convection will always occur.

Convection helps the shock by transporting energy from the heated material at 100-200 km to the shock front. Shocked material can continue to accrete at the same time as the shock gains energy. Fingers of cool material flow downwards towards the proto-neutron star in between hot bubbles of buoyant material, which drive the shock outwards.

Early two-dimensional models did indeed show vigorous convection taking place and eventually launching an explosion (Burrows, Hayes & Fryxell 1995, Herant et al. 1994, Fryer 1999). This result was repeated in three dimensional models (Fryer & Warren 2004). However, the simplified, “grey”, neutrino transport used in these models is thought to increase the neutrino energy deposited behind the shock. Buras et al. (2003) employed more accurate neutrino transport in their two dimensional simulations. They found that convection gave a transient increase in the shock radius but was not strong enough to produce an explosion, although it came tantalisingly close. It must be noted that the angular extent of their simulations was  $\pi/4$ , meaning that any possible instabilities that cause the polar,  $l = 1$  mode to grow would not be observed.

The validity of this approach was called into question by Janka et al. (2005a,b) who ran simulations with an angular extent of  $\pi/4$  and  $\pi/2$ . They found that when the  $\pi/2$

segment was used the  $l = 1$  mode was able to grow, ultimately driving an explosion. This result is reminiscent of that of Blondin, Mezzacappa & DeMarino (2003) (and more recently Blondin & Mezzacappa (2005)), where the stability of a spherical standing accretion shock (SAS) was studied in two dimensions. The SAS consists of a spherical shock surrounding a radiation cavity with an absorbent inner boundary, and approximately describes a stalled supernova shock. They found that small perturbations to the shock front caused instabilities to grow due to the infalling material hitting the perturbed shock at oblique angles. This led to turbulence within the shock, which occurred even with flat or positive entropy gradients there, conditions stable to convection. In particular, it was found that the  $l = 1$  mode grows and forces the shock to expand. This effect was not found in a previous one dimensional study (Houck & Chevalier 1992), which hints that there may be further, unexpected multi-dimensional effects yet to be discovered.

### 1.7.2 Rotational effects

An obvious effect that cannot be included adequately in one-dimensional models of core collapse is rotation. It is common sense to assume that rotation plays some sort of role, since observations of massive stars show that they rotate with equatorial velocities of hundreds of kilometres per second (Halbedel 1996, Penny 1996, Fukuda 1982). The remnants of core collapse, neutron stars, are observed as pulsars with rotation periods of a fraction of a second. Magnetars – strongly magnetized neutron stars – may have had their fields produced by rotational effects.

Rotation also gives rise to instabilities which may help to explain observations of supernovae. As mentioned in Section 1.7, in SN1987A the decay of  $^{56}\text{Co}$  was observed earlier than would have been possible had mixing not taken place. Mixing instabilities caused by rotation, such as the dynamical shear instability or the Solberg-Høiland instability, may have been responsible.

As well as being useful for explaining the observed asymmetries in supernovae, rotational energy may be harnessed to make supernova explosions successful. There are a number of ways in which rotation may enhance the explosion:

- The centrifugal force produced by rotation reduces the “effective gravity”, which allows the shock to reach a larger radius before stalling. This results in a larger gain region in which neutrino heating can take place.
- Neutrino heating is enhanced along the poles relative to the equator due to the neutrinospheres becoming non-spherical.

- Infall proceeds more quickly at the poles than at the equator, creating a funnel of low density material along which the shock can propagate more easily.
- Rotation induces vortices which could dredge up heat from below the neutrinospheres to power the shock.

The second and third of these factors will dominate in the presence of strong rotation and are likely to produce an explosion that is stronger along the poles. Slower rotation, even if it is insufficient to drive an explosion in this way, could lower effective gravity enough in the equatorial region to induce an equatorial explosion.

It is known that a positive angular momentum gradient can suppress convection (Endal & Sofia 1978). This effect is evident in the more rapidly rotating simulations of Fryer & Heger (2000) and Fryer & Warren (2004). However, rather than weaken the shock, the suppression of convection at the equator led to a dominant  $l = 1$  convective mode and subsequent polar explosion.

Rotation is likely to enhance the neutrino heating mechanism. Shimizu et al. (2001) found that anisotropic neutrino emission would increase the vigour of convective overturn, thus driving the shock more strongly. The simulations of Kotake, Yamada & Sato (2003a) showed that neutrino emission is enhanced by rotation due to deformation of the neutrinospheres, with neutrino heating rates an order of magnitude higher along the rotation axis than at the equator. Madokoro & Shimizu (2004) investigated the effect of setting the neutrino emission to be stronger at either the equator or the poles. They found that this produced oblate and prolate explosions respectively, of which the prolate explosions were more energetic.

It has also been proposed that supernovae may be powered in part by magnetohydrodynamic (MHD) jets. Differential rotation in the core of a collapsing star might rapidly enhance its magnetic field via the magneto-rotational instability (MRI), which goes on to drive polar jets (Akiyama et al. 2003, Höflich, Wheeler & Wang 1999). If this is indeed the case, in rare cases of very rapid rotation MHD processes could dominate the explosion, the rapidly-moving jets giving rise to a hypernova or gamma ray burst, depending on how much of the envelope remains. These phenomena will be discussed in Section 1.8 below.

Might there be two mechanisms for producing explosions - both neutrino heating and MHD jets? This possibility is discussed by Burrows et al. (2005) (and references therein). The authors prefer the “neutrino-driven mechanism, perhaps with rotation”, with explosions that would otherwise fail being enhanced to the point of success (and

correct explosion energies) by moderate amounts of rotation (a “rotation boost”). They speculate that for a minority of cases, those with rapid rotation, MHD could be “dynamically influential”. Weak jets would form and become evident after the explosion by modifying the shape of the debris.

Other groups argue that there is no need for jets except in very extreme circumstances (Janka et al. 2005a,b). They claim that while some rotation is helpful, rapid rotation is not necessary for successful explosions with the neutrino-driven mechanism.

Rotation will also affect the compact remnant. A neutron star of above the Chandrasekhar mass may be formed and supported by differential rotation, delaying collapse to a black hole. A centrifugally-supported accretion disc may form during the collapse which is able to power a jet (Section 1.8). At the densities achieved at core bounce, rotation produces gravitational wave emission, especially if the core becomes unstable to triaxial deformations. Many groups are investigating the gravitational wave signatures produced by rotational collapse (Ott et al. 2004, Rampp, Mueller & Ruffert 1998, Shibata & Sekiguchi 2005).

## 1.8 Gamma Ray Bursts

Possibly the foremost astronomical mystery of our time is the origin of gamma ray bursts (GRB). Outshining the whole gamma ray sky for their duration, these flashes of radiation occur roughly once a day. They may last for an amount of time ranging from a fraction of a second to several hours, with variations in intensity on a timescale of milliseconds.

GRB were discovered in the 1960s by the American Vela satellites and rumour has it that they were thought to be evidence of the Russians performing nuclear tests on the moon. Once this was ruled out and their existence de-classified it was thought that they might be related in some way to supernovae. The original paper describes a search for supernovae coincident in time with the GRB, in which none were found (Klebesadel, Strong & Olson 1973).

As the number of observed GRBs has accumulated, it has become evident that they have a bimodal distribution in duration (Kouveliotou et al. 1993), with the transition occurring at  $\sim 2$ s (see Figure 1.7). Long GRBs, which generally have softer X-ray spectra than short GRBs, are defined as having a duration of  $> 2$ s.

The first afterglow for a GRB was discovered by the X-ray satellite BeppoSAX (Costa et al. 1997, van Paradijs et al. 1997, Frail et al. 1997). Further pinpointing of

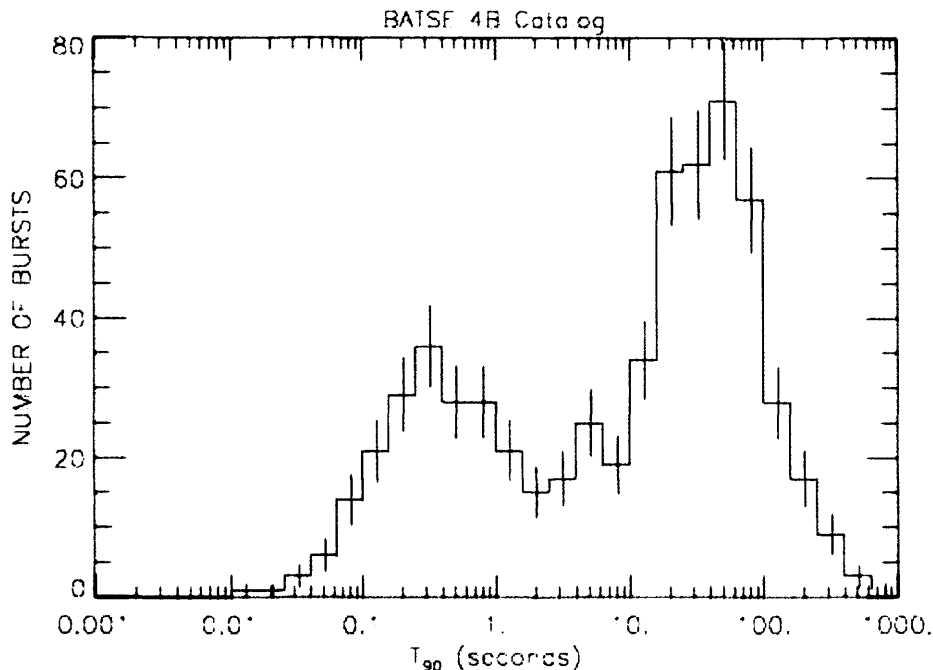


FIGURE 1.7. Distribution of the durations of GRB detected by the Burst and Transient Source Experiment (BATSE) on board NASA's Compton Gamma-Ray Observatory.  $T_{90}$  is the time from which 5% to 95% of the total measured counts for a burst are detected. The distribution shows two distinct peaks, occurring at  $\sim 0.3$  and  $\sim 30$  seconds.

the locations of long GRB revealed them to be distributed isotropically, hinting at a cosmological origin which was later confirmed by observations of the afterglow redshifts (Metzger et al. 1997). Not all long GRB have been observed to be followed by X-ray and/or optical afterglows and no afterglows at all had been discovered for short GRB prior to the launch of the Swift satellite in November 2004. Swift has since found afterglows for 2 of the 4 short bursts it has detected (Gehrels 2005, Barthelmy 2005).

Once the distances to GRB had been ascertained another problem became apparent – if the luminosity of a GRB was assumed to have been emitted isotropically, its total energy would be around  $10^{54}$  erg. Temporal variations in the burst can be no shorter than the light crossing time, meaning that all this energy must come from a compact area of less than a few hundred kilometres in diameter. There is no known mechanism for producing this much energy in so small a space – an order of magnitude more than the total energy released in core collapse.

This dilemma seems to have been solved by the “fireball” model of GRB, in which a low density plasma is emitted in a narrow jet from the central engine (whatever that may be). The gamma rays are produced by the annihilation of electron-positron pairs and can

only be observed when the line of sight is along the jet. These jets may have Lorentz factor  $\Gamma \simeq 1000$ , blueshifting the gamma rays emitted to the high energies observed.

### 1.8.1 The Supernova–GRB Connection

Despite the original non-observation of coincident supernovae, a link has now been established between supernovae and the long GRB. Bumps have been identified in afterglow light curves at late times and attributed to the peak of the light from the underlying supernovae (Bloom et al. 1999, Zeh, Klose & Hartmann 2004).

The SN–GRB connection was given credibility with the discovery of supernova SN1998bw in the error box of GRB 980425 (Galama et al. 1998). However, this GRB had an unusually small redshift of  $z = 0.0085$ , revealing it to be located at less than cosmological distances and underenergetic by 4 orders of magnitude compared to the “normal” GRB. In addition to this, the Type Ib/c SN1998bw was also observed to be unusual, with expansion velocities 3–4 times higher than a normal Ib/c and a peak luminosity about 10 times brighter. Explanations offered were that the supernova was the product of the C/O core of a star of originally  $40 M_{\odot}$  that had had its envelope stripped, or alternatively, that the explosion was bipolar and viewed along the jet (Höflich et al. 1999).

Clinching evidence for a relationship between supernovae and GRB came in April 2003 when supernova SN2003dh was discovered spectroscopically in the afterglow emission of GRB 030329 (Stanek et al. 2003). The redshift of  $z = 0.1685$  placed it relatively nearby, and the supernova spectrum bore a very close resemblance to that of the unusual SN1998bw. It therefore seems likely that GRB are produced by an unusual class of supernovae, possibly with small envelopes and rapid rotation. Hypernovae may also form part of this class. The observation that the host galaxies of long GRB have high levels of star formation (Christensen, Hjorth & Gorosabel 2004) and that the locations of GRB within these galaxies are within regions of star formation (Bloom, Kulkarni & Djorgovski 2002) provides further support for a link between GRB and massive stars.

There have been claims that lines due to iron and other metals have been observed in the X-ray spectra of GRB afterglows (Reeves et al. 2002, Antonelli et al. 2000, Piro et al. 1999). The validity of these claims has been highly contested, but if true, they imply a delay between the supernova explosion (which may take several days to reach an observable magnitude) and the launch of the GRB. This scenario would support the “supranova” model proposed by Vietri & Stella (1998), in which the GRB is launched by the collapse of a neutron star to a black hole months after the supernova explosion.

However, estimations of the time lag for a collection of GRB with associated supernovae show little evidence of a delay (see Della Valle (2004) and references therein).

### 1.8.2 The Collapsar Model

Today, the leading model for the origin of long GRBs is the “collapsar” (Woosley 1993, Paczynski 1998, MacFadyen & Woosley 1999). In this model, the core collapse of a massive, rapidly rotating star produces a black hole (either immediately or after fall-back of material from the stalled shock) surrounded by a centrifugally supported accretion disc. Accretion continues as material falls in from further out in the star, lasting for tens of seconds. The energy released by accretion is channelled by neutrino annihilation or MHD effects into high Lorentz factor jets that punch through the central regions of the star. The energy dissipated by the disc may contribute to a partial or full supernova explosion, or the supernova may “fail” entirely and the star collapse into the black hole. A schematic diagram of a collapsar can be found in Figure 1.8.

The jet becomes what is observed as a GRB once it has emerged from the star and the gamma rays are thought to be produced by internal shocks. Current thinking is that the large envelope of a supergiant would attenuate the jet too much and that massive stars which have lost their envelopes (Wolf Rayet stars) are the most likely GRB progenitors (Zhang, Woosley & Heger 2004).

### 1.8.3 One Lump or Two?

A uniformly rotating spheroid will become dynamically unstable to triaxial (bar-like) deformations if its ratio of rotational to gravitational energy  $\beta = T/|W| > 0.27$ . For a differentially rotating body, such as the core of a collapsing star, this ratio may be much lower. Since  $\beta$  will increase as the core of a star collapses, it is plausible to imagine that with a moderate amount of rotation the collapsing core may become bar-like.

It was pointed out by Bonnell & Pringle (1995) that during star formation, the collapse of prestellar cores can result in fragmentation of the core and that similar processes may take place during supernova collapse. Up-to-date models of rotating supernova progenitors (Heger, Langer & Woosley 2000) have core angular momenta immediately before collapse equivalent to those of neutron stars rotating close to break-up, making fragmentation a bewitching possibility.

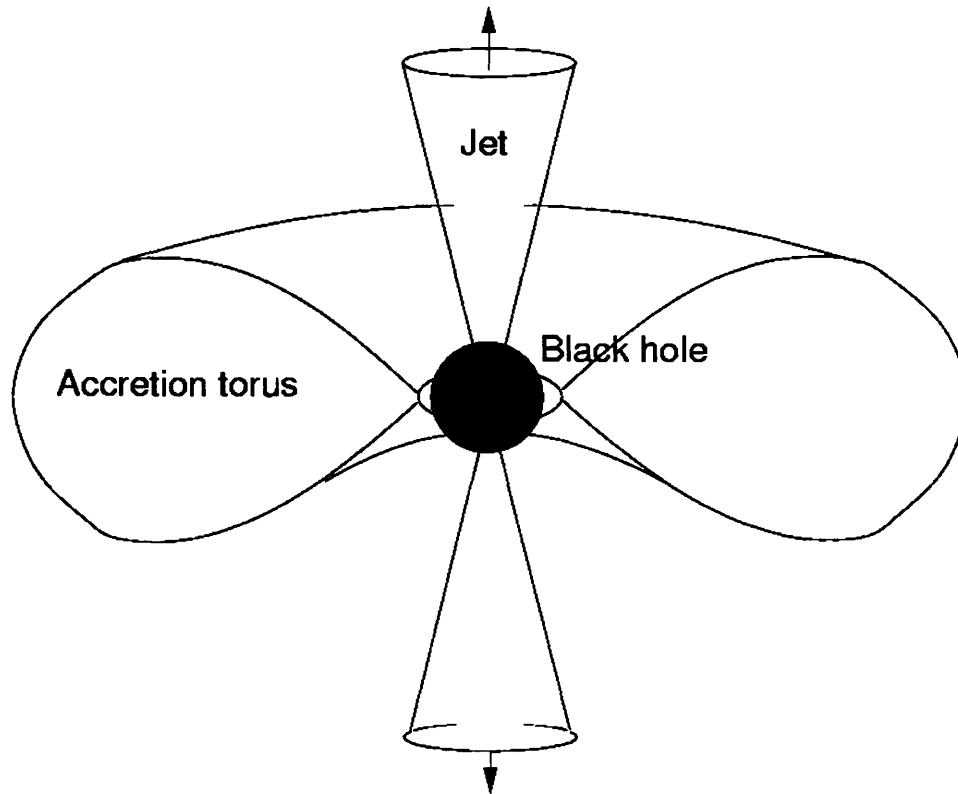


FIGURE 1.8. Schematic diagram of a collapsar. The stellar core has collapsed along the poles to produce a black hole surrounded by a torus of centrifugally supported material. The energy released through accretion drives jets along the evacuated poles.

The idea of core fragmentation was expanded by Davies et al. (2002). If the core of a collapsing star fragmented at around the time of bounce, the “lumps” would be of nuclear density. A system of two lumps would be akin to a binary neutron star system, with the lumps spiralling inwards under the emission of gravitational radiation, and merging through a period of unstable mass transfer towards the end of the inspiral. The transfer of mass could produce substantial ejecta, giving the merged object a recoil velocity.

This scenario was put forward as a possible explanation for two separate problems. The first was neutron star kick velocities, which could be explained by the recoil of the merged lump from its ejecta. The second, which would occur only in the absence of the first, was that the merged lump and ejecta could form a black hole and accretion disc which could power a GRB. The beauty of this method of production is that it would give a delay between the supernova and the GRB due to the time taken for the lumps to inspiral, which could be several hours. Alternatively, the larger of the lumps may itself produce a GRB that is reignited after a delay by the tidal shredding and accretion of

the second lump. It has been suggested that this is what occurred in the case of GRB 050502b, for which a highly energetic X-ray flare was detected 400 s after the initial burst (King et al. 2005).

This idea is the subject of much current research – core collapse simulations showing secular instabilities in the core (developing on timescales greater than the dynamical timescale) have been undertaken by Rampp et al. (1998) and a transient fragmentation has been found by Shibata & Sekiguchi (2005). However, in other three dimensional simulations the cores have not obtained the rotational energies required for fragmentation, as high angular momentum material is prevented from falling in by the centrifugal force (Fryer & Warren 2004).

## 1.9 Supernovae in Binary Systems

The ratio of Type II to Type Ib/c supernovae is highly uncertain – between 1.2 and 16 in spiral galaxies, depending on the type (Cappellaro et al. 1997). Estimates of the fraction of Type Ib/c supernovae that produce GRB are also highly uncertain, given the dependence of the number of events observed on the beaming of the jets. Radio observations give this fraction as less than 5% (Berger et al. 2003), while optical observations put it at less than 1% (Podsiadlowski et al. 2004). GRB are clearly an extremely rare form of core collapse and their production must therefore require an extraordinary set of conditions.

Indeed, the conditions required for a collapsar are stringent:

- The stellar core must collapse to a black hole - this will result in no, or a weak, explosion initially.
- The star must have enough angular momentum for infalling material to form a disc around the black hole. The specific angular momentum required in the core before collapse is  $\gtrsim 3 \times 10^{16} \text{ cm}^2 \text{ s}^{-1}$  (MacFadyen & Woosley 1999).
- The star must have lost its hydrogen envelope in order for the jet to remain relativistic as travels through the star.

It is thought that, in the absence of mass loss, stars with masses in excess of 18-25  $M_{\odot}$  will collapse to black holes (Fryer 1999). Even when envelope loss is considered there will still be enough stars that will collapse to black holes to explain the rate of GRB/hypernovae. The problem the loss of the envelope introduces is that with it is lost angular momentum. It is not clear whether single stars that lose their envelopes will

retain enough angular momentum to form an accretion disc (Heger et al. 2000, Petrovic et al. 2005).

It is very likely that a plausible scenario for the production of GRB lies within the parameter space of binary systems. Mass transfer at various stages in the evolution of the system can dramatically affect the final mass of the core, the amount of mass loss, the rate of rotation and the final fate of the star (Podsiadlowski 1992). Pfahl et al. (2002) have suggested that stars which lose their hydrogen envelopes by mass transfer soon after leaving the main sequence may avoid losing their angular momentum in a stellar wind.

Fryer, Woosley & Hartmann (1999), inspired by a proposed model for the formation of SN1987A (Podsiadlowski 1992), suggested that a common envelope phase in a binary system could result in the merging of the stellar cores and ejection of the envelope. This scenario requires the stars in the binary to have very similar masses, so that the first common envelope phase, when the larger star evolves off the main sequence, does not lead to a merger of its helium core with the secondary star. Instead, before this can happen the secondary star evolves off the main sequence and the two helium cores merge in a second common envelope phase. In merging, a proportion of the orbital angular momentum of the system becomes the spin of the merged object, fulfilling the condition for production of a GRB. Binaries of almost equal masses may form very rarely but often enough to explain the observed rates of GRB and hypernovae.

In order to explore the plausibility of this scenario, Fryer & Heger (2005) simulated such a merger. Two stars were evolved individually to the point where the merger begins, the end of the main sequence phase. At this point, the results of the stellar evolution calculations were mapped to a three dimensional hydrodynamics code (SPH – see Chapter 2) to model the merger of the helium cores. The merged core was then mapped back into the stellar evolution code and evolved until the onset of core collapse.

The authors performed their calculations using three different binary systems:  $8 M_{\odot} + 8 M_{\odot}$ ;  $8 M_{\odot} + 16 M_{\odot}$ ; and  $16 M_{\odot} + 16 M_{\odot}$ . They experienced difficulties in switching between the codes, which resulted in them testing several different methods for controlling the post-merger conditions. In most cases, both the  $8 M_{\odot} + 16 M_{\odot}$  and  $16 M_{\odot} + 16 M_{\odot}$  models produced black holes. All of the models that formed black holes had enough angular momentum to form an accretion disc and some had 3-10 times the core angular momentum of single massive stars. Although many approximations were made in order for these calculations to be possible, the results give credence to the possibility that GRB result from binary mergers.

## 1.10 Summary

The advent of three dimensional simulations has and will improve our knowledge of how SNe explode. It will be possible to determine whether explosions are made possible by three dimensional effects such as neutrino-driven convection. Modellers will be able to study the effects of asymmetry on explosion energies, chemical composition and mixing, as well as instabilities and asphericity caused by rotation. The mechanism and likelihood of jet formation may be established, helping us to understand whether they play an important role in enhancing explosions and what it is that powers the engines of GRB. The future is bright, and much awaits discovery.

In this thesis I take a step towards that future by running three dimensional simulations of the core collapse of rotating stars. I use the computational method of Smoothed Particle Hydrodynamics to follow the collapse of sophisticated progenitor models with a variety of rotation rates up until core bounce. In some models I enhance the rotation to resemble that of a progenitor formed from a merged binary. I am especially interested in the prospect of core fragmentation, or otherwise creating conditions suitable for producing GRB. I therefore pay particular attention to the structures formed and how the ratio of rotational to gravitational energy grows as the collapse proceeds.

In Chapters 2 and 3 the numerical method used and its adaptation to this problem is described. This is followed in Chapter 4 by tests of the code on a control model with rotation added using a simple parametrization. State-of-the-art rotating progenitor models are used in Chapter 5 to investigate core collapse with various rotation rates, the fastest of which is close to Keplerian. The gravitational wave signals produced in the collapse are described in Chapter 6 and a brief summary of all the results is provided in Chapter 7.

# Chapter 2

## *Numerical Method*

“I would’ve said you weren’t a geek because you always express a dislike of computers.”

*Roger Light*

## 2.1 Introduction

Since the first simulations of gravitational core collapse in massive stars were performed by Colgate & White (1966), vast progress has been made in both high energy astrophysics and computing. Early supernova codes were one dimensional, employing 100 or so zones, progenitors were modelled as simple polytropes and approximate terms for neutrino emission and deposition were used. These days, when considering what to include in their codes, supernova modellers take their pick from multi-energy, multi-dimensional neutrino transport, multi-dimensional hydrodynamics, rotation, magnetic fields, general relativity and the latest equations of state for nuclear matter (although the day when it will be possible to include them all is still far off). The end products of sophisticated stellar evolution models are used as a starting point for collapse. The ability to model such a complex variety of physical effects is a result of the vast increases in the speed and performance of computers. In addition to single processor machines, parallel computers which run programs on multiple processors enable simulations that use millions of fluid elements.

In this chapter I describe the hydrodynamics code I use to simulate core collapse in massive stars. The code is that of Rosswog (Rosswog & Davies 2002), which has been run on various multi-processor machines, including the 128-processor U.K. Astrophysical Fluids Facility (UKAFF), to perform high resolution, three dimensional simulations of merging neutron stars. This code is tailor-made for modelling fluids at neutron star densities, which are of the same order as the maximum density obtained in core collapse supernovae, just over  $10^{14}$  g cm<sup>-3</sup>. Despite this, significant modifications to the code were required to make it suitable for my simulations. I will discuss these modifications and the initial conditions used for my simulations in chapter 3.

In this chapter I will discuss the equations of fluid dynamics and their conversion to the form used in the hydrodynamics code, a scheme known as Smoothed Particle Hydrodynamics. I will describe the implementation of the “tree” structure used for evaluating the gravitational forces. I will also touch briefly on how the code is adapted for use on a parallel computer.

## 2.2 Equations of Fluid Dynamics

The behaviour of a fluid is governed by the three conservation laws — those of mass, momentum and energy. A full derivation of these laws can be found in many texts,

including Landau & Lifshitz (1959).

The Mass Conservation or Continuity Equation accounts for changes in density caused by the transport of mass and can be stated as

$$\frac{\partial \rho}{\partial t} + \nabla \cdot (\rho \mathbf{v}) = 0, \quad (2.1)$$

*i.e.* a positive divergence in mass flux at a fixed reference point results in a decrease in the mass density at that point.

The Equation of Momentum Conservation is the fluid equivalent of Newton's second law, with fluid elements rather than objects being accelerated and density rather than mass taken as the measure of inertia. In addition to any net external force, an element of fluid will be accelerated by a pressure difference between its surfaces. Expressed at a point, this difference becomes the gradient of the pressure:

$$\rho \left[ \frac{\partial \mathbf{v}}{\partial t} + (\mathbf{v} \cdot \nabla) \mathbf{v} \right] = -\nabla P + \mathbf{f}. \quad (2.2)$$

Here, the vector  $\mathbf{f}$  includes all other forces per unit volume.

The third conservation law of fluid dynamics is that of energy. In addition to the macroscopic potential and kinetic energies of a fluid element, which depend on its density and velocity, it also possesses microscopic, internal energy, related to its pressure, density and temperature. The equation of energy conservation is

$$\frac{\partial}{\partial t} \left( \frac{1}{2} \rho v^2 + \rho u \right) + \nabla \cdot \left[ \left( \frac{1}{2} \rho v^2 + \rho u + P \right) \mathbf{v} \right] = \mathbf{f} \cdot \mathbf{v} - \nabla \cdot \mathbf{F}_{rad} - \nabla \cdot \mathbf{q}. \quad (2.3)$$

The left hand side of this equation expresses the kinetic, internal and potential energies of the fluid. The right hand side includes mechanisms whereby energy is transported to or from a fluid element: the work done by forces and energy carried away by radiation and heat conduction. In the adiabatic case with no external forces Equation 2.3 simplifies to

$$\frac{\partial u}{\partial t} + (\mathbf{v} \cdot \nabla) u = -\frac{P}{\rho} \nabla \cdot \mathbf{v}. \quad (2.4)$$

In the equations 2.1, 2.2 and 2.4 above, the time derivatives of the fluid variables are for a "fixed" frame of reference, independent of the flow. This is known as the Eulerian formulation. The time derivative of a fluid variable can also be expressed as a Lagrangian – the derivative in a frame moving with the fluid, along a flow line. Transformations from a fixed to a Lagrangian frame will therefore involve the bulk velocity of the fluid. For

any quantity  $Q$  the Lagrangian derivative is

$$\frac{DQ}{Dt} = \frac{\partial Q}{\partial t} + (\mathbf{v} \cdot \nabla)Q \quad (2.5)$$

The continuity equation therefore becomes

$$\frac{D\rho}{Dt} + \rho \nabla \cdot \mathbf{v} = 0 \quad (2.6)$$

and converting the remaining equations, 2.2 and 2.4, into Lagrangian form gives

$$\rho \frac{D\mathbf{v}}{Dt} = -\nabla P + \mathbf{f} \quad (2.7)$$

$$\frac{Du}{Dt} = -\frac{P}{\rho} \nabla \cdot \mathbf{v} . \quad (2.8)$$

The set of equations above can be completed by the equation of state, which gives the pressure as a function of the density and temperature or internal energy, rendering a completely deterministic description of the fluid.

## 2.3 Smoothed Particle Hydrodynamics

Smoothed Particle Hydrodynamics (SPH) is a numerical scheme which takes advantage of the simplicity of integrating the Lagrangian equations of fluid dynamics over time. It was first used by Lucy (1977) to model the fission of a rotating protostar and has since been developed as a tool for modelling a wide variety of astrophysical fluids.

In SPH a fluid is represented by a collection of elements, or “particles”, each with its own mass. The local density of the fluid relates to both the mass of the particles and the number density. If the particles have equal masses, the mass density is directly proportional to the number density.

SPH particles are not point masses - their properties are “smoothed” spatially. The function that gives the spatial distribution of the particle, or how the particle is smoothed, is called the kernel. It can be helpful to envisage the particles as overlapping, with the value for a property of the fluid given by the sum of the contributions from all particles at that point (see Figure 2.1). This is the “scatter” interpretation and the one I choose to use in this chapter. (There is an alternative interpretation of the mathematical formulation, which I will discuss in Chapter 3.) Below I give a summary of the SPH equations used by my code. More detailed reviews, with discussion of the relative merits of different forms

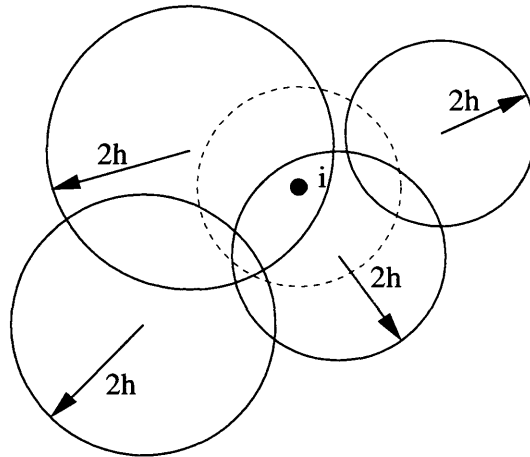


FIGURE 2.1. SPH particles are smoothed over a radius  $2h$ . The density of particle  $i$  is the sum of the densities of all other particles at its centre.

of the equations, can be found in Benz (1990), Monaghan (1992) and more recently in the PhD thesis of Price (2004).

### 2.3.1 SPH Representation of a Variable

Consider a fluid variable  $f(\mathbf{r})$ . This function can be approximated by the integral

$$\langle f(\mathbf{r}) \rangle = \int W(\mathbf{r} - \mathbf{r}', h) f(\mathbf{r}') d\mathbf{r}' \quad (2.9)$$

where

$$\int W(\mathbf{r} - \mathbf{r}', h) d\mathbf{r}' = 1. \quad (2.10)$$

$W$  is the kernel and  $h$  is a measure of its extent, known as the “smoothing length”. If  $W$  is chosen to be strongly peaked at  $\mathbf{r}' = \mathbf{r}$  then

$$\lim_{h \rightarrow 0} W(\mathbf{r} - \mathbf{r}', h) = \delta(\mathbf{r} - \mathbf{r}') \quad (2.11)$$

and, as  $h \rightarrow 0$ ,

$$\langle f(\mathbf{r}) \rangle \rightarrow f(\mathbf{r}). \quad (2.12)$$

We can discretize equation 2.9 for a collection of discrete points  $\mathbf{r}_j$  at which the value

of  $f$  is known, so that

$$\langle f(\mathbf{r}) \rangle = \sum_{j=1}^N \frac{m_j}{\rho_j} f(\mathbf{r}_j) W(\mathbf{r} - \mathbf{r}_j, h) \quad (2.13)$$

Here the mass  $m_j$  of each point, or particle, is defined such that  $\frac{\rho_j}{m_j}$  represents the number density of the particles. The reciprocal of this term replaces the volume term  $d\mathbf{r}'$  of the original integral. At particle  $i$ , the summation becomes

$$f_i = \sum_{j=1}^N \frac{m_j}{\rho_j} f_j W_{ij} \quad (2.14)$$

where  $f_i = \langle f(\mathbf{r}_i) \rangle$  is any property of the fluid at  $i$  and  $W_{ij} = W(\mathbf{r}_i - \mathbf{r}_j, h)$ . This is the basic SPH summation.

Applying this to the density at particle  $i$  we obtain

$$\rho_i = \sum_{j=1}^N m_j W_{ij} . \quad (2.15)$$

It follows that the kernel represents the density distribution of a single particle. The density at particle  $i$  is given by the sum of the densities of all other particles  $j$  at  $i$  (Figure 2.1). Usually the kernel is limited so that the particle has a finite extent, *i.e.*  $W_{ij} = 0$  when the distance between the particles  $r_{ij}$  is greater than some multiple of  $h$ .

If the kernel is differentiable it is possible to differentiate the properties of SPH particles directly. As described in Monaghan (1992), the gradient of  $f$  can be obtained by using the expansion

$$\rho \nabla f = \nabla(\rho f) - f \nabla \rho \quad (2.16)$$

and writing out the SPH summation for the right hand side. When written in this way the summation in  $j$  is performed over the variables operated on by  $\nabla$ . Those outside the operator take the value at  $i$ .

Also useful for future reference is the result

$$\rho \nabla \cdot \mathbf{v} = \nabla \cdot \rho \mathbf{v} - \mathbf{v} \cdot \nabla \rho \quad (2.17)$$

which gives the SPH velocity divergence at particle  $i$ :

$$\begin{aligned}\rho_i(\nabla \cdot \mathbf{v})_i &= \sum_{j=1}^N \frac{m_j}{\rho_j} \rho_j \mathbf{v}_j \nabla_i W_{ij} - \mathbf{v}_i \sum_{j=1}^N m_j \nabla_i W_{ij} \\ &= - \sum_{j=1}^N m_j (\mathbf{v}_{ij} \cdot \nabla_i) W_{ij}.\end{aligned}\tag{2.18}$$

The abbreviation  $\mathbf{v}_{ij} = \mathbf{v}_i - \mathbf{v}_j$  will be used throughout this chapter.

As is illustrated above, the beauty of SPH is its simplicity: mass is automatically conserved and time-dependent equations can be derived from the conservation equations, making it possible to evolve all the properties of the system by numerical integration. No grid or outer boundary is required — particles are followed wherever they go, meaning that computational effort is focused purely where the mass is, with none wasted on empty space. SPH is therefore highly suited to astrophysical problems, where there are often no clear boundaries and regions of interest may be highly asymmetric, for example, when two objects merge, or where mass is ejected from an object.

### 2.3.2 The Kernel

Certain qualities are required of the kernel: for it to approximate a delta function as  $h \rightarrow 0$  it must be strongly peaked at  $r_{ij} = 0$ , where  $r_{ij} = |\mathbf{r}_i - \mathbf{r}_j|$ ; it must be positive in the region of interest and vanish at infinity; it must have a flat top, *i.e.* its first derivative must vanish at  $r_{ij} = 0$ ; and it must have continuous first and second derivatives.

Early SPH simulations used a spherical Gaussian kernel to fulfill these criteria. This has tended to be replaced by a cubic spline kernel that approximates the Gaussian, and conveniently vanishes outside  $2h$ , giving a clear limit on which neighbours must be included in the summation. The most commonly used spline kernel has the form

$$W(r, h) = \frac{\sigma}{h^3} \begin{cases} 1 - \frac{3}{2}q^2 + \frac{3}{4}q^3 & 0 \leq q < 1 \\ \frac{1}{4}(2 - q)^3 & 1 \leq q < 2 \\ 0 & q \geq 2 \end{cases}\tag{2.19}$$

where  $q = r_{ij}/h$  and  $\sigma = 1/\pi$  is the normalisation in three dimensions.

## 2.4 SPH Equations Used in the Code

In this section I will give an outline of how the conservation equations of fluid dynamics are converted into the SPH form used by the code before its modification. Since the particles' motion represents the motion of the fluid, SPH is Lagrangian, and the operator  $\frac{d}{dt}$  is taken to mean  $\frac{D}{Dt}$ .

### 2.4.1 The Continuity Equation

We saw in Section 2.3 that the density at particle  $i$  is expressed as

$$\rho_i = \sum_{j=1}^N m_j W_{ij}. \quad (2.20)$$

If the mass of a particle is constant this means that mass is automatically conserved. However, at the edges of the modelled region the density will drop off due to the reduced number of neighbours within  $2h$  of a particle. This causes a rarefaction wave to propagate inwards on a dynamical time and may lead to unphysical oscillations. The bad behaviour of SPH at boundaries is perhaps its Achilles heel – indeed, it is very difficult to model any discontinuity to a precision of less than two smoothing lengths, due to the averaging of particle properties over this distance.

### 2.4.2 Variable Smoothing Lengths

A little should be said about what  $W_{ij}$  stands for in the equation above and in subsequent equations. The SPH formulation discussed in Section 2.3 is derived under the assumption that the smoothing length  $h$  is constant in both space and time. In practice, in order to achieve adequate resolution and accuracy, it is preferable to maintain a roughly constant number of neighbours by allowing the smoothing length of each individual particle  $h_i$  to vary with time.

If the smoothing length for each particle is different, the meaning of  $W_{ij}$  is now ambiguous, as it not clear which  $h$  the kernel is a function of. The solution is usually to symmetrize the equation for each interacting pair of particles by taking the average of either the kernel

$$\overline{W}_{ij} = \frac{1}{2} [W(\mathbf{r}_{ij}, h_i) + W(\mathbf{r}_{ij}, h_j)] \quad (2.21)$$

or the smoothing lengths  $h_{ij} = \frac{1}{2}(h_i + h_j)$ . In the unmodified version of my code, the latter formulation is used throughout. Symmetrization of the kernel ensures that the equations are conservative - the force on particle  $i$  due to  $j$  is equal to that on  $j$  due to  $i$ .

### 2.4.3 The Momentum Equation

To obtain the velocities of the particles we use equation 2.2 for the conservation of momentum. Neglecting external forces and dividing by  $\rho$  we can write

$$\frac{d\mathbf{v}}{dt} = - \left( \frac{\nabla P}{\rho} \right) = -\nabla \frac{P}{\rho} - \frac{P \nabla \rho}{\rho^2} \quad (2.22)$$

which results in the SPH equation

$$\frac{d\mathbf{v}_i}{dt} = - \sum_{j=1}^N m_j \nabla_i W_{ij} \frac{P_j}{\rho_j^2} - \frac{P_i}{\rho_i^2} \sum_{j=1}^N m_j \nabla_i W_{ij} \quad (2.23)$$

$$= - \sum_{j=1}^N m_j \nabla_i W_{ij} \left( \frac{P_i}{\rho_i^2} + \frac{P_j}{\rho_j^2} \right) . \quad (2.24)$$

This is the form of the momentum equation that is used in the code. Convention holds that it is preferable to use an equation that is symmetrized in this way in order to ensure conservation of total momentum, although it is possible to derive other forms, both symmetric and asymmetric.

Particle positions can be evolved simply by integrating their velocities with respect to time,

$$\frac{d\mathbf{r}_i}{dt} = \mathbf{v}_i \quad (2.25)$$

where  $\mathbf{v}_i$  is obtained by integrating the momentum equation (2.23).

### 2.4.4 Energy Conservation

In contrast to the momentum equation, the unmodified code uses an asymmetric form of the energy equation derived directly from equation 2.4:

$$\frac{du_i}{dt} = - \frac{P_i}{\rho_i^2} \sum_{j=1}^N m_j \mathbf{v}_{ij} \cdot \nabla_i W_{ij} . \quad (2.26)$$

This form is used because it avoids the possibility of negative internal energies that can arise if the symmetric form is used.

The total energy of the system is obtained by summing the specific internal, gravitational potential and kinetic energies ( $\frac{1}{2}mv_i^2$ ) of all the particles.

## 2.5 Treatment of Self Gravity

The introduction of gravitational forces into the SPH equations brings with it a degree of complexity. The gravitational field at particle  $i$  due to a distribution of point masses  $j$  is

$$-\nabla\phi_i = -G \sum_{j=1}^N \frac{m_j}{r_{ij}^2} \frac{\mathbf{r}_{ij}}{r_{ij}}, \quad (2.27)$$

however, SPH particles are not point masses. Particles whose kernels overlap will experience a reduced interaction that is complicated to calculate analytically. The force calculation requires us to approximate particle  $i$  as a point mass while  $j$  maintains its spherical distribution. The mass “seen” by  $i$  is then

$$M_j(r_{ij}, h_{ij}) = \int_0^{r_{ij}} 4\pi r^2 m_j W(r, h_{ij}) dr. \quad (2.28)$$

The field experienced at  $i$  due to the rest of the fluid will then be

$$-\nabla\phi_i = -G \sum_{j=1}^N \frac{M_j(r_{ij}, h_{ij})}{r_{ij}^2} \frac{\mathbf{r}_{ij}}{r_{ij}}. \quad (2.29)$$

This quantity must be computed for each particle before it can be added on to the momentum equation, which becomes

$$\frac{d\mathbf{v}_i}{dt} = - \sum_{j=1}^N m_j \nabla_i W_{ij} \left( \frac{P_i}{\rho_i^2} + \frac{P_j}{\rho_j^2} \right) - \nabla\phi_i. \quad (2.30)$$

### 2.5.1 The Tree

In contrast to the pressure force on a particle, which derives only from the particles within  $2h$  of it, the gravitational force depends on every other particle in the simulation. If the quantity  $\nabla\phi_i$  is calculated from the interaction of every pair of particles the number of calculations required is  $N^2/2$ . Even for a small simulations with a few thousand particles several million calculations would be required! It is clear that an algorithm for aggregating the gravitational contributions from distant groups of particles is necessary to make large simulations possible. This is referred to as a “tree”.

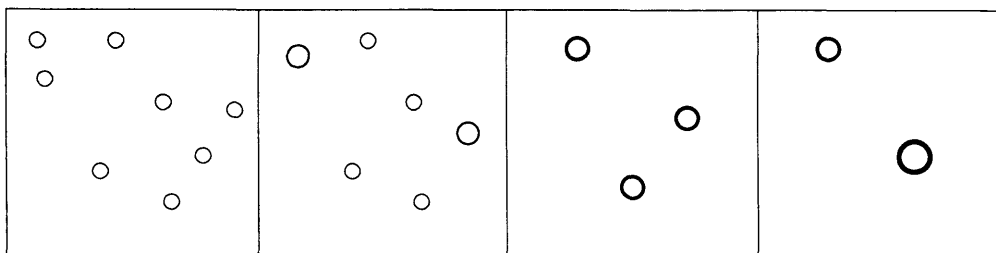


FIGURE 2.2. The tree is built by a process of replacing mutual nearest neighbours with a composite “node” and repeating until all particles are contained in a single node. The node structure traces the clumps in the fluid.

Below I give a brief outline of how the tree used by my code is constructed. A full description of this algorithm can be found in the Appendix of Benz et al. (1990).

### 2.5.2 Building the Tree

Particles are grouped together using the principle of “mutual nearest neighbours” – if a pair of particles are mutual nearest neighbours they are replaced by a second-level “node”, located at their centre of mass. This process is then repeated for the second-level nodes and any unpaired particles, and so on until all particles have been collected into a single node (the “root” of the tree, see Figure 2.2). The advantage of this method of building the tree is that the nodes accurately reflect the physical clumping of the particles.

The first stage of the tree algorithm is the identification of each particle’s nearest neighbours. To do this, the three dimensional space occupied by the particles is divided into an uneven grid with the spacing of the boundary planes following the spacing of the particles. The aim is for each grid cell to contain roughly one particle. Linked lists are constructed to enable all the particles in a particular cell to be found efficiently.

Starting from the cell a particle is in, the particle’s nearest neighbour is found by comparing the distance to the other particles in the cell with the distance to the nearest of the six walls of the cell. If there are no particles closer than the nearest wall, the cell is expanded to include the cell on the other side of the nearest wall. Each time a cell is expanded, the particles contained in the new, enlarged cell are looped over until a particle closer than the present nearest wall is found - this is the nearest neighbour. This is shown schematically in Figure 2.3.

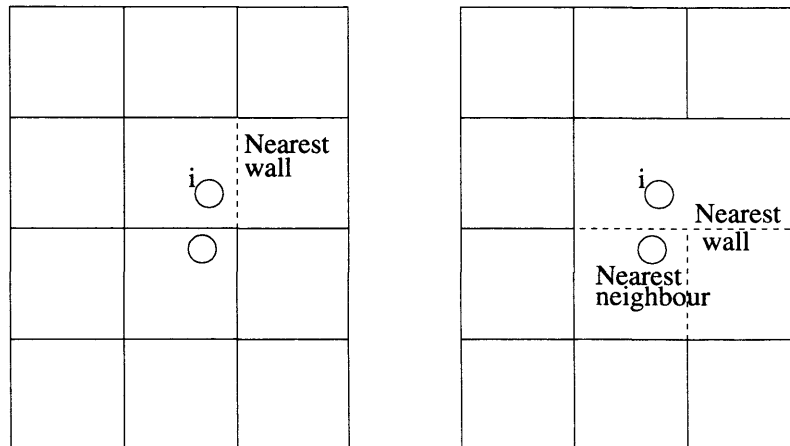


FIGURE 2.3. Location of the nearest neighbour. If the nearest wall is closer than all neighbours within the same cell, it is removed. This process is repeated with the new, expanded cell until a particle nearer than the nearest wall is found. This particle is the nearest neighbour.

Once the nearest neighbour of each particle has been located, the tree is constructed. For each level of the tree, all “active points” – the composite as well as unpaired “atomic” nodes are looped over. If two nodes are mutual nearest neighbours, *i.e.*

```
if neighbour(neighbour(point)) == point
```

then a new node is created and the number of nodes `topnode` is incremented. Arrays are created containing, for each node, pointers to its parent node (the node in the level above that it is part of), to one daughter node (one of the pair that it is made up of) and to one sibling (its mutual nearest neighbour). Because the tree is binary, *i.e.* it works by pairing particles, the total number of nodes will always be  $2n_{part} - 1$  where  $n_{part}$  is the number of particles.

For a filled binary tree (meaning that all nodes pair on every level) the number of levels  $m$  would be

$$m = \log_2 n_{part} . \quad (2.31)$$

For a random distribution of points,  $m$  can be estimated as

$$m = \frac{\log_2 n_{part}}{\log_2(1 - \frac{1}{2}P)} \approx 1.98 \log_2 n_{part} \quad (2.32)$$

where  $P \approx 0.59$  is the probability that a particular point is part of a mutual nearest neighbour pair (Benz et al. 1990). In practice, the factor 1.98 is usually substantially

lower, as levels are not independent of each other and unpaired nodes become more and more likely to find partners.

### 2.5.3 Calculating the Forces

The third component required in the gravitational algorithm is the inclusion of the physics! For each node created, *composition formulae* are used to calculate its total mass  $M$ , position  $\mathbf{r}$  and three-tensor quadrupole moment  $\mathbf{Q}$ . These formulae are:

$$M_{node} = M_1 + M_2 \quad (2.33)$$

$$\mathbf{r}_{node} = \frac{M_1 \mathbf{r}_1 + M_2 \mathbf{r}_2}{M_1 + M_2} \quad (2.34)$$

$$\mathbf{Q}_{node} = \mathbf{Q}_1 + \mathbf{Q}_2 + \frac{M_1 M_2}{M_1 + M_2} (\mathbf{r}_2 - \mathbf{r}_1) \otimes (\mathbf{r}_2 - \mathbf{r}_1). \quad (2.35)$$

At the same time as this calculation is made, the code also calculates and stores the radius  $R$  of a sphere centred on the centre of mass of the node that is guaranteed to contain all its constituents.

Once the tree has been constructed, the code walks through it for each particle, creating three lists. The first is a list of which atoms can have their force contribution evaluated using the Newtonian formula (equation 2.29) and the second a list of which nodes require their contribution to be calculated by multipole expansion of the quadrupole. The third is a list of which nodes are within a cutoff radius  $R_{cut}$ .  $R_{cut}$  specifies the radius within which a node must be “opened up” into its constituents, and is set equal to a multiple of  $R$ .

For each particle the force contributions from the nodes it sees are summed. The force on a particle of mass  $m$  due to a clump with parameters  $M$  and  $\mathbf{Q}$  is

$$\frac{\mathbf{F}}{m} = M f(r) \mathbf{r} + \frac{f'(r)}{r} \mathbf{Q} \cdot \mathbf{r} + \frac{1}{2} \left[ \frac{f''(r)}{r^2} \mathbf{r} \cdot \mathbf{Q} \cdot \mathbf{r} + \frac{f'(r)}{r} \left( tr(\mathbf{Q}) - \frac{\mathbf{r} \cdot \mathbf{Q} \cdot \mathbf{r}}{r^2} \right) \right] \mathbf{r} \quad (2.36)$$

and for Newtonian gravity with  $G = 1$ ,  $f(r) = r^{-3}$ .

## 2.6 Time Evolution of Smoothing Lengths

To keep the number of neighbours for each particle approximately constant,  $h$  is usually scaled with the average local particle separation, which itself depends on local density,

so that

$$h = h_0 \left( \frac{\rho}{\rho_0} \right)^{-\frac{1}{3}} \quad (2.37)$$

where  $h_0$  and  $\rho_0$  are constants. Taking the derivative with respect to time we obtain

$$\frac{dh}{dt} = -\frac{1}{3} \frac{h}{\rho} \frac{d\rho}{dt} . \quad (2.38)$$

Using the continuity equation 2.6 to substitute for  $\frac{d\rho}{dt}$  we end up with

$$\frac{dh_i}{dt} = \frac{1}{3} h_i (\nabla \cdot \mathbf{v})_i . \quad (2.39)$$

The divergence can be calculated from its SPH summation (equation 2.18), evolved in the same loop as the density and used to evolve  $h_i$ . However, using this formula does not guarantee that the number of neighbours will stay within the desired range and so the code uses it only to obtain a first approximation for  $\frac{dh_i}{dt}$ . If the number of neighbours is too close to the upper or lower bound of a specified range (the default is 80 to 120),  $\frac{dh_i}{dt}$  is adjusted. When the number of neighbours  $nn$  is too close to the upper bound  $nn_{max}$  the derivative is decreased using

$$\frac{dh_i}{dt} = \frac{\frac{dh_i}{dt} e^x - \frac{dh_{max}}{dt} e^{-x}}{e^x + e^{-x}} \quad (2.40)$$

where  $\frac{dh_{max}}{dt}$  is the maximum  $\frac{dh_i}{dt}$  for all  $i$  and

$$x = \frac{nn_{max} - nn}{3.5} . \quad (2.41)$$

Similarly, when  $nn$  is too close to the lower bound  $nn_{min}$  then

$$\frac{dh_i}{dt} = \frac{\frac{dh_i}{dt} e^y + \frac{dh_{max}}{dt} e^{-y}}{e^y + e^{-y}} \quad (2.42)$$

where

$$y = \frac{nn - nn_{min}}{3.5} . \quad (2.43)$$

This algorithm is extremely effective for keeping the number of neighbours within a fixed range and thereby reducing noise.

## 2.7 Treatment of Viscosity

None of the SPH equations discussed so far include any dissipation mechanism. In their present form, if two “slabs” of particles collide there is nothing to stop them passing, unphysically, straight through each other. Clearly this cannot be allowed to happen—a vital ingredient is missing from our formulation. The missing ingredient is viscosity, which converts the kinetic energy of colliding slabs of fluid into internal energy. Adding an artificial viscosity term to the SPH equations solves the problem of particle interpenetration and enables SPH to handle shocks accurately. The standard SPH artificial viscosity (hereafter AV) parameter has the form

$$\Pi_{ij} = \begin{cases} \frac{-\alpha c_{ij} \mu_{ij} + \beta \mu_{ij}^2}{\rho_{ij}} & \mathbf{v}_{ij} \cdot \mathbf{r}_{ij} \leq 0 \\ 0 & \mathbf{v}_{ij} \cdot \mathbf{r}_{ij} > 0 \end{cases} \quad (2.44)$$

where  $c_{ij} = 0.5(c_i + c_j)$  is the average of the sound speed at  $i$  and  $j$ ,  $\rho_{ij} = 0.5(\rho_i + \rho_j)$ ,  $\alpha$  and  $\beta$  are free parameters (usually  $\beta = 2\alpha = 2.0$ ) and

$$\mu_{ij} = \frac{h_{ij} \mathbf{v}_{ij} \cdot \mathbf{r}_{ij}}{r_{ij}^2 + \eta h_{ij}^2}. \quad (2.45)$$

The term containing  $\alpha$  accounts for a combination of bulk and shear viscosity, while the term containing  $\beta$  is similar to the von Neumann-Richtmeyer viscosity and is useful for handling high Mach number shocks, where  $\mu_{ij}$  is large. The  $\mathbf{v}_{ij} \cdot \mathbf{r}_{ij}$  term in the AV parameter means that particles only experience a viscous force when they are approaching each other.

In most astrophysical situations viscosity is small and only important when the fluid is shocked, and the AV term can introduce spurious forces into pure shear flows. It would be preferable for the default value of AV to be close to zero, only rising significantly in the presence of shocks. The code therefore employs modified, time-dependent viscosity parameters (Morris & Monaghan 1997) with the Balsara switch (Balsara 1995) for suppressing viscosity in shear flows. Thus the AV prescription becomes:

$$\Pi_{ij} = \begin{cases} \frac{-\alpha(t) c_{ij} \mu_{ij} + \beta(t) \mu_{ij}^2}{\rho_{ij}} & \mathbf{v}_{ij} \cdot \mathbf{r}_{ij} \leq 0 \\ 0 & \mathbf{v}_{ij} \cdot \mathbf{r}_{ij} > 0 \end{cases}. \quad (2.46)$$

The parameters  $\alpha$  and  $\beta (= 2\alpha)$  are now evolved along with the other SPH quantities, according to

$$\frac{d\alpha_i}{dt} = -\frac{\alpha_i - \alpha_{min}}{\tau_i} + S_i \quad (2.47)$$

where

$$S_i = \max(-(\nabla \cdot \mathbf{v})_i (\alpha_{max} - \alpha_i), 0) . \quad (2.48)$$

In this formulation,  $\alpha$  is evolved along with the other SPH quantities and tends towards a minimum  $\alpha_{min} = 0.05$  on a timescale  $\tau$ . In the presence of shocks it rises according to the source term  $S_i$  to a maximum of  $\alpha_{max} = 1.5$ . The timescale is set to  $\tau_i = \frac{h_i}{\epsilon c_i}$  with  $\epsilon = 0.2$ .

The term  $\mu_{ij}$  now becomes

$$\mu_{ij} = \frac{h_{ij} \mathbf{v}_{ij} \cdot \mathbf{r}_{ij}}{r_{ij}^2 + \eta h_{ij}^2} \frac{f_i + f_j}{2} \quad (2.49)$$

where  $\eta = 0.01$ . The term containing  $f_i$  and  $f_j$  is the Balsara switch, with

$$f_i = \frac{|\nabla \cdot \mathbf{v}|_i}{|\nabla \cdot \mathbf{v}|_i + |\nabla \times \mathbf{v}|_i + \eta' c_i / h_i} . \quad (2.50)$$

This term approaches unity in the presence of pure shocks, where  $|\nabla \cdot \mathbf{v}|_i \gg |\nabla \times \mathbf{v}|_i$ , but tends to zero in the case of pure shear flows, where  $|\nabla \times \mathbf{v}|_i \gg |\nabla \cdot \mathbf{v}|_i$ , ensuring that unphysical forces are kept to a minimum. A fuller description of this scheme can be found in the Appendix of Rosswog et al. (2000).

The AV term is added into the momentum equation. 2.23 to give

$$\frac{d\mathbf{v}_i}{dt} = - \sum_{j=1}^N m_j \nabla_i W_{ij} \left( \frac{P_i}{\rho_i^2} + \frac{P_j}{\rho_j^2} + \Pi_{ij} \right) . \quad (2.51)$$

Similarly, for the specific internal energy equation,

$$\frac{du}{dt} = - \sum_{j=1}^N m_j \nabla_i W_{ij} \left( \frac{P_i}{\rho_i^2} + \frac{1}{2} \Pi_{ij} \right) . \quad (2.52)$$

## 2.8 Equation of State

For the SPH equations to be able to describe a fluid completely there must be a way of obtaining the pressure from the density and internal energy. This is provided by the equation of state (EOS).

The code uses the high density Shen EOS (Shen et al. 1998a, Shen et al. 1998b), which is available from its authors in tabular form. The EOS is tabulated up to a density of  $2.5 \times 10^{15} \text{ g cm}^{-3}$ , an order of magnitude greater than that of an atomic nucleus. It is

extended to “low” densities using the EOS of a gas made up of baryons,  $\alpha$ -particles and electrons. The EOS subroutine is called using the density, electron fraction per baryon and either the temperature or specific internal energy of each particle. It returns values for the pressure, sound speed, entropy per baryon and abundances of electrons, baryons,  $\alpha$ -particles and a “representative” heavy nucleus. If it is called using the specific internal energy, the temperature  $T$  must first be found by interpolation in the table for given  $u$ ,  $\rho$  and electron fraction per baryon  $Y_e$ . A three-dimensional interpolation is then performed using  $\rho$ ,  $T$  and  $Y_e$  to return  $P$  and other variables.

## 2.9 Time Evolution

The SPH equations are integrated using the third order Adams-Bashforth integrator, which advances the variables from step  $n$  to  $n + 1$  using the formula

$$x_{n+1} = x_n + \frac{dt}{12} (23v_{x,n} - 16v_{x,n-1} + 5v_{x,n-2}) \quad (2.53)$$

and similarly for all other variables.

It can be seen above that to advance by one step, derivatives from the beginning of the present step and the previous two steps are required. Each time the program enters the integrator two steps of second order Runge-Kutta (RK) integration are taken in order to accumulate these derivatives. In second order RK the derivatives are determined at the midpoint of a step and used to advance a full step, *i.e.*

$$x_{n+1/2} = x_n + v_{x,n} \cdot \frac{dt}{2} \quad (2.54)$$

$$v_{x,n+1/2} = v_{x,n} + \left( \frac{dv_x}{dt} \right)_n \frac{dt}{2}, \quad (2.55)$$

followed by

$$x_{n+1} = x_n + v_{x,n+1/2} \cdot dt \quad (2.56)$$

$$v_{x,n+1} = v_{x,n} + \left( \frac{dv_x}{dt} \right)_{n+1/2} dt. \quad (2.57)$$

Before the first step is taken the tree must be constructed in order for the gravitational forces to be calculated. On subsequent steps, the tree is revised using the updated positions of the particles.

Once the gravitational forces have been evaluated, the SPH derivatives are computed.

Each calculation of the derivatives requires two sets of summations for each particle. The following steps are taken to obtain the derivatives:

- The density is computed by summation for each SPH particle, with  $\rho_i(\nabla \cdot \mathbf{v})_i$ ,  $\rho_i(\nabla \times \mathbf{v})_i$  and  $(\nabla \cdot \mathbf{v})_{max}$  computed in the same loop. This is the first sweep through  $i$  and  $j$ .
- The equation of state is called, using the newly calculated  $\rho_i$  to obtain  $P_i$ .
- The time derivative of the smoothing length  $\frac{dh_i}{dt}$  is calculated using the expressions calculated in the density summation and the neighbour numbers.
- The rate of change of the artificial viscosity parameter  $\frac{d\alpha_i}{dt}$  is calculated, also using quantities from the density summation.
- A second sweep through  $i$  and  $j$  is performed in order to evaluate the momentum equation (including viscosity) and return the acceleration of each particle  $\frac{d\mathbf{v}_i}{dt}$ .
- The time derivative of specific internal energy  $\frac{du_i}{dt}$  is calculated.

### 2.9.1 Timestepping

The routine that calculates the accelerations also sets the new timestep for all particles. Following Monaghan (1992), the criteria for setting the timestep is

$$\delta t_f = \min_i \left( \frac{h_i}{|\mathbf{f}_i|} \right)^{1/2} \quad (2.58)$$

$$\delta t_{cv} = \min_i \left( \frac{h_i}{c_i + 0.6(c_i + \max_j \mu_{ij})} \right) \quad (2.59)$$

where

$$\delta t = 0.25 \min(\delta t_f, \delta t_{cv}) . \quad (2.60)$$

Here, the time condition  $\delta t_f$  is based on the acceleration of the particle and  $\delta t_{cv}$  combines the Courant and viscous time conditions.

Running all particles on a single, smallest timestep greatly simplifies the integration and for merging neutron stars, where the majority of the material has the density of nuclear matter, the code has proved itself more than adequate. However, the inner layers of

a massive star during core collapse possess a vast range of densities and hence dynamical times ( $\tau_{dyn} \sim (G\rho)^{-1/2}$ ). A minority of particles require the smallest timestep and advancing all particles on this timestep is grossly inefficient.

In addition to this, since the timestep is set at the beginning of the step with no monitoring of the accuracy at the end of the step, this method of integration is most suited to problems where the dynamical time does not change rapidly. In runaway core collapse  $\tau_{dyn}$  decreases non-linearly, so that the timestep required at the end of a step is shorter than that required at the beginning of the step. Errors thus build up over the course of a simulation, increasing as the collapse accelerates.

It is clear, from the considerations above, that it would be preferable by far for each particle to run on its own timestep, with the accuracy of each step monitored. I will discuss this further in Chapter 3, Section 3.4.

The flowchart in Figure 2.4 provides a summary of the SPH algorithm in the code, before modification.

## 2.10 Parallelization

Upon my acquisition of the code, it was already fully parallelized for use on a shared-memory machine, in this case the U.K. Astrophysical Fluids Facility (UKAFF). The purpose of parallel processing it to decrease the length of a run in real time by distributing the workload over multiple “threads”, each running on a different processor, typically 32 or 64 for this code, but potentially many hundreds. Parallelization on UKAFF is done using the *OpenMP* compiler directives. A loop is parallelized by a simple declaration specifying which variables are to be treated as local to the processor it is sent to and which are to be shared among all processors used, as shown in the example below:

```
C$OMP PARALLEL default(none)

C$OMP& shared(npart,divv,rho,tm,ilen,neighb)

C$OMP& private(ipart,xi,yi,zi,vxi,vyi,vzi,pmassi,hi)

C$OMP DO SCHEDULE(runtime)

  do ipart=1,npart
    .....
    .....
  enddo
```

```
C$OMP END DO
```

The iterations of the do loop are divided up into “chunks” before being allocated to the processors. These chunks can be assigned to a predetermined thread or assigned on-the-fly to whichever thread has finished its previous chunk. The `DO SCHEDULE(runtime)` declaration allows the method of assigning chunks of work to be set as an environment variable at the beginning of a run.

The simplicity of this kind of parallelization is by virtue of the shared memory, meaning that every processor can “see” the values declared as shared. This simplicity comes with a high price tag, therefore there is competition for computing resources of this kind. A limited number of simulations can be run on high performance machines such as UKAFF (or its successor, UKAFF1A). The majority of scientific computations are carried out on smaller machines and PC clusters.

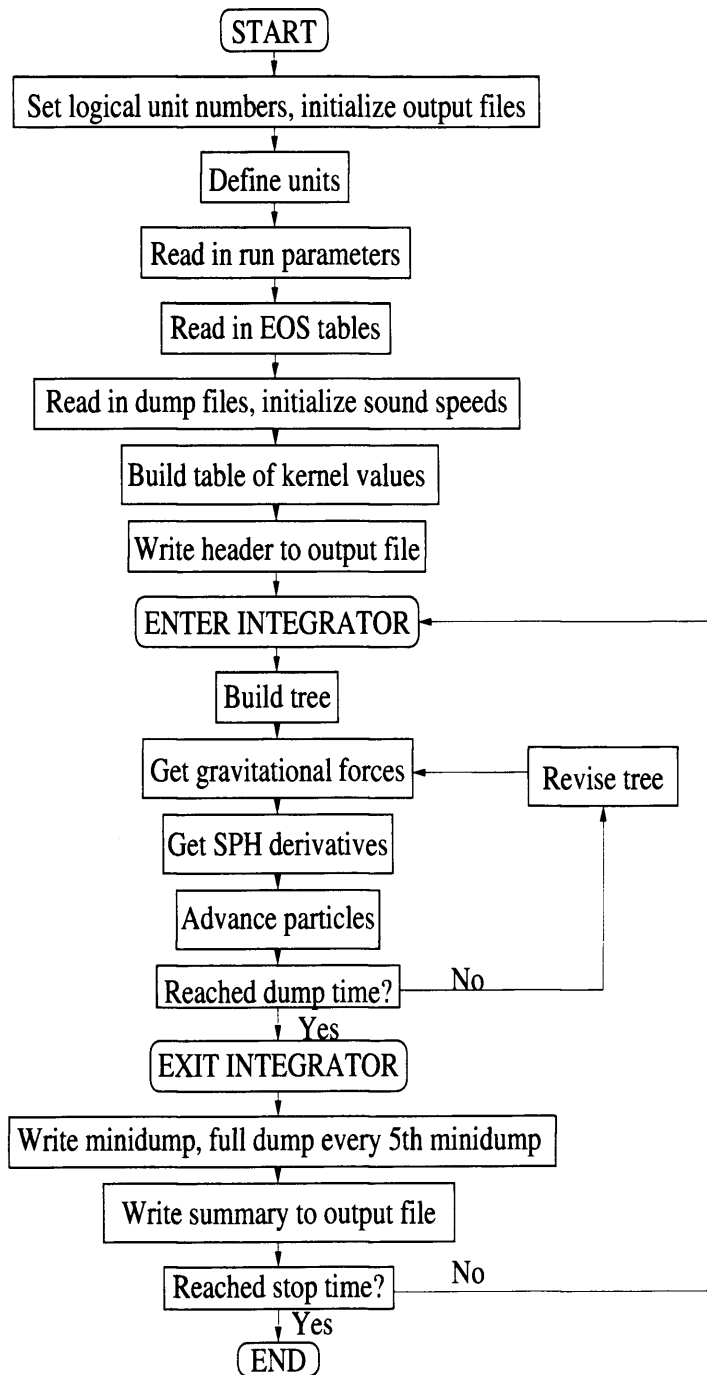


FIGURE 2.4. Summary of the algorithm.

# Chapter 3

## *Code Adaptations for Core Collapse*

“Don’t worry, head – the computer will do all the thinking from now on.”

*Homer Simpson*

## 3.1 Introduction

A computer program designed to model the high-density environment of merging neutron star systems will not be directly amenable to simulating the core collapse of massive stars. The cold, uniform, deleptonized nuclear matter that makes up neutron stars is a far cry from the hot, lower density gas of electrons, nucleons, alpha particles and nuclei that composes the core of an evolved, massive star. My SPH code required significant alterations to make it suitable for simulations of supernovae.

In this chapter I describe how I adapted the code to make it suitable for simulations of core collapse. I begin in Section 3.2 by describing how one dimensional supernova progenitor models were used to set up the three dimensional initial distribution and values of the SPH particles.

The Adams-Bashforth integrator described in the previous chapter turned out to be poorly suited to this problem. At the same time, variations in dynamical time from particle to particle due to the large range of densities involved made running on a single timestep highly inefficient. In Section 3.4 I describe replacing the integrator with a scheme that uses multiple particle timesteps and monitors the truncation errors at the end of each step.

In addition to causing variations in the required length of timestep, large spatial and temporal density variations also lead to large variations in the smoothing length  $h$ . In the formulation of SPH described in the previous chapter the error introduced by changes in  $h$  was neglected. In Section 3.5 I describe the alterations made to the code in order to take the “grad  $h$ ” terms into account.

Very rapid rotation in the core of a collapsing star inhibits collapse, with the possibility of centrifugally “hung up” material forming a disc. In order to investigate how this disc might affect the collapse, I added an option for enhancing shear viscosity. This is described in Section 3.6

Apart from the alterations listed above, the numerical methods employed in the present code are the same as those described in the previous chapter.

## 3.2 Progenitor Models

In Section 1.3 of Chapter 1 I described the evolution of massive stars after they leave the main sequence. In the moments before collapse the core of the star has an onion-like

structure with iron-group elements at the centre surrounded by concentric shells fusing decreasingly massive nuclei.

It is difficult for stellar evolution codes to model the final stages before collapse, since the temperature, pressure and density far exceed those obtained during hydrogen burning and reaction networks including many more elements are required. In addition, the increasing brevity of successive burning stages, especially when compared to the main sequence lifetime, leads to problems in time resolution. Only a fraction of the groups modelling stellar evolution go to the trouble of evolving their stars to the presupernova stage.

Of the presupernova models that have been produced down the years, the  $15M_{\odot}$  model s15 of Woosley & Weaver (1995) has become the “standard” progenitor. This model is one dimensional and does not include rotational effects. More recently, Heger et al. (2000) have produced rotating supernova progenitor models. These models are also one dimensional, meaning that equations quantifying rotational effects must be included explicitly in the stellar evolution code. Rotational instabilities that may arise and cause mixing (and thus transport of angular momentum) must be identified and an assessment made of how likely they are to significantly affect the evolution. In many cases this is not known, resulting in a huge number of free parameters.

The output files for progenitor models contain a vast number of quantities describing the star’s structure and composition. All the quantities required to set the initial conditions in my supernova code are included. In the case of the Heger models the files give, for each radial grid cell: mass coordinate at top of cell, radius at top of cell, radial velocity at top of cell, average density, temperature, pressure, specific energy, specific entropy, angular velocity, mean mass number of nuclei and electron fraction per baryon, as well as nuclear abundances. More information about the stellar evolution calculations used to generate these models are given in Chapter 5.

The quantities required by my code for each particle are the position and velocity vectors, mass, specific internal energy or temperature, electron fraction per baryon and entropy per baryon in units of Boltzmann’s constant. I describe below the method I used to map the variables from a one dimensional grid code into a three dimensional particle code.

### 3.2.1 Distributing the particles

In SPH the density at a point in the fluid depends on two things: the number density of particles close to that point and the mass of each particle. In order to create a variation in density it is therefore necessary to vary the spacing of the particles or the mass of the particles or both.

Throughout core collapse the density remains centrally peaked. It would therefore be possible to produce this density distribution using particles with masses that decrease with increasing radius. However, spurious effects can occur when particles of very different masses interact, as would happen after bounce as the shock moves outwards into lower density material. For this reason, and because it is in the high density core that the highest spatial resolution is desired, I use particles with equal masses.

Setting up a spherical distribution of particles with spatially varying density is no mean feat. The most straightforward method is to begin by creating a sphere of equally spaced particles and then map each particle to a “stretched” radius that is a function of the density.

Initial attempts to set up the particles in a cubic grid and stretch it resulted in artifacts of the initial grid persisting throughout the simulations. It was therefore decided that particles should be set up following a Sobol, or quasi-random, distribution. A quasi-random distribution is not actually random at all, but each successive point is chosen to “maximally avoid” all the other points, *i.e.* it is placed in the region with the most empty space. In other words, a quasi-random distribution fills up space uniformly with the resolution increasing with the number of points. This avoids the clustering of points that happens in truly random distributions. It also allows the resolution to be set by the number of points, rather than the opposite. A more in-depth description of quasi-random sequences can be found in Press et al. (1992).

To obtain the initial coordinates for each particle a call is made to the Sobol sequence generator which returns a vector  $X$  of three values, each between 0 and 1. The particle is then assigned polar coordinates, using the enclosed mass as a radial coordinate, *i.e.*:

$$\begin{aligned} m_i &= M_* X(1) \\ \cos \theta_i &= 2(X(2) - 1/2) \\ \phi_i &= 2\pi X(3) \end{aligned} \tag{3.1}$$

where  $M_*$  is the total mass of the distribution. Two-dimensional Sobol distributions are shown in figure 3.2.1 for two different resolutions.

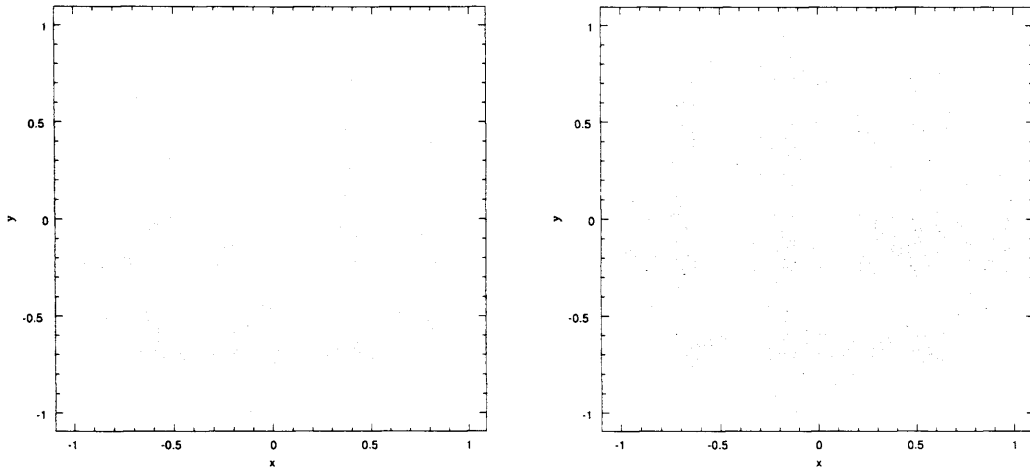


FIGURE 3.1. Two dimensional Sobol distribution, with 1500 (left) and 6000 (right) points produced in polar coordinates.

These particles are now evenly spaced in enclosed mass and each particle's radial coordinate can be calculated by using the mass-radius relation given by interpolation between the grid cells of the progenitor model. Cartesian coordinates for each particle are then calculated using

$$\begin{aligned}
 x_i &= r_i \cos \phi_i \sqrt{(1 - \cos^2 \theta_i^2)} \\
 y_i &= r_i \sin \phi_i \sqrt{(1 - \cos^2 \theta_i^2)} \\
 z_i &= r_i \cos \theta_i
 \end{aligned}
 \tag{3.2}$$

This creates the correct density distribution, albeit with some noise.

The inner  $10^9$  cm of each progenitor was mapped to an SPH particle distribution. At this radius the dynamical time is around 1s, several times larger than the time until core bounce. Quantities here thus remain virtually unchanged during the course of the simulation and it is not necessary to model the layers above.

### 3.2.2 Initial values for particles

The remaining physical variables are determined at each particle by interpolation between the grid points of the progenitor model for the particle's radial position.

Since the velocities in the progenitors are given as radial and angular components, once these have been found by interpolation the velocity of each particle is set by resolv-

ing the components along Cartesian unit vectors. For radial velocity,

$$v_x = v_r \frac{x}{r} \quad (3.3)$$

and similarly for  $v_y, v_z$ .

The progenitors are assumed to rotate about the z-axis. In previous studies there has been some confusion as to whether the angular velocity should be constant on cylinders or shells about the z-axis (see Ott et al. (2004) for a discussion of this). I give the option for either shellular or cylindrical rotation. Shellular means that the angular velocity  $\Omega$  is constant with constant radius, *i.e.*

$$v_x = -\Omega(r)y \quad (3.4)$$

$$v_y = \Omega(r)x \quad (3.5)$$

Cylindrical means that  $\omega$  is constant with constant distance from the z-axis, *i.e.*

$$v_x = -\Omega(s)y \quad (3.6)$$

$$v_y = \Omega(s)x \quad (3.7)$$

where  $s = \sqrt{x^2 + y^2}$ . When the components of the angular velocity have been calculated they are added to those of the radial velocity.

As with the other variables, the electron fraction  $Y_e$  at a particle is set by interpolation. The temperature and internal energy can be set in one of two ways. In initial trials the temperature was determined by interpolation of the progenitor model and used, along with  $\rho$  and  $Y_e$ , to return the internal energy and pressure. However, because the stellar evolution code and the supernova code use different equations of state, the pressure returned was different from the pressure in the progenitor model, resulting in a shallower pressure gradient and hence reduced forces. In addition to this, centrifugal terms are not included in Heger's stellar evolution code, so that when the progenitor model is mapped to three dimensions it experiences an extra outward force. The upshot of these differences was that the more rapidly rotating models failed to collapse in three dimensions.

In later runs this problem was solved by calling the equation of state using the progenitor's pressure along with density and  $Y_e$  to return a new value for the temperature. In this way the pressure gradients in the progenitor model are preserved and the models collapse.

### 3.2.3 Setting the Smoothing Length

Particle smoothing lengths are estimated from the initial density using

$$h_i = h_0 \left( \frac{m_i}{\rho_i} \right)^{1/3} \quad (3.8)$$

where  $h_0 = 1.3$ , following Price (private communication). Once this is set the tree can be created and the density summation called to return a new value for the density. This density is used to calculate a new value for  $h$  and the density summation is repeated, the iteration continuing until the value of  $h$  is converged. This process is described in more detail in Section 3.5 below.

After the starting values for  $h$  and  $\rho$  have been determined, the values of all particles are written to the initial output or “dump” file.

## 3.3 Single Timestep Trials

After the particle distributions for the progenitor models had been set up, the original SPH code was tested. It was discovered that while early phases of the collapse proceeded in a physical manner, at late stages as the collapse accelerated unphysical results were produced.

Figure 3.2 shows the densities of the particles at various stages towards the end of collapse. It can be seen that at earlier times homologous collapse occurs, leading to density profiles that are similar. However, when the centre of the star reaches nuclear densities, although material begins to shock, some continues to collapse to densities far exceeding nuclear (and the top end of the EOS table). This is clearly unphysical – the core is far too small to be collapsing directly to a black hole – and is caused by numerical errors.

These numerical errors have two main causes:

- Under the Adams-Bashforth scheme, to advance by one timestep requires particle values stored from the previous 3 timesteps, where each of these is assumed to be the same size. This approximation is accurate enough in the case of slowly varying timestep size, but when the timestep is decreasing rapidly it no longer holds.
- The timestep size is set at the beginning of each step with no “quality control” at the end of the step. In conditions of slowly-varying density the Courant and

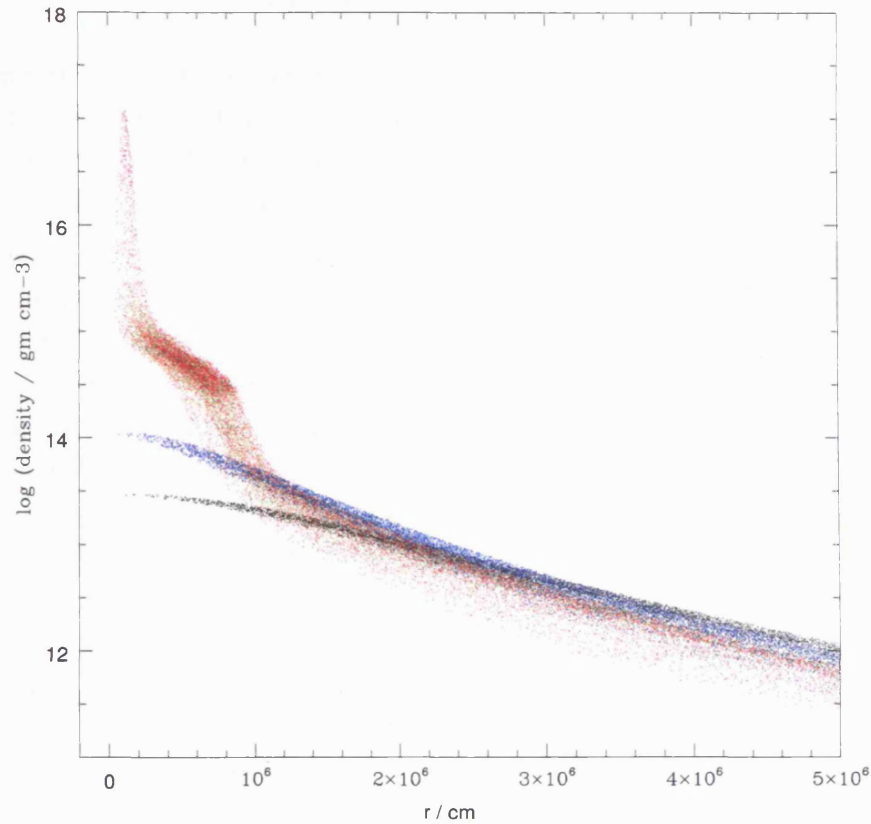


FIGURE 3.2. Weakly-rotating model E20A as the central density approaches and reaches nuclear density ( $\sim 3 \times 10^{14} \text{ g cm}^{-3}$ ). A shock forms but some particles continue to collapse due to numerical errors in the time integration.

dynamical conditions on the timestep may be assumed to produce results of the required accuracy. In catastrophic collapse, however, the timestep required at the end of the step is almost always going to be smaller than that required at the beginning of the step, leading to a systematic overestimate of the length of timestep required. A check must be set at the end of the step to prevent too large a timestep being used.

It became clear that the Adams-Bashforth integrator was not suitable for solving this numerical problem.

## 3.4 Multi-timestepping

Neutron stars, being made entirely of nuclear matter, have a fairly uniform density throughout, which only drops below nuclear at the edges. Since the dynamical timescale goes as  $\rho^{-1/2}$ , in an SPH simulation all particles will have roughly the same dynamical times and it is practical to run all the particles on the same timestep.

The core of a massive star is a completely different environment. At the end of a star's evolution the iron core has a central density of around  $10^{10} \text{ g cm}^{-3}$ . At core bounce, the central density is above  $10^{14} \text{ g cm}^{-3}$ . In the time it takes for the core to collapse and bounce, the density at a radius of  $10^9 \text{ cm}$  has barely changed from a value of  $\sim 10^5 \text{ g cm}^{-3}$ . Clearly the code needs to be capable of handling this enormous range of densities, with corresponding dynamical times ranging over 4-5 orders of magnitude. As mentioned in Section 2.9 of Chapter 2, running all the particles on the smallest timestep becomes unnecessary and highly inefficient.

In the previous section I discussed how the integrator was failing to produce physical results for core collapse around the time of bounce. A new integrator was required and I decided to kill two birds with one stone by replacing the old one with one that would:

- monitor the error at the end of a step to ensure that each step is taken with the correct precision;
- move each particle forward on its own timestep;
- be simple enough to make the above feasible, *i.e.* require a minimum of past steps to be saved.

A method of integration that fulfills all these criteria is 2nd/3rd order Runge-Kutta-Fehlberg (RKF). The Fehlberg method enhances simple second order Runge-Kutta with a third order error estimate obtained via a slight alteration to the scheme.

### 3.4.1 Runge-Kutta-Fehlberg integration

RKF methods can be used for any order of Runge-Kutta integration. In these methods the truncation error at the end of each step is calculated by comparing the result obtained using a Runge-Kutta formula with that obtained from one of a higher order. The most commonly used and derived formula is 4th/5th order, which can be found in many texts, including Numerical Recipes (Press et al. 1992).

To derive the Runge-Kutta-Fehlberg 2nd/3rd order integrator we start from the formulae for 2nd and 3rd order Runge-Kutta estimates for a function  $x(t)$ , where  $f(t, x) = \frac{dx}{dt}$ , at step  $n + 1$ :

$$\hat{x}_{n+1} = x_n + a_1 k_1 + a_2 k_2 \quad (3.9)$$

$$x_{n+1} = x_n + b_1 k_1 + b_2 k_2 + b_3 k_3 \quad (3.10)$$

where

$$k_1 = \delta t f(t, x) \quad (3.11)$$

$$k_2 = \delta t f(t + \alpha_1 \delta t, x + \beta_{11} k_1) \quad (3.11)$$

$$k_3 = \delta t f(t + \alpha_2 \delta t, x + \beta_{21} k_1 + \beta_{22} k_2)$$

The derivation of the 2nd order method (Atkinson 1989) results in a set of 3 simultaneous equations satisfied when:

$$a_1 + a_2 = 1 \quad (3.12)$$

$$\alpha_1 = \beta_{11} = \frac{1}{2a_2} \quad (3.13)$$

For RKF, three constraints for the 3rd order Runge-Kutta terms must be satisfied:

$$b_1 + b_2 + b_3 = 1 \quad (3.14)$$

$$b_2 \alpha_1 + b_3 \alpha_2 = \frac{1}{2} \quad (3.15)$$

$$b_2 \beta_{11} + b_3 (\beta_{21} + \beta_{22}) = \frac{1}{2} \quad (3.16)$$

The integration is begun by advancing the variables by a half step and determining the derivatives at this point. To advance a variable by one full step a mixture of the half-step derivatives and those at the beginning of the step is used, *i.e.*

$$a_1 = \frac{1}{256} \quad (3.17)$$

$$a_2 = \frac{255}{256} \quad (3.18)$$

$$\alpha_1 = \beta_{11} = \frac{255}{512} \approx \frac{1}{2} \quad (3.19)$$

so that

$$\hat{x}_{n+1} = x_n + \frac{1}{256}k_1 + \frac{255}{256}k_2$$

$$k_1 = \delta t f(t, x)$$

$$k_2 = \delta t f\left(t + \frac{1}{2}\delta t, x + \frac{1}{2}\delta t f(t, x)\right). \quad (3.20)$$

To convert this second order solution to third order while making use of results already calculated we set  $\alpha_2 = 1$  so that the derivatives calculated at the end of the full step can be used to achieve third order accuracy. Then

$$\beta_{21} = a_1 = \frac{1}{256} \quad (3.21)$$

$$\beta_{22} = a_2 = \frac{255}{256} \quad (3.22)$$

gives

$$k_3 = \delta t f\left(t + \delta t, x_n + \frac{1}{256}k_1 + \frac{255}{256}k_2\right)$$

$$= \delta t f(t + \delta t, \hat{x}_{n+1}). \quad (3.23)$$

Setting the constants  $\beta_{21}$  and  $\beta_{22}$  in this way means that at the end of the second order step, derivatives can be determined that fit automatically into the third order method.

Setting

$$b_1 = \frac{1}{512} \quad (3.24)$$

$$b_2 = \frac{255}{256} \quad (3.25)$$

$$b_3 = \frac{1}{512} \quad (3.26)$$

and using equation 3.20 we obtain

$$x_{n+1} = x_n + \frac{1}{512}k_1 + \frac{255}{256}k_2 + \frac{1}{512}k_3$$

$$= \hat{x}_{n+1} + \frac{k_3 - k_1}{512} \quad (3.27)$$

giving an error estimate

$$|x_{n+1} - \hat{x}_{n+1}| = \frac{|k_3 - k_1|}{512}. \quad (3.28)$$

The 2nd/3rd order Runge-Kutta-Fehlberg method therefore requires three evaluations of the tree and derivatives for each step taken. However, the derivatives at the end of the step are also the derivatives at the beginning of the new step so that in practice only 2 calls to the tree are required per step. This is the same as for 2nd order Runge-Kutta and is what makes RKF methods so powerful. Once the full step has been taken, the derivatives at the half step need not be stored as they are not required for the error estimate.

The implementation of this method of integration is described below.

### 3.4.2 Initialization

In the method of individual timestepping that I adopted, particles are not assigned timesteps from a continuous range. Instead, particles are sorted into a discrete set of timestep bins and the particles in each bin are advanced together. Forces and other SPH derivatives are calculated for a list of particles in the same time bin rather than for all the particles at once.

To initialize the integrator at the beginning of a dump step all the particles are placed in the same time bin and synchronised in time. The tree, forces and derivatives routines are then called. The forces routine, which calculates the net force on a particle, also sets each particle's desired timestep, according to the Monaghan criteria given in Chapter 2.

Having found the smallest desired timestep  $\min(\delta t_i)$ , the size of the smallest time bin is set to this value multiplied by a safety factor ( $< 1$ ). The size of the bins ranges from  $\delta t_{min}$  to  $2^{n-1}\delta t_{min}$ , where  $n$  is the desired number of levels, set at the beginning of a run. If  $2^{n-1}\delta t_{min}$  is greater than the maximum allowed timestep  $dt_{max}$  (also set at the beginning of the run), the smallest time bin size is reduced to  $dt_{max}/2^{n-1}$ .

Once the size of the time bins has been determined each particle is allocated to the largest bin whose timestep is smaller than its desired timestep.

### 3.4.3 The Outer Loop

The integrator is based on a set of two loops. The outer loop repeats for each step taken in the smallest time bin.

### 3.4.4 The Inner Loop

The inner loop integrates over one step for all bins which are to be advanced, starting from the smallest. A bin is advanced when the end of its step is synchronised with the end of the step of the smallest bin.

A RKF half-step is taken. For the velocity in the  $x$ -direction this is:

$$v_{x,temp} = v_x + dt_{f11} \times f_{v_{x1}} \quad (3.29)$$

where  $dt_{f11} = dt/2$  and  $f_{v_{x1}}$  is the derivative of the velocity at the beginning of the step.

The derivatives at the half step are needed, so the properties of the non-advancing particles must be extrapolated to this point in time. The RKF half step and extrapolated values are used to call the tree and derivatives. The particles are then advanced by a full RKF step, for example:

$$v_{x,temp} = v_x + dt_{f21} \times f_{v_{x1}} + dt_{f22} \times f_{v_{x2}} \quad (3.30)$$

where  $dt_{f21} = dt/256$ ,  $dt_{f22} = (255/256)dt$  and  $f_{v_{x2}}$  is the derivative of the velocity at the half step.

At the end of this step, the tree and derivatives are called a third time to give a new  $f_{v_{x2}}$  etc., which are used to monitor the errors. The errors are calculated from the changes in the derivatives of the quantities and have the dimensions  $(\text{time})^{-1}$ , following from equation 3.28:

$$error_{v_x} = \frac{|f_{v_{x1}} - f_{v_{x2}}|}{|v_{x,temp}|} \quad (3.31)$$

An dimensionless accuracy parameter is calculated from the error and the required tolerance  $\epsilon$ :

$$A = \frac{error_{max} dt}{512\epsilon} \quad (3.32)$$

$A$  is then multiplied by  $dt$  to give the new desired timestep. If this timestep is shorter than that of the smallest bin, a smaller time bin (or bins) is created (subject to a minimum bin size and maximum number of bins). This means that only at the beginning of each dump step are the Monaghan criteria used – from then on the timestep is determined by monitoring the errors.

The particle properties are now updated to their full step values, regardless of their errors. If the bin being advanced is the largest to be advanced this step, its full step will correspond in time to the half step of the larger bin above it. In this case the half-step

derivatives can be called for the bin above, ready for the next cycle. The result of this is that only the smallest bin needs to be advanced a half step upon entry to the inner loop.

### 3.4.5 Rearranging the Particles

After exiting the inner loop the particles that have been advanced are put into the correct time bins for the next step. Since any required extra bins have already been created, all that is required is for the list to be updated. Particles are only allowed to stay put or move to smaller bins at this stage.

If the step that has just been taken is that of the largest existing bin (*i.e.* all particles are synchronised in time) and if the integrator is to continue, the time bins are emptied and the particles are redistributed according to their desired timesteps (obtained from the error monitoring). The code then returns to the beginning of the outer loop. If the time exceeds the next dump time no rearrangement is needed. The code exits the integrator and writes a dump. The whole cycle is then repeated.

## 3.5 Including grad h terms

In Section 2.3 of the previous chapter I referred to the “scatter” interpretation of SPH, in which a quantity at a particle  $i$  is determined by the sum of the contributions from all particles that overlap the centre of  $i$ . The overlapping particles are considered smoothed out in space while  $i$  acts as a point.

In this section, for reasons that will become clear, I use the “gather” interpretation, in which the particles summed over are those which fall within the kernel of particle  $i$  itself. The particles are thus regarded as point markers in the fluid, whose contributions are weighted by the kernel of particle  $i$ , which is extended in space (see Figure 3.3, and compare to Figure 2.1 of Chapter 2).

The gather and scatter interpretations of SPH are equivalent only if the smoothing length is the same for all particles. With individual particle smoothing lengths the neighbours are defined in different ways for each method. If the gather method is used, the neighbours of particle  $i$  are those within  $2h_i$  of it. In the scatter method, the neighbours  $j$  are those particles to which  $i$  is closer than  $2h_j$ . Summations are therefore performed over different sets of particles for each method.

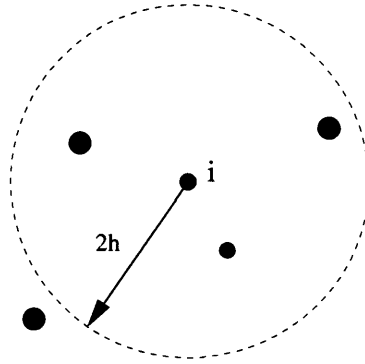


FIGURE 3.3. In the “gather” interpretation of SPH the density of particle  $i$  is the sum of the masses of all particles within the kernel of  $i$ , weighted by the kernel.

### 3.5.1 Effects of individual $h$

Hernquist (1993) first discussed the inaccuracies caused by using individual and time-dependent smoothing lengths for each particle. In Chapter 2, Section 2.4 I explained that the specific internal energy could be evolved alongside the velocities to complete the hydrodynamic description of the system. The equation of state relates this quantity to other quantities, such as temperature and entropy. But evolving the specific internal energy is not the only option - in some cases it is possible to evolve the entropy equation instead of the energy equation, and obtain the specific internal energy from the equation of state. Hernquist (1993) used simulations of colliding polytropes to show that if the entropy equation was evolved, the energy did not stay constant, and if the internal energy equation was evolved, the entropy did not stay constant.

The reason for the energy discrepancy is that the kernel is a function of both position and smoothing length  $W_{ij} = W(\mathbf{r}_{ij}, h_i)$ . When the hydrodynamic equations are derived by differentiating the kernel, the  $\nabla W$  terms are considered but the  $\frac{\partial W}{\partial h}$  is neglected. For example, Hernquist differentiates the continuity equation

$$\rho_i = \sum_{j=1}^N m_j W_{ij} \quad (3.33)$$

to obtain

$$\frac{d\rho_i}{dt} = \sum_{j=1}^N m_j \mathbf{v}_{ij} \cdot \nabla_i W_{ij} + \sum_{j=1}^N m_j \frac{\partial W_{ij}}{\partial h} \frac{\partial h}{\partial t}. \quad (3.34)$$

In the description of SPH I have provided so far, the second term on the right hand side in Equation 3.34 has been ignored. These terms are often referred to as the “grad h” terms, and for temporally- and spatially-varying smoothing lengths they are generally not negligible.

Nelson & Papaloizou (1994) derived a method for including the grad h terms in full. Unfortunately this method requires a third loop through the SPH equations each time the derivatives are called, which makes it time consuming for the small increase in accuracy it produces. It also requires keeping a strictly constant number of neighbours for each particle, making it extremely tricky to implement.

Only recently have Springel & Hernquist (2002) derived a self-consistent method for including smoothing length terms without requiring an extra summation. Evolving the entropy rather than the energy equation and starting from the Euler-Lagrange equation they used Lagrange multipliers to obtain the velocity equation. The multipliers were constrained by requiring that the smoothing volume for each particle enclose a “constant mass”  $M_{sph}$  rather than a constant number of neighbours, such that

$$\frac{4\pi}{3}h_i^3\rho_i - M_{sph} = 0 . \quad (3.35)$$

The resulting velocity equation is modified by terms containing the smoothing lengths  $h_i$ ,  $h_j$  and their derivatives.

It is clear that in Equation 3.35 the extent of a particle is defined only by the particle’s own smoothing length. It follows that in this formulation the neighbours of a particle  $i$  are those within  $2h_i$  of it— in other words, the kernel depends only on  $h_i$ ,

$$\rho_i = \sum_{j=1}^N m_j W(\mathbf{r}_{ij}, h_i) \quad (3.36)$$

*i.e.* in this method the gather interpretation is assumed.

An alternative derivation of the same scheme was produced by Monaghan (2002). Rather than preserve a constant number of neighbours or a constant mass in the smoothing volume,  $h$  was defined as a function of the density, *i.e.*  $h = h(\rho)$ , and therefore of the particle coordinates. Density is also a function of  $h$  in the form of equation 3.36. Hence the density and the smoothing length are functions of each other and can be iterated to convergence. At the same time they are both functions of the particle coordinates.

With this in mind, taking the time derivative of 3.36 gives

$$\frac{d\rho}{dt} = \frac{1}{\Omega_i} \sum_{j=1}^N m_j \mathbf{v}_{ij} \cdot \nabla_i W_{ij}(h_i) \quad (3.37)$$

where

$$\Omega_i = \left[ 1 - \frac{\partial h}{\partial \rho} \sum_{k=1}^N m_k \frac{\partial W_{ij}(h_i)}{\partial h_i} \right]. \quad (3.38)$$

In a similar fashion, the Euler-Lagrange equations can be solved to give the momentum equation

$$\frac{d\mathbf{v}_i}{dt} = - \sum_{j=1}^N m_j \left[ \frac{P_i}{\Omega_i \rho_i^2} \nabla_i W_{ij}(h_i) + \frac{P_j}{\Omega_j \rho_j^2} \nabla_i W_{ij}(h_j) \right] \quad (3.39)$$

and the thermal energy equation becomes

$$\frac{du_i}{dt} = \frac{P_i}{\Omega_i \rho_i^2} \sum_{j=1}^N m_j \mathbf{v}_{ij} \cdot \nabla_i W_{ij}(h_i). \quad (3.40)$$

This formulation is exactly the same as that of Springel & Hernquist (2002) as long as the smoothing length

$$h \propto \left( \frac{1}{\rho} \right)^{\frac{1}{3}} \quad (3.41)$$

and automatically conserves linear and angular momentum. It should be noted that in every equation where the  $\Omega_i$  factor is included the kernel should be a function of  $h_i$  only.

Where artificial viscosity is added, the symmetrized kernel is used, with the factors  $\Omega_i, \Omega_j$  included, so that the velocity term becomes

$$- \sum_{j=1}^N m_j \Pi_{ij} \overline{\nabla_i W_{ij}} \quad (3.42)$$

where

$$\overline{\nabla_i W_{ij}} = \frac{1}{2} \left[ \frac{\nabla_i W_{ij}(h_i)}{\Omega_i} + \frac{\nabla_i W_{ij}(h_j)}{\Omega_j} \right]. \quad (3.43)$$

### 3.5.2 Altering the code

Following the description of Price & Monaghan (2004) and Price (2004) I altered the code to include the variable smoothing length terms. The essence of the algorithm is as follows:

1. The density is a function of the smoothing length, but the smoothing length is also a function of the density.
2. Therefore make an initial estimate of  $h$  using the old value of  $\rho$ .
3. Evaluate the density summation as usual using this value of  $h$ .
4. Use the new value calculated for  $\rho$  to set a new value of  $h$ .
5. Repeat the summation for  $\rho$  using the new value of  $h$ .
6. Iterate until the criterion for convergence is met.

In my implementation the initial estimate for  $h_i$  is obtained from its time derivative, as given in Section 2.6 of Chapter 2, which is evolved alongside the other variables as before. It should be noted that this method assumes that  $h \propto \rho^{-1/3}$ .

In creating the tree, the neighbours of a particle are defined as those within  $\max(2h_i, 2h_j)$ . This ensures that for each interacting pair of particles, each particle counts the other as a neighbour. (A separate count is kept of the number of neighbours within  $2h_i$  of a particle and this number is that which is to be kept within the upper and lower bounds in the  $\dot{h}$  routine.)

Once the neighbours lists have been constructed the density summation is calculated as in 3.36. In addition to the density we also calculate

$$\frac{\partial \rho_i}{\partial h_i} = \sum_{j=1}^N m_j \frac{\partial W_{ij}(h_i)}{\partial h_i} \quad (3.44)$$

This requires the calculation of  $\partial W/\partial h$  alongside the other the kernel quantities. The extra factor  $\Omega_i$  can then be computed as in equation 3.38, using

$$\frac{\partial h}{\partial \rho} = -\frac{h_i}{3\rho_i}. \quad (3.45)$$

Having obtained these values, a new value for  $h_i$  can be determined. To begin with, a Newton Raphson scheme is used. First, a  $\rho$  consistent with the old smoothing length is calculated:

$$\rho_{rep} = \frac{m_i}{(h_i/h_0)^3} \quad (3.46)$$

where  $h_0$  is the constant used to set the initial smoothing length (see Section 3.2.3). Then

$$y(h) = \rho_{rep} - \rho_i \quad (3.47)$$

$$\begin{aligned}
\frac{\partial y}{\partial h} &= \frac{\partial \rho}{\partial h} - \sum_{j=1}^N m_j \frac{\partial W_{ij}(h_i)}{\partial h_i} \\
&= \frac{\partial \rho}{\partial h} \left( 1 - \frac{\partial h}{\partial \rho} \sum_{j=1}^N m_j \frac{\partial W_{ij}(h_i)}{\partial h_i} \right) \\
&= -\frac{3\rho_i}{h_i} \Omega_i .
\end{aligned} \tag{3.48}$$

The new  $h_i$  is calculated as

$$h_{new} = h_i - \frac{y}{\partial y / \partial h} \tag{3.49}$$

and a particle is considered converged if

$$\frac{|h_{new} - h_i|}{h_i} < 0.01 . \tag{3.50}$$

I found that using Newton-Raphson most particles converge within one or two iterations. If a particle has failed to converge after the third Newton-Raphson iteration, I switch to a fixed-point iteration scheme, where

$$h_{new} = h_0 \left( \frac{m_i}{\rho_i} \right)^{\frac{1}{3}} . \tag{3.51}$$

If convergence has been reached, the old value of  $h_i$  is kept, in order to be consistent with the calculated  $\rho_i$ . The code does not continue iterating on converged particles. If one or more of the particles requires another iteration, the tree and the density are called, but only unconverged particles have their density re-evaluated. This method has been tested extensively by Price (2004), who found that it significantly improved the match with analytic results in simple test problems.

## 3.6 Including shear viscosity

In order to examine the effect of angular momentum transport on the pre-bounce dynamics of core collapse we require a prescription for the, as yet unknown, transport mechanism. It is likely that magnetic fields could play a strong role in the transport of angular momentum during the course of the collapse. It is possible that some form of the magneto-rotational instability, which is thought to be responsible for angular momentum transport in accretion discs, may be active (Balbus & Hawley 1991). However the details of the physics of any such instability are very uncertain at best, and certainly beyond the scope of this thesis.

Rather than implement a detailed scheme for an unknown angular momentum transport mechanism, we choose to parametrise it in the form of a Shakura-Sunyaev  $\alpha$  viscosity (Shakura & Sunyaev 1973). This semi-empirical model has been used for many years, with great success, to study the effects of angular momentum transport in accretion discs (see Frank, King & Raine (2002) for a discussion). Much progress was made in this field even before a viable physical candidate for the transport mechanism (the MRI) was established. The main advantages of the  $\alpha$  viscosity are that it is extremely easy to add to a SPH code, and can be adapted quickly and simply to examine different forms of angular momentum transport. I discuss the implementation of the viscosity in the code below.

In the Shakura-Sunyaev model, it is assumed that the stress tensor in the disc can be approximated as a scalar, with a shear force produced at right angles to the pressure gradient. The viscous force density is approximated by

$$f_{visc, shear} \sim \rho \lambda \tilde{v} \frac{\partial^2 v_\phi}{\partial R^2} \sim \rho \lambda \tilde{v} \frac{v_\phi}{R^2} \quad (3.52)$$

where  $\lambda$  is the typical lengthscale on which viscosity operates,  $\tilde{v}$  is the speed of the fluid,  $v_\phi$  is the tangential velocity of the disc and  $R$  is the distance from the centre of the disc. The viscosity  $\nu$  is defined as

$$\nu \sim \lambda \tilde{v} \quad (3.53)$$

which in the SS model is written as

$$\nu = \alpha_{ss} H c \quad (3.54)$$

where  $H$  is a typical length scale in the disc (e.g. the disc thickness or the pressure scale height) and  $c$  is a typical speed (e.g. the sound speed). It should be noted that the SS formulation of viscosity does not contain any information about its physical origin - it merely assumes that the scales on which viscosity acts are related to the typical scales of the disc.

It has been shown by Murray (1996) that the SPH artificial viscosity can be made equivalent to SS viscosity. In the limit of number of particles  $N \rightarrow \infty$  and  $h \rightarrow 0$  in which the density and sound speed vary on lengthscales much longer than the sound speed then

$$\alpha_{sph} = \frac{\kappa \alpha_{ss} H}{2 h} \quad (3.55)$$

where  $\kappa = 1/5$  in 3 dimensions.

It was simple to alter the code to include this formulation. Normally in SPH the artificial viscosity is a tool for handling shocks and therefore only desired when the fluid is in compression, i.e. the particles are moving towards each other. In the case of SS viscosity, we require a shear, dissipative force between particles whether they are moving towards or away from each other. This is achieved by altering the  $\alpha$  term in the current time-dependent treatment of viscosity while maintaining the usual, time-dependent  $\beta$  term. As a first approximation we set  $\alpha$  constant, which implicitly assumes that the sound speed, typical length scale and smoothing length are constant. The AV prescription becomes:

$$\Pi_{ij} = \begin{cases} \frac{-\alpha_{sph} c_{ij} \mu_{ij} + \beta(t) \mu_{ij}^2}{\rho_{ij}} & \mathbf{v}_{ij} \cdot \mathbf{r}_{ij} \leq 0 \\ \frac{-\alpha_{sph} c_{ij} \mu_{ij}}{\rho_{ij}} & \mathbf{v}_{ij} \cdot \mathbf{r}_{ij} > 0 \end{cases} \quad (3.56)$$

In the future it will probably be best to set  $\alpha_{sph}$  according to equation 3.55 and also set this treatment to be triggered by the formation of a disc. The present formulation is suitable only for a qualitative investigation of the effects of viscosity.

### 3.7 Tests

The unaltered SPH code had been tested extensively on “standard” analytical problems such as the Sod shock tube and in high Mach number shocks at every stage of its development. A high performance code such as this tends to be developed as it passes between users, and a description of the primeval version can be found in Benz et al. (1990). This paper includes tests to identify the effects of numerical viscosity, which was found to be insignificant. The addition and testing of the time-dependent artificial viscosity formulation described in Chapter 2, Section 2.7 is described in Rosswog et al. (2000). When the Shen EOS was added simulations were run comparing it to the Lattimer-Swesty EOS (Rosswog & Davies 2002).

I tested the altered code on a particle distribution representing a neutron star in equilibrium, which was allowed to relax. The code proved stable and after 1000 dynamical times the change in total energy was only 1.2% and the density had retained its initial profile. Rotation was then added to the initial model and it was run for 100 dynamical times. During this time the rotation rate was maintained and the change in energy was 2.0%. The same rotating model was then run with the “ $\alpha$ ” viscosity formulation as described in Section 3.6. After 100 dynamical times the change in energy was 1.4%.

## 3.8 Summary

In this chapter I have described the alterations made to my SPH code to make it suitable for simulating core collapse supernovae. The main changes undertaken are listed below.

- A routine was written to map the variables from the one dimensional progenitor models to a three dimensional distribution of particles. The particles were distributed uniformly and quasi-randomly and then stretched radially to produce the correct density distribution. Variable values were set by interpolation in the progenitor models, except for temperature, which was set so that the EOS would return the required pressure. Rotation was set to be constant either on spherical shells or cylinders.
- The Adams-Bashforth integrator was replaced by a 2nd/3rd order Runge-Kutta-Fehlberg method, allowing the error to be estimated at the end of each step.
- Individual particle timesteps were introduced, with each particle advanced on the largest timestep possible.
- The previously neglected “grad h” terms, which take into account the time-dependence of the smoothing length, were included, following the description of Monaghan (2002).
- An option for including artificial shear viscosity in a run was added, based on the Sunyaev-Shakura “ $\alpha$ ” viscosity, which is used in simulations of accretion discs.
- The altered code was tested by letting a neutron star in equilibrium relax. Energy was conserved for 1000 dynamical times. A rotating neutron star was also tested and maintained its rotation rate for  $> 100$  dynamical times.

# Chapter 4

## *Collapse of the Woosley Progenitor*

“I recently learnt that, contrary to popular belief, bumble bees don’t actually defy the laws of physics by being too heavy to fly, because of some strange air flow they get going around them by batting their wings. But before I learnt that, I asked people whether or not they thought it worrying that thousands of bees were busily flying around disproving everything we think we know about the world. And no one seemed the least bit bothered by it. Whereas I was pulling my hair out. That’s the kind of attitude I’m up against when I try to learn more about science.”

*Clare Jordin*

## 4.1 Introduction

A recurrent problem in the field of supernova modelling is the difficulty of comparing results of simulations. Given the size of the parameter space to be tested and the imperative to break new ground, modellers tend not to repeat the simulations of other groups but to produce new models that highlight the differences in their codes and initial conditions. It is a rare and notable occasion when separate groups collaborate to test their codes with identical initial conditions, as in Liebendörfer et al. (2005).

With this in mind, I sought a control model with which to test my code. Happily, in the past decade a “standard” supernova progenitor has emerged from the multitude of stellar evolution calculations. This is the catchily-named model S15A of Woosley & Weaver (1995). In Section 4.3 of this chapter I describe the results of running my supernova code on this progenitor model and compare them with those of another group who used the same progenitor.

This progenitor has also been widely used in studies of rotation using a simple parametrization for the initial angular velocity. Following these studies, I have added rotation to S15A to obtain a qualitative picture of how core collapse is affected by increasing amounts of rotation. This is described in Sections 4.4 and 4.5. In particular, the effect on the structure and rotation rate of the core at bounce is discussed, with a view to whether or not instabilities are able to set in by the time bounce occurs.

## 4.2 Stellar Evolution Models

From the beginning of the era of computers the ability to perform repetitive calculations has been applied to the question of exactly what goes on inside stars. The complexity of the problem, with hundreds of variables and timescales that vary by many orders of magnitude, means that, despite vast increases in computing capabilities, calculations are still performed in one dimension. However, as time goes on, more and more detailed models of stellar evolution are being produced, using hundreds of zones with nuclear reactions followed in detail and effects such as winds, mixing, convection, rotation and magnetic fields included. Because there are so many parameters it will be some time before speculation as to which effects are truly significant can be tested and the accuracy of these models can be established.

Calculation of the evolution of massive stars right up to the brink of core collapse requires all the nuclear reactions up to the iron group elements to be followed and the

code to be able to handle the increasing density (and degeneracy) of the core. Modelling supernova progenitors is an ambitious and arduous task and the mantle of producing detailed calculations has only been taken on by a few groups worldwide.

In the mid-90s a sophisticated assault on this problem was undertaken by Woosley & Weaver (1995), who evolved around 80 non-rotating stellar models with masses ranging from 11 to  $40 M_{\odot}$ . They used initial metallicities of 0,  $10^{-4}$ ,  $10^{-2}$ , 0.1 and 1 times solar metallicity  $Z_{\odot}$  and during the evolution employed a nuclear reaction network of 200 isotopes. Mixing by convection and semiconvection was also included. Two models, S15A and S25A were evolved with a network of 476 isotopes for calibration purposes. S15A (sometimes known as s15s7b2) has become somewhat of a “standard” progenitor model in the supernova community. This  $15 M_{\odot}$  model has an initial metallicity of  $Z_{\odot}$  and a final iron core mass of  $1.32 M_{\odot}$ .

The authors simulated the subsequent supernova explosion by placing an outward-moving piston at the edge of the iron core. The piston was stopped when it reached  $10^9$  cm, corresponding to a mass  $M_9 = 1.99 M_{\odot}$ , and from this point the explosion continued unaided. The nucleosynthetic yields of the explosion were calculated using the reaction network and a simplified treatment of neutrino emission from the core.

What this study did not follow was the collapse of the iron core, meaning that I could not make use of it to test my core collapse code. However, even before this paper was published, Burrows et al. (1995) had simulated the core collapse and explosion of S15A using a piecewise parabolic method (PPM) in two dimensions. It is with the results of this simulation that I compare my models, using the progenitor S15A as a control.

### 4.3 Collapse of the $15 M_{\odot}$ Progenitor

All the simulations described in this chapter were run with 300 000 particles on the SRIF2 cluster at the University of Leicester. The Woosley progenitor S15A was mapped to an SPH particle distribution as described in Chapter 3, Section 3.2. Parameters for this non-rotating run, hereafter referred to as “Woos”, can be found in Table 4.1.

Snapshots of the model at and just after bounce and profiles of a selection of variables can be found in Figure 4.10 at the end of this chapter. It can be seen from the snapshots that at bounce the density distribution is centrally peaked and spherically symmetric, as is the shock that forms at the edge of the inner core (visible in the snapshot of entropy). Around 1 ms after bounce the shock has reached a radius of about 100 km and the snapshot of radial velocity shows that it remains roughly spherical.

Burrows et al. (1995), hereafter B95, simulated the collapse and explosion of S15A in two dimensions and included neutrino transport by flux-limited diffusion, ignoring neutrino-electron scattering. Because my code does not include neutrinos it is not suitable for modelling the collapsed core for more than a few milliseconds after bounce. Indeed, the absence of neutrino trapping in my models will affect the densities obtained in the core as it collapses. I therefore compare the behaviour of my model with B95 only up to core bounce.

Figures 4.1-4.6 show the evolution of density, radial velocity, entropy and electron fraction per baryon as a function of enclosed mass for the B95 and Woos models. In each of the B95 graphs the curve labelled “c” shows the profile at just under 2 ms post-bounce, and marks the last point at which the models can be safely compared. Core bounce takes place at around 100 ms in my model, whilst the B95 takes 209 ms. This is most likely due to variations produced by differences in the mapping of the one dimensional progenitor model to two dimensional PPM and three dimensional SPH respectively causing the initial stages of collapse to proceed at different rates. From the point where the central density reaches  $10^{12} \text{ g cm}^{-3}$  the time to bounce is approximately the same for both models.

Evolution of the density profiles are shown in Figure 4.1. The region of homologous collapse can be seen in the first three curves in each graph. Comparing the two graphs, the behaviour of the density is qualitatively the same, although the drop off in the density at the edge of the inner core (around  $0.8 M_{\odot}$ ) is steeper in model Woos. In model Woos the central density takes 66 ms to go from  $10^{10}$  to  $10^{11} \text{ g cm}^{-3}$ , 15 ms to go from  $10^{11}$  to  $10^{12} \text{ g cm}^{-3}$ , then less than 5 ms to reach  $10^{13} \text{ g cm}^{-3}$  and around 1.5 ms to reach  $10^{14} \text{ g cm}^{-3}$ . Upon reaching nuclear density a shock is observed to form at the centre of the core and in a fraction of a millisecond the core reaches “maximum scrunch”, the topmost curve in the Woos model. In the following few milliseconds the core relaxes slightly as the shock travels outwards, with the central density undergoing a correspondingly slight decrease. Because of the lack of neutrinos in my model, the shock does not stall completely and can be seen at around  $1.2 M_{\odot}$  in the last of the Woos curves, petering out as it becomes less well resolved. In B95 the shock stalls at around this point due to neutrino losses and the core subsequently grows by accretion.

The behaviour of the core around bounce can be observed more clearly by plotting the radial velocity profile, as in Figure 4.2. The homologous infall (compare the first two curves with Figure 1.5 in Chapter 1) is followed by a sudden reversal of the velocities in the inner core, starting at the centre. The velocity reaches a maximum at the edge of the inner core, after which the shock slows and becomes an accretion shock (curve “d”

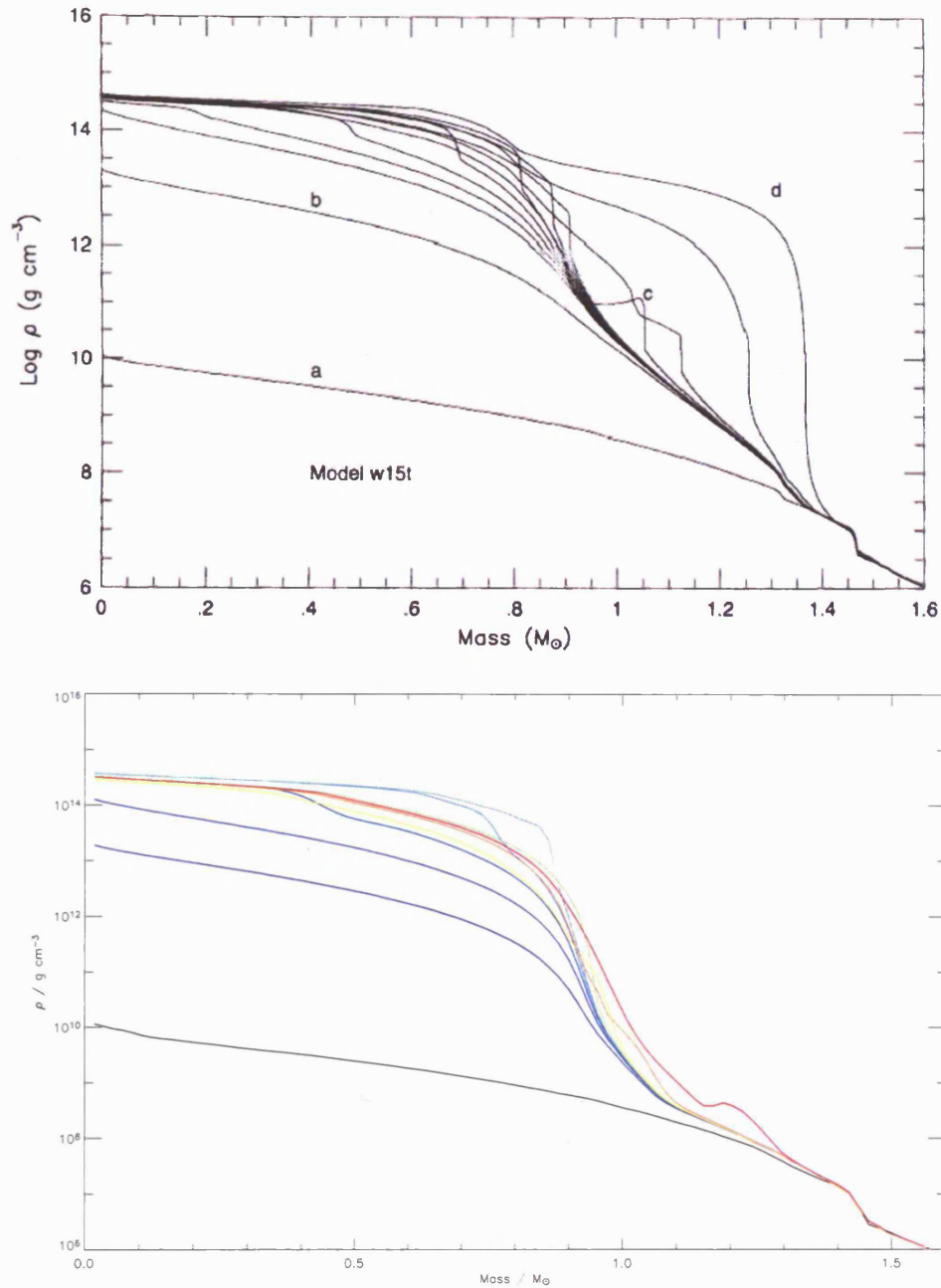


FIGURE 4.1. Top: Density plotted logarithmically versus enclosed mass for model B95. The curves marked “a” through “d” correspond to  $t = 20.0, 207.5, 210.6$  and  $269.1$  ms, with core bounce occurring at around 209 ms. Bottom: Similar plot for model Woos at  $t = 19.21, 98.30, 99.34, 99.67, 99.84, 99.95, 100.3, 100.9, 103.7$  and  $122.0$  ms, line colours progressing from black through blue and green to red. Core bounce occurred at 100.0 ms. Both models show the shock forming in a similar manner, but in model Woos the density falls off more steeply at the edge of the inner core, around  $0.8 M_{\odot}$ .

in B95). The agreement between Woos and B95 is good in terms of the shape of the pre-bounce curve and location and magnitude of the shock at bounce. However, model Woos shows an oscillation in the velocity curve around bounce – it appears that concentric shells of material are driven outwards with different velocities.

These oscillations are characteristic of the way SPH handles shocks. Artificial viscosity is included in SPH to stop the particles getting unphysically close together or passing through each other in regions under compression. When the AV parameter is too small the motion of shocked particles is not damped sufficiently and unphysical oscillations can occur. This code uses time-dependent viscosity, which is set to grow when the divergence of the density decreases, *i.e.* the particles are moving towards each other. Because the shock forms as a result of the equation of state suddenly becoming hard, rather than the particles suddenly getting closer to each other, in this case the AV parameter does not increase as much as it should. Therefore oscillations appear in the shocked material.

The radial velocities for individual particles during bounce are shown in Figure 4.3. It can be seen that as the shock grows on its way out of the inner core, the amplitude of the oscillations increases. Once the shock reaches the mantle it begins to compress infalling matter, at which point the AV parameter increases enough to damp the oscillations.

The specific entropy profile of the collapsing core is also in good agreement with B95 (Figure 4.5). Because different equations of state were used in the models the initial entropy profile is somewhat different, but the subsequent evolution of the entropy around the shock is qualitatively similar. A peak in entropy appears at the location of the shock and soon broadens to produce an extended region of negative entropy gradient. It is in this region that convective overturn can take place.

It can be seen in Figure 4.5 that the entropy appears not to be conserved—in the central regions just before bounce the entropy drops to 0 before rising again. This is because in my SPH code the entropy is not an evolved variable, but is set by the call to the equation of state, which is a function of the temperature, density and electron fraction. The temperature itself is calculated from the specific internal energy. In regions of temperature degeneracy, *i.e.* the pre-bounce core, a small change in internal energy causes a large change in temperature and entropy. Thus neither variable carries much meaning and their values are set to 0.

The final variable for comparison is that of the electron fraction per baryon  $Y_e$ , shown in Figure 4.6. It is immediately obvious that the evolution of this variable in each model is very different. In the Woos model,  $Y_e$  remains unchanged. This is because all changes

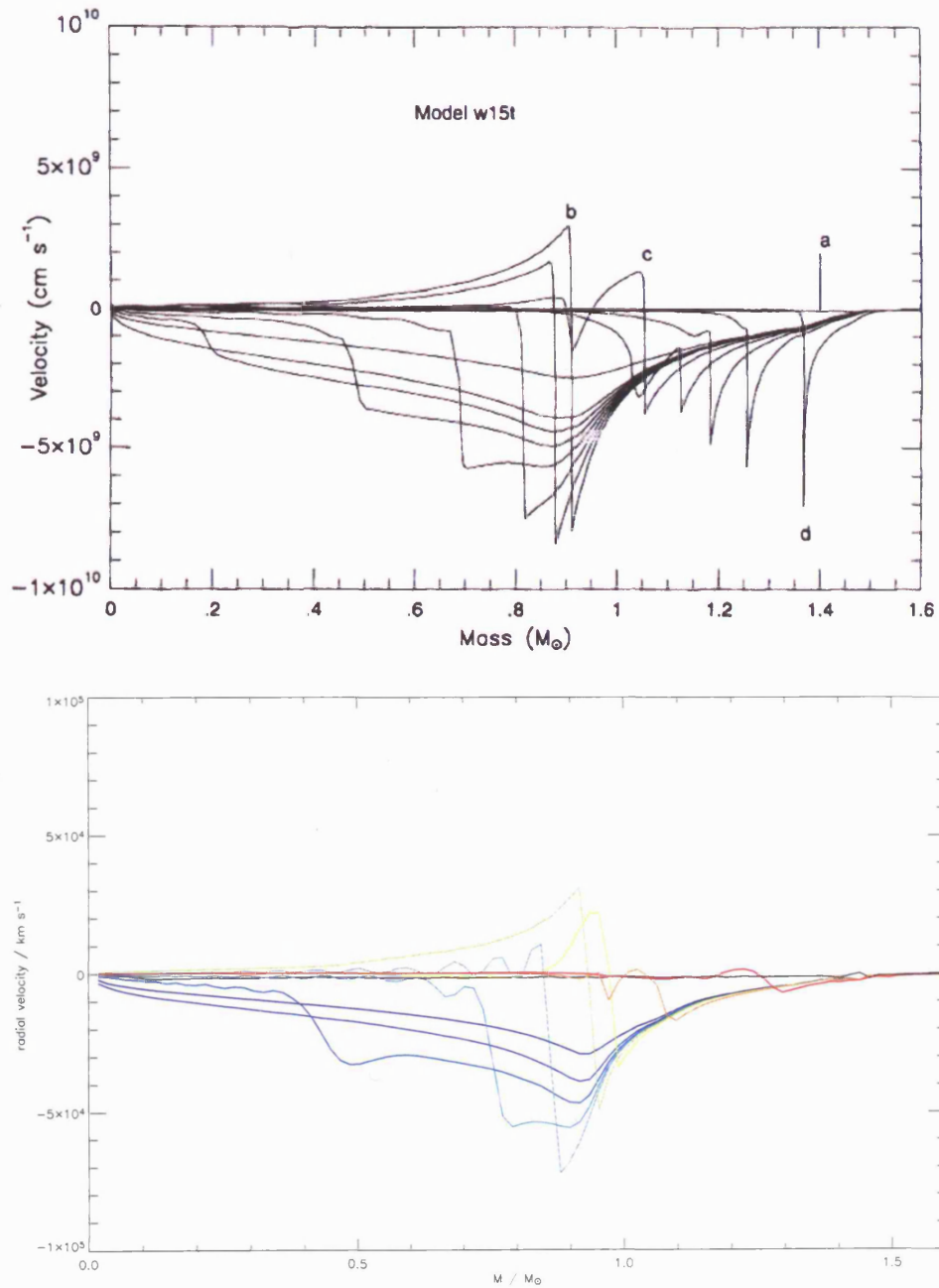


FIGURE 4.2. Top: Radial velocity versus enclosed mass for model B95. The curves marked “a” through “d” correspond to  $t = 20.0, 207.5, 210.6$  and  $269.1$  ms, with core bounce occurring at around 209 ms. Bottom: Similar plot for model Woos at  $t = 19.21, 98.30, 99.34, 99.67, 99.84, 99.95, 100.3, 100.9, 103.7$  and  $122.0$  ms. Core bounce occurred at 100.0 ms. The location and size of the shock are in very good agreement, but in model Woos the radial velocity exhibits an oscillation behind the shock as it forms.

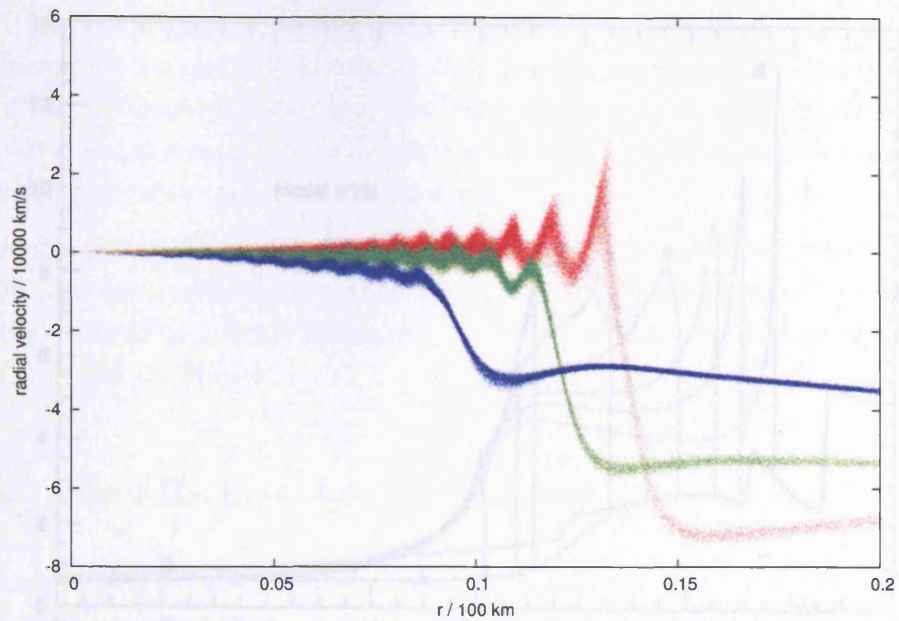


FIGURE 4.3. Radial velocities of individual particles versus radius at  $t = 99.67$  (blue),  $99.84$  (green) and  $99.95$  ms (red), as the shock is forming. Oscillations in the radial velocity are clearly visible.

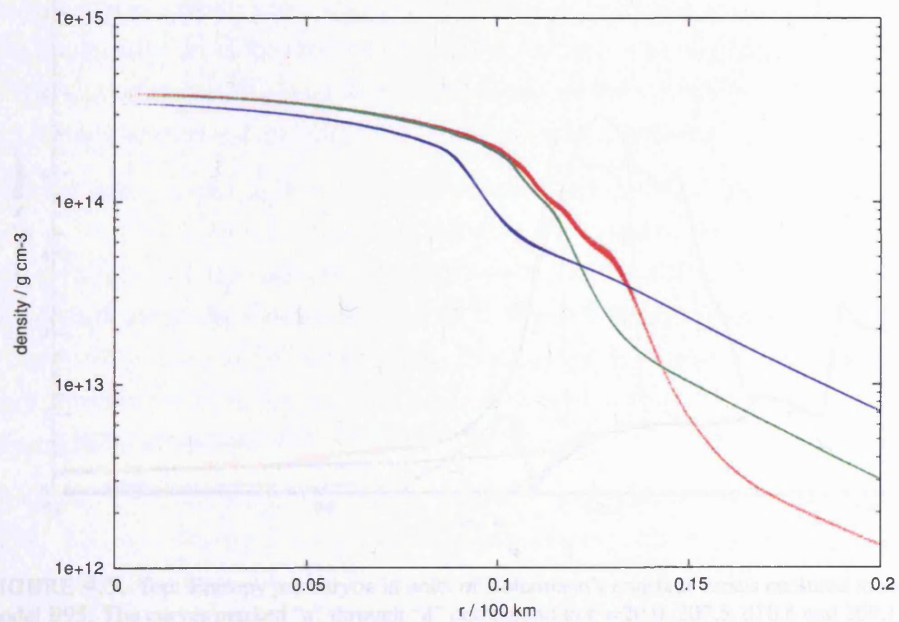


FIGURE 4.4. Densities of individual particles versus radius at  $t = 99.67$  (blue),  $99.84$  (green) and  $99.95$  ms (red), as the shock is forming. At the latter two times density perturbations are visible where the oscillations in radial velocity are large.

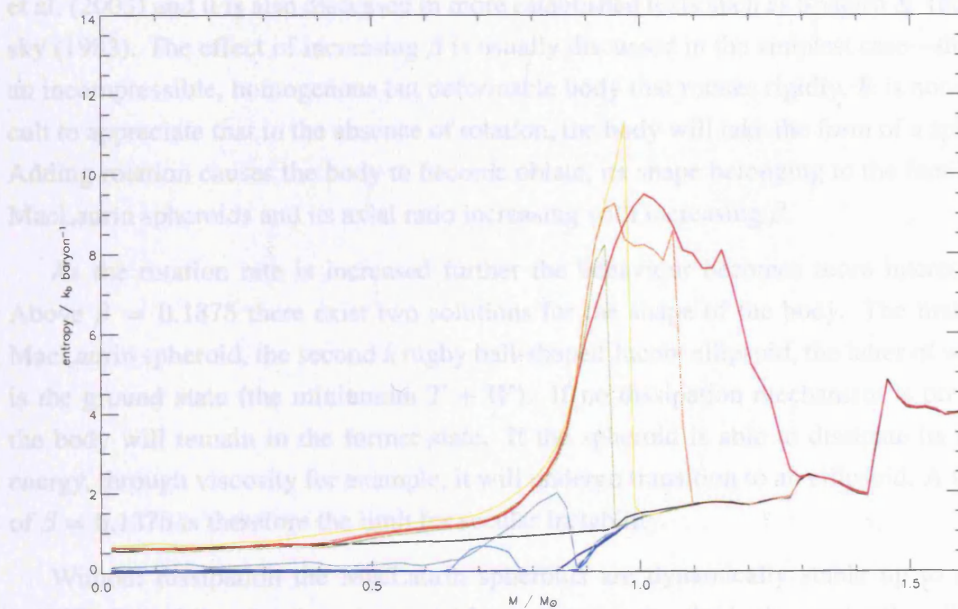
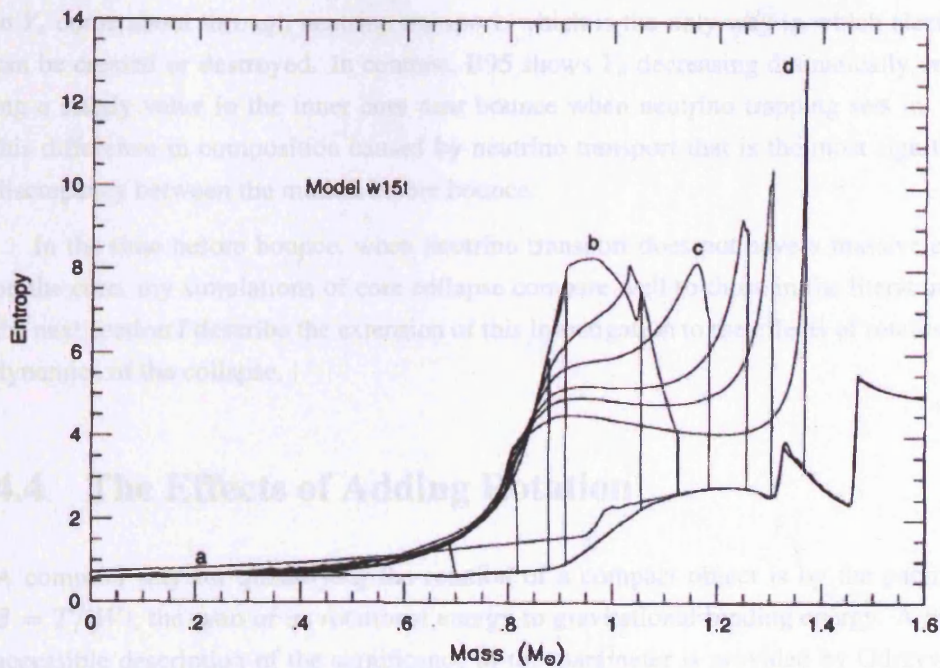


FIGURE 4.5. Top: Entropy per baryon in units of Boltzmann's constant versus enclosed mass for model B95. The curves marked "a" through "d" correspond to  $t = 20.0, 207.5, 210.6$  and  $269.1$  ms, with core bounce occurring at around 209 ms. Bottom: Similar plot for model Woos at  $t = 19.21, 98.30, 99.34, 99.67, 99.84, 99.95, 100.3, 100.9, 103.7$  and  $122.0$  ms. Core bounce occurred at 100.0 ms. In model Woos the entropy is set to 0 by the code in regions of temperature degeneracy. Despite the different EOS used, the entropy profiles are in good agreement qualitatively, with peaks of a similar magnitude and regions of negative entropy gradient forming in both.

to  $Y_e$  come about through neutrino transport, which is the only way in which electrons can be created or destroyed. In contrast, B95 shows  $Y_e$  decreasing dramatically, reaching a steady value in the inner core near bounce when neutrino trapping sets in. It is this difference in composition caused by neutrino transport that is the most significant discrepancy between the models before bounce.

In the time before bounce, when neutrino transport does not have a massive effect on the core, my simulations of core collapse compare well to those in the literature. In the next section I describe the extension of this investigation to the effects of rotation the dynamics of the collapse.

## 4.4 The Effects of Adding Rotation

A common way for quantifying the rotation of a compact object is by the parameter  $\beta = T/|W|$ , the ratio of its rotational energy to gravitational binding energy. A highly accessible description of the significance of this parameter is provided by Odrzywolek et al. (2003) and it is also discussed in more established texts such as Shapiro & Teukolsky (1983). The effect of increasing  $\beta$  is usually discussed in the simplest case—that of an incompressible, homogenous but deformable body that rotates rigidly. It is not difficult to appreciate that in the absence of rotation, the body will take the form of a sphere. Adding rotation causes the body to become oblate, its shape belonging to the family of MacLaurin spheroids and its axial ratio increasing with increasing  $\beta$ .

As the rotation rate is increased further the behaviour becomes more interesting. Above  $\beta = 0.1375$  there exist two solutions for the shape of the body. The first is a MacLaurin spheroid, the second a rugby ball-shaped Jacobi ellipsoid, the latter of which is the ground state (the minimum  $T + W$ ). If no dissipation mechanism is present, the body will remain in the former state. If the spheroid is able to dissipate its extra energy, through viscosity for example, it will undergo transition to an ellipsoid. A value of  $\beta = 0.1375$  is therefore the limit for secular instability.

Without dissipation the MacLaurin spheroids are dynamically stable up to  $\beta = 0.2738$ . Past this point there is no stable configuration – the body must either dissipate its energy to become a Jacobi ellipsoid or break up.

The limits for  $\beta$  are different (and may be reduced) for differentially rotating or compressible bodies. For a toroidal density distribution, the limits are much reduced. Simulations of rotating core collapse have been carried out in which the core forms a toroidal density distribution after bounce, is able to deform triaxially and finally fission

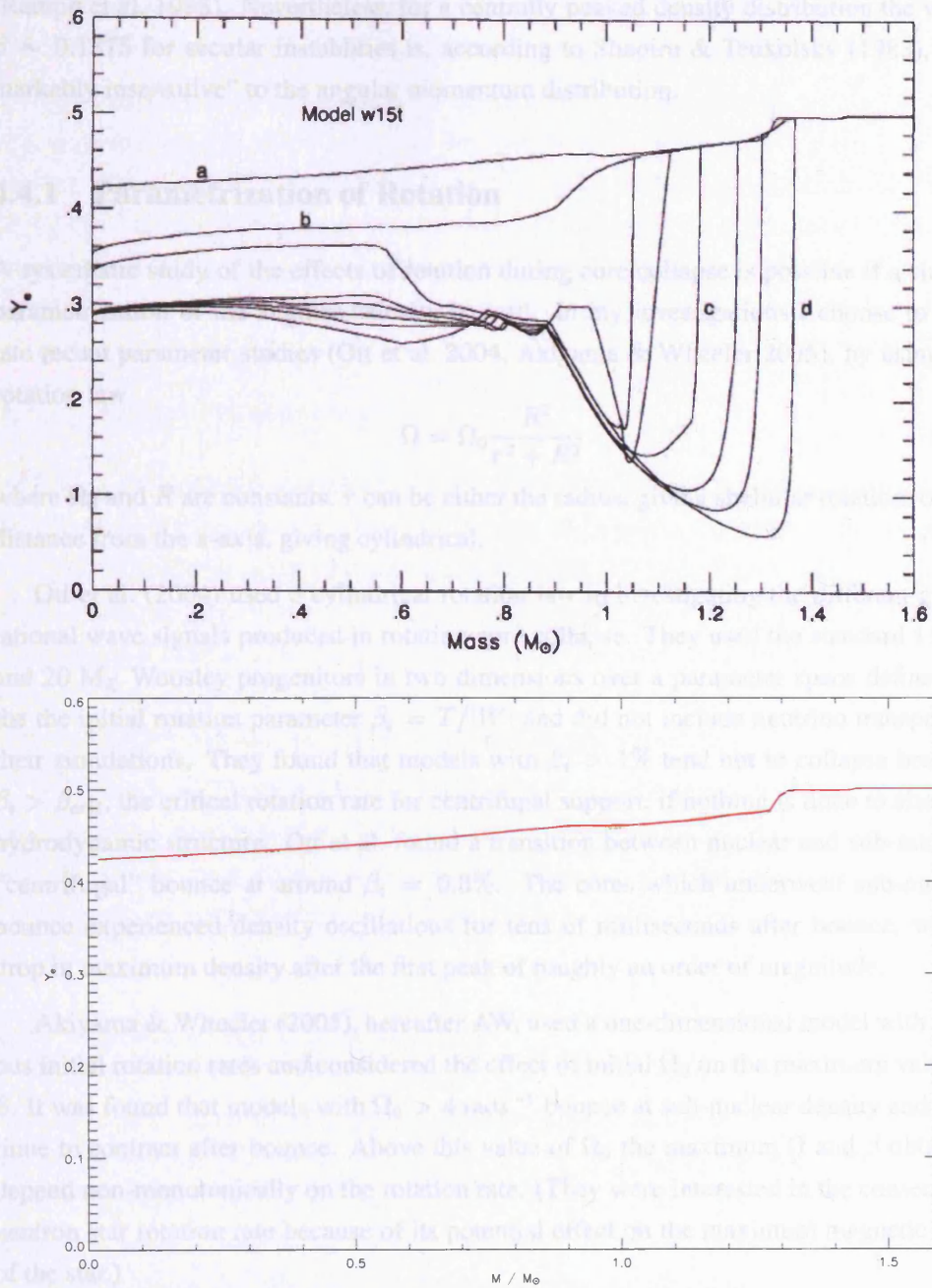


FIGURE 4.6. Top: Electron fraction per baryon versus enclosed mass for model B95. The curves marked “a” through “d” correspond to  $t = 20.0, 207.5, 210.6$  and  $269.1$  ms, with core bounce occurring at around 209 ms. Bottom: Similar plot for model Woos at  $t = 19.21, 98.30, 99.34, 99.67, 99.84, 99.95, 100.3, 100.9, 103.7$  and  $122.0$  ms. Core bounce occurred at 100.0 ms. In model Woos the electron fraction does not evolve, due to the absence of neutrino emission.

(Rampp et al. 1998). Nevertheless, for a centrally peaked density distribution the value  $\beta \sim 0.1375$  for secular instabilities is, according to Shapiro & Teukolsky (1983), “remarkably insensitive” to the angular momentum distribution.

#### 4.4.1 Parametrization of Rotation

A systematic study of the effects of rotation during core collapse is possible if a simple parametrization of the angular velocity is used. In my investigations I choose to imitate recent parameter studies (Ott et al. 2004, Akiyama & Wheeler 2005), by using the rotation law

$$\Omega = \Omega_0 \frac{R^2}{r^2 + R^2} \quad (4.1)$$

where  $\Omega_0$  and  $R$  are constants.  $r$  can be either the radius, giving shellular rotation, or the distance from the  $z$ -axis, giving cylindrical.

Ott et al. (2004) used a cylindrical rotation law in investigating the different gravitational wave signals produced in rotating core collapse. They used the standard 11, 15 and 20  $M_\odot$  Woosley progenitors in two dimensions over a parameter space defined by the the initial rotation parameter  $\beta_i = T/|W|$  and did not include neutrino transport in their simulations. They found that models with  $\beta_i > 1\%$  tend not to collapse because  $\beta_i > \beta_{crit}$ , the critical rotation rate for centrifugal support, if nothing is done to alter the hydrodynamic structure. Ott et al. found a transition between nuclear and sub-nuclear, “centrifugal” bounce at around  $\beta_i = 0.3\%$ . The cores which underwent sub-nuclear bounce experienced density oscillations for tens of milliseconds after bounce, with a drop in maximum density after the first peak of roughly an order of magnitude.

Akiyama & Wheeler (2005), hereafter AW, used a one-dimensional model with various initial rotation rates and considered the effect of initial  $\Omega_0$  on the maximum value of  $\beta$ . It was found that models with  $\Omega_0 > 4 \text{ rads}^{-1}$  bounce at sub-nuclear density and continue to contract after bounce. Above this value of  $\Omega_0$  the maximum  $\Omega$  and  $\beta$  obtained depend non-monotonically on the rotation rate. (They were interested in the consequent neutron star rotation rate because of its potential effect on the maximum magnetic field of the star.)

Kotake, Yamada & Sato (2003b) used both a shellular rotation law and a cylindrical law with a steep dependence on the distance from the equatorial plane in their two-dimensional investigations of rotating core collapse. Their models were run with  $\beta_i$  of 0.25, 0.5 and 1.5%. In their “standard” model, which is roughly equivalent to the Heger models E15B (described in the next chapter) core bounce is at nuclear densities. They

find that all shellular models bounce at nuclear densities and that sub-nuclear density bounce is only ever achieved with cylindrical and highly differential rotation.

There appears to be some confusion about what constitutes a “sub-nuclear” bounce. AW describe a model that bounces at a central density of  $1.0 \times 10^{14} \text{ g cm}^{-3}$  as sub-nuclear, whilst Kotake et al. (2003*b*) classify a model with a bounce density of  $0.53 \times 10^{14} \text{ g cm}^{-3}$  as “Type I”, nuclear density bounce. In all of my models I classify “nuclear” bounce as occurring if the central density at bounce is greater than  $2.0 \times 10^{14} \text{ g cm}^{-3}$ , which is the density at which the sharp increase in the effective  $\Gamma$  of the EOS takes place.

#### 4.4.2 Model Parameters

Following AW, rotation was added to the Woos model with a shellular angular velocity law, as given in Equation 4.1, with  $R = 10^8 \text{ cm}$ . We reproduce a subset of their models, with initial central rotation rates  $\Omega_0$  of 0.6, 0.8, 2.0, 3.0, 4.0, 5.0, 6.0 and 8.0  $\text{rad s}^{-1}$ . These and other properties of the models are shown in Table 4.1. It should be noted that in the original draft of AW, the figures given for  $T/|W|$  were roughly a factor of 2.5 too high due to a bug in their code (Akiyama, private communication). These figures were amended before publication and are now in agreement with those in Table 4.1.

To give a more intuitive idea of the magnitude of the rotation, the rotation period at the edge of the iron core of model w06lr has a rotation period of 28 seconds at the start of collapse. The most rapidly rotating model, w80lr, has a period of just over 2 seconds. For comparison, the dynamical time of the core is  $\sim (R^3/GM)^{1/2} \sim 0.1 \text{ s}$ .

## 4.5 Results and Discussion

Snapshots of all the models at and shortly after bounce and profiles of density, entropy and radial velocity can be found in Figures 4.11-4.21 at the end of this chapter. For all models quantities were binned spherically in enclosed mass. For the models rotating with  $\Omega_0 = 2 \text{ rad s}^{-1}$  and above the displacement of the centre of mass and the dipole and quadrupole moments of the core as a function of time are also shown.

Comparing models W06lr and W08lr in Figures 4.11 and 4.12 with model Woos in Figure 4.10 reveals that imposing a small amount of rotation on the progenitor model has very little effect on the collapse and bounce. The slow rotators remain essentially spherical and the density, entropy and radial velocity profiles show almost identical features. (The slight variation in the position and height of peaks is due to the bounce being

viewed at slightly different times.) The time taken to reach core bounce varies by less than a millisecond between all three models. From the snapshots of entropy it can be seen that a spherical shock forms at the same position in each one.

At moderate rotation rates changes to the dynamics of the bounce become visible. In model W20lr (Figure 4.13) the snapshot of entropy shows the shock beginning more strongly at the poles, but a short time later the radial velocity shows it to have become almost spherical. Model W30lr (Figure 4.14) appears to mark a transition region in which the density distribution becomes more flattened. The entropy snapshot shows an oblate shock that is stronger at the poles, with a low entropy, unshocked torus surrounding the inner core. A millisecond later the shock has become slightly prolate, but the snapshot of radial velocity shows that it is greater away from the poles.

The cylindrical rotators W20cyl and W30cyl (Figures 4.15 and 4.16) are not hugely different from the shellular rotators with the same  $\Omega_0$ . The density distribution appears slightly squarer in the  $x$ - $z$  plane but the shock is still only slightly non-spherical. (The difference in the shape of the entropy and angular velocity profiles probably originates from the use of spherical rather than cylindrical mass bins.)

With  $\Omega_0$  greater than 3 or 4  $\text{rad s}^{-1}$  the core becomes significantly flattened during collapse, with the density distribution in the outer regions becoming toroidal. It should

Table 4.1. Model parameters and results for model Woos with various degrees of rotation added and angular velocity constant on either shells or cylinders. The parameter varied was the initial central rotation rate  $\Omega_0$ , which correlates with the initial rotation parameter  $\beta_i$ . The total angular momentum and the initial specific angular momentum of the iron core are also shown. The last three columns show the resulting time of bounce  $t_b$ , and the rotation parameter and density at bounce.

Model	Rotation type	$\Omega_0$ ( $\text{s}^{-1}$ )	$\beta_i$ (%)	$J_{Fe}$ ( $10^{49}$ erg $\text{s}^{-1}$ )	$j_{Fe,i}$ ( $10^{16}$ $\text{cm}^2 \text{s}^{-1}$ )	$t_b$ (ms)	$\beta_b$ (%)	$\rho_b$ ( $\text{g cm}^{-3}$ )
Woos	—	—	0	0	0	100	0	$3.8 \times 10^{14}$
W06lr	Shellular	0.6	0.012	0.24	0.38	100	0.29	$3.8 \times 10^{14}$
W08lr	Shellular	0.8	0.021	0.31	0.5	100	0.41	$3.9 \times 10^{14}$
W20lr	Shellular	2.0	0.13	0.79	1.3	101	3.4	$3.7 \times 10^{14}$
W30lr	Shellular	3.0	0.29	1.2	1.9	103	6.6	$3.5 \times 10^{14}$
W40lr	Shellular	4.0	0.52	1.6	2.5	105	9.0	$3.1 \times 10^{14}$
W50lr	Shellular	5.0	0.81	2.0	3.2	110	7.5	$3.1 \times 10^{14}$
W60lr	Shellular	6.0	1.2	2.4	3.8	119	7.5	$3.2 \times 10^{14}$
W80lr	Shellular	8.0	2.1	3.1	5.0	153	8.3	$3.0 \times 10^{14}$
W20cyl	Cylindrical	2.0	0.15	0.85	1.3	101	3.5	$3.7 \times 10^{14}$
W30cyl	Cylindrical	3.0	0.34	1.3	1.9	103	6.2	$3.4 \times 10^{14}$
W50visc	Shellular	5.0	0.81	2.0	3.2	110	9.1	$2.6 \times 10^{14}$

be noted, however, that the inner regions of the core remain only slightly oblate even for the most rapidly rotating models. In W40lr and W50lr (Figures 4.15 and 4.16) the shock is only visible above the poles where infall is most rapid. With faster rotation the bounce becomes weaker due to the shallower effective potential well the centrifugal force produces. In these two models the shock begins at the poles but after only a millisecond it has become oblate.

When  $\Omega_0 \gtrsim 6$  (Figures 4.17 and 4.18) the infall of the outer core is held up significantly and the density snapshot shows a disc-like structure around the central core. The shock formed is weak and expands along the evacuated regions above the poles. (For these models the density distribution is far from spherical so binning quantities does not give particularly meaningful results.)

All rotating models show a similar behaviour in  $\Omega$  over time. The angular velocity starts off centrally peaked but the peak moves outwards as low angular momentum material falls in along the poles whilst high angular momentum material is held up further out. The more slowly rotating models retain a flatter profile for longer as the equatorial material is more able to fall in, the transition coming between models W40lr and W50lr. The angular velocity profile of W50lr very quickly becomes peaked at around 20 km.

#### 4.5.1 Effect of Rotation on Bounce Density and Rotation Parameter

Table 4.1 shows that despite significant differences in the dynamics of the collapse all the models here studied bounce at nuclear densities. This is surprising, since all the studies I have referred to have some models which undergo my definition of sub-nuclear bounce (Ott et al. 2004, Akiyama & Wheeler 2005, Kotake et al. 2003b). However, it can also be seen that the maximum density obtained at bounce decreases monotonically with the initial rotation of the progenitor. The reduction in effective gravitational potential provided by rotation means that the time taken to reach bounce increases with the rotation rate. The most rapidly rotating model, W80lr, takes just over one and a half times as long to reach bounce as the non-rotating control.

The cylindrical models W20cyl and W30cyl show very similar behaviour to their shellular counterparts W20lr and W30lr. They have the same maximum densities at bounce and similar initial and final  $\beta$ . Contrary to the claims of Kotake et al. (2003b) it appears likely that the difference in effect of shellular and cylindrical rotation is much less significant than, for example, that of the degree of differential rotation (parametrized by  $R$ ).

After reaching maximum density at bounce all models expand somewhat and begin to oscillate, whilst remaining above nuclear density. The maximum density as a function of time for models Woos, W08lr, W20lr, W30lr and W50lr is plotted in Figure 4.7. As would be expected, the more rapidly rotating models reach bounce at a later time and a lower density. None of the models were followed past the second peak in density and we plot only those whose evolution was followed to the second peak. All the same, it can be seen that the time interval between the first and second density peaks lengthens with increasing rotation. The trough between the peaks also deepens with increasing rotation, with the exception of model W50lr. In this model the structure is significantly affected by rotation, to the extent that material is still infalling along the equator as bounce is occurring at the poles. The time between peaks and the difference between the density maximum and minimum after bounce will be reflected in the gravitational wave signal, which I will discuss further in Chapter 6.

It can be seen in Figure 4.8 that the value of  $\beta$  in the rotating models exhibits similar behaviour to the density, peaking at bounce and at the subsequent compression. The maximum  $\beta$  over all models is 9.0% for model W40lr, which was not followed past bounce. Since the density remains centrally peaked in all these models this is well below the limit for secular instability.

The parameter  $\beta$  is, of course, a function of the enclosed mass as well as time. Figure 4.9 shows the profile of  $\beta$  at bounce for all rotating models, calculated on spherical mass shells. The shape of the curve is similar for all models, with  $\beta$  increasing almost linearly with enclosed mass before reaching a peak and levelling off. The left hand graph shows the more slowly rotating models, including those with cylindrical rotation. The cylindrical rotators show a similar behaviour to those with shellular rotation. The type of rotation does not appear even to correlate with the maximum  $\beta$  at bounce – model W20cyl has a greater maximum  $\beta$  than W20lr, but for the W30 models the shellular rotator has the higher  $\beta$ . All of the more slowly rotating models have their peak  $\beta$  at the edge of the inner core, around  $0.9M_{\odot}$ , and the height of the peak increases with increasing  $\Omega_0$ .

In the more rapidly rotating models the peak in  $\beta$  moves outwards slightly with increasing rotation, as material with high angular momentum falls in more slowly than that with low angular momentum, in effect transporting angular momentum outwards in (spherical) mass. The peak  $\beta$  here is maximum for model W40lr, lower for models W50lr and W60lr, and increases again for model W80lr. Again, this hints at a transition in behaviour around  $\Omega_0 = 4 \text{ rad s}^{-1}$  when rotation begins to affect the collapse dynamics significantly.

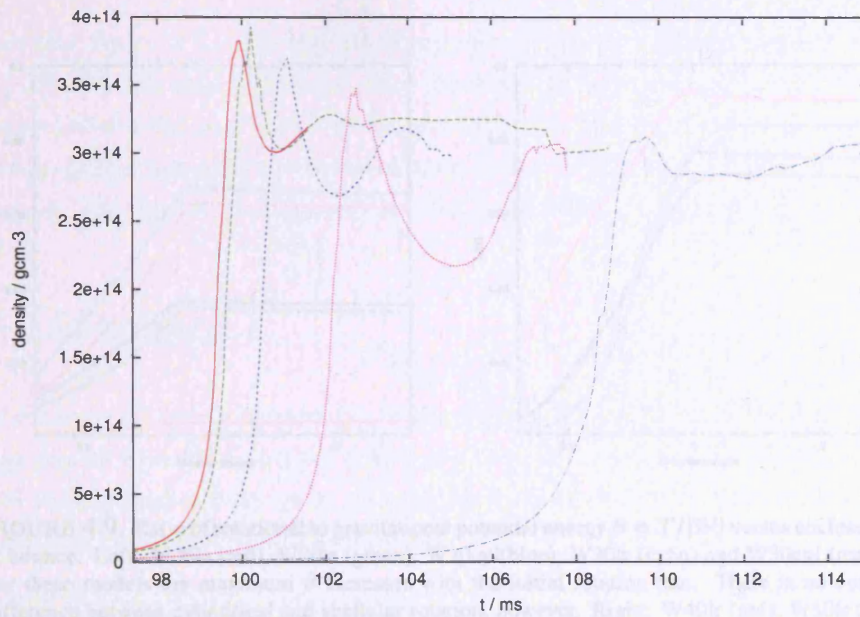


FIGURE 4.7. Maximum density of models Woos (red), W08lr (green), W20lr (blue), W30lr (magenta) and W50lr as a function of time. The more rapid the initial rotation rate, the later the bounce and the longer the time between the first and second density peaks.

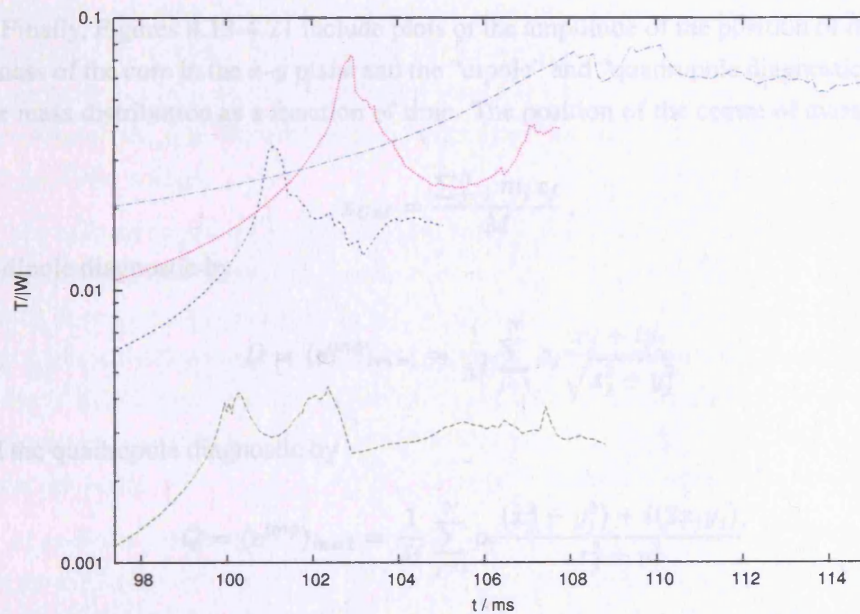


FIGURE 4.8. The ratio of rotational to gravitational potential energy  $\beta = T/|W|$  for models W08lr (green), W20lr (blue), W30lr (magenta) and W50lr as a function of time. Peaks occur at the same time as the peaks in density. For models W08lr, W20lr and W30lr the maximum  $\beta$  increases with increasing initial rotation. For models with rotation faster than that of W40lr,  $\beta$  becomes non-monotonic.

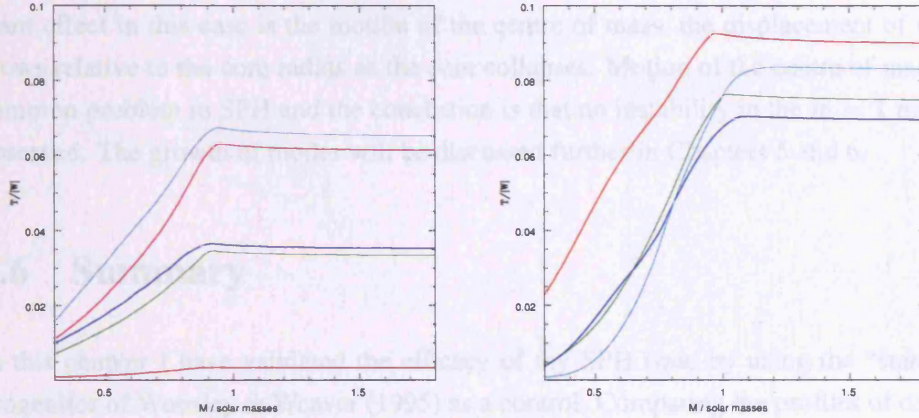


FIGURE 4.9. Ratio of rotational to gravitational potential energy  $\beta = T/|W|$  versus enclosed mass at bounce. Left: W06lr (red), W20lr (green), W20cyl (blue), W30lr (cyan) and W30cyl (magenta). For these models the maximum  $\beta$  increases with the initial rotation rate. There is no consistent difference between cylindrical and shellular rotation, however. Right: W40lr (red), W50lr (green), W60lr (blue) and W80lr (cyan). For these models the dependence of  $\beta$  on initial rotation rate is non-monotonic.

Finally, Figures 4.13-4.21 include plots of the amplitude of the position of the centre of mass of the core in the  $x$ - $y$  plane and the “dipole” and “quadrupole diagnostics” of the core mass distribution as a function of time. The position of the centre of mass is given by

$$x_{CM} = \frac{\sum_{j=1}^N m_j x_j}{M}, \quad (4.2)$$

the dipole diagnostic by

$$D = \langle e^{im\phi} \rangle_{m=1} = \frac{1}{M} \sum_{j=1}^N \rho_j \frac{x_j + iy_j}{\sqrt{x_j^2 + y_j^2}} \quad (4.3)$$

and the quadrupole diagnostic by

$$Q = \langle e^{im\phi} \rangle_{m=2} = \frac{1}{M} \sum_{j=1}^N \rho_j \frac{(x_j^2 - y_j^2) + i(2x_j y_j)}{x_j^2 + y_j^2} \quad (4.4)$$

where  $M = \sum_{j=1}^N m_i$ , following Ott et al. (2005) and Saijo, Baumgarte & Shapiro (2003). These give a measure of the azimuthal  $m = 1$  and  $m = 2$  modes which may grow if the collapsing core becomes rotationally unstable. Inspection of these curves shows clearly that the quadrupole diagnostic does not grow for any of the models (although oscillations due to noise increase in frequency as the dynamical time decreases).

In contrast, the  $m = 1$  mode appears to grow for all rotating models. However, the dominant effect in this case is the motion of the centre of mass, the displacement of which grows relative to the core radius as the core collapses. Motion of the centre of mass is a common problem in SPH and the conclusion is that no instability in the  $m = 1$  mode is observed. The growth of modes will be discussed further in Chapters 5 and 6.

## 4.6 Summary

In this chapter I have validated the efficacy of my SPH code by using the “standard” progenitor of Woosley & Weaver (1995) as a control. Comparing the profiles of density, radial velocity and entropy up to bounce with those simulated by Burrows et al. (1995) shows good agreement between the models.

Various rotation rates were added to this model using a simple parametrization of the angular velocity. Shellular rotation was used for most models, with two test models run with cylindrical rotation. With the rotation rates used, the difference between these and the shellular models was slight. It was found that slow rotation has an insignificant effect on collapse. At higher rotation rates the maximum density at bounce decreases slightly with increasing rotation. This decrease was found to be smaller than in previous studies. For the models which were followed past bounce a second density peak is observed. The time between the first and second peaks increases with increasing rotation, in agreement with previous studies.

The ratio of rotational to gravitational energy  $\beta$  at bounce increases with initial rotation up to moderate rotation rates. Above a rate of around  $\Omega_0 = 4 \text{ rad s}^{-1}$ ,  $\beta$  at bounce becomes non-monotonic in  $\Omega_0$ . This rotation rate seems to mark a transition region where centrifugal effects become important. For the fastest two rotators a disc-like structure is observed surrounding the core at bounce and the peak in  $\beta$  versus enclosed mass moves outwards as equatorial material is prevented from falling in as quickly as that at the poles.

At no point does  $\beta$  approach the limit of  $\sim 0.14$  for secular instability. The maximum beta for all models at bounce is  $< 0.1$ . No sign of fragmentation or significant growth of  $m = 1$  or  $m = 2$  modes is observed.

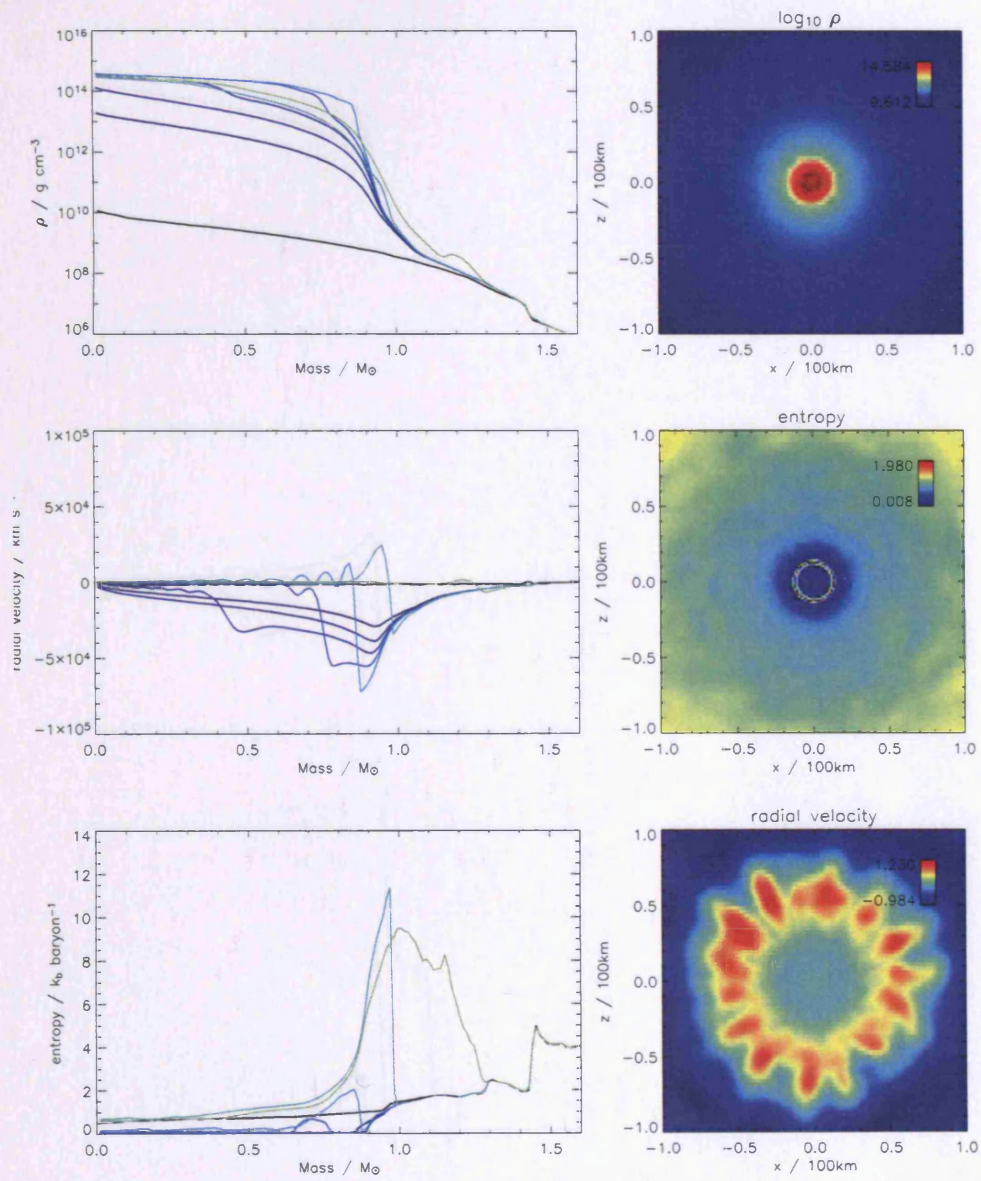


FIGURE 4.10. Density, radial velocity and entropy versus enclosed mass for model Woosley at  $t = 19.2, 98.3, 99.3, 99.7, 99.8, 100.0, 100.9,$  and  $122.0$  ms. Core bounce occurs at  $100.0$  ms. Snapshots show the density and entropy at bounce and the radial velocity at  $100.9$  ms.

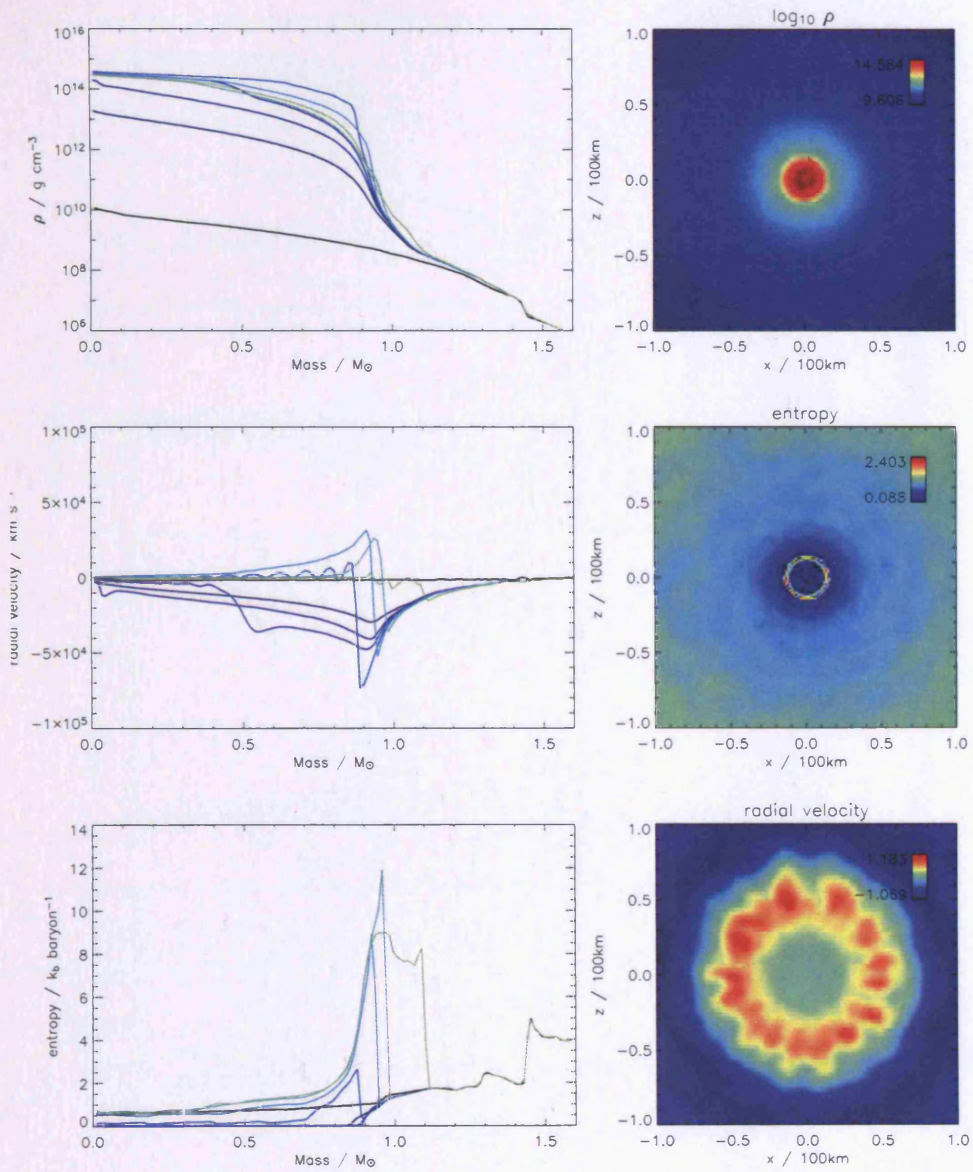


FIGURE 4.11. Density, radial velocity and entropy versus enclosed mass for model Woos\_06 at  $t = 19.2, 98.4, 99.6, 99.8, 100.1, 100.4, 100.9$  and  $105.1$  ms. Core bounce occurs at  $100.1$  ms. Snapshots show the density and entropy at bounce and the radial velocity at  $100.9$  ms.

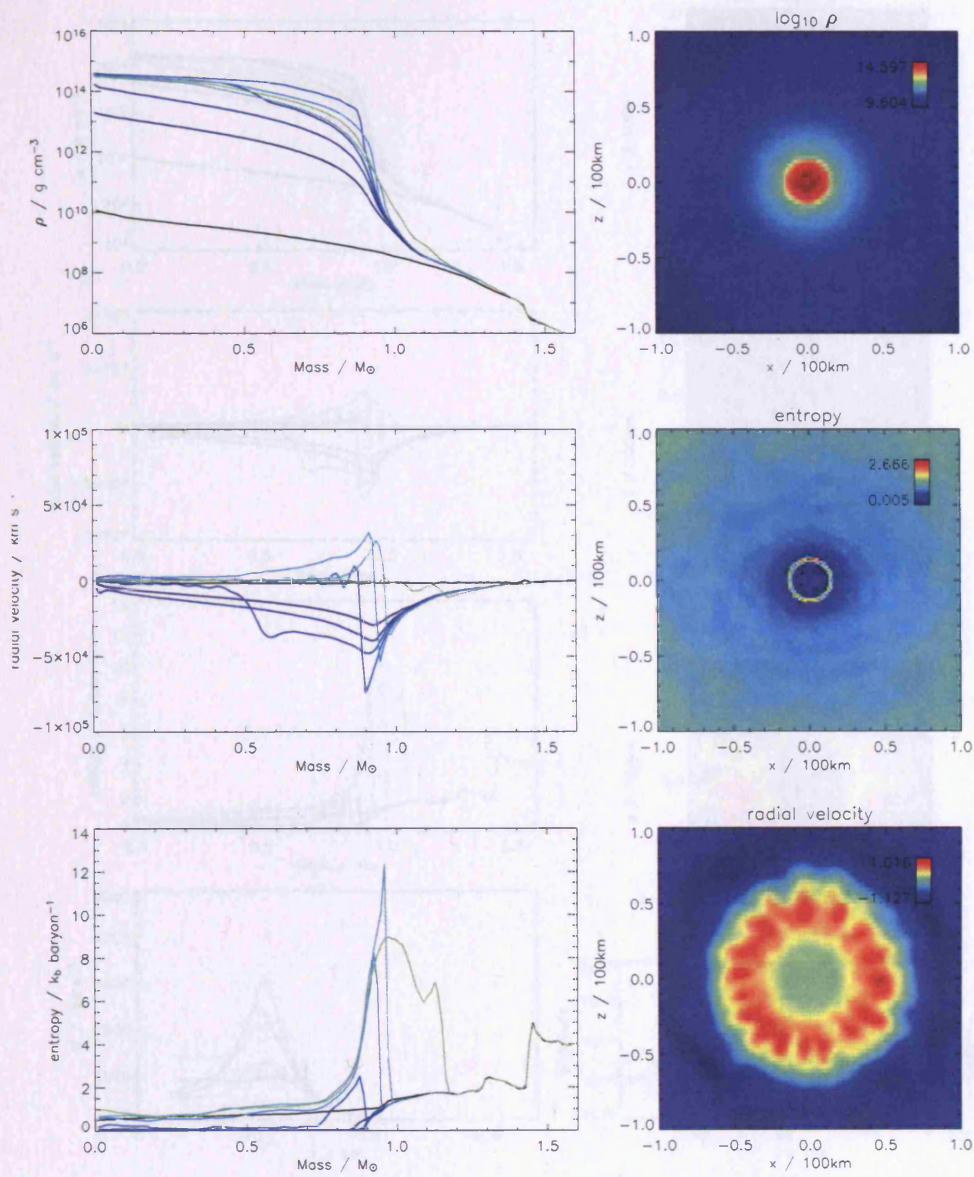


FIGURE 4.12. Density, radial velocity and entropy versus enclosed mass for model Woos\_08 at  $t = 19.2, 98.5, 99.6, 100.0, 100.2, 100.5, 101.0$  and  $108.8$  ms. Core bounce occurs at  $100.2$  ms. Snapshots show the density and entropy at bounce and the radial velocity at  $101.0$  ms.

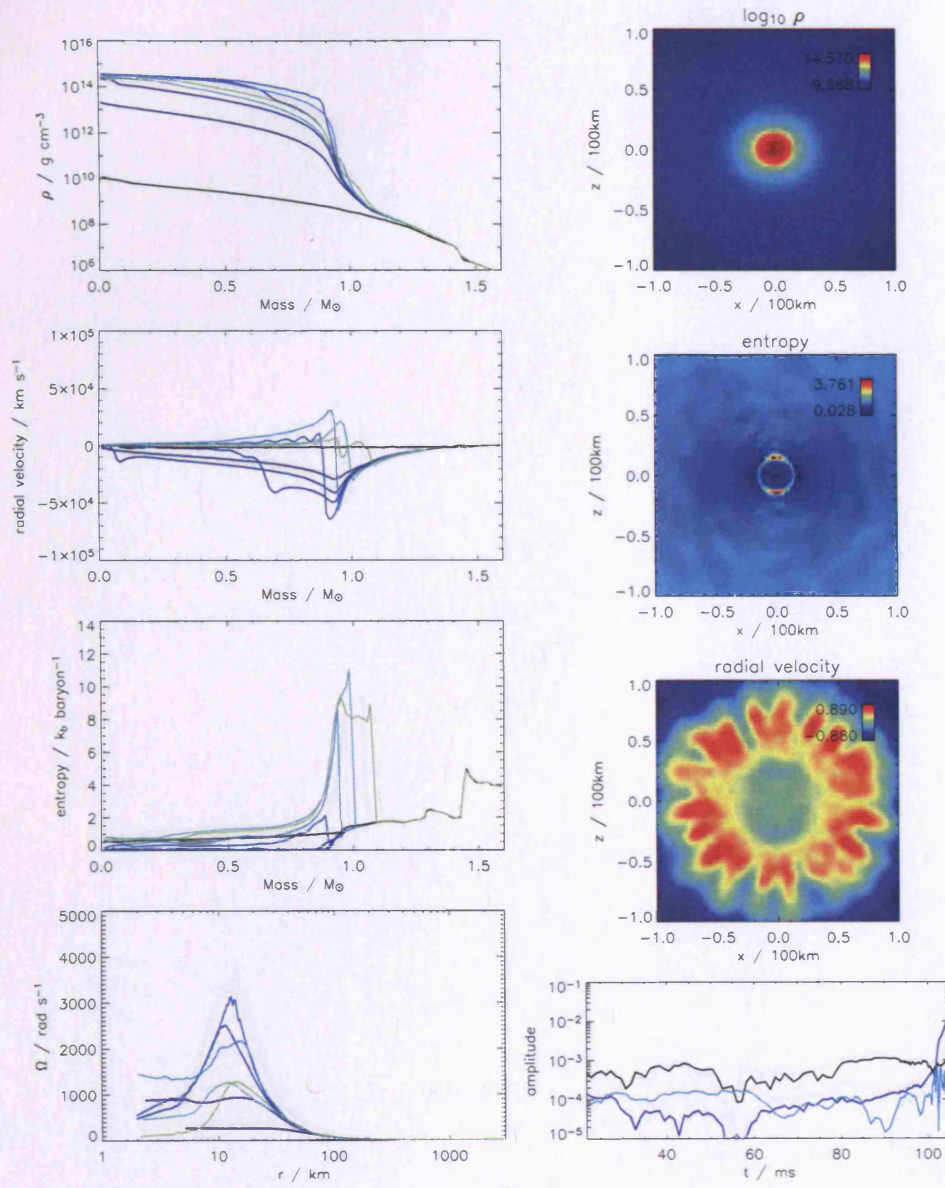


FIGURE 4.13. Density, radial velocity and entropy versus enclosed mass and angular velocity versus radius for model Woos\_20 at  $t = 19.8, 99.3, 100.6, 100.9, 101.1, 101.3, 102.3$  and  $105.1$  ms. Core bounce occurs at  $101.1$  ms. Snapshots show the density and entropy at bounce and the radial velocity at  $102.3$  ms. The graph at the bottom right shows the displacement of the centre of mass (black) and the amplitudes of the dipole (blue) and quadrupole (cyan) moments.

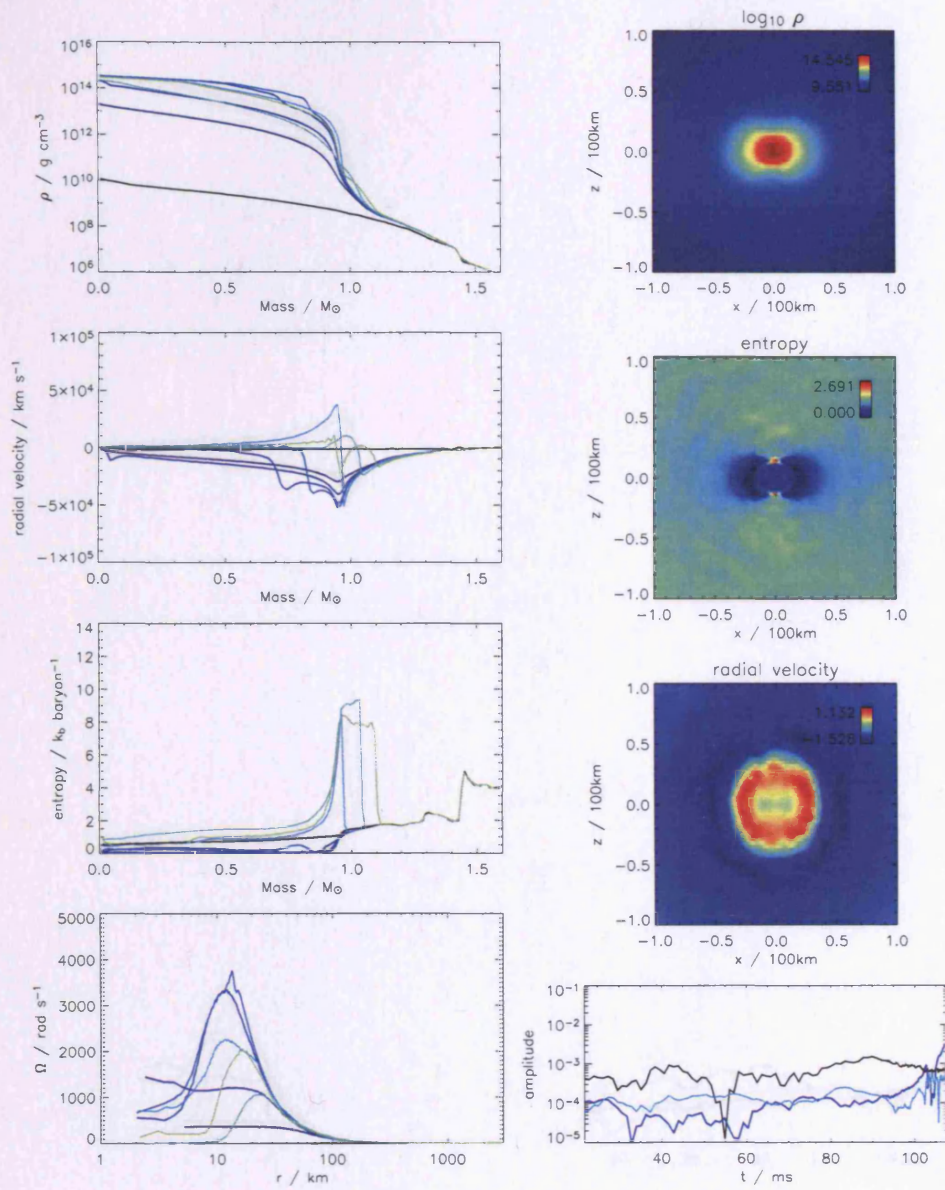


FIGURE 4.14. Density, radial velocity and entropy versus enclosed mass and angular velocity versus radius for model Woos\_30 at  $t = 19.8, 100.9, 102.2, 102.8, 102.9, 103.2, 105.2$  and  $107.8$  ms. Core bounce occurs at  $102.9$  ms. Snapshots show the density and entropy at bounce and the radial velocity at  $103.2$  ms. The graph at the bottom right shows the displacement of the centre of mass (black) and the amplitudes of the dipole (blue) and quadrupole (cyan) moments.

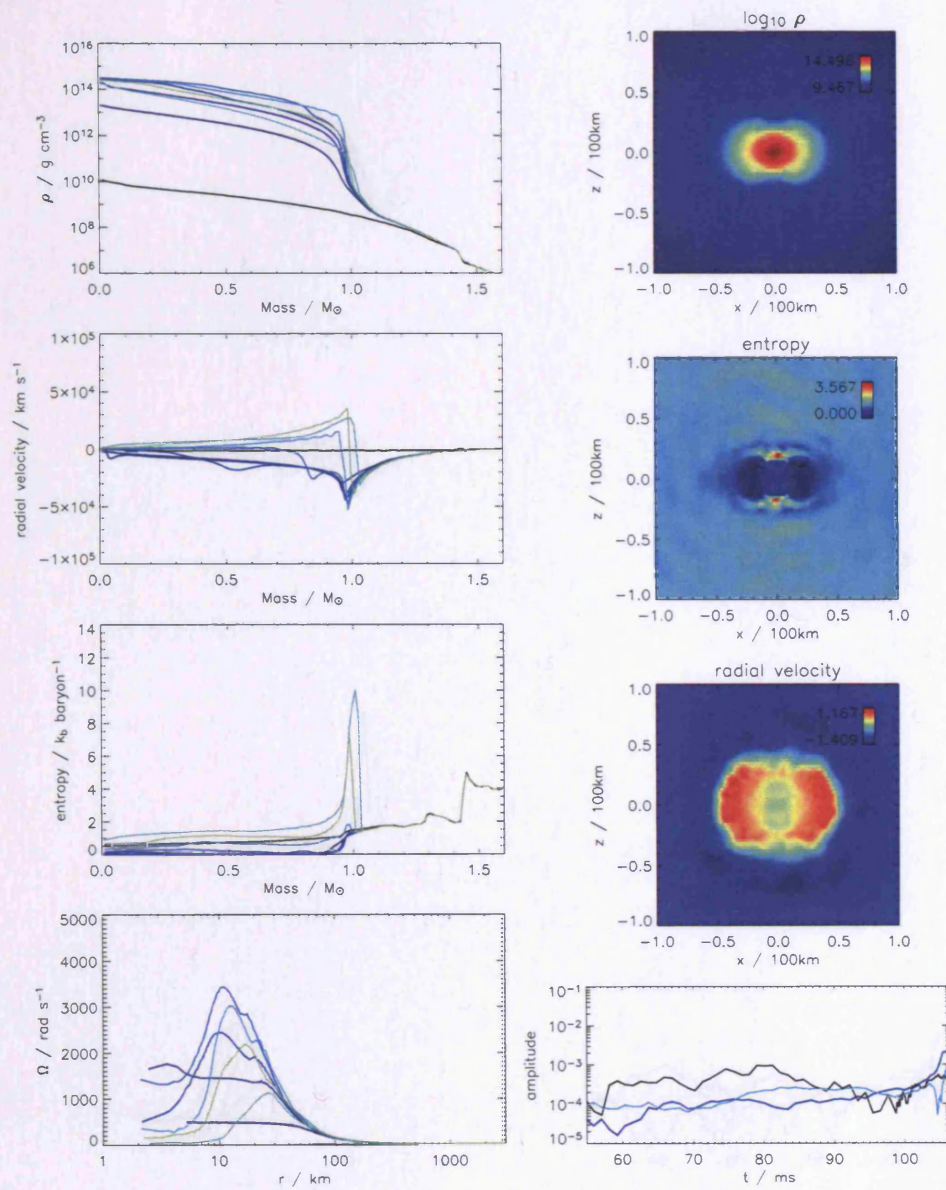


FIGURE 4.15. Density, radial velocity and entropy versus enclosed mass and angular velocity versus radius for model Woosley\_40 at  $t = 19.8, 103.2, 104.7, 105.1, 105.4, 105.7, 106.0$  and  $106.2$  ms. Core bounce occurs at  $105.4$  ms. Snapshots show the density and entropy at bounce and the radial velocity at  $106.2$  ms. The graph at the bottom right shows the displacement of the centre of mass (black) and the amplitudes of the dipole (blue) and quadrupole (cyan) moments.

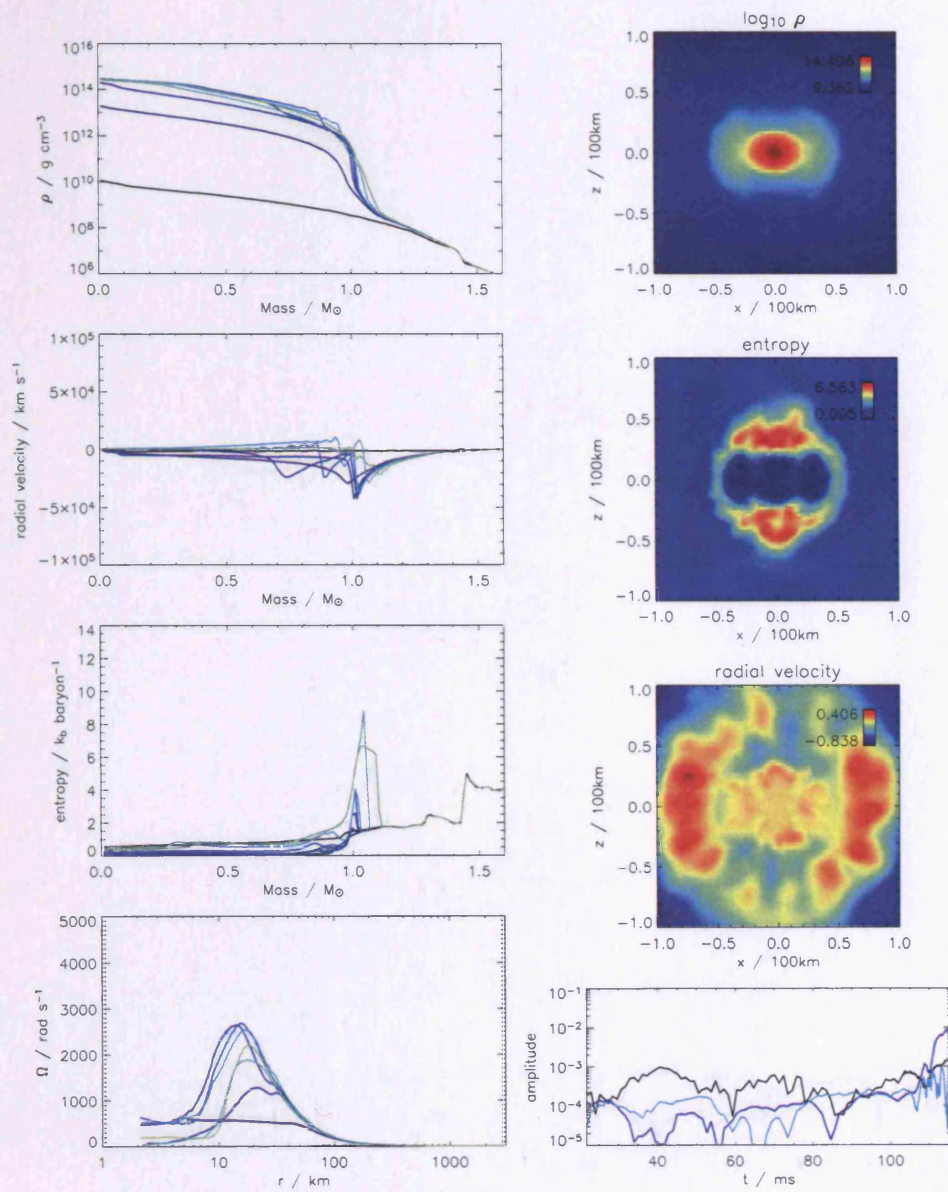


FIGURE 4.16. Density, radial velocity and entropy versus enclosed mass and angular velocity versus radius for model Woos\_50 at  $t = 19.8, 106.4, 108.8, 109.3, 109.7, 110.0, 112.1$  and  $115.5$  ms. Core bounce occurs at  $109.7$  ms. Snapshots show the density and entropy at bounce and the radial velocity at  $112.1$  ms. The graph at the bottom right shows the displacement of the centre of mass (black) and the amplitudes of the dipole (blue) and quadrupole (cyan) moments.

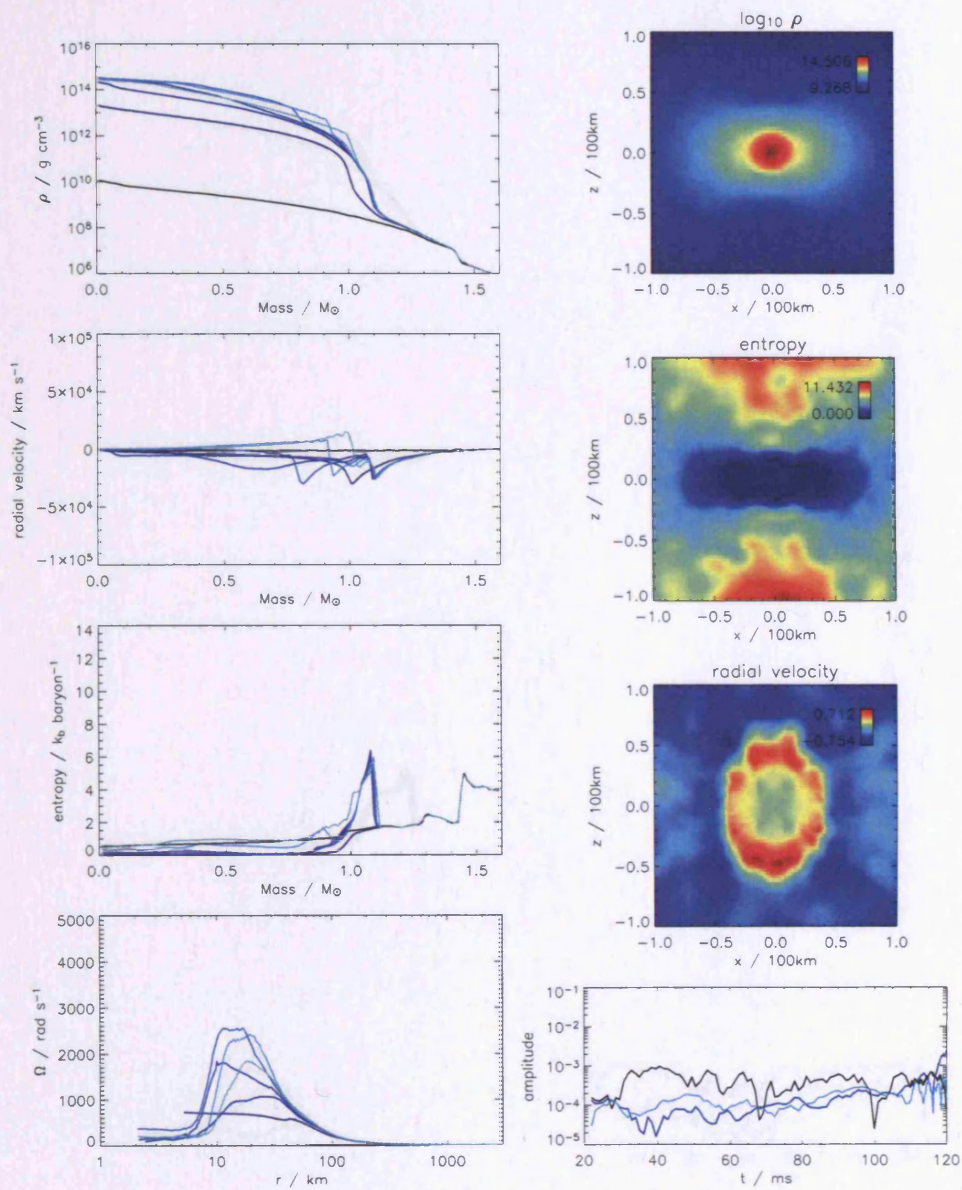


FIGURE 4.17. Density, radial velocity and entropy versus enclosed mass and angular velocity versus radius for model Woos.60 at  $t = 19.8, 111.0, 118.1, 118.6, 118.9, 119.3$  and  $120.8$  ms. Core bounce occurs at  $118.9$  ms. Snapshots show the density and entropy at bounce and the radial velocity at  $120.8$  ms. The graph at the bottom right shows the displacement of the centre of mass (black) and the amplitudes of the dipole (blue) and quadrupole (cyan) moments.

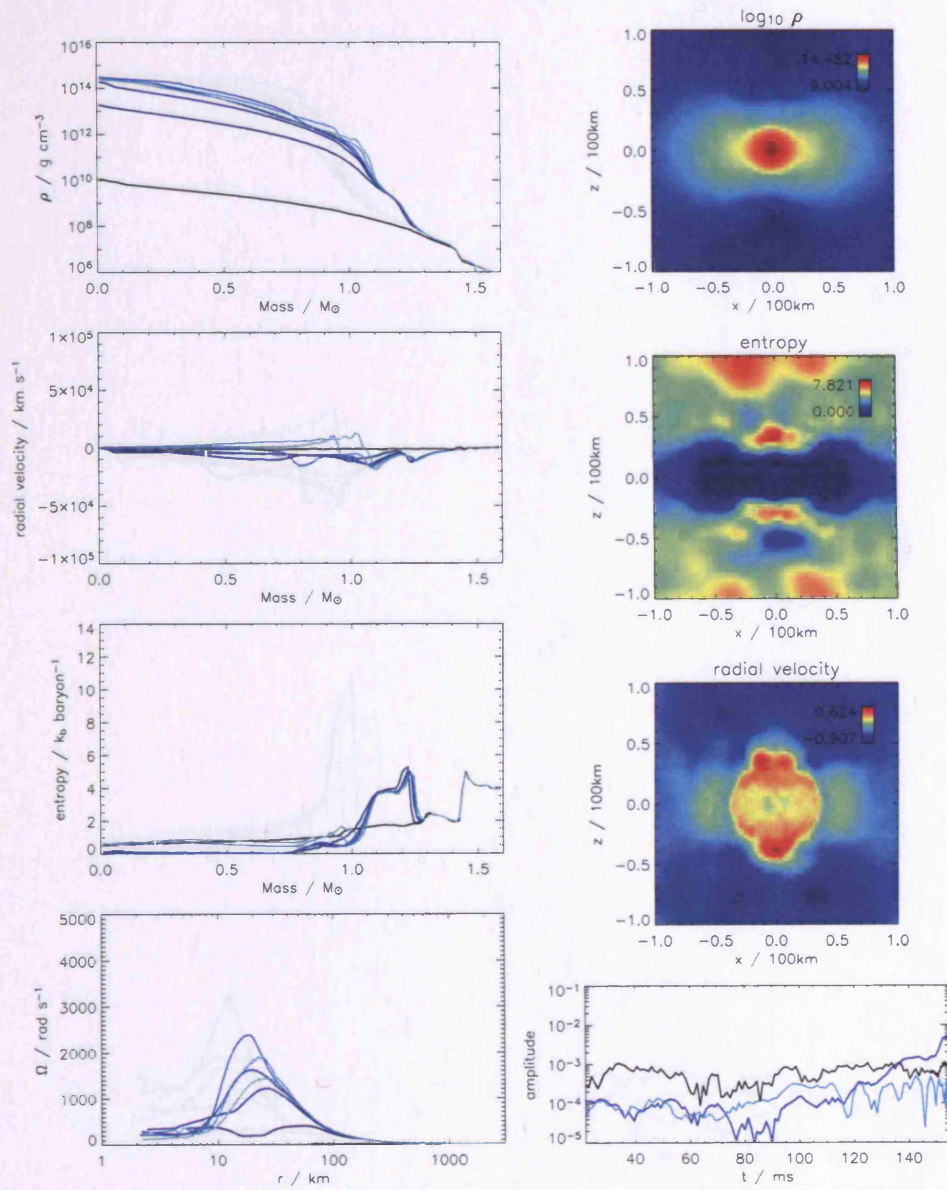


FIGURE 4.18. Density, radial velocity and entropy versus enclosed mass and angular velocity versus radius for model Woos.80 at  $t = 19.8, 149.0, 152.0, 152.6, 153.0, 153.8$  and  $154.6$  ms. Core bounce occurs at  $153.0$  ms. Snapshots show the density and entropy at bounce and the radial velocity at  $153.6$  ms. The graph at the bottom right shows the displacement of the centre of mass (black) and the amplitudes of the dipole (blue) and quadrupole (cyan) moments.

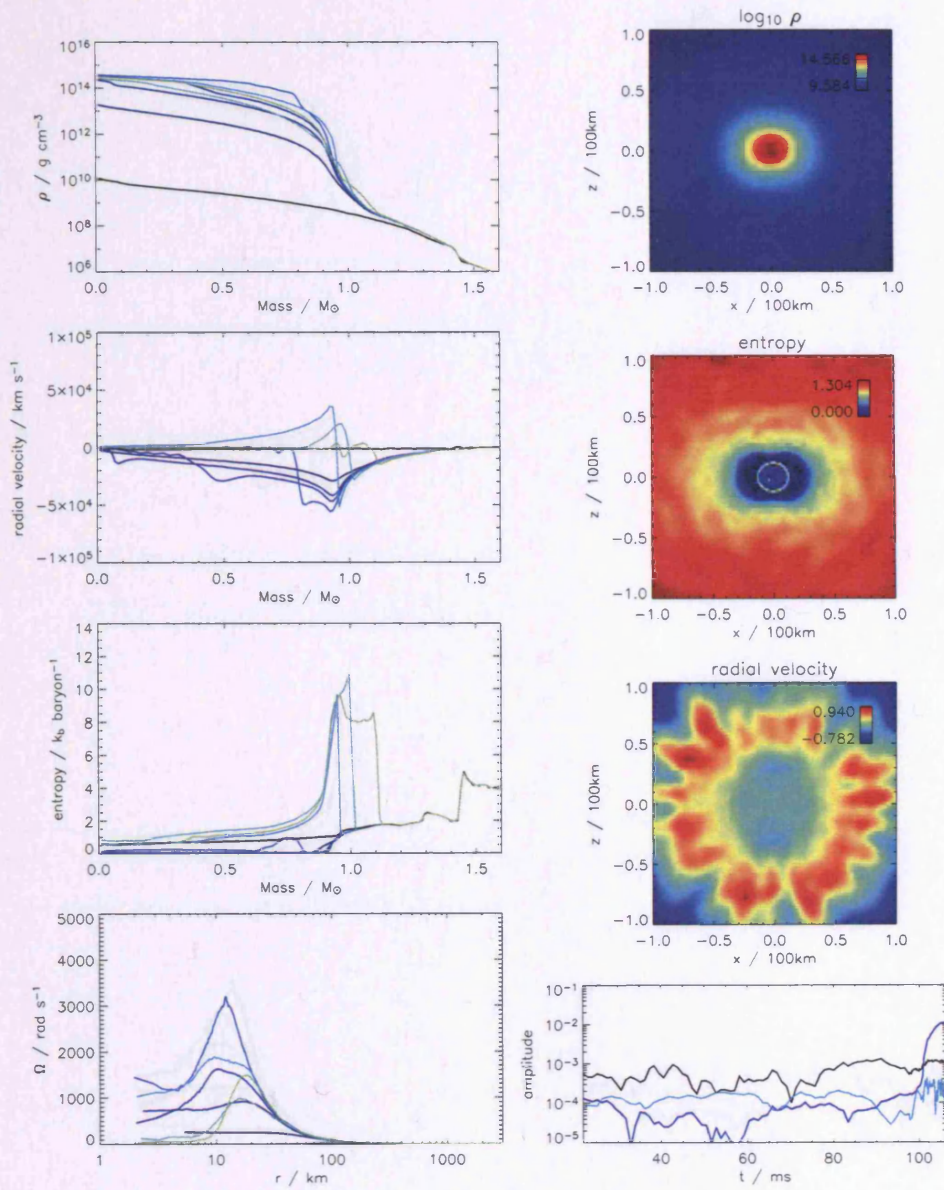


FIGURE 4.19. Density, radial velocity and entropy versus enclosed mass and angular velocity versus radius for model Woos\_cyl20 at  $t = 19.8, 99.3, 100.7, 100.9, 101.1, 101.5, 102.6$  and  $106.4$  ms. Core bounce occurs at 101.1 ms. Snapshots show the density and entropy at bounce and the radial velocity at 102.6 ms. The graph at the bottom right shows the displacement of the centre of mass (black) and the amplitudes of the dipole (blue) and quadrupole (cyan) moments.

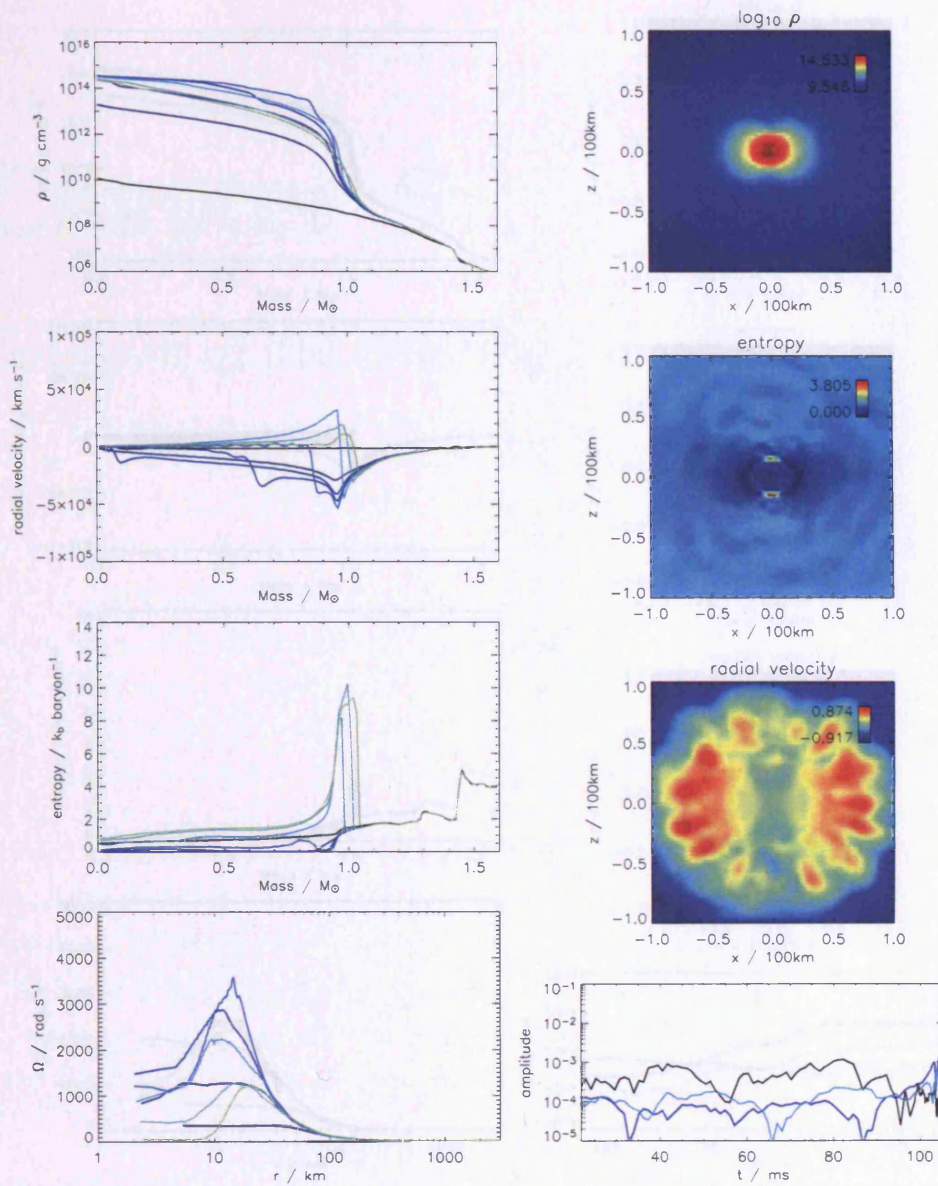


FIGURE 4.20. Density, radial velocity and entropy versus enclosed mass and angular velocity versus radius for model Woos\_cyl30 at  $t = 19.8, 101.3, 102.8, 103.1, 103.3, 103.8, 104.7$  and  $105.6$  ms. Core bounce occurs at  $103.3$  ms. Snapshots show the density and entropy at bounce and the radial velocity at  $104.7$  ms. The graph at the bottom right shows the displacement of the centre of mass (black) and the amplitudes of the dipole (blue) and quadrupole (cyan) moments.

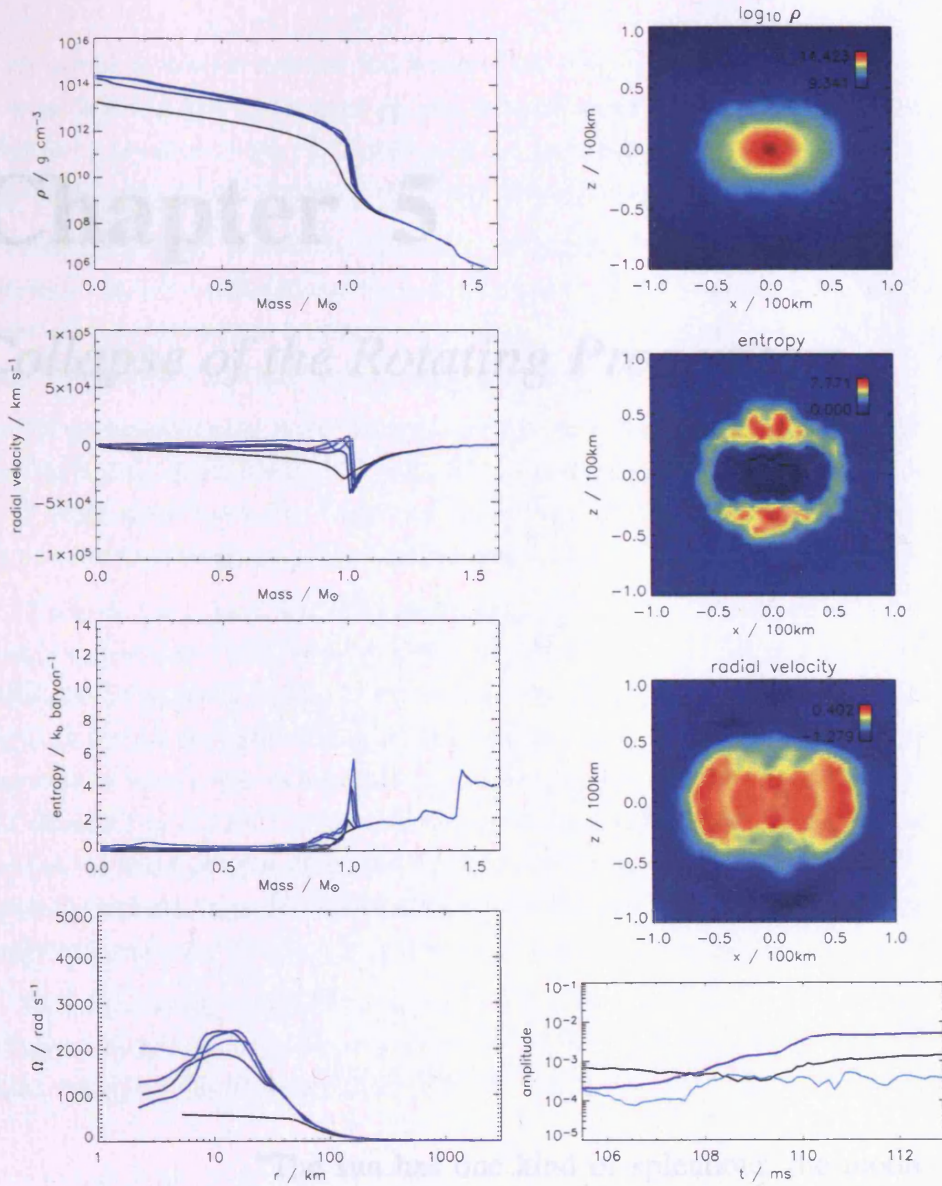


FIGURE 4.21. Density, radial velocity and entropy versus enclosed mass and angular velocity versus radius for model Woos\_visc50, which had shear viscosity added at 105.5 ms, at  $t = 106.4, 109.0, 109.7, 110.0$  and  $110.4$  ms. Core bounce occurs at  $110.0$  ms. Snapshots show the density and entropy at bounce and the radial velocity at  $110.4$  ms. The graph at the bottom right shows the displacement of the centre of mass (black) and the amplitudes of the dipole (blue) and quadrupole (cyan) moments.

# Chapter 5

## *Collapse of the Rotating Progenitors*

“The sun has one kind of splendour, the moon another and the stars another; and star differs from star in splendour.”

*St. Paul*

## 5.1 Introduction

In the previous chapter rotation was imposed on a non-rotating supernova progenitor in order to study how the bounce density, time of bounce and rotation parameter was affected as rotation increased. Rotation in this case was enough to slow the collapse significantly but did not prevent bounce from occurring at nuclear densities.

With more rapid rotation the dynamical evolution of the core will be affected significantly. In this chapter I investigate what happens to the structure of the core when rotation is large enough to dominate the collapse. In particular, rapid rotation may cause instabilities to grow, possibly to the extent of inducing core fragmentation.

The progenitors used in this chapter are those of Heger et al. (2000), who included rotation in their stellar evolution models. They also produced a set of non-rotating models. I begin in Section 5.3 by comparing the collapse of these non-rotating models with the non-rotating Woosley model of the previous chapter.

There are two distinct sets of rotating progenitor models. Those in the first set rotate weakly and produce results similar to those obtained in the moderately rotating Woosley models of the previous chapter. They are discussed in Section 5.4 below. More interesting to us are the strongly rotating models, which have core rotation rates on the lower boundary of what might be expected to produce gamma ray bursts (GRB). These models, discussed in Section 5.5, experience significant rotational effects as they collapse, and bounce at sub-nuclear densities. A third set of models was run with the rotation enhanced artificially in an effort to simulate what would happen in the core of a progenitor produced by a binary merger. These models are covered in Section 5.6.

With fast enough rotation, a centrifugally supported disc is likely to form as the core collapses. By analogy with accretion discs, several models were run with shear viscosity added. These are described in Section 5.7.

## 5.2 Models and Parameters Used

In recent years it has become possible to include the effects of rotation in stellar evolution codes. The simulations described in this chapter were run using the rotating supernova progenitor models of Heger et al. (2000). They used the STERN (Langer et al. 1988) and KEPLER (Weaver, Zimmerman & Woosley 1978, Woosley & Weaver 1988) stellar evolution codes to model stars with masses ranging from  $10 M_{\odot}$  to  $25 M_{\odot}$  from zero-age main sequence (ZAMS) until the onset of core collapse. STERN was used for the

evolution up to central neon ignition and KEPLER to model the remaining stages up to the onset of core collapse, defined as when the infall velocity in the iron core exceeds  $900 \text{ km s}^{-1}$ .

Rotation in these models is defined as the equatorial surface rotation velocity at core hydrogen ignition (ZAMS). Stars in the mass range  $8\text{-}25M_{\odot}$  typically have rotational velocities of  $200 \text{ m s}^{-1}$  (Halbedel 1996, Penny 1996) and so this rotation speed is used in the principal set of models. These models are denoted “E”, with other groups denoted “D” (non rotating), “F” ( $300 \text{ m s}^{-1}$ ) and “G” ( $100 \text{ m s}^{-1}$ ). Parameters for these models can be found in Table 5.1.

Gradients in the mean molecular weight  $\mu$  inhibit rotationally induced instabilities, but just how sensitive mixing is to these gradients is greatly uncertain, therefore Heger et al. use an efficiency parameter  $f_{\mu}$  to adjust the amount of mixing. Through trial and error and comparison to observed stellar surface abundances a “best value” was obtained of  $f_{\mu} = 0.05$ , corresponding to the models suffixed B in Table 5.1. A set of models were also produced in which  $\mu$ -gradients were completely neglected ( $f_{\mu} = 0$ ), resulting in stronger mixing, with another parameter adjusted to produce similar surface abundances to the B models. I refer to these models as the A models. The strong mixing transported angular momentum out of the core to give a final rotation rate that was slower by roughly an order of magnitude. However, in the inner regions, the B models resemble the non rotators more closely in composition than do the A models.

Simulations employing 50,000 SPH particles were run for all of the models in Table 5.1. Higher resolution runs were undertaken for the “D” and “E” models using the UKAFF and HEX supercomputers and the SRIF2 cluster at the University of Leicester. These are what I focus on in my discussion. Owing to a slight defect in the initial conditions, all models run on HEX and UKAFF begin with slightly enhanced density and entropy at the very centre. As will be seen when comparing these models to those run on SRIF2, the effect of this on the overall dynamics of collapse is small.

It should be mentioned that during the evolution of the progenitors, the shells of different compositions each develop their own, roughly constant, angular velocities. These velocities were mapped directly to the SPH particles with no smoothing between shells. I therefore pay careful attention to the shell boundaries in case spurious effects are caused by the sudden discontinuities in rotation speeds.

Initial conditions and results of all the simulations run at high resolution can be found in Table 5.9 at the end of this chapter.

### 5.3 Models Without Rotation

Once again the discussion begins with the non-rotating models, D15 and D20. D15 was run with 250 000 particles on HEX and both models were run with 300 000 particles on the SRIF2 cluster. The results of these runs can be seen in Figures 5.23-5.25. Figures 5.1-5.9 show the density, radial velocity and entropy profiles of these models in more detail. The time of bounce and maximum density obtained for each of these models can be found in Table 5.9.

Comparing the density profiles of both D15 runs (Figures 5.1 and 5.2) with the model Woos shows them to be virtually indistinguishable. The progenitors themselves have very similar profiles, and collapse takes place on the same timescale, roughly 100 ms. At bounce the shock proceeds very quickly to around  $0.9 - 1.0 M_{\odot}$  with the central density settling to  $\sim 3 \times 10^{14} \text{ g cm}^{-3}$ . Model D20 (Figures 5.3) behaves similarly to the other two progenitors, reaching bounce in 105 ms with a strong shock just below  $1 M_{\odot}$ .

The radial velocity curves for these three models (Figures 5.4-5.6) again have a similar shape to model Woos (and consequently B95). As the shock is forming the radial velocity exhibits the same oscillations as in model Woos, caused by the artificial parameter not increasing sufficiently to damp the particles' motion completely.

The entropy profiles for these models (Figures 5.7-5.9) is also very similar to that of Woos, including the region in which the entropy is set to 0.

Table 5.1. Details of the Heger progenitor models. The mass of each star at the beginning and end of its evolution is given along with the mass of the iron core at the onset of collapse.  $v_{ZAMS}$  refers to the equatorial velocity at ZAMS and  $j_{Fe}$  is the specific angular momentum at the edge of the iron core at collapse. This chapter focuses on the D and E models.

Model	$M_{initial}$ ( $M_{\odot}$ )	$M_{final}$ ( $M_{\odot}$ )	$M_{Fe}$ ( $M_{\odot}$ )	$v_{ZAMS}$ ( $\text{km s}^{-1}$ )	Mixing	$j_{Fe}$ ( $\text{cm}^2 \text{s}^{-1}$ )
D15	15	13.55	1.33	0	...	0
D20	20	16.31	1.64	0	...	0
E15	15	10.86	1.46	206	strong	$6.40 \times 10^{15}$
E20	20	11.00	1.73	201	strong	$5.58 \times 10^{15}$
E15B	15	13.26	1.40	206	weak	$1.46 \times 10^{16}$
E20B	20	15.19	1.38	201	weak	$1.26 \times 10^{16}$
F15B	15	12.89	1.38	323	weak	$1.33 \times 10^{16}$
F20B	20	14.76	1.36	307	weak	$1.37 \times 10^{16}$
G15B	15	13.46	1.34	102	weak	$1.23 \times 10^{16}$
G20B	20	16.03	1.38	103	weak	$1.14 \times 10^{16}$

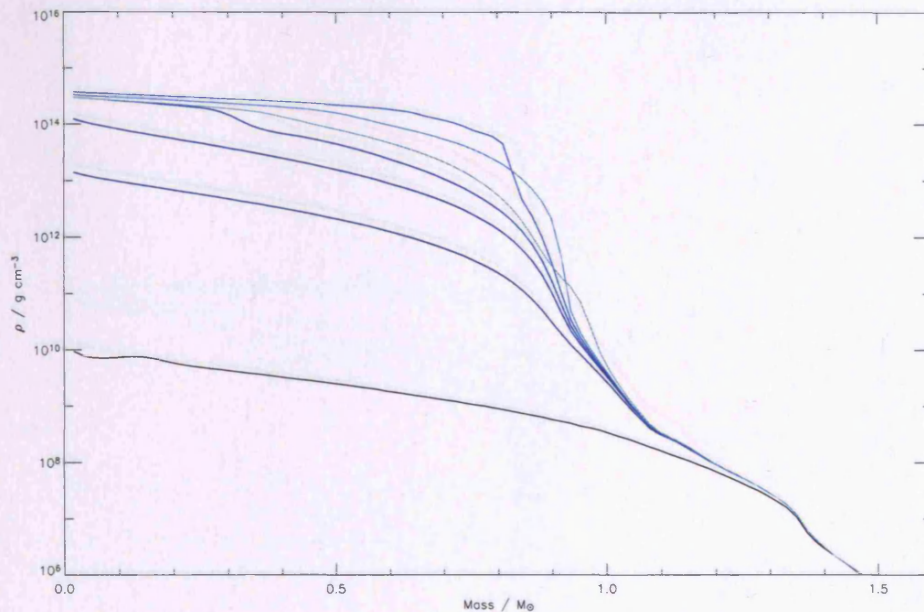


FIGURE 5.1. Density plotted logarithmically versus enclosed mass for Heger model D15 run on HEX. Line colours progress from black to blue then through the rainbow towards red, corresponding to  $t = 13.72, 103.6, 104.8, 105.1, 105.4, 105.7$  and  $106.5$  ms. Core bounce occurred at around  $105.4$  ms.

It is not unexpected that the cores of these three progenitors, one more massive than the others, collapse in a similar fashion. At the onset of collapse the density profile in the inner core is almost identical across all three models. Collapse happens on the dynamical timescale of the inner core – the main difference between the cores of D15 and D20 is the location of the outer core boundary, which is unaffected on this timescale.

Following the use of the standard Woosley progenitor as a control for comparing the results of collapse with a model from the literature, Heger models D15 and D20 provide a further check. This check proved satisfactory, with the collapse of these models almost identical to that of model Woos in the previous chapter. We arrive at the conclusion that the differences between non-rotating progenitor models have only a slight effect on their collapse. Rotation will have a much larger influence on the dynamics of the collapse, and it is to this we look next.

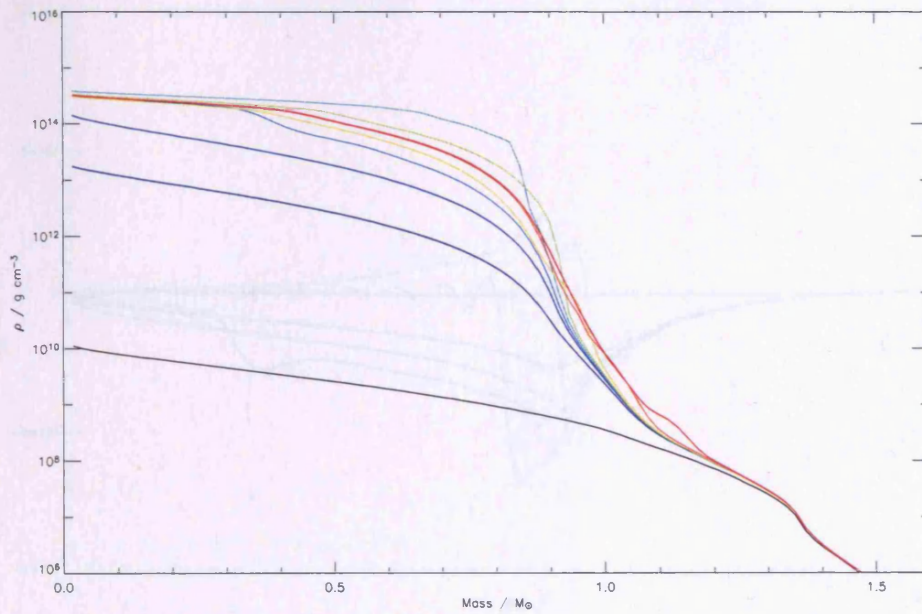


FIGURE 5.2. Density plotted logarithmically versus enclosed mass for Heger model D15 run on SRIF2 at  $t = 19.21, 101.0, 102.1, 102.4, 102.6, 102.9, 103.7, 106.5$  and  $112.1$  ms. Core bounce occurred at around  $102.6$  ms.

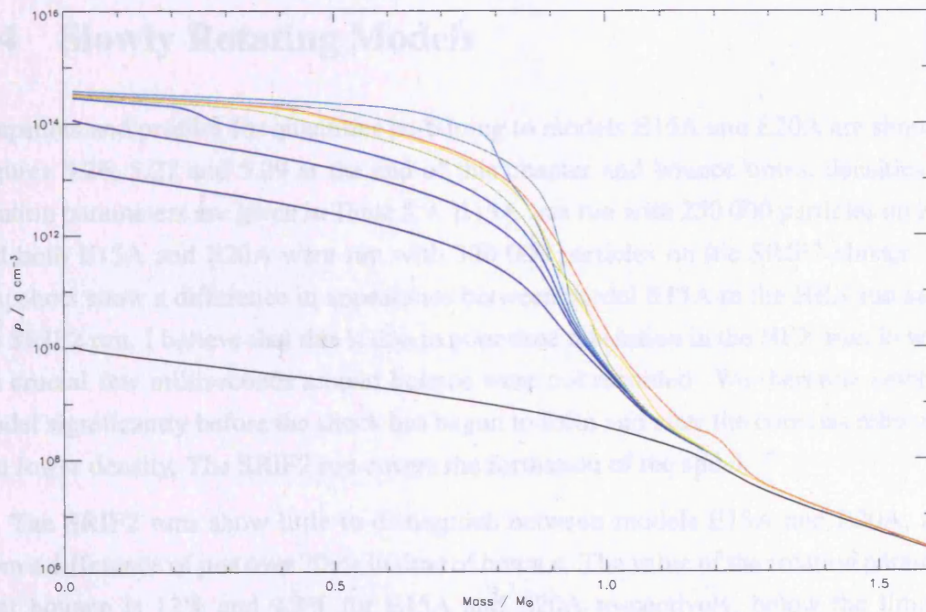


FIGURE 5.3. Density plotted logarithmically versus enclosed mass for Heger model D20 run on SRIF2 cluster at  $t = 19.21, 104.0, 105.1, 105.4, 105.7, 105.9, 106.8, 109.5$  and  $123.5$  ms. Core bounce occurred at around  $105.7$  ms.

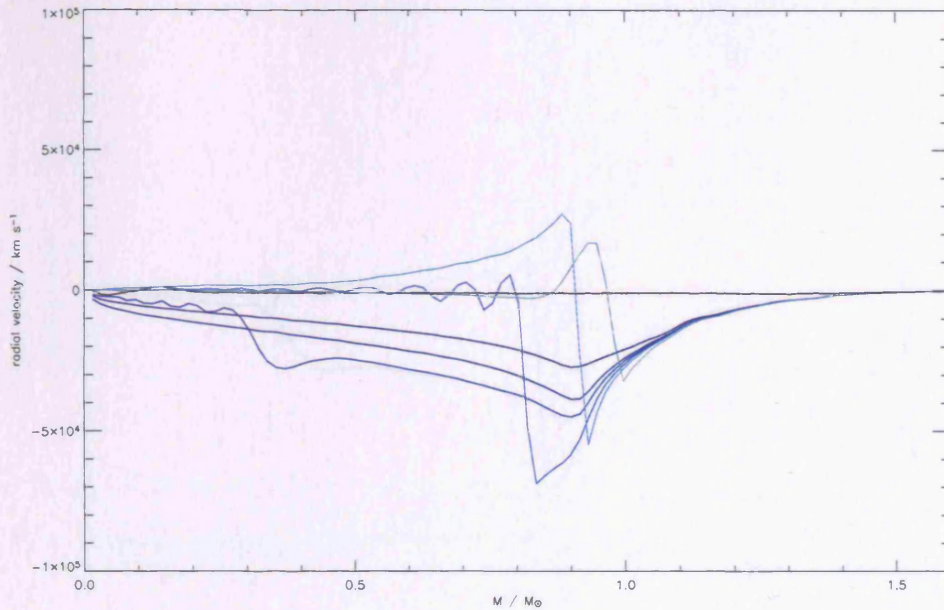


FIGURE 5.4. Radial velocity versus enclosed mass for Heger model D15 run on HEX at  $t = 13.72$ , 103.6, 104.8, 105.1, 105.4, 105.7 and 106.5 ms. Core bounce occurred at around 105.4 ms. As in model Woos, oscillations are visible in the inner core as the shock forms.

## 5.4 Slowly Rotating Models

Snapshots and profiles for quantities pertaining to models E15A and E20A are shown in Figures 5.26, 5.27 and 5.29 at the end of this chapter and bounce times, densities and rotation parameters are given in Table 5.9. E15A was run with 250 000 particles on HEX and both E15A and E20A were run with 300 000 particles on the SRIF2 cluster. The snapshots show a difference in appearance between model E15A in the HEX run and in the SRIF2 run. I believe that this is due to poor time resolution in the HEX run, in which the crucial few milliseconds around bounce were not recorded. We therefore catch the model significantly before the shock has begun to form and after the core has rebounded to a lower density. The SRIF2 run covers the formation of the shock.

The SRIF2 runs show little to distinguish between models E15A and E20A, apart from a difference of just over 20ms in time of bounce. The value of the rotation parameter  $\beta$  at bounce is 12% and 9.8% for E15A and E20A respectively, below the limit for secular instability. Figures 5.10 and 5.11 shows the angular velocity as a function of enclosed mass when the particles are binned on spheroidal shells following the mass distribution. This gives a more accurate representation of what is actually happening

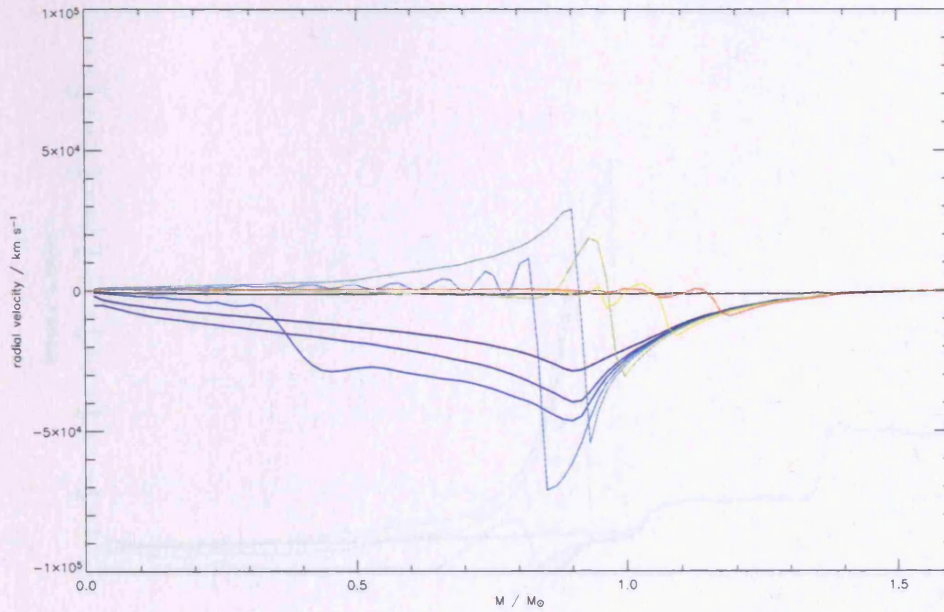


FIGURE 5.5. Radial velocity versus enclosed mass for Heger model D15 run on SRIF2 at  $t = 19.21, 101.0, 102.1, 102.4, 102.6, 102.9, 103.7, 106.5, 112.1$  ms. Core bounce occurred at around 102.6 ms.

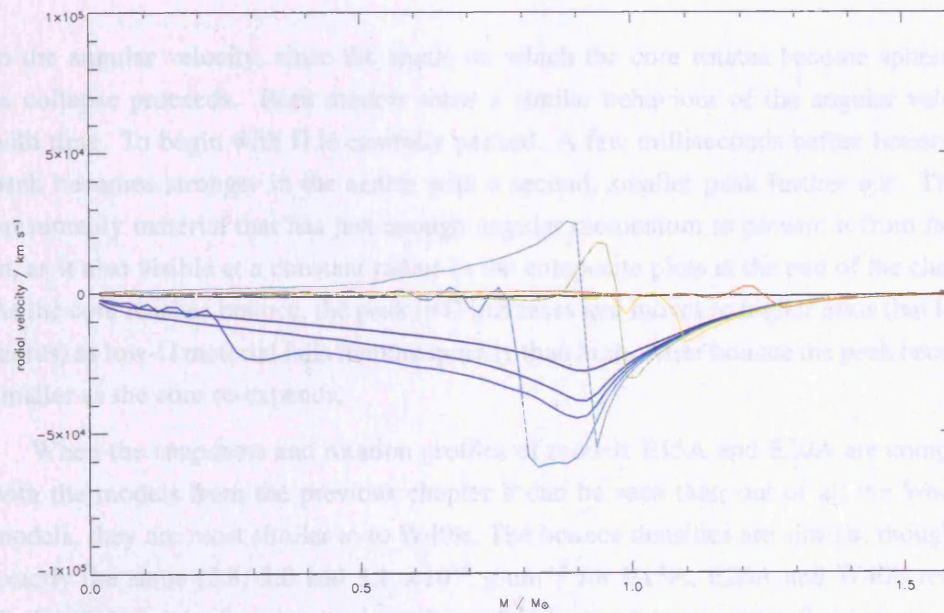


FIGURE 5.6. Radial velocity versus enclosed mass for Heger model D20 run on SRIF2 at  $t = 19.21, 104.0, 105.1, 105.4, 105.7, 105.9, 106.8, 109.5, 123.5$  ms. Core bounce occurred at around 105.7 ms.

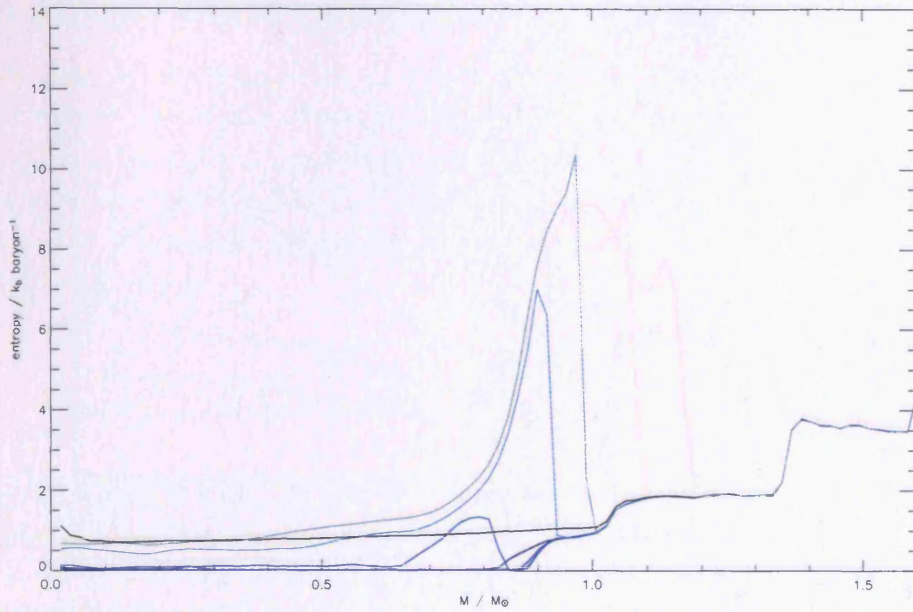


FIGURE 5.7. Entropy per baryon in units of Boltzmann's constant versus enclosed mass for Heger model D15 run on HEX at  $t = 13.72, 103.6, 104.8, 105.1, 105.4, 105.7$  and  $106.5$  ms. Core bounce occurred at around  $105.4$  ms.

to the angular velocity, since the shells on which the core rotates become spheroidal as collapse proceeds. Both models show a similar behaviour of the angular velocity with time. To begin with  $\Omega$  is centrally peaked. A few milliseconds before bounce the peak becomes stronger in the centre with a second, smaller peak further out. This is presumably material that has just enough angular momentum to prevent it from falling in, as it also visible at a constant radius in the composite plots at the end of the chapter. As the core reaches bounce, the peak in  $\Omega$  increases and moves to higher mass (but lower radius) as low- $\Omega$  material falls in more quickly than high. After bounce the peak becomes smaller as the core re-expands.

When the snapshots and rotation profiles of models E15A and E20A are compared with the models from the previous chapter it can be seen that, out of all the Woosley models, they are most similar to W40lr. The bounce densities are similar, though not exactly the same ( $2.8, 3.0$  and  $3.1 \times 10^{14} \text{ g cm}^{-3}$  for E15A, E20A and W40lr respectively). It is interesting to note that this model obtains the maximum  $\beta$  at bounce of all the Woosley models. Its rate of rotation seems to be optimum for achieving rapid rotation at bounce – centrifugal support is not quite enough to delay the infall of equatorial material, consequently rotation is amplified by the maximum possible amount. It is a

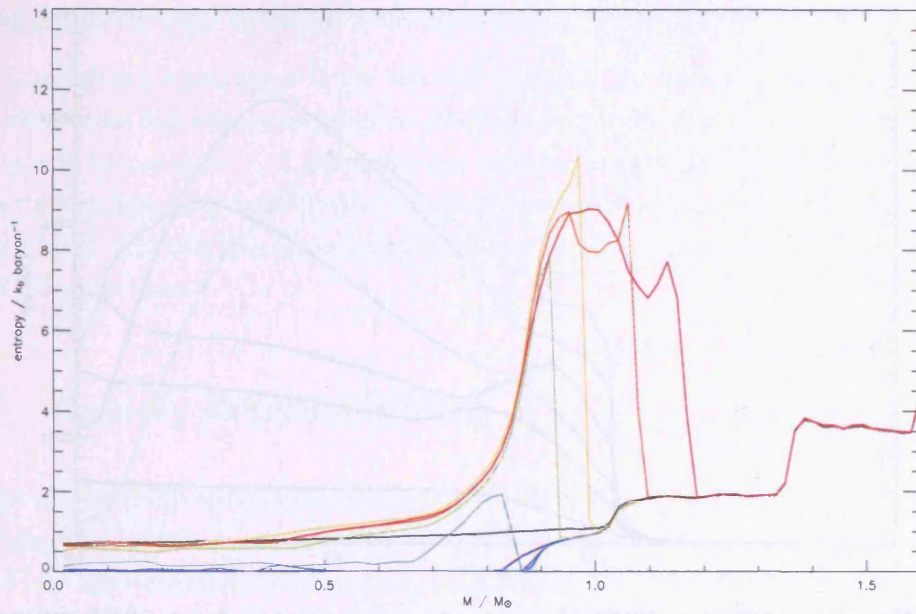


FIGURE 5.8. Entropy per baryon in units of Boltzmann's constant versus enclosed mass for Heger model D15 run on SRIF2 at  $t = 19.21, 101.0, 102.1, 102.4, 102.6, 102.9, 103.7, 106.5$  and  $112.1$  ms. Core bounce occurred at around  $102.6$  ms.

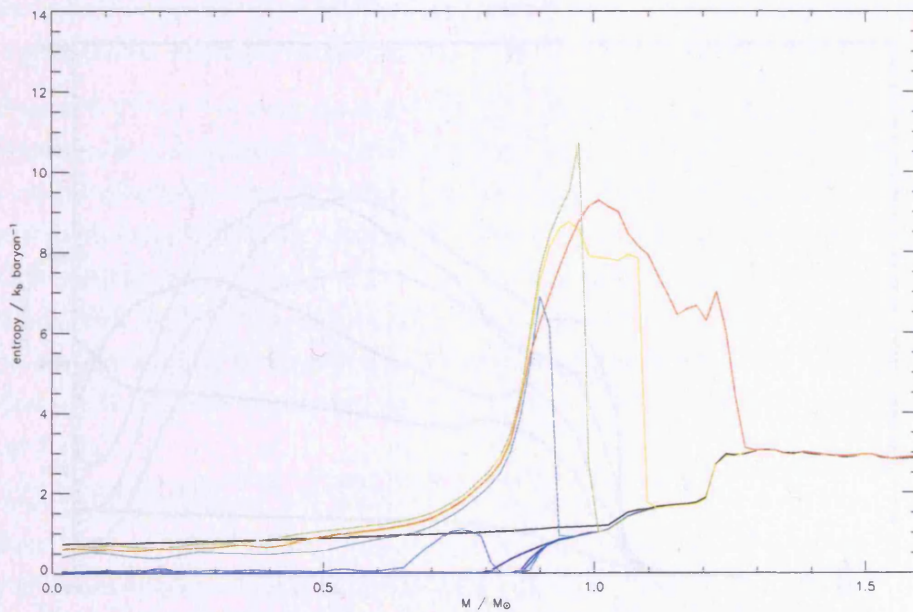


FIGURE 5.9. Entropy per baryon in units of Boltzmann's constant versus enclosed mass for Heger model D20 run on SRIF2 cluster at  $t = 19.21, 104.0, 105.1, 105.4, 105.7, 105.9, 106.8, 109.5$  and  $123.5$  ms. Core bounce occurred at around  $105.7$  ms.

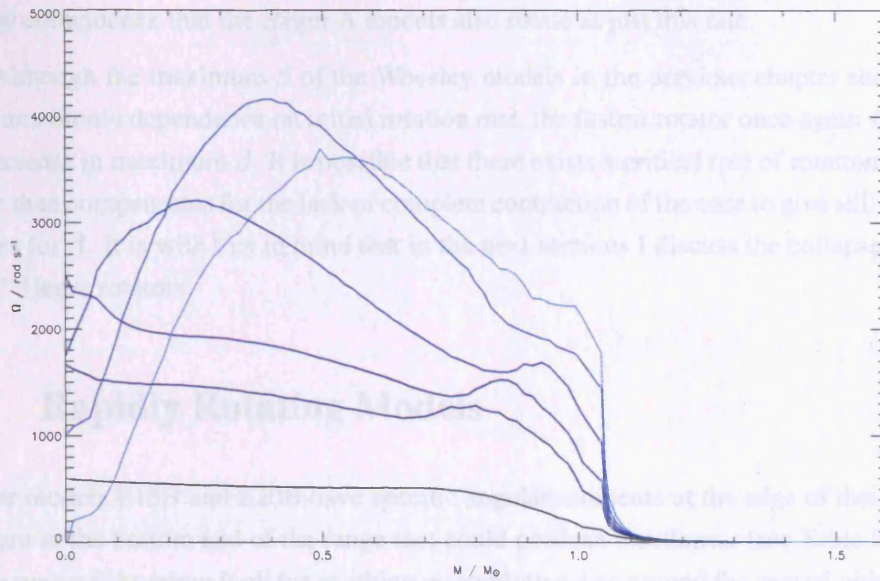


FIGURE 5.10. Angular velocity versus enclosed mass for SRIF2 model E15A at  $t = 137.2, 138.6, 138.9, 139.1, 139.4$  and  $139.7$  ms, binned on spheroidal shells following the mass distribution. Bounce occurs at around  $139.4$  ms. Line colours progress from black through blue to cyan. The angular velocity is initially centrally peaked, but this peak grows and moves outwards as the model approaches bounce.

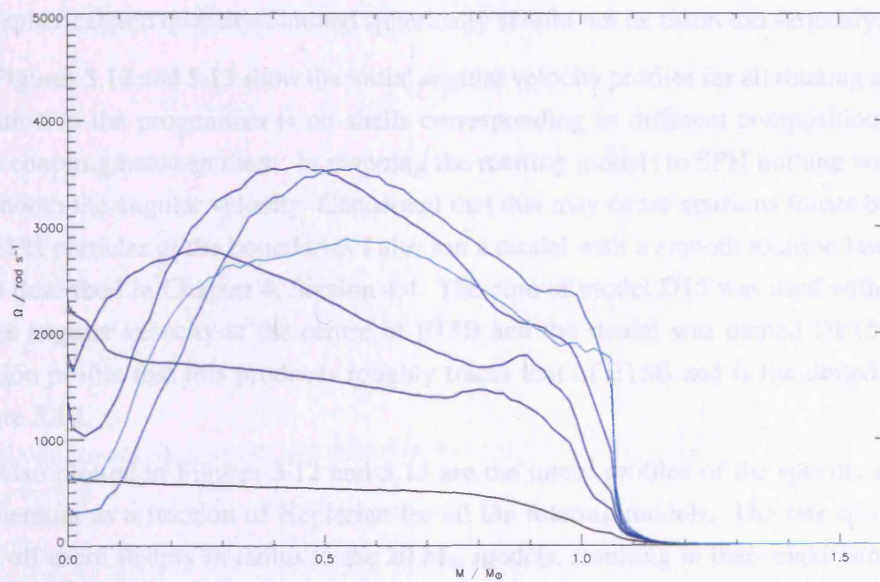


FIGURE 5.11. Angular velocity versus enclosed mass for model E20A at  $t = 159.4, 160.8, 161.1, 161.4, 161.6$  and  $161.9$  ms, binned on spheroidal shells following the mass distribution. Bounce occurs at around  $139.4$  ms.

happy coincidence that the Heger A models also rotate at just this rate.

Although the maximum  $\beta$  of the Woosley models in the previous chapter showed a non-monotonic dependence on initial rotation rate, the fastest rotator once again showed an increase in maximum  $\beta$ . It is possible that there exists a critical rate of rotation which more than compensates for the lack of complete contraction of the core to give still higher values for  $\beta$ . It is with this in mind that in the next sections I discuss the collapse of the “fast” Heger rotators.

## 5.5 Rapidly Rotating Models

Heger models E15B and E20B have specific angular momenta at the edge of their cores that are at the bottom end of the range that could produce a collapsar (see Table 5.1). In these runs we therefore look for anything resembling a disc around the central object and pay particular attention to the possibility of core fragmentation. Model E15B was run with 250 000 particles on HEX, but did not reach nuclear density in the time the simulation was run for. Models E15B and E20B were both run with 300 000 particles on SRIF2. Figures 5.30, 5.32 and 5.35 show snapshots and profiles of these models at interesting points in their evolution. (It should be noted that all these models become significantly non-spherical and quantities binned spherically should not be taken too seriously.)

Figures 5.12 and 5.13 show the initial angular velocity profiles for all rotating models. Rotation in the progenitors is on shells corresponding to different compositions, with little coupling between them. In mapping the rotating models to SPH nothing was done to smooth the angular velocity. Concerned that this may cause spurious forces between the SPH particles at the boundaries I also ran a model with a smooth rotation law of the form described in Chapter 4, Section 4.4. The core of model D15 was used with  $\Omega_0$  set to the angular velocity at the centre of E15B and the model was named DE15B. The rotation profile that this produces roughly traces that of E15B and is the dotted line in Figure 5.12.

Also plotted in Figures 5.12 and 5.13 are the initial profiles of the specific angular momentum as a fraction of Keplerian for all the rotating models. The rate of rotation falls off more steeply in radius in the 20  $M_\odot$  models, resulting in their maximum angular momentum as a fraction of Keplerian being smaller, but for the B models it is still appreciable. For a rigidly rotating, spherical core, this fraction is proportional to  $r^{-\frac{1}{2}}$ , therefore if the core radius shrinks by a factor of 10, the Keplerian limit will be reached. During collapse (in the non-rotating case) the core actually shrinks by a factor of  $\sim 100$ .

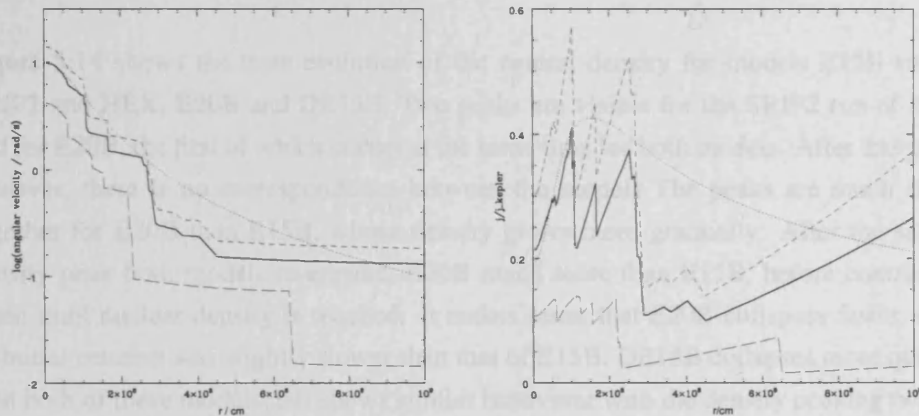


FIGURE 5.12. Initial rotation profiles and specific angular momentum as a fraction of Keplerian for models E15 (long dash), E15B (solid), E15C (short dash) and model D15 with added rotation (dotted).

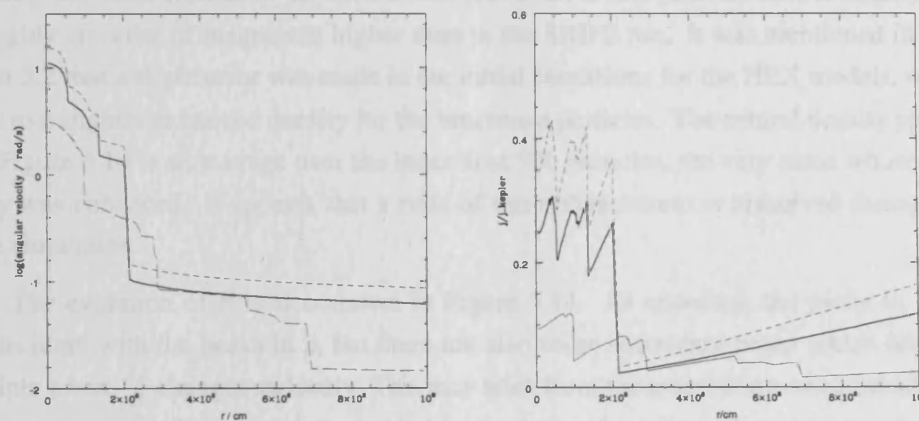


FIGURE 5.13. Initial rotation profiles and specific angular momentum as a fraction of Keplerian for models E20 (long dash), E20B (solid) and E20C (short dash).

In the absence of dissipation it is therefore certain that the core will become centrifugally supported at some point.

Also of note is that for all of the B models  $\beta_i$  exceeds that of the fastest rotating of the Woosley models. W081r shows structure in the outer core and a significantly delayed bounce. Even more extreme behaviour should be expected of these models.

### 5.5.1 Results

Figure 5.14 shows the time evolution of the central density for models E15B run on SRIF2 and HEX, E20B and DE15B. Two peaks are visible for the SRIF2 run of E15B and for E20B, the first of which occurs at the same time for both models. After this point, however, there is no correspondence between the models. The peaks are much closer together for E20B than E15B, whose density grows more gradually. After the second density peak both models re-expand, E20B much more than E15B, before contracting again until nuclear density is reached. It makes sense that E20B collapses faster, since its initial rotation was slightly slower than that of E15B. DE15B collapses more quickly than both of these models, but shows similar behaviour with the density peaking twice – the second time at just below nuclear densities. Information about the first two bounces and the final central density for these models are shown in Table 5.9.

The HEX model E15B was only run past the first peak, which occurred at approximately the same time as in the SRIF2 run. However, at this peak its central density was roughly an order of magnitude higher than in the SRIF2 run. It was mentioned in Section 5.2 that a slight error was made in the initial conditions for the HEX models, which led to a slightly enhanced density for the innermost particles. The central density plotted in Figure 5.14 is an average over the innermost 500 particles, the very same whose density was enhanced. It appears that a relic of this enhancement is preserved throughout the simulation.

The evolution of  $\beta$  is also shown in Figure 5.14. As expected, the peaks in  $\beta$  are coincident with the peaks in  $\rho$ , but there are also some secondary peaks which occur at points where  $\frac{d\rho}{dt}$  changes suddenly. This may arise from the assumption when calculating  $\beta$  that the mass of the core is contained in a sphere. At points when the core changes shape suddenly material that is rotating much more quickly or slowly may suddenly fall within this shell. It should be noted that the first peak for model E15B is the same height for both the SRIF2 and HEX runs. The effect of the erroneous density enhancement on the rotational dynamics is small.

Another clue to what is happening in these models is obtained by looking at their structure along the polar and equatorial axes. Figure 5.15 shows the density distribution at times of maximum and minimum central density along the  $x$ - and  $z$ -axes for the SRIF2 model E15B. At the time of the first density maximum there is a steep drop in density at around 200 km along the  $x$ -axis, while along the  $z$ -axis the density distribution is smoother. At the density minimum this discontinuity has moved to around 350 km, and it moves inwards again for the subsequent maximum. Looking at the radial velocity along

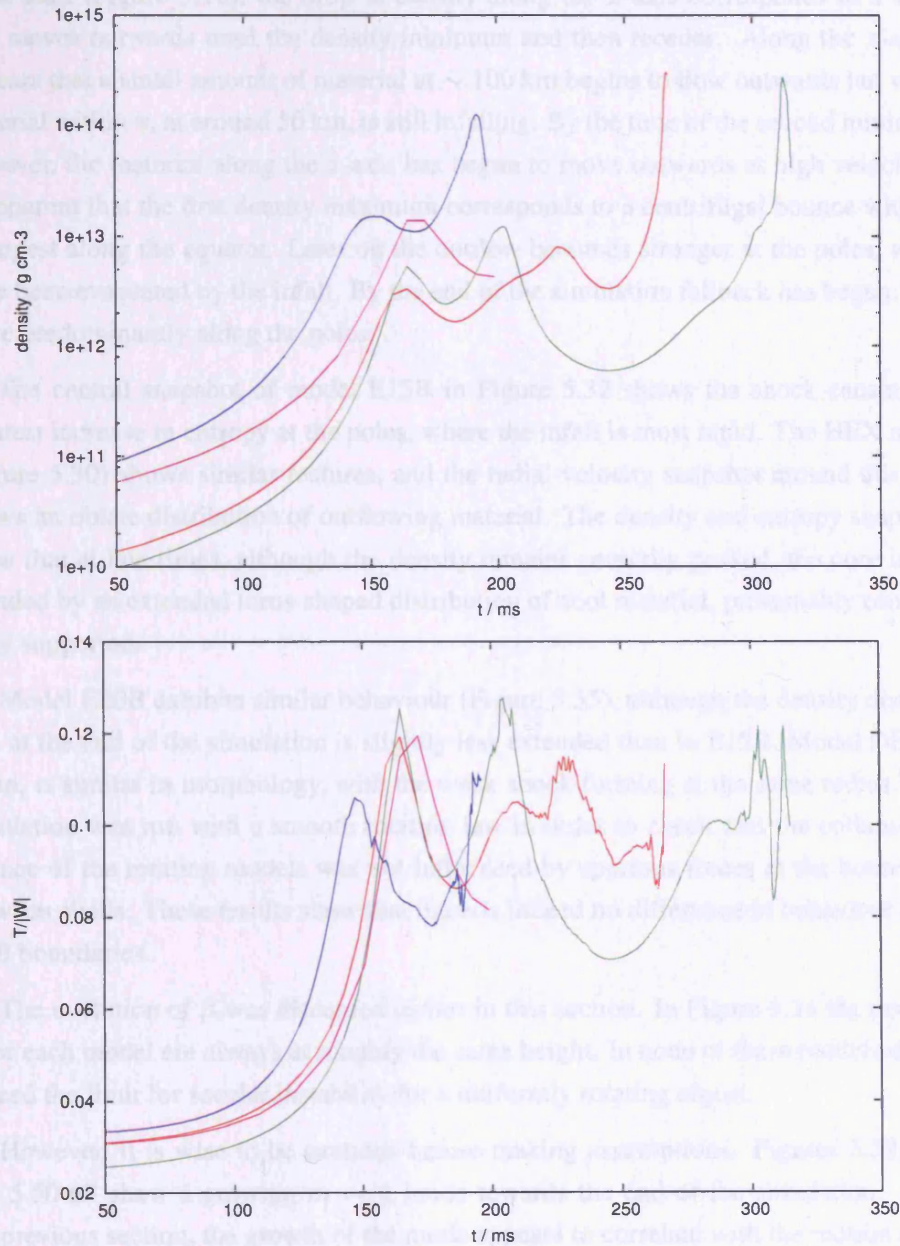


FIGURE 5.14. Top: Evolution of the central density for models E15B (red), E20B (green) and DE15B (blue) run on SRIF2 and for E15B run on HEX (magenta). Each SRIF2 model experiences two centrifugal bounces. In models E15B and E20B the collapse then proceeds to nuclear densities. Bottom: Evolution of the core rotation parameter  $\beta = T/|W|$  for the same models. Peaks coincide not only with peaks in density but also with changes in  $\frac{d\rho}{dt}$ .

these axes (Figure 5.16), the drop in density along the  $x$ -axis corresponds to a shock that moves outwards until the density minimum and then recedes. Along the  $z$ -axis it appears that a small amount of material at  $\sim 100$  km begins to flow outwards but whilst material within it, at around 50 km, is still infalling. By the time of the second minimum, however, the material along the  $z$ -axis has begun to move outwards at high velocity. It is apparent that the first density maximum corresponds to a centrifugal bounce which is strongest along the equator. Later on the outflow becomes stronger at the poles, which have been evacuated by the infall. By the end of the simulation fallback has begun, once more predominantly along the poles.

The central snapshot of model E15B in Figure 5.32 shows the shock causing the greatest increase in entropy at the poles, where the infall is most rapid. The HEX model (Figure 5.30) shows similar features, and the radial velocity snapshot around this time shows an oblate distribution of outflowing material. The density and entropy snapshots show that at late times, although the density remains centrally peaked, the core is surrounded by an extended torus-shaped distribution of cool material, presumably centrifugally supported.

Model E20B exhibits similar behaviour (Figure 5.35), although the density distribution at the end of the simulation is slightly less extended than in E15B. Model DE15B, again, is similar in morphology, with the weak shock forming at the same radius. This simulation was run with a smooth rotation law in order to check that the collapse and bounce of the rotating models was not influenced by spurious forces at the boundaries between shells. These results show that there is indeed no difference in behaviour at the shell boundaries.

The evolution of  $\beta$  was discussed earlier in this section. In Figure 5.14 the peaks in  $\beta$  for each model are always at roughly the same height. In none of these models does  $\beta$  exceed the limit for secular instability for a uniformly rotating object.

However, it is wise to be cautious before making assumptions. Figures 5.32, 5.35 and 5.50 all show a growing  $m = 1$  mode towards the end of the simulation. As in the previous section, the growth of the mode appears to correlate with the motion of the centre of mass. To verify that this is indeed the case and nothing more, density contours of models E15B and E20B in the  $x - y$  plane are plotted in Figure 5.17. These show that even at the end of the calculation the core remains circular, with no sign of deformation or fragmentation. If rotational instabilities occur at all, they must require still faster rotation.

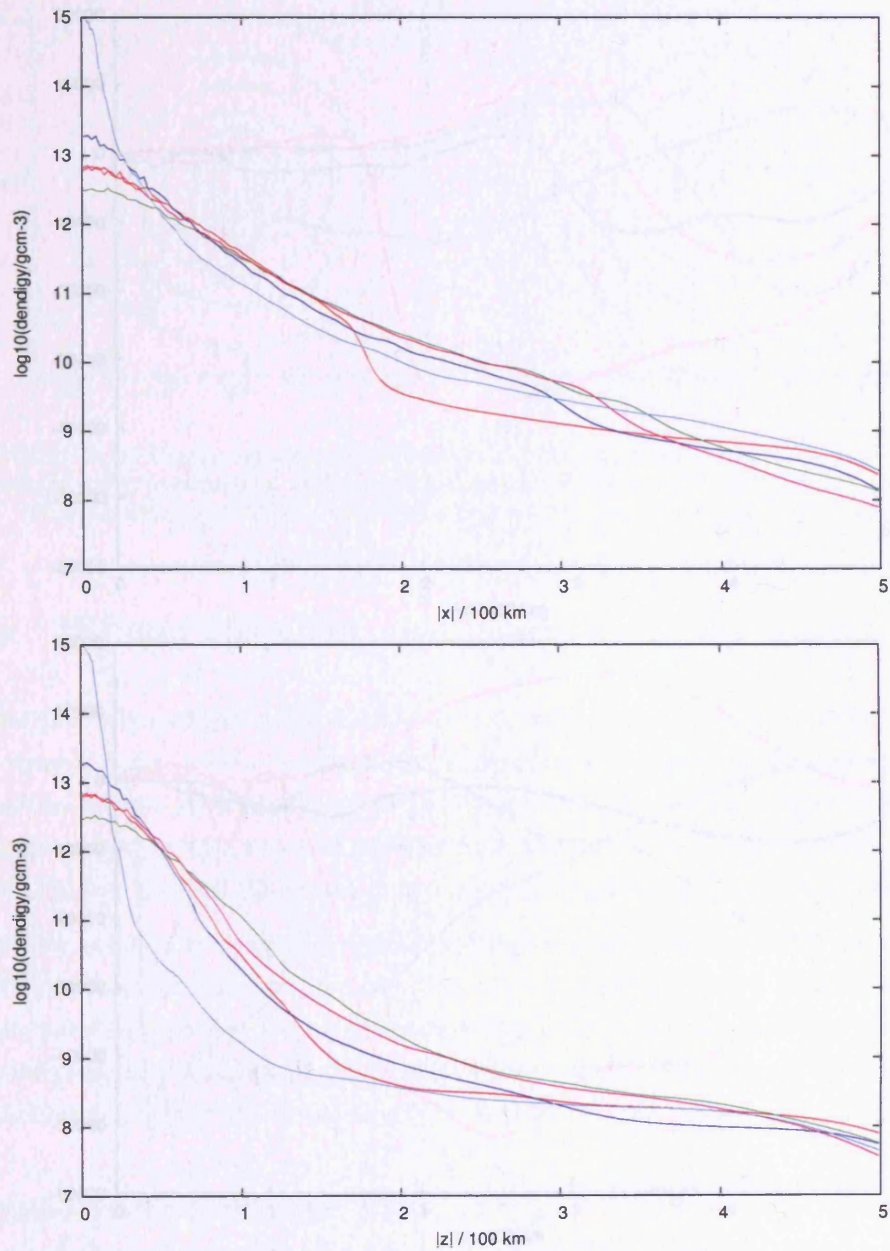


FIGURE 5.15. Density profiles along the  $x$ -axis (top) and  $z$ -axis (bottom) for the SRIF2 model E15B. Curves are plotted at the first peak in density when  $t = 164.7$  ms (red), the subsequent minimum at  $t = 183.9$  (green), second peak at  $t = 223.9$  (blue), second trough at  $t = 244.2$  (magenta) and just as nuclear density is reached at  $266.3$  ms (cyan). When the first peak in density occurs a discontinuity in density is visible at around 200 km along the  $x$ -axis, which subsequently moves outwards.

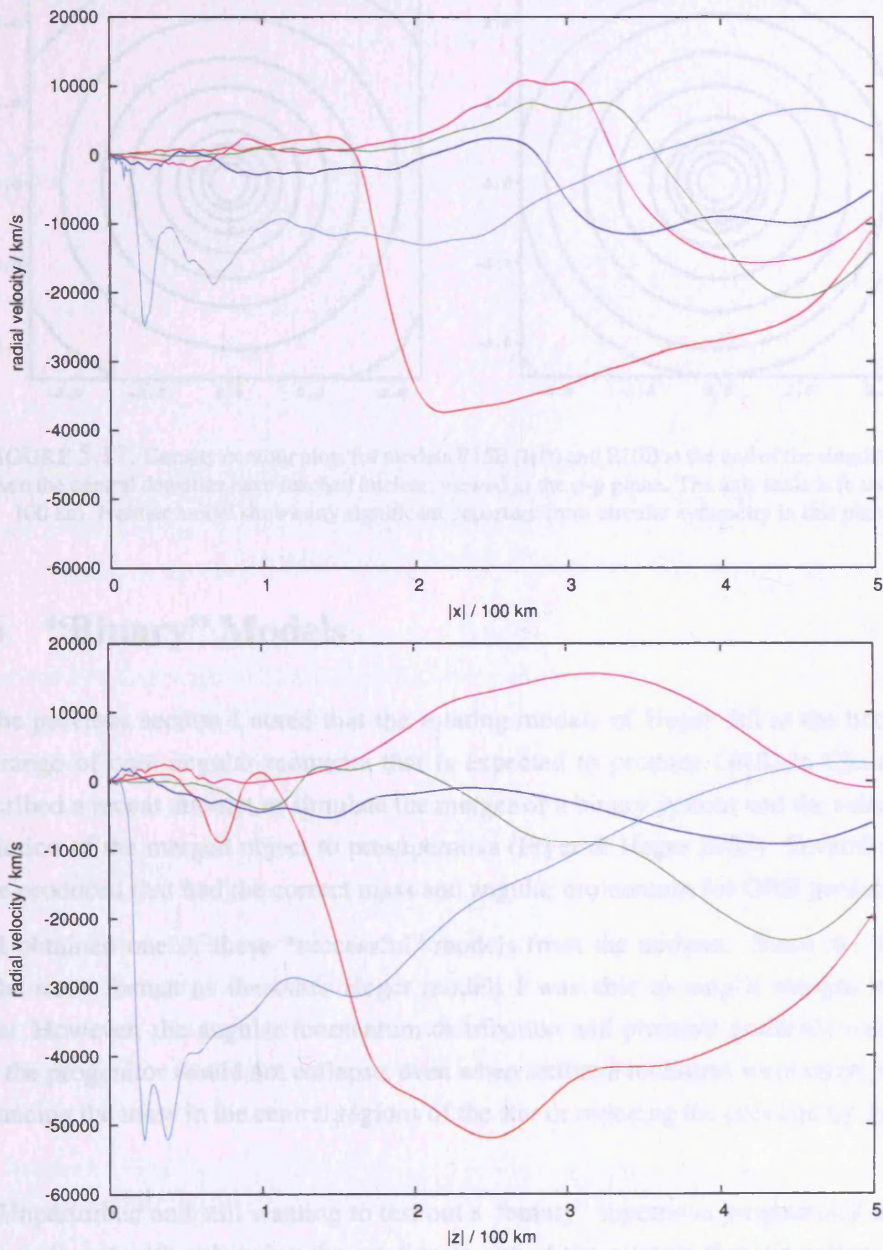


FIGURE 5.16. Radial velocity profiles along the  $x$ -axis (top) and  $z$ -axis (bottom) for the SRIF2 model E15B. Curves are plotted at the first peak in density when  $t = 164.7$  ms (red), the subsequent minimum at  $t = 183.9$  (green), second peak at  $t = 223.9$  (blue), second trough at  $t = 244.2$  (magenta) and just as nuclear density is reached at 266.3 ms (cyan). The discontinuity in the density profile at around 200 km along the  $x$ -axis corresponds to a shock forming at this distance. Along the  $z$ -axis the shock is weaker and closer in, but the outward motion becomes stronger at later times.

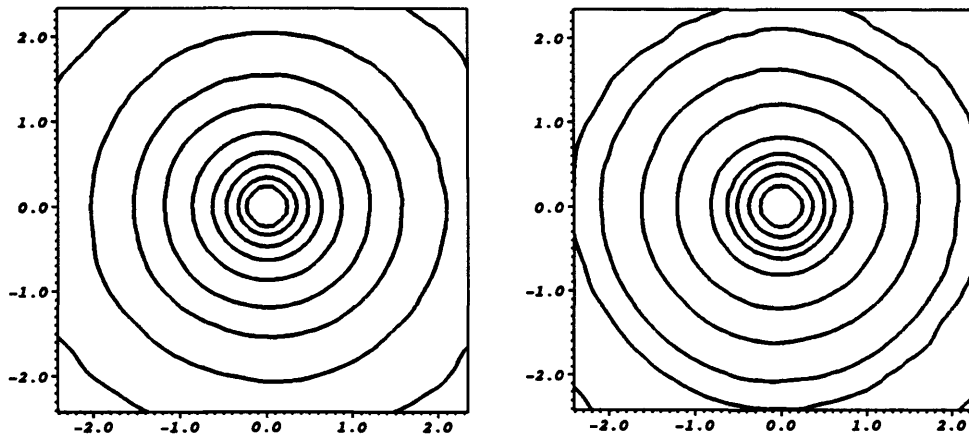


FIGURE 5.17. Density contour plots for models E15B (left) and E20B at the end of the simulations, when the central densities have reached nuclear, viewed in the  $x$ - $y$  plane. The axis scale is in units of 100 km. Neither model shows any significant departure from circular symmetry in this plane.

## 5.6 “Binary” Models

In the previous section I noted that the rotating models of Heger fall at the bottom of the range of core angular momenta that is expected to produce GRB. In Chapter 1 I described a recent attempt to simulate the merger of a binary system and the subsequent evolution of the merged object to presupernova (Fryer & Heger 2005). Several models were produced that had the correct mass and angular momentum for GRB production.

I obtained one of these “successful” models from the authors. Since the file was in the same format as the other Heger models I was able to map it straight into my code. However, the angular momentum distribution and pressure gradients were such that the progenitor would not collapse, even when artificial measures were taken, such as enhancing the mass in the central regions of the star or reducing the pressure by reducing  $Y_e$ .

Unperturbed and still wanting to test out a “binary” supernova progenitor, I decided to experiment with enhancing the rotation in one of the rotators that did collapse. The motivation for this was that in the inner core ( $\lesssim 10^8$  cm) the binary model was actually less dense than the “normal” rotators (Figure 5.18). I surmised that a more massive inner core would assist the collapse.

The model I chose initially was E15B and I produced models with the angular velocity multiplied by a factor of 1.4 (E15C) and 1.5 (E15D), values which gave a rotation profile that was fairly similar to that of the binary model. Figure 5.18 shows the rotation

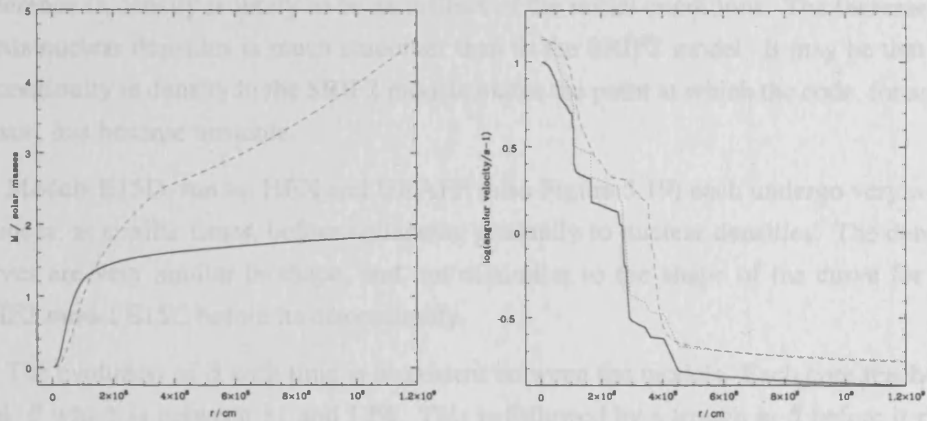


FIGURE 5.18. Left: Enclosed mass versus radius for model E15B (solid line) and the binary merger progenitor. The central density of the binary progenitor is less than that of the single star. Right: Rotation profiles of model E15B before (solid) and after (dotted) multiplication by a factor of 1.4, compared with the binary progenitor (dashed).

curve for E15C alongside that of the “binary” merger model. (I also tested out a model with the rotation multiplied by a factor of 2, but this model failed to collapse.) This rotation profile is also shown alongside those of E15A and E15B in Figure 5.12.

### 5.6.1 Results

Models E15C and E15D were run with 250 000 particles on HEX. Snapshots and profiles for these are in Figures 5.38 and 5.47. Due to an unfortunate blunder the first 200 dumps of E15C were lost, so only the behaviour of this model late on in the simulation can be described. Model E15D was run with 1 million particles on UKAFF (Figure 5.46). Models E15C and E20C were run with 300 000 particles on SRIF2 (Figures 5.40 and 5.43).

Figure 5.19 shows the evolution of central density and rotation parameter for all of the models with enhanced rotation, and Table 5.9 gives more information about the density peaks.

Models E15C and E20C, run on SRIF2, undergo a centrifugal bounce at similar times and densities, following which the density increases smoothly until a sudden central collapse occurs, which takes E20C to nuclear densities. As in the B models, the behaviour is qualitatively similar but the collapse faster for the  $20 M_{\odot}$  model. The density at the first dump available for the HEX run of E15C is around an order of magnitude higher than that in the SRIF2 run. As was mentioned in the discussion of the B models, this

difference in density is likely to be an artifact of the initial conditions. The increase towards nuclear densities is much smoother than in the SRIF2 model. It may be that the discontinuity in density in the SRIF2 models marks the point at which the code, for some reason, has become unstable.

Models E15D, run on HEX and UKAFF (also Figure 5.19) each undergo very weak bounces, at similar times, before collapsing gradually to nuclear densities. The density curves are very similar in shape, and not dissimilar to the shape of the curve for the SRIF2 model E15C before its discontinuity.

The evolution of  $\beta$  with time is consistent between the models. Each core reaches a peak  $\beta$  which is between 11 and 13%. This is followed by a trough in  $\beta$  before it rises again to a plateau.  $\beta$  decreases again as nuclear densities are approached, presumably because the core, which is assumed spherical in the calculation of  $\beta$ , becomes increasingly flattened. This effect is very sudden for the SRIF2 models and it corresponds to the sudden density increase.

It is also interesting to note that the composite figures show a flat rotation profile for the HEX and UKAFF runs right up to nuclear densities (although only E15C on HEX reaches this density). In contrast, the SRIF2 runs show the angular velocity profile becoming peaked as in the B models.

All of the “binary” models have interesting structures, as can be seen from the snapshots at various points in their evolution. Their density distributions become highly extended in the equatorial plane and at late times a low entropy disc is visible, with high entropy material above the poles. The density profiles along the  $x$ - and  $z$ -axes for model E20C are shown in Figure 5.20, at the times of the first density maximum and the minimum that follows, the second density maximum and the final density. At the first density maximum a shock/discontinuity is visible along the  $x$ -axis, which has moved outwards by the time the subsequent minimum is reached. After this time the profile is fairly featureless, with rapid collapse taking place in the innermost regions after the second density peak. The  $z$ -axis profile remains fairly featureless at all times and is much steeper near the centre, showing that the core is flattened (see also Figure 5.43). At late times the runaway collapse of the inner core is visible.

The C and D models all take a similar amount of time to collapse and end up with similar shapes and similar density profiles in enclosed mass. These profiles show that by the end of the simulations the density has increased at mass coordinates right out to  $1.6M_{\odot}$ . This mass coordinate corresponds to a radius approaching the outer edge of the particle distribution, and since the dynamical time at this edge is of the order of the time

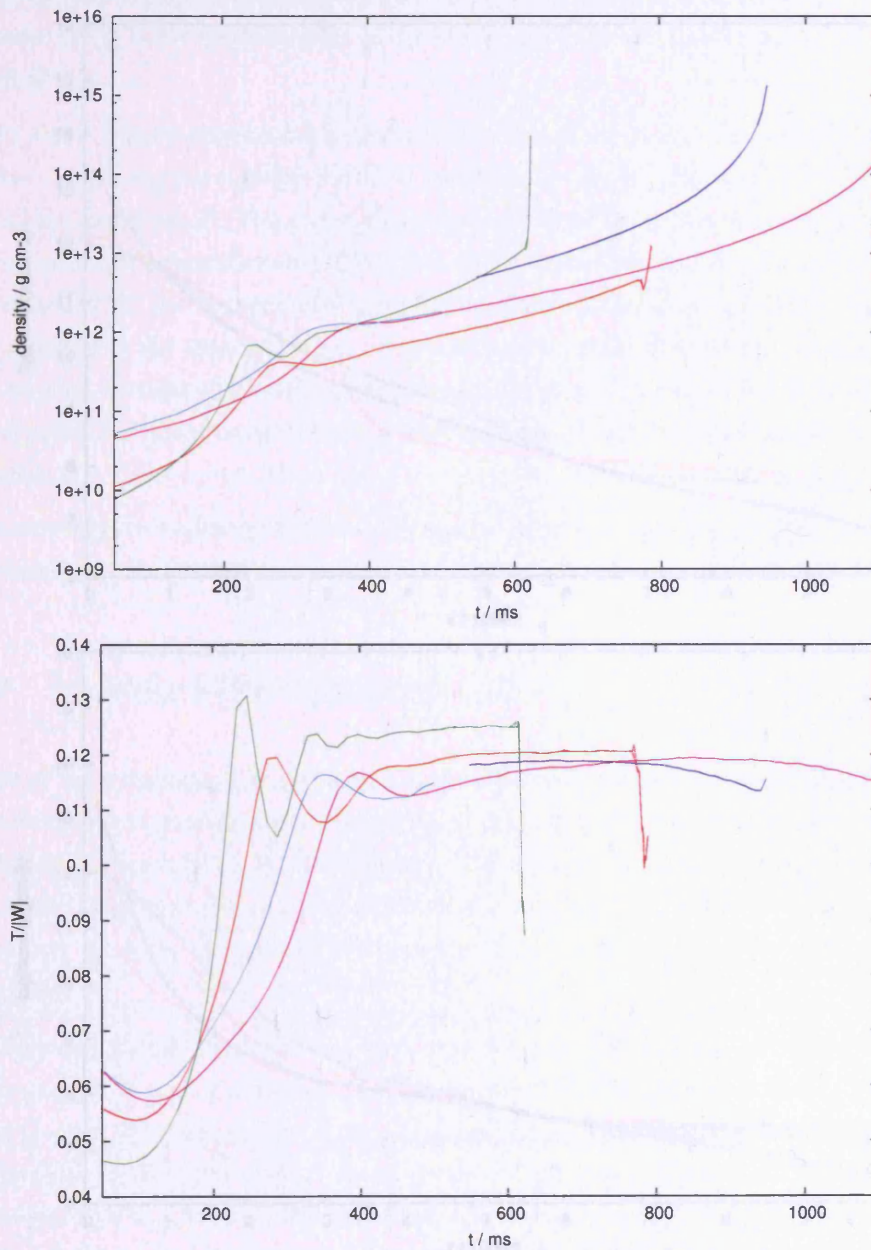


FIGURE 5.19. Top: Evolution of the central density for the SRIF2 runs of E15C (red) and E20C (green), HEX runs of E15C (blue) and E15D (magenta) and UKAFF run of E15D (cyan). Both E15C models experience their first centrifugal bounce at the same time, but with peak densities differing by an order of magnitude. Model E15D collapses slightly quicker on UKAFF than on HEX but appears qualitatively similar. Bottom: Evolution of the core rotation parameter  $\beta = T/|W|$  for the same models. Here, the E15C runs show similar behaviour up to  $\sim 400$  ms.

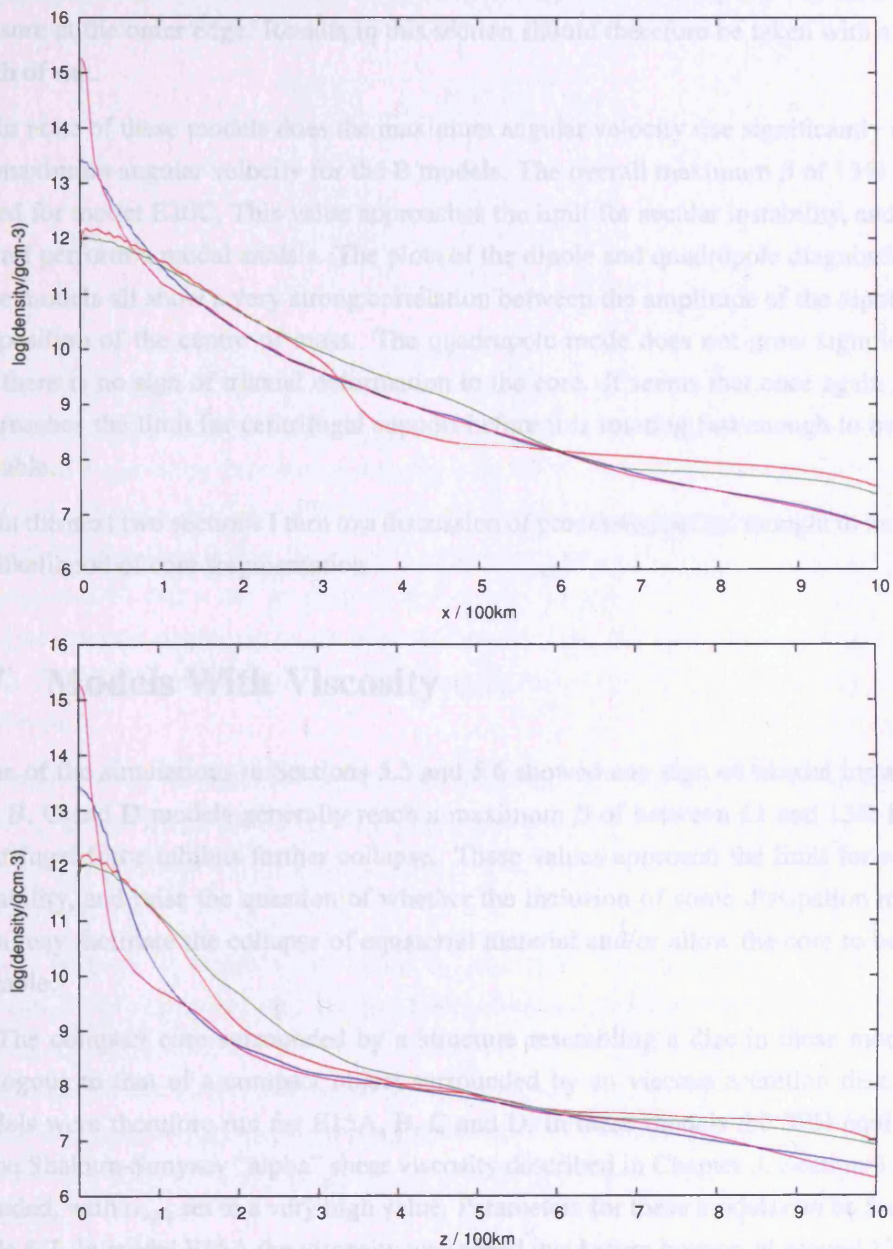


FIGURE 5.20. Density profiles along the  $x$ -axis (top) and  $z$ -axis (bottom) for the SRIF2 model E20C. Curves are plotted at the first peak in density when  $t = 247.0$  ms (red), the subsequent minimum at  $t = 274.4$  ms (green), second peak at  $t = 616.8$  ms (blue), and the end of the simulation at  $t = 623.8$  ms (magenta). When the first peak in density occurs a discontinuity in density is visible just past 300 km along the  $x$ -axis, which subsequently moves outwards.

taken for these models to collapse, inaccuracies may have developed from the lack of pressure at the outer edge. Results in this section should therefore be taken with a hefty pinch of salt.

In none of these models does the maximum angular velocity rise significantly above the maximum angular velocity for the B models. The overall maximum  $\beta$  of 13% is obtained for model E20C. This value approaches the limit for secular instability, and once again I perform a modal analysis. The plots of the dipole and quadrupole diagnostics for these models all show a very strong correlation between the amplitude of the dipole and the position of the centre of mass. The quadrupole mode does not grow significantly and there is no sign of triaxial deformation in the core. It seems that once again material reaches the limit for centrifugal support before it is rotating fast enough to become unstable.

In the next two sections I turn to a discussion of processes that are thought to increase the likelihood of core fragmentation.

## 5.7 Models With Viscosity

None of the simulations in Sections 5.5 and 5.6 showed any sign of triaxial instability. The B, C and D models generally reach a maximum  $\beta$  of between 11 and 13% before centrifugal force inhibits further collapse. These values approach the limit for secular instability, and raise the question of whether the inclusion of some dissipation mechanism may facilitate the collapse of equatorial material and/or allow the core to become unstable.

The compact core surrounded by a structure resembling a disc in these models is analogous to that of a compact object surrounded by an viscous accretion disc. Test models were therefore run for E15A, B, C and D. In these models the SPH equivalent of the Shakura-Sunyaev “alpha” shear viscosity described in Chapter 3, Section 3.6 was included, with  $\alpha_{sph}$  set to a very high value. Parameters for these models can be found in Table 5.7. In model E15A the viscosity was added just before bounce, at around 137 ms, to observe its effect on the bounce dynamics.

The viscous models were run predominantly on HEX and the time evolution of the central density resembles that found for the non-viscous models (Figure 5.21, compare with Figure 5.19). The D models with and without viscosity are very similar, the main difference being that the viscous models collapse faster due to the removal of angular momentum. The knee that occurs at around 400 ms for model E15D is visible at around

Table 5.2. Viscosity parameters for models in which Sunyaev-Shakura “ $\alpha$ ”-viscosity was used. The value of the SPH  $\alpha$  used is given in the third column.

Model	Run on	$\alpha_{SPH}$
E15A_visc	SRIF2	2.0
E15Bvisc	HEX	5.0
E15Cvisc	HEX	5.0
E15Dvisc	HEX	5.0
E15Dvisc	UKAFF	2.0

350 ms for E15Dvisc. It is difficult to compare models E15C and E15Cvisc because the data for E15C early on is missing, but the curves at late times have the same shape. E15C reaches nuclear densities just under 300 ms after E15Cvisc. Models E15B and E15Bvisc are also similar, with the first density peak occurring just after 150 ms. The main difference here is that the viscous model does not show a second peak in density (at around 200 ms) – the gradient of the curve changes at this point but the density increases monotonically up to nuclear, which it reaches at around the same time as does E15B. None of these models have a maximum  $\beta$  that is higher than in their non-viscous counterparts.

Snapshots and profiles of these models at various times can be seen in Figures 5.28, 5.31, 5.39, 5.49 and 5.48. Comparing the viscous and non-viscous models it can be seen that overall, the extra viscosity has the effect of smoothing the profiles and damping any shock that forms.

It is difficult to compare the snapshots and profiles of models E15B and E15Bvisc because model E15B on HEX had not reached nuclear densities by the end of the simulation. Comparing model E15Bvisc with E15B run on SRIF2 shows that the shock at centrifugal bounce is less defined in the viscous model. The viscous model E15B maintains a flat angular velocity profile right up to the end of the simulation, in contrast to the non-viscous SRIF2 model which forms a peak at just past 10 km soon after centrifugal bounce.

Also difficult to compare are the snapshots and profiles for models E15C and E15D with and without viscosity due to the faster collapse of the viscous models enabling them to be run to later stages in their evolution. A change in the shape of the density profile accompanied by the formation of a peak in entropy occurs in the viscous runs at a time equivalent to after the end of the simulations in the non-viscous runs. What is perceivable in the snapshots is that the viscous models are basically same shape as the non-viscous

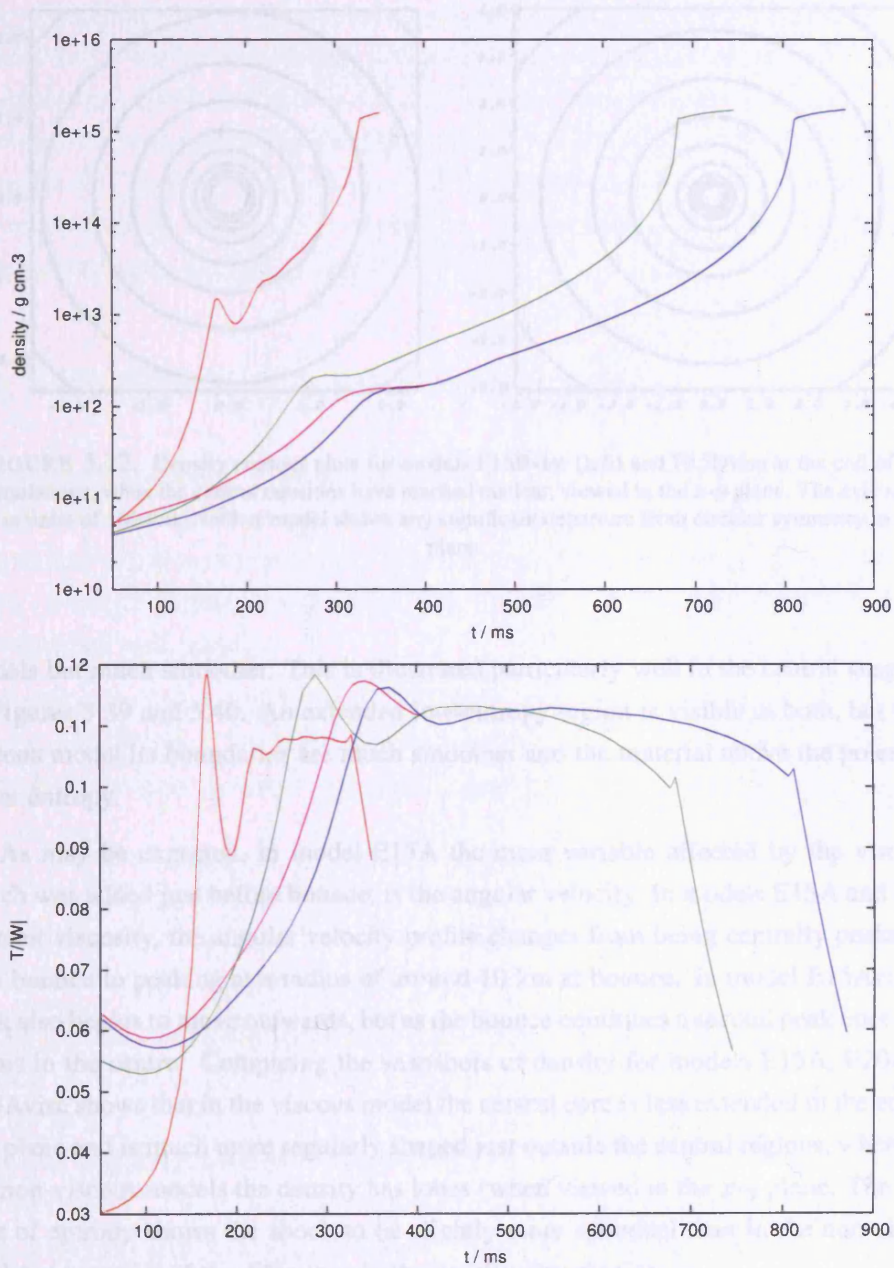


FIGURE 5.21. Top: Evolution of the central density for viscous models E15Bvisc (red), E15Cvisc (green) and the HEX (blue) and UKAFF (magenta) runs of E15Dvisc. The first 200 dumps of E15Cvisc have been lost. Model E15Bvisc shows very similar to the non-viscous model E15B, although the second peak is damped out. Both E15Dvisc models show almost identical behaviour to their non-viscous counterparts.

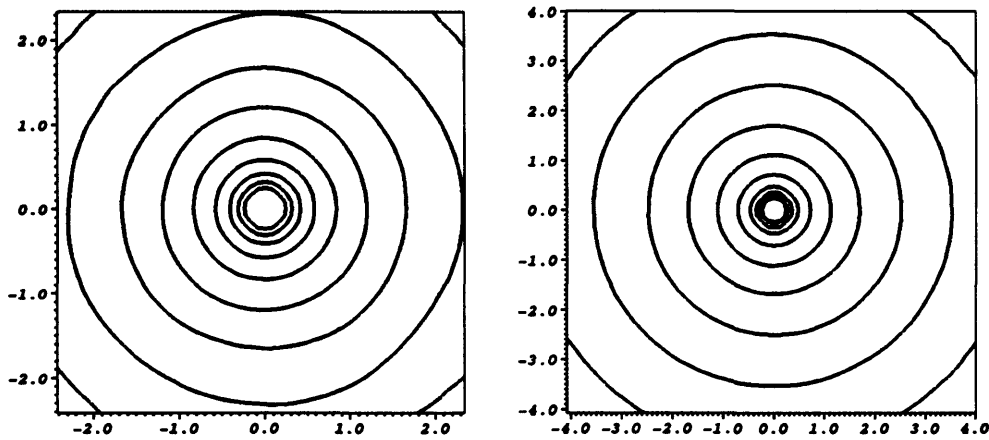


FIGURE 5.22. Density contour plots for models E15Bvisc (left) and E15Dvisc at the end of the simulations, when the central densities have reached nuclear, viewed in the  $x$ - $y$  plane. The axis scale is in units of 100 km. Neither model shows any significant departure from circular symmetry in this plane.

models but much smoother. This is illustrated particularly well in the central snapshots of Figures 5.39 and 5.40. An extended low-entropy region is visible in both, but in the viscous model its boundaries are much smoother and the material above the poles is of lower entropy.

As may be expected, in model E15A the main variable affected by the viscosity, which was added just before bounce, is the angular velocity. In models E15A and E20A without viscosity, the angular velocity profile changes from being centrally peaked before bounce to peaking at a radius of around 10 km at bounce. In model E15Avisc the peak also begins to move outwards, but as the bounce continues a second peak once again forms in the centre. Comparing the snapshots of density for models E15A, E20A and E15Avisc shows that in the viscous model the central core is less extended in the equatorial plane and is much more regularly shaped just outside the central regions, whereas in the non-viscous models the density has lobes (when viewed in the  $x$ - $y$  plane. The snapshot of entropy shows the shock to be slightly more spherical than in the non-viscous models as a result of the difference in the density distribution.

It has already been observed that the parameter  $\beta$  does not exceed the limit for secular instability for any of these models, but since once again the dipole diagnostic grows with time, it is wise to plot contours in the  $x$ - $y$  plane for selected models. Figure 5.22 shows model E15Cvisc and E15Dvisc at their final dump. Neither of these models shows any significant azimuthal perturbation—indeed, model E15Dvisc is perfectly circular.

It appears that the addition of viscosity is not sufficient to produce instabilities in the cores of any of our rotating models. Although collapse proceeds more quickly due to the dissipation of angular momentum the core still does not condense enough for the ratio of rotational energy to gravitational binding energy to exceed the limit for secular instability. In fact, viscosity may even work against instabilities by damping small density perturbations in the outer regions of the core. If instabilities in the core during collapse are to occur it must be through another mechanism.

## 5.8 Models With Density Perturbations

One difference between the models described in the preceding sections and those in the literature which experience core deformation or fragmentation is that I have added no artificial perturbations to the density to act as seeds for instabilities. For completeness, I now described simulations produced as a follow up to these runs in which density perturbations were added.

Rapidly rotating models E15B, E20B, E15C and E20C were given  $m = 1$  and  $m = 2$  density perturbations. The position of each particle was altered according to its initial azimuthal coordinate  $\phi$ , the new coordinate given by:

$$\phi_{new} = \phi + \delta_1 \sin(\phi + \pi/4) + \delta_2 \sin(2\phi + \pi/2) \quad (5.1)$$

where  $\delta_1$  and  $\delta_2$  are constants. After the particles were perturbed the resulting position of the centre of mass was subtracted from the positions of the particles.

For one set of models perturbations were added at the first density minimum after bounce, as in Ott et al. (2005) with values of  $\delta_1$  and  $\delta_2$  of 0.1%. These are denoted by the suffix “\_p.” A second set of models were run with the perturbations added to the initial particle distribution with a  $\delta_1$  and  $\delta_2$  of 1%. The names of these models are prefixed by “p”. Just to see what happened, a single model was run with  $\delta_1$  and  $\delta_2$  of 20%, added at the first density minimum. This model is named “Bumps”. All of these runs are tabulated in Table 5.8.

Table 5.9 includes the bounce times and densities for the perturbed models. The first bounce of the \_p models is not included since it is listed for the unperturbed models.

All four of the models that were perturbed from the start of the simulation show the same number of bounces with similar bounce times, densities and  $\beta$  as their unperturbed counterparts. Snapshots of these models in the  $x$ - $y$  plane at times of density maxima can

**Table 5.3.** Details of the density perturbations added to the rapidly rotating models. The second column gives the time at which the perturbations were added, and  $\delta_1$  and  $\delta_2$  give the magnitude of the perturbations, as defined in Equation 5.1.

Model	$t_{\text{perturb}}$ (ms)	$\delta_1$	$\delta_2$
E15B.p	184	$10^{-3}$	$10^{-3}$
E20B.p	180	$10^{-3}$	$10^{-3}$
E15C.p	329	$10^{-3}$	$10^{-3}$
E20C.p	274	$10^{-3}$	$10^{-3}$
pE15B	0	$10^{-2}$	$10^{-2}$
pE20B	0	$10^{-2}$	$10^{-2}$
pE15C	0	$10^{-2}$	$10^{-2}$
pE20C	0	$10^{-2}$	$10^{-2}$
Bumps	184	0.2	0.2

be found in Figures 5.34, 5.37, 5.42 and 5.45. In none of these models can any sign of deformation of the core be seen, and once again the growing dipole diagnostic traces the motion of the centre of mass.

The picture is much the same for the models perturbed after their first bounce (Figures 5.33, 5.36, 5.41 and 5.44). Although the models do not bounce at the same times or densities as their unperturbed counterparts, once again there is no evidence for triaxial deformation.

Model Bumps was given an extremely large density perturbation at the density minimum after the first peak (Figure 5.51). From this point on the central density increased while the distribution in the  $x$ - $y$  plane returned to rotundity within 30 ms. The snapshot of entropy at the end of the simulation shows spiral waves having been created as the bumps in the density spiralled together. It is interesting that, rather than being unstable to fragmentation, this model is resistant to large density perturbations, implying that the ground state of this density distribution is spheroidal.

## 5.9 Summary

In this chapter I have used state-of-the-art supernova progenitor models to simulate core collapse in a variety of rotating cases. I began by comparing the collapse of the non-rotating progenitors with that of the control model Woos of the previous chapter. These models behaved very similarly to the control.

Following on from this, the collapse of the “weakly-rotating” Heger progenitors

E15A and E20A was followed. By an interesting twist of fate these models begin with values of  $\beta$  very close to that of model W40lr. Of the Woosley models, this is the one that had the highest  $\beta$  at bounce. It seems that models E15A and E20A rotate at the optimum rate for enhancement of the rotational energy. The collapse that ensued was indeed very similar to that of model W40lr, with a maximum  $\beta$  of 10% and 12% for E15A and E20A respectively.

The next set of models used were the rapid rotators, E15B and E20B, whose collapse was held up significantly by centrifugal support, and whose central densities peaked several times before nuclear density was reached. By the end of the simulations these models were highly flattened along the  $z$ -axis with a torus-like distribution of material surrounding the central object. In none of these models did  $\beta$  rise much above 12%.

Since none of the rotating models had shown any sign of instabilities the rotation of the Heger rapid rotators was enhanced to a rate similar to that obtained in a binary merger simulation (Fryer & Heger 2005). These models experienced repeated centrifugal bounces at very low densities and collapse proceeded very slowly. Once again the centrifugal hang-up of equatorial material prevented  $\beta$  from rising above 12-13%.

None of the rotating models showed any sign of triaxial deformation or growth of the  $m = 1$  mode. In all cases the density distribution remained centrally peaked although in the rapidly rotating and “binary” models the central peak was surrounded by a torus of centrifugally supported material.

In an attempt to provoke interesting effects a parametrization of viscosity was added to the rapidly rotating models. This caused the collapse to proceed slightly more rapidly as angular momentum was dissipated and gave a smoother mass distribution, but ultimately had little effect on the shape of the core.

Another set of models was run with  $m = 1$  and  $m = 2$  mode density perturbations added, some from the start of the simulations and others from the density minimum that follows the first peak. Although the rate of collapse was somewhat affected by these perturbations they had little effect on the shape of the core, which proved resistant to deformation, even when the density perturbed significantly.

I therefore conclude that the collapse of rotating stellar cores does not result in triaxial deformations or fragmentation, at least before bounce. This appears to rule out the delayed model of GRB described in Chapter 1. However, the presence of the torus-like object around the core in all of these models gives some hope to the model of GRB. In the presence of a magnetic field that was amplified by collapse and a mechanism

for driving dissipation in the disc, causing the central object to accrete, it would still be possible to power a GRB.

Table 5.4. Initial parameters and results for all Heger runs undertaken on the HEX and UKAFF supercomputers and the SRIF2 cluster.  $t_{max1}$  and  $t_{max2}$  are the times of the first and second (if present) density peaks, for which the central density and rotation parameter  $\beta$  are also given. If density the peaks again after the second maximum,  $\rho_{final}$  is this density, otherwise  $\rho_{final}$  is the density at the end of the simulation. <sup>p</sup>Perturbations added at minimum after first peak, therefore first peak identical to non-perturbed model and  $t_{max1}$  thus gives time of second peak. <sup>u</sup>Under-resolved in time. <sup>\*</sup>Accidentally deleted first 199 dumps.

Model	Run on	$n_{particles}$	$\beta_i$ (%)	$t_{max1}$ (ms)	$\rho_{max1}$ ( $\text{g cm}^{-3}$ )	$\beta_{max1}$ (%)	$t_{max2}$ (ms)	$\rho_{max2}$ ( $\text{g cm}^{-3}$ )	$\beta_{max2}$ (%)	$\rho_{final}$ ( $\text{g cm}^{-3}$ )
D15	HEX	250000	—	105	$1.9 \times 10^{15}$	—	—	—	—	—
D15	SRIF2	300000	—	103	$3.8 \times 10^{14}$	—	—	—	—	—
D20	SRIF2	300000	—	106	$3.8 \times 10^{14}$	—	—	—	—	—
E15A	HEX	250000	0.50	137 <sup>u</sup>	$7.9 \times 10^{13}$	4.2	—	—	—	—
E15A	SRIF2	300000	0.50	139	$2.8 \times 10^{14}$	12	—	—	—	—
E15A <sub>visc</sub>	SRIF2	300000	0.50	139	$2.9 \times 10^{14}$	11	—	—	—	—
E20A	SRIF2	300000	0.31	161	$3.0 \times 10^{14}$	9.8	—	—	—	—
E15B	HEX	250000	2.9	165 <sup>u</sup>	$1.4 \times 10^{13}$	11	—	—	—	$4.2 \times 10^{12}$
E15B	SRIF2	300000	2.9	165	$3.2 \times 10^{12}$	12	224	$7.9 \times 10^{12}$	11	$2.9 \times 10^{14}$
E15B <sub>visc</sub>	HEX	250000	2.9	167	$1.5 \times 10^{14}$	12	—	—	—	$1.6 \times 10^{15}$
E15B <sub>p</sub> <sup>p</sup>	SRIF2	300000	2.9	220	$6.3 \times 10^{12}$	11	271	$5.7 \times 10^{13}$	11	$2.6 \times 10^{14}$
pE15B	SRIF2	300000	2.9	164	$3.2 \times 10^{12}$	12	237	$6.8 \times 10^{12}$	11	$2.9 \times 10^{15}$
DE15B	SRIF2	300000	3.3	151	$1.5 \times 10^{13}$	10	192	$1.2 \times 10^{14}$	10	$4.2 \times 10^{13}$
E20B	SRIF2	300000	2.4	165	$5.2 \times 10^{12}$	13	203	$1.2 \times 10^{14}$	12	$2.7 \times 10^{13}$
E20B <sub>p</sub>	SRIF2	300000	2.4	201	$1.0 \times 10^{13}$	12	—	—	—	$2.7 \times 10^{14}$
pE20B	SRIF2	300000	2.4	161	$5.2 \times 10^{12}$	12	200	$8.1 \times 10^{12}$	12	$3.1 \times 10^{15}$
E15C	HEX <sup>*</sup>	250000	5.7	???	???	???	???	???	???	$1.3 \times 10^{15}$
E15C	SRIF2	300000	5.7	274	$4.1 \times 10^{11}$	12	772	$4.5 \times 10^{12}$	12	$1.2 \times 10^{13}$
E15C <sub>visc</sub>	HEX	250000	5.7	288	$2.2 \times 10^{12}$	12	—	—	—	$1.7 \times 10^{15}$
E15C <sub>p</sub> <sup>p</sup>	SRIF2	300000	5.7	—	—	—	—	—	—	$5.6 \times 10^{13}$
pE15C	SRIF2	300000	5.7	280	$4.1 \times 10^{11}$	12	—	—	—	$9.8 \times 10^{12}$
E20C	SRIF2	300000	4.7	247	$6.9 \times 10^{11}$	13	616	$1.2 \times 10^{13}$	13	$3.1 \times 10^{15}$
E20C <sub>p</sub> <sup>p</sup>	SRIF2	300000	4.7	—	—	—	—	—	—	$2.0 \times 10^{13}$
pE20C	SRIF2	300000	4.6	233	$7.5 \times 10^{11}$	13	554	$5.1 \times 10^{12}$	13	$4.1 \times 10^{13}$
E15D	UKAFF	$10^6$	6.5	364	$1.3 \times 10^{12}$	12	—	—	—	$1.8 \times 10^{12}$
E15D	HEX	250000	6.5	412	$1.3 \times 10^{12}$	12	—	—	—	$1.4 \times 10^{14}$
E15D <sub>visc</sub>	UKAFF	$10^6$	6.5	357	$1.5 \times 10^{12}$	12	—	—	—	$1.7 \times 10^{12}$
E15D <sub>visc</sub>	HEX	250000	6.5	—	—	—	—	—	—	$1.7 \times 10^{15}$
Bumps <sup>p</sup>	SRIF2	300000	2.9	—	—	—	—	—	—	$3.7 \times 10^{15}$

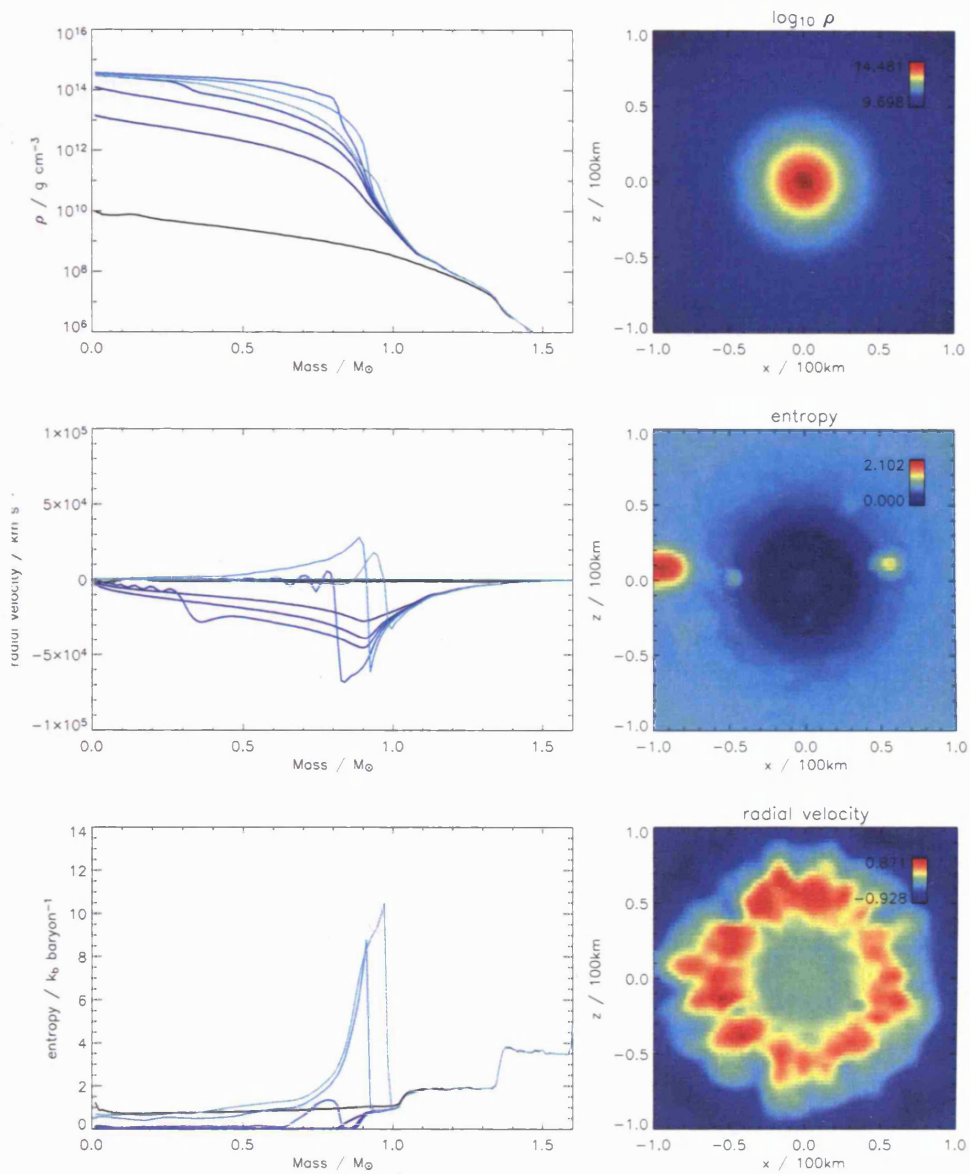


FIGURE 5.23. HEX run of model D15. Density, radial velocity and entropy versus enclosed mass at  $t = 13.7, 103.6, 104.8, 105.1, 105.4, 105.7$  and  $106.5$  ms are shown. Core bounce occurs at  $105.4$  ms. Snapshots show the density and entropy just before bounce and the radial velocity at  $106.5$  ms.

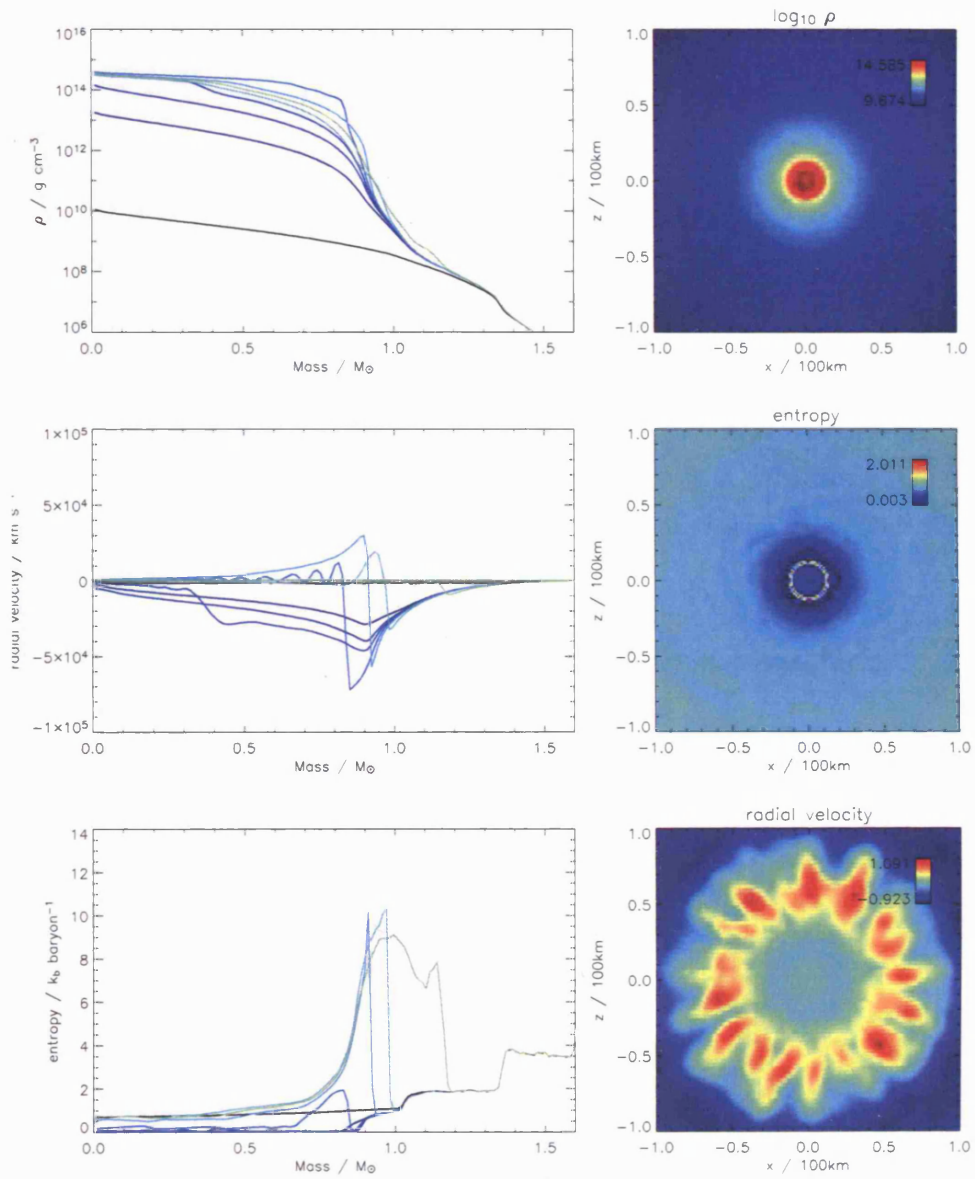


FIGURE 5.24. SRIF2 run of model D15. Density, radial velocity and entropy versus enclosed mass at  $t = 19.2, 101.0, 102.1, 102.4, 102.6, 102.9, 103.7$  and  $112.1$  ms are shown. Core bounce occurs at  $102.6$  ms. Snapshots show the density and entropy at bounce and the radial velocity at  $103.7$  ms.

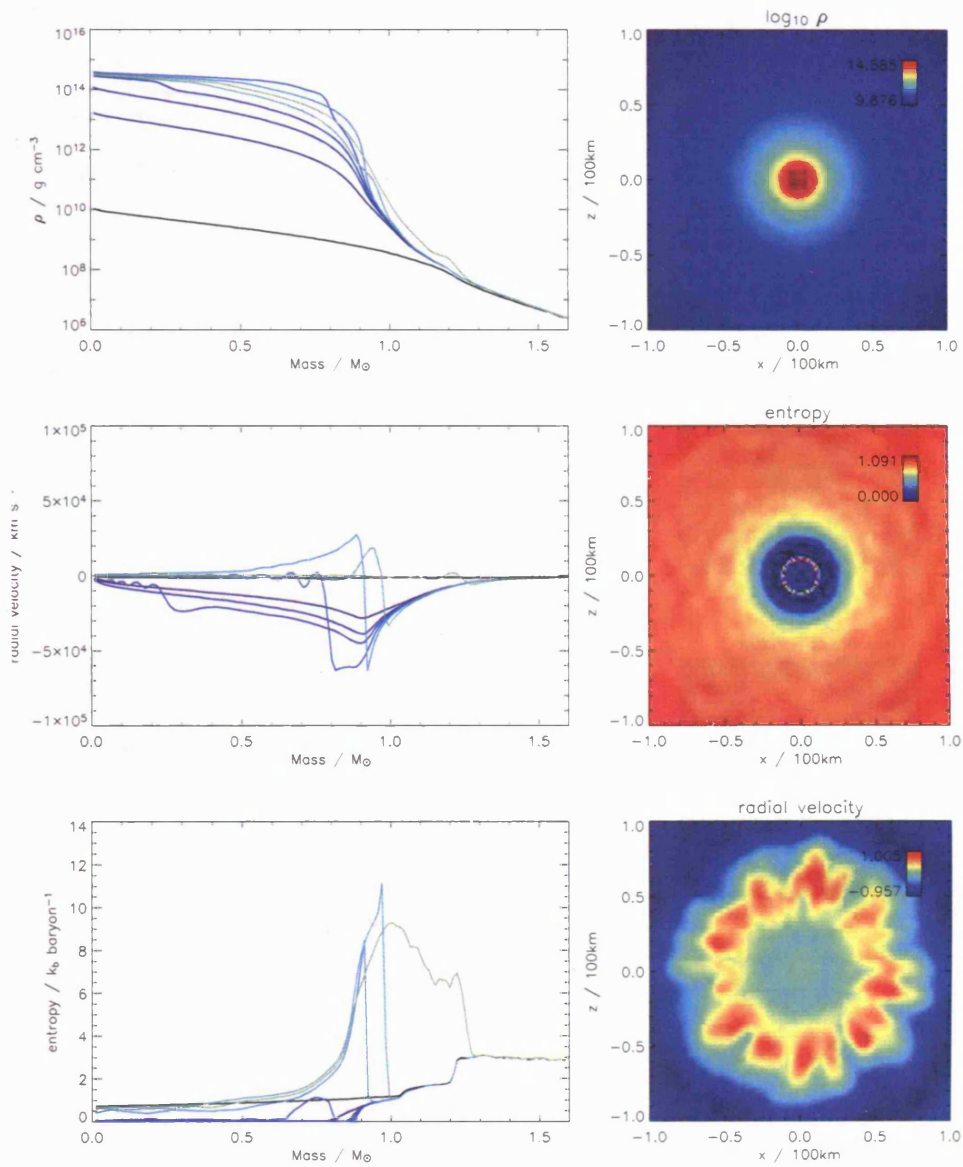


FIGURE 5.25. SRIF2 run of model D20. Density, radial velocity and entropy versus enclosed mass at  $t = 19.2, 104.0, 105.1, 105.4, 105.7, 105.9, 106.8$  and  $123.6$  ms are shown. Core bounce occurs at  $105.7$  ms. Snapshots show the density and entropy at bounce and the radial velocity at  $106.8$  ms.

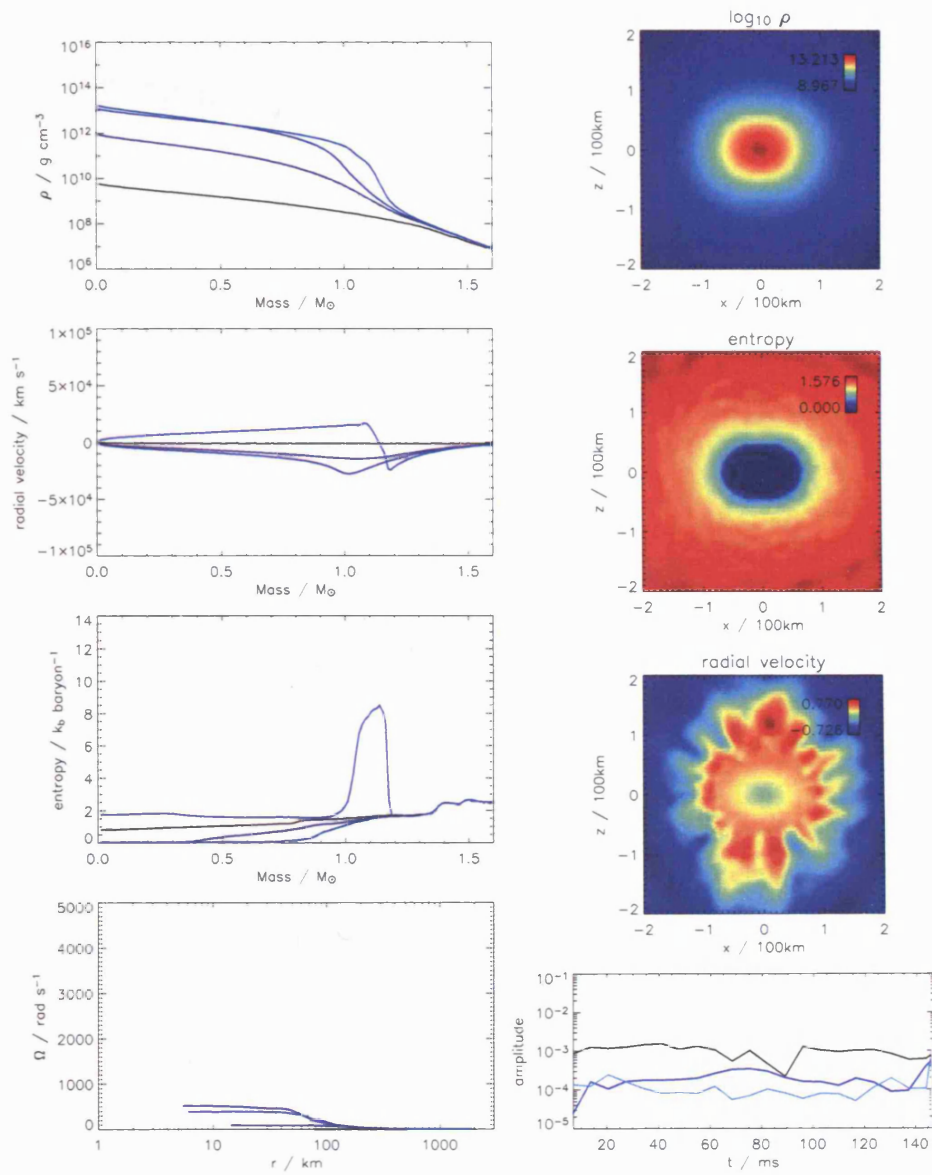


FIGURE 5.26. HEX run of model E15A. Density, radial velocity and entropy versus enclosed mass and angular velocity versus radius at  $t = 13.7, 130.4, 137.2$  and  $144.1$  ms are shown. Core bounce occurs at around  $140$  ms. Snapshots show the density and entropy at  $137.2$  ms and the radial velocity at  $144.1$  ms. The graph at the bottom right shows the displacement of the centre of mass (black) and the amplitudes of the dipole (blue) and quadrupole (cyan) moments.

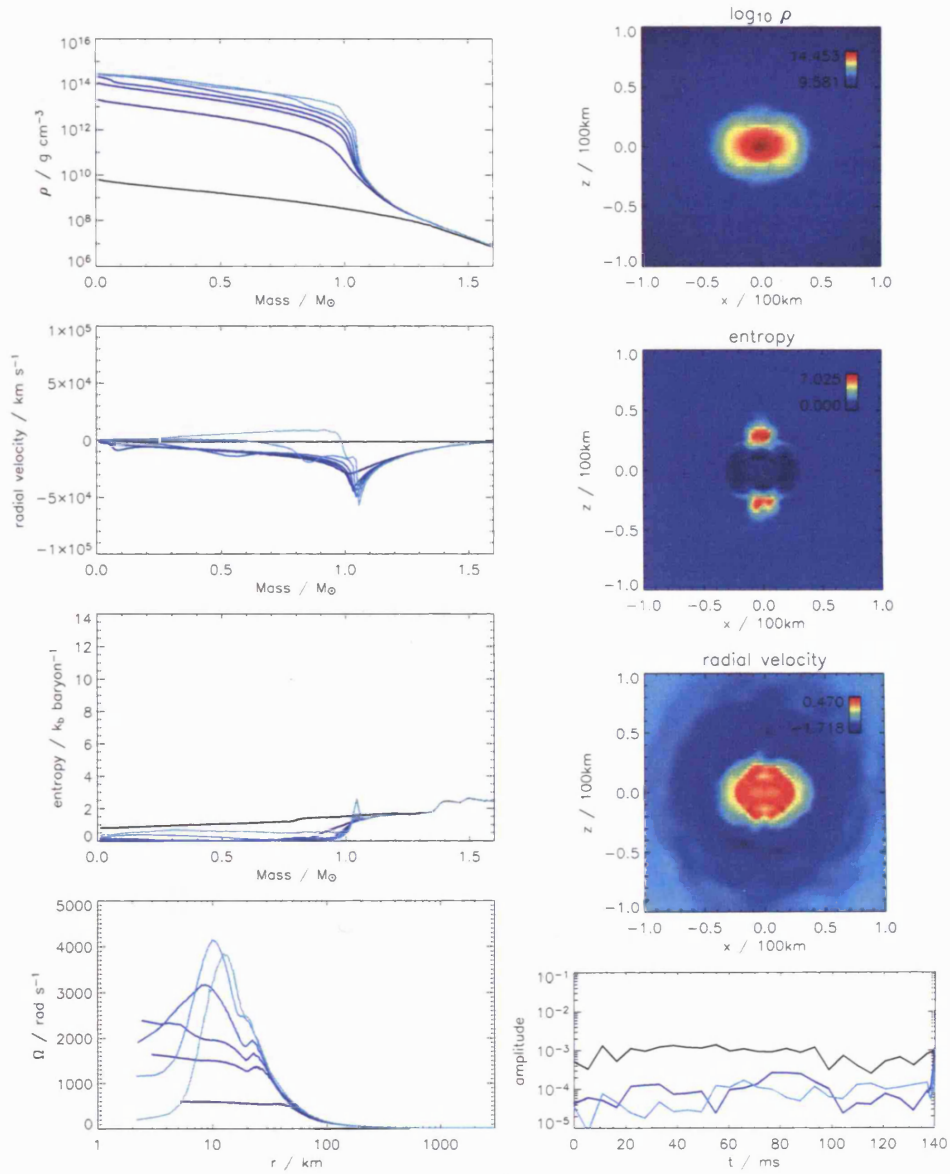


FIGURE 5.27. SRIF2 run of model E15A. Density, radial velocity and entropy versus enclosed mass and angular velocity versus radius at  $t = 22.0, 137.2, 138.6, 138.9, 139.1, 139.4$  and  $139.7$  ms are shown. Core bounce occurs at  $139.4$  ms. Snapshots show the density and entropy at bounce and the radial velocity at  $139.7$  ms. The graph at the bottom right shows the displacement of the centre of mass (black) and the amplitudes of the dipole (blue) and quadrupole (cyan) moments.

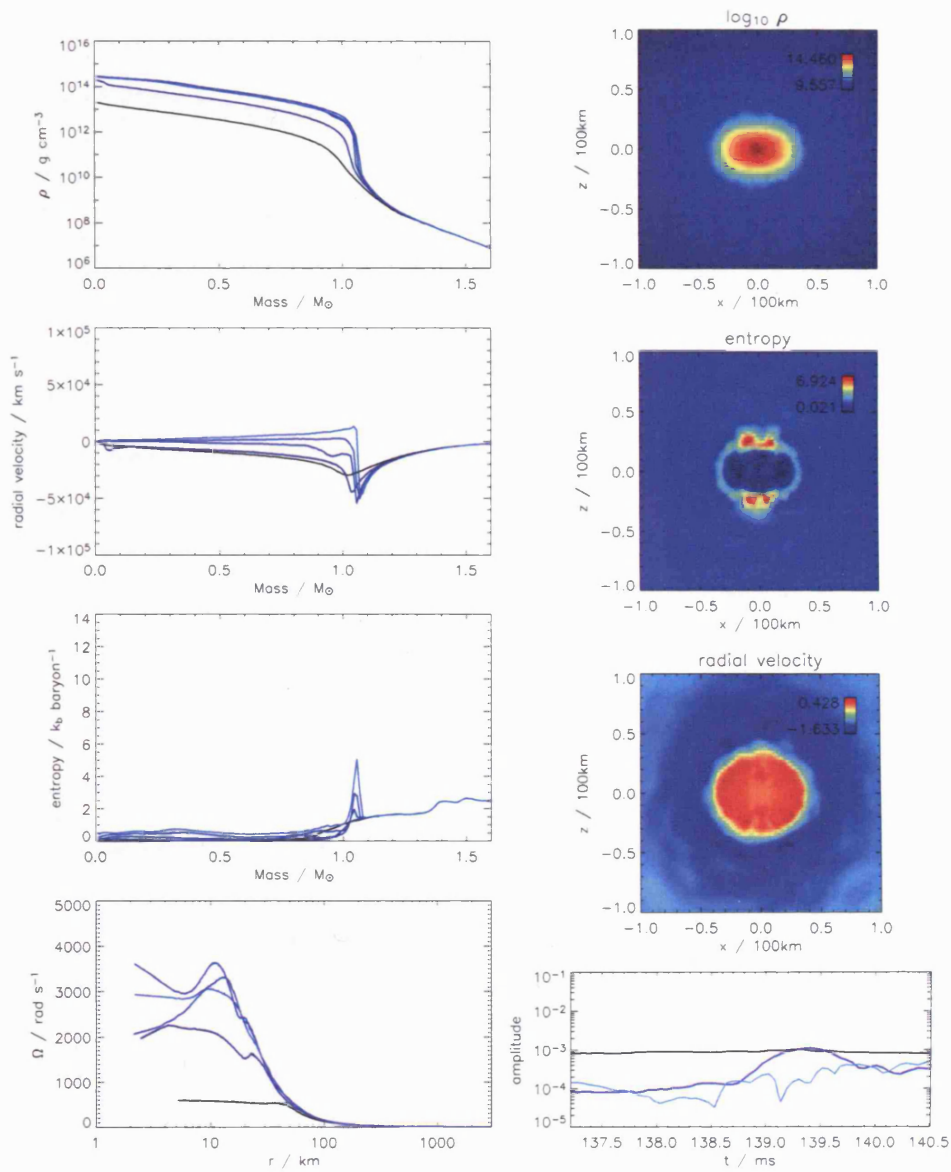


FIGURE 5.28. SRIF2 run of model E15Avisc, which had viscosity added at 137.2 ms. Density, radial velocity and entropy versus enclosed mass and angular velocity versus radius at  $t = 137.2, 138.9, 139.6, 139.9$  and  $140.1$  ms are shown. Core bounce occurs at 139.9 ms. Snapshots show the density and entropy at bounce and the radial velocity at 140.1 ms. The graph at the bottom right shows the displacement of the centre of mass (black) and the amplitudes of the dipole (blue) and quadrupole (cyan) moments.

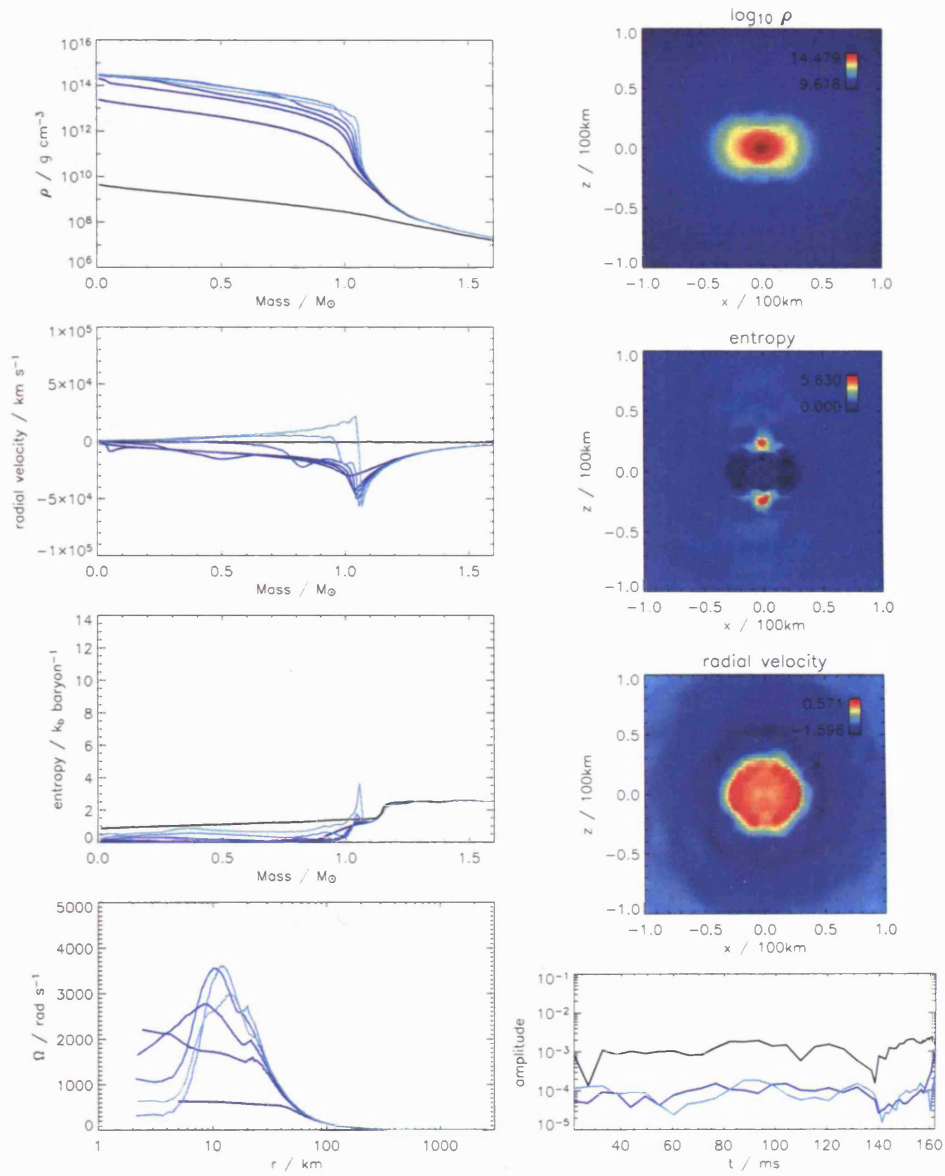


FIGURE 5.29. SRIF2 run of model E20A. Density, radial velocity and entropy versus enclosed mass and angular velocity versus radius at  $t = 22.0, 159.4, 160.8, 161.1, 161.4, 161.6$  and  $161.9$  ms are shown. Core bounce occurs at  $161.4$  ms. Snapshots show the density and entropy at bounce and the radial velocity at  $161.9$  ms. The graph at the bottom right shows the displacement of the centre of mass (black) and the amplitudes of the dipole (blue) and quadrupole (cyan) moments.

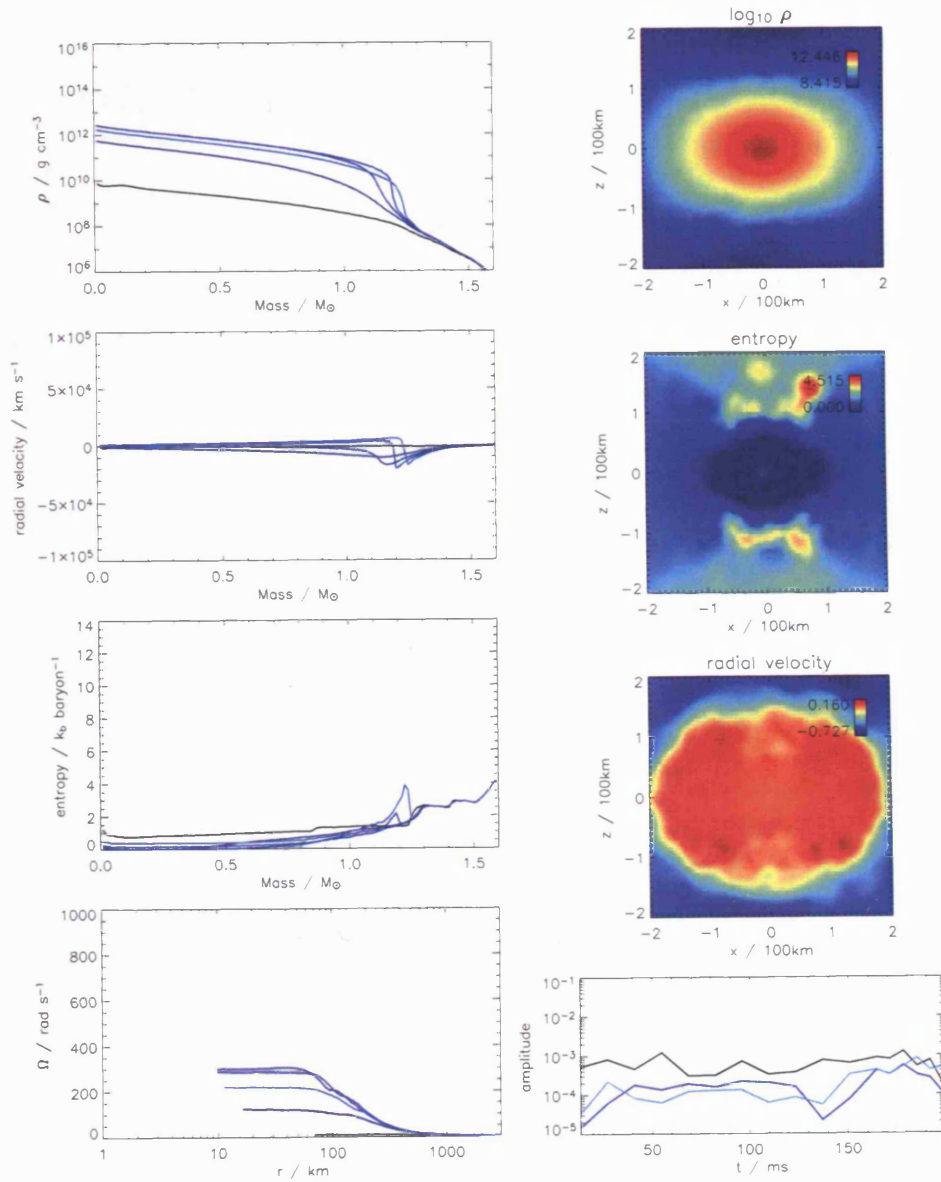


FIGURE 5.30. HEX run of model E15B. Density, radial velocity and entropy versus enclosed mass and angular velocity versus radius at  $t = 13.7, 150.9, 164.7, 171.5$  and  $178.4$  ms are shown. A centrifugal bounce occurs sometime between  $165$  and  $170$  ms. Snapshots show the density and entropy  $164.7$  ms and the radial velocity at  $171.5$  ms. The graph at the bottom right shows the displacement of the centre of mass (black) and the amplitudes of the dipole (blue) and quadrupole (cyan) moments.

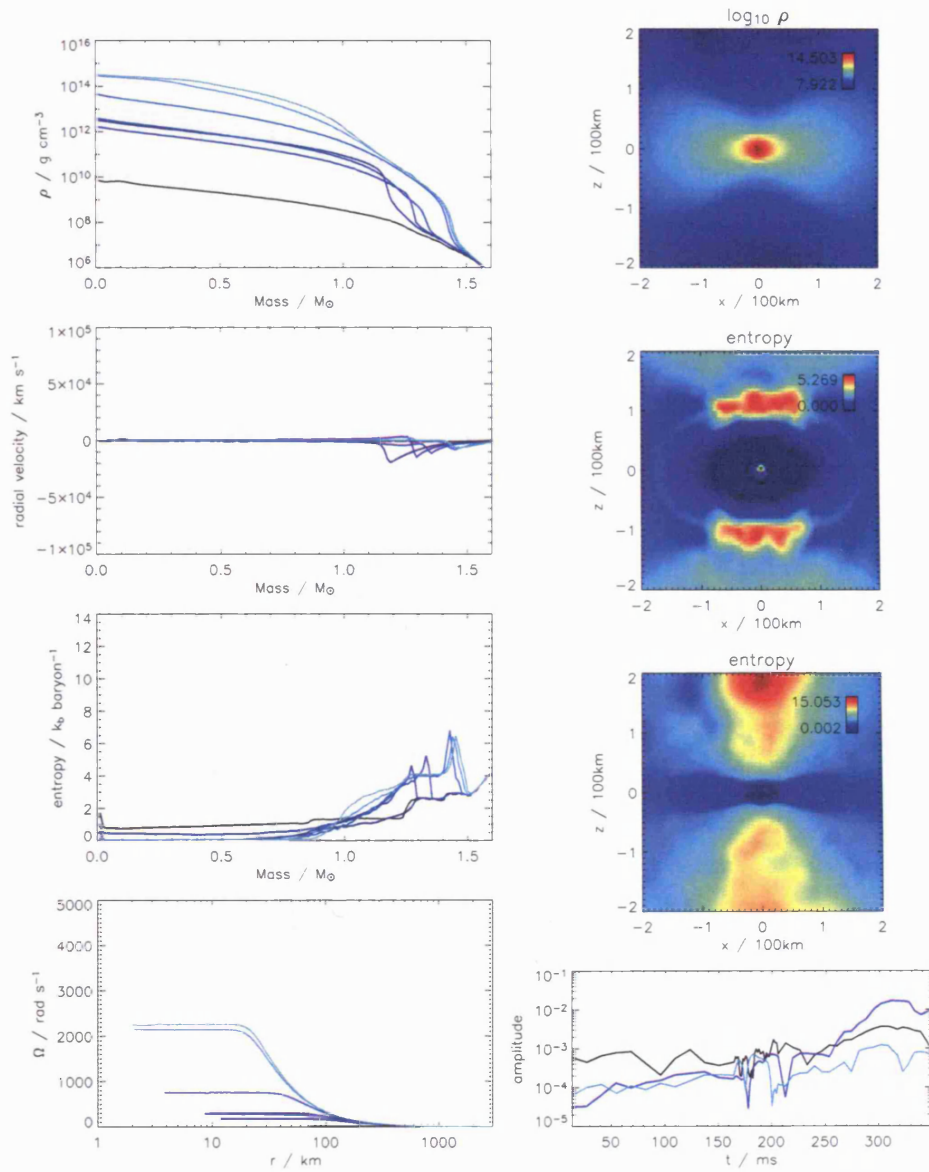


FIGURE 5.31. HEX run of model E15Bvisc, which had viscosity included with  $\alpha_{sph} = 5.0$ . Density, radial velocity and entropy versus enclosed mass and angular velocity versus radius at  $t = 13.7, 167.4, 188.0, 212.7, 308.7, 333.4$  and  $349.9$  ms are shown. A centrifugal bounce occurs around 167 ms and nuclear densities are reached by 310 ms. Snapshots show the density at 349.9 ms and the entropy at 167.4 and 349.9 ms. The graph at the bottom right shows the displacement of the centre of mass (black) and the amplitudes of the dipole (blue) and quadrupole (cyan) moments.

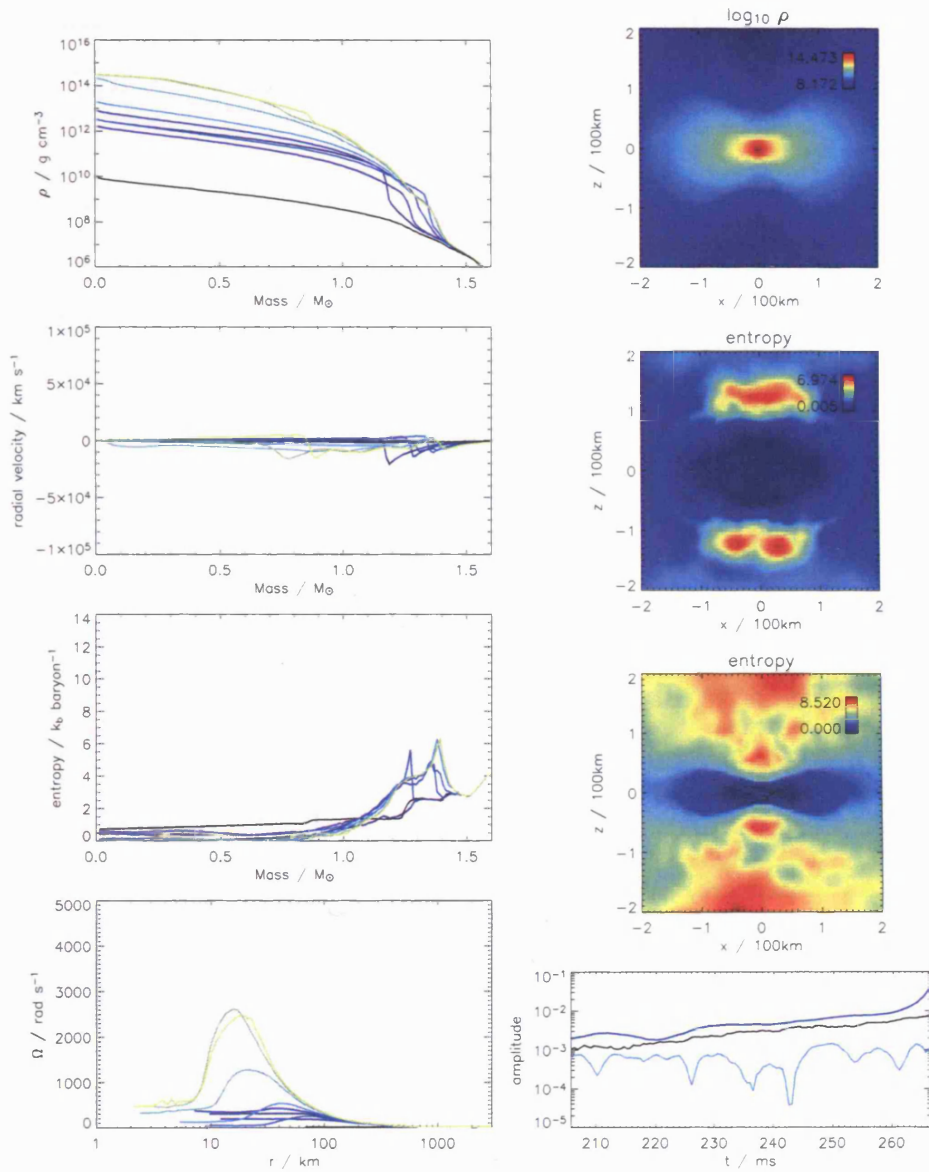


FIGURE 5.32. SRIF2 run of model E15B. Density, radial velocity and entropy versus enclosed mass and angular velocity versus radius at  $t = 22.0, 164.7, 183.9, 223.9, 244.2, 261.8, 265.8, 266.3$  and  $266.6$  ms are shown. A centrifugal bounce occurs at around 165 ms and nuclear densities are reached by 265 ms. Snapshots show the density at 266.3 ms and the entropy at 164.7 and 266.3 ms. The graph at the bottom right shows the displacement of the centre of mass (black) and the amplitudes of the dipole (blue) and quadrupole (cyan) moments.

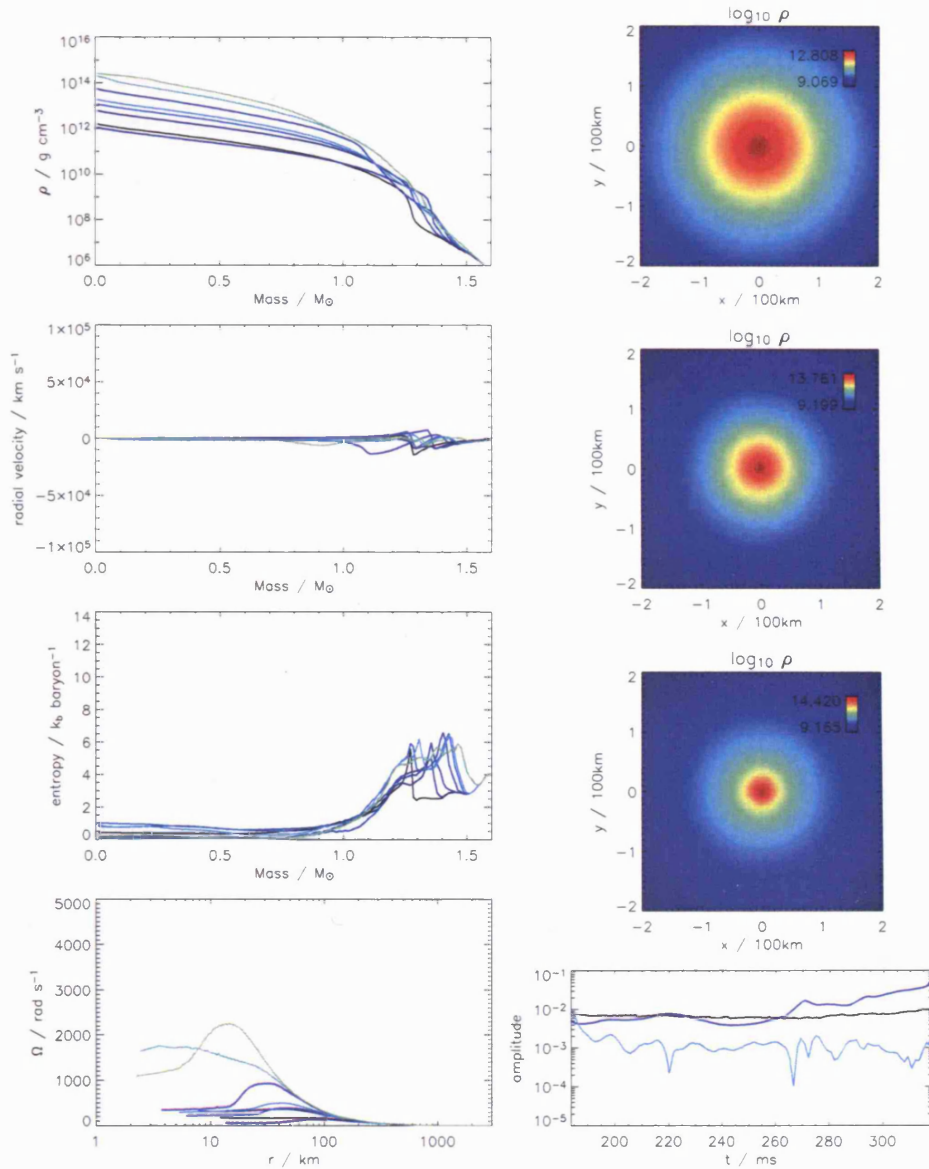


FIGURE 5.33. SRIF2 run of model E15B\_p, which had density perturbations added at 183.9 ms. Density, radial velocity and entropy versus enclosed mass and angular velocity versus radius at  $t = 183.9, 220.1, 246.4, 270.9, 283.2, 288.7, 316.4$  and  $317.5$  ms are shown. A second centrifugal bounce occurs at around 220 ms and nuclear densities are reached at around 316 ms. Snapshots show the density in the  $x$ - $y$  plane at 220.1, 270.9 and 317.5 ms. The graph at the bottom right shows the displacement of the centre of mass (black) and the amplitudes of the dipole (blue) and quadrupole (cyan) moments.

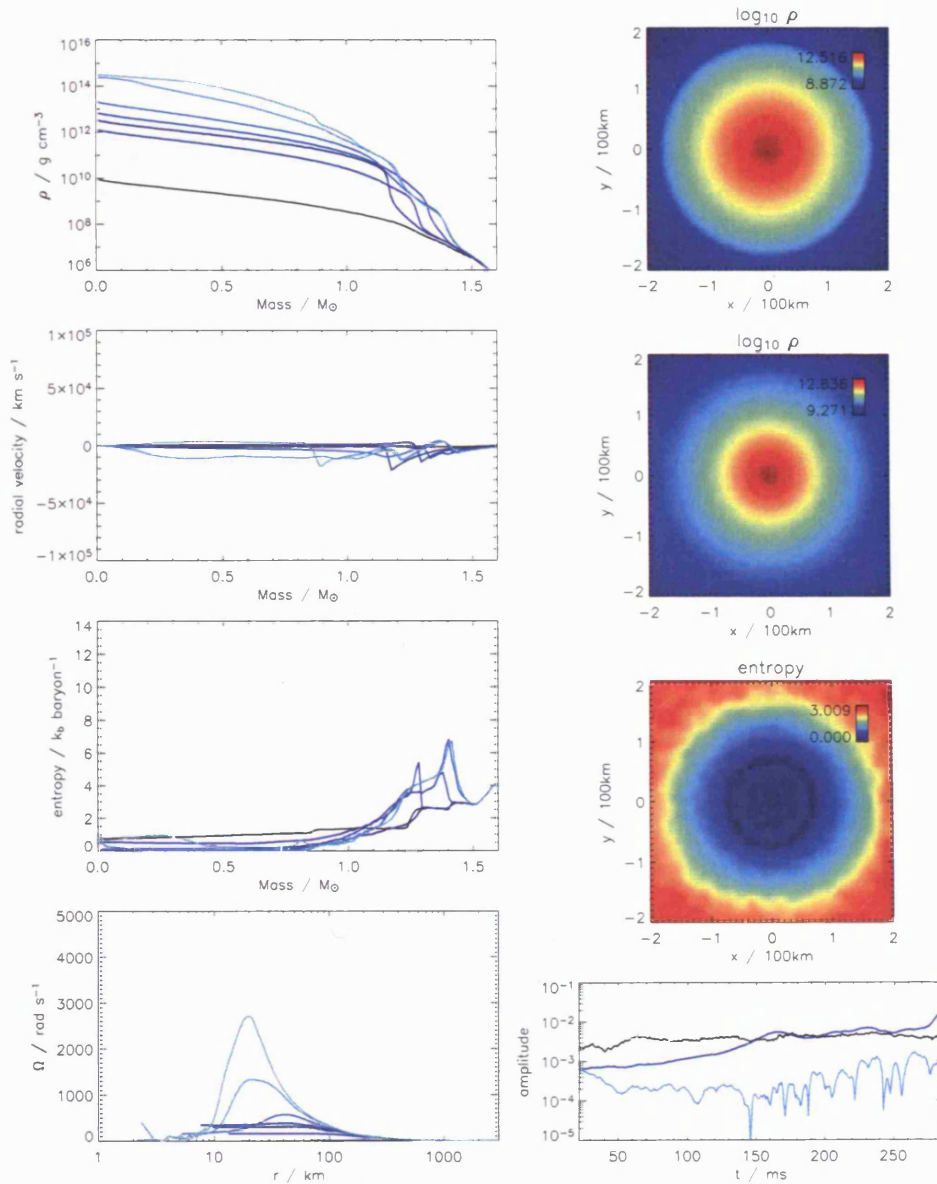


FIGURE 5.34. SRIF2 run of model pE15B, which had density perturbations added from the start. Density, radial velocity and entropy versus enclosed mass and angular velocity versus radius at  $t = 22.0, 163.6, 186.6, 236.3, 281.3, 285.4$  and  $286.2$  ms are shown. Centrifugal bounces occur at around  $163.5$  and  $236.5$  ms and nuclear densities are reached at around  $281$  ms. Snapshots show the density in the  $x$ - $y$  plane at  $163.6$  and  $236.3$  ms and the entropy at  $281.3$  ms. The graph at the bottom right shows the displacement of the centre of mass (black) and the amplitudes of the dipole (blue) and quadrupole (cyan) moments.

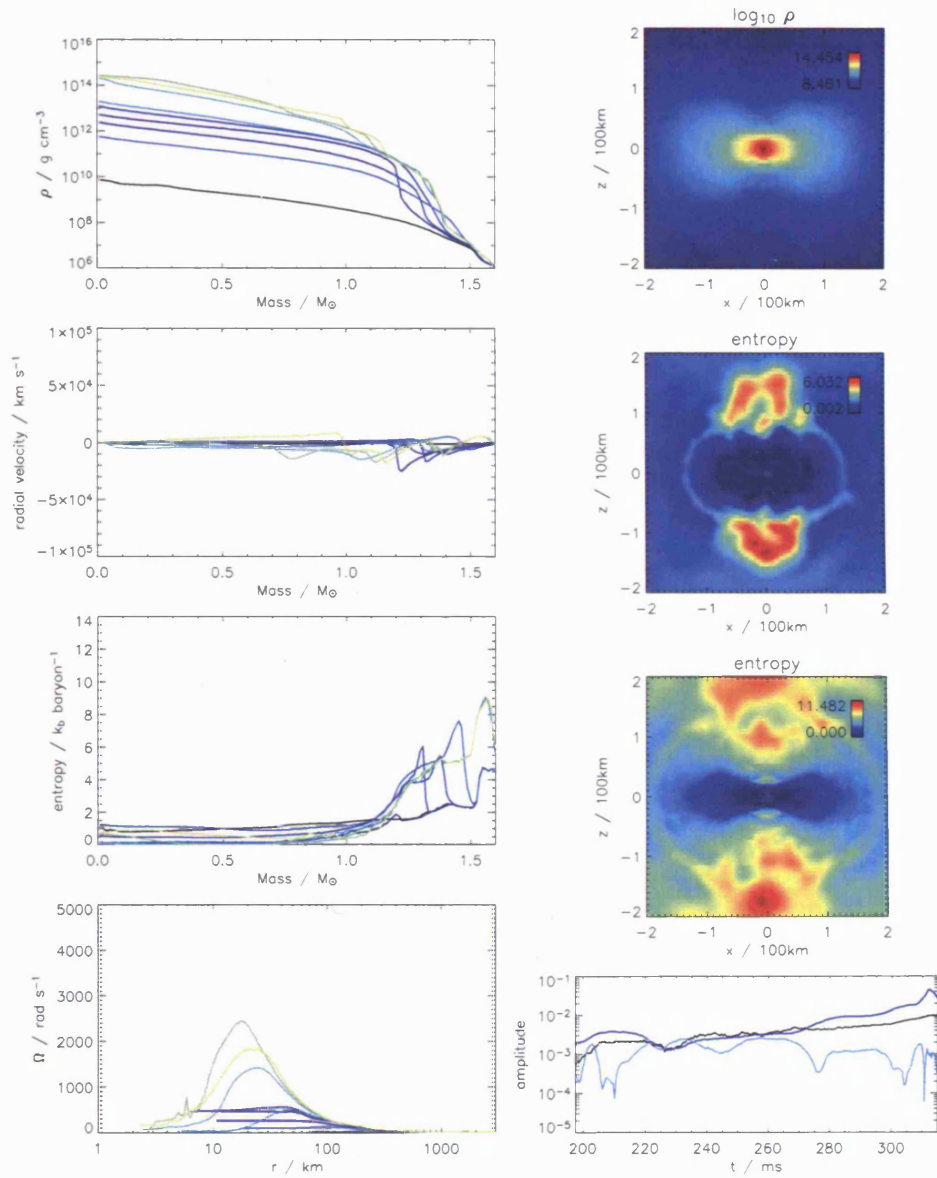


FIGURE 5.35. SRIF2 run of model E20B. Density, radial velocity and entropy versus enclosed mass and angular velocity versus radius at  $t = 22.0, 164.7, 179.8, 202.5, 243.1, 308.5, 311.2, 312.0$  and  $312.6$  ms are shown. A centrifugal bounce occurs at around 165 ms and nuclear densities are reached at around 311 ms. Snapshots show the density at 312.0 ms and the entropy at 164.7 and 312.0 ms. The graph at the bottom right shows the displacement of the centre of mass (black) and the amplitudes of the dipole (blue) and quadrupole (cyan) moments.

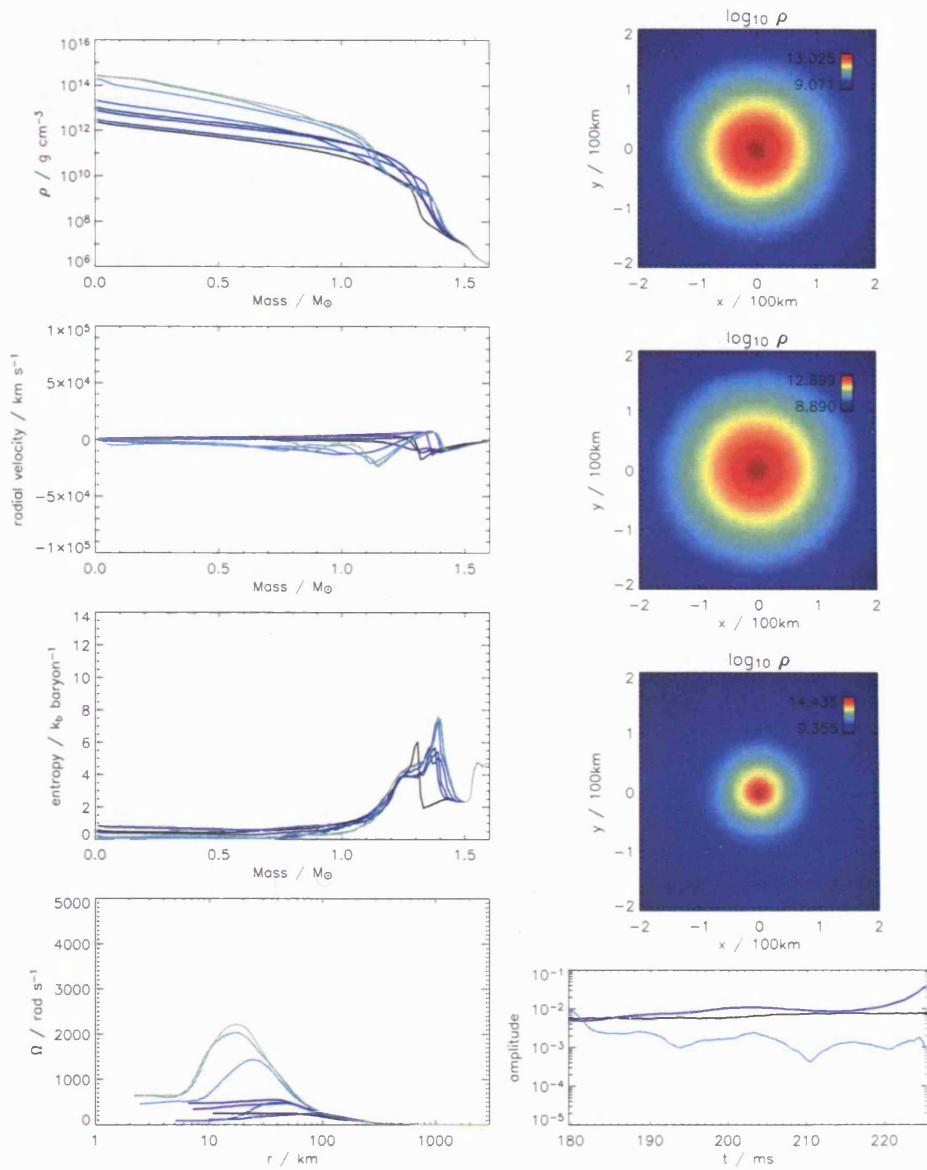


FIGURE 5.36. SRIF2 run of model E20B\_p, which had density perturbations added at 179.8 ms. Density, radial velocity and entropy versus enclosed mass and angular velocity versus radius at  $t = 179.8, 200.9, 205.3, 212.7, 222.0, 224.4, 225.1$  and  $225.4$  ms are shown. A second centrifugal bounce occurs at around 201 ms and nuclear densities are reached by 225 ms. Snapshots show the density in the  $x$ - $y$  plane at 200.9, 205.3 and 325.4 ms. The graph at the bottom right shows the displacement of the centre of mass (black) and the amplitudes of the dipole (blue) and quadrupole (cyan) moments.

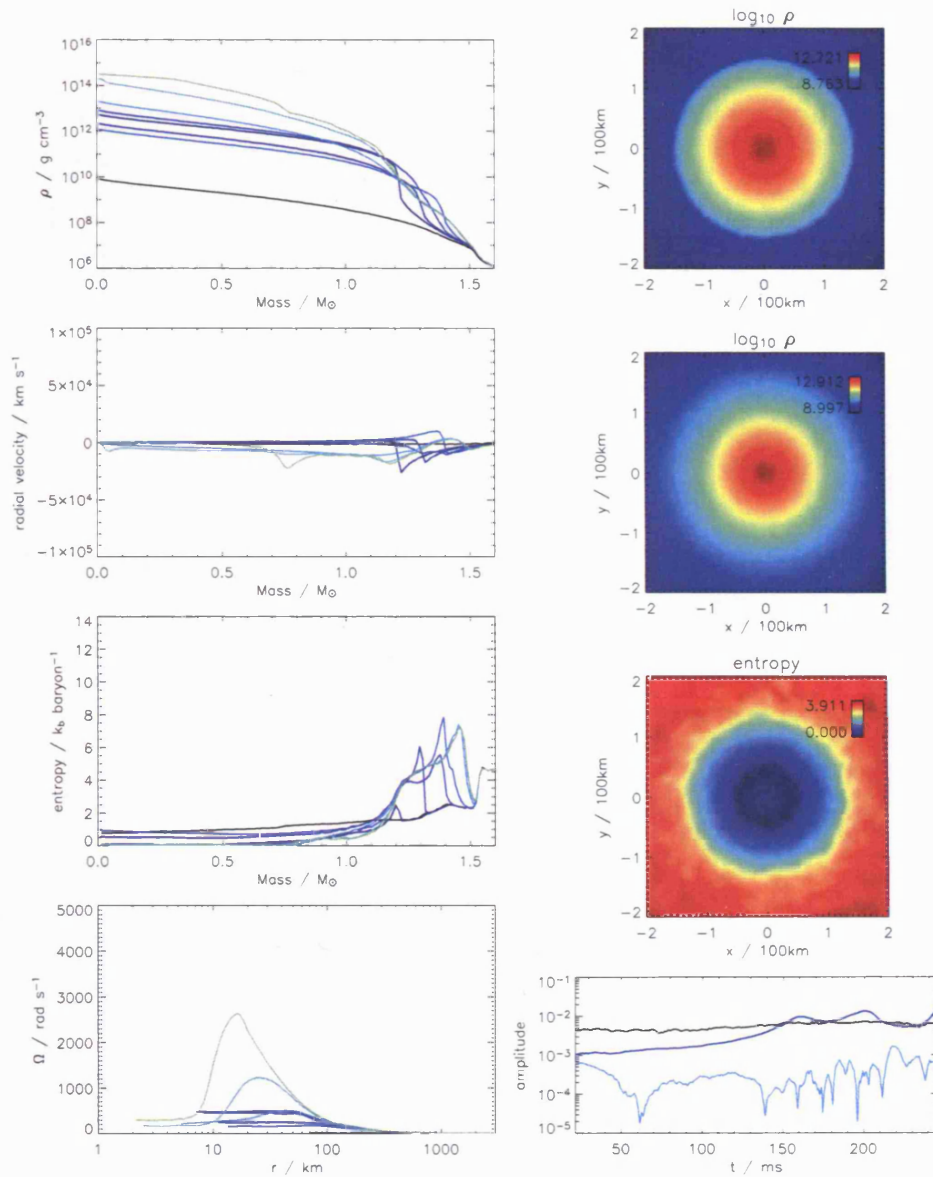


FIGURE 5.37. SRIF2 run of model pE15B, which had density perturbations added from the start. Density, radial velocity and entropy versus enclosed mass and angular velocity versus radius at  $t = 22.0, 161.4, 175.9, 199.5, 220.9, 242.9, 245.5$  and  $246.2$  are shown. Centrifugal bounces occur at around 161.4 and 199.5 ms and nuclear densities are reached at around 245.5 ms. Snapshots show the density in the  $x$ - $y$  plane at 161.4 and 199.5 ms and the entropy at 246.2 ms. The graph at the bottom right shows the displacement of the centre of mass (black) and the amplitudes of the dipole (blue) and quadrupole (cyan) moments.

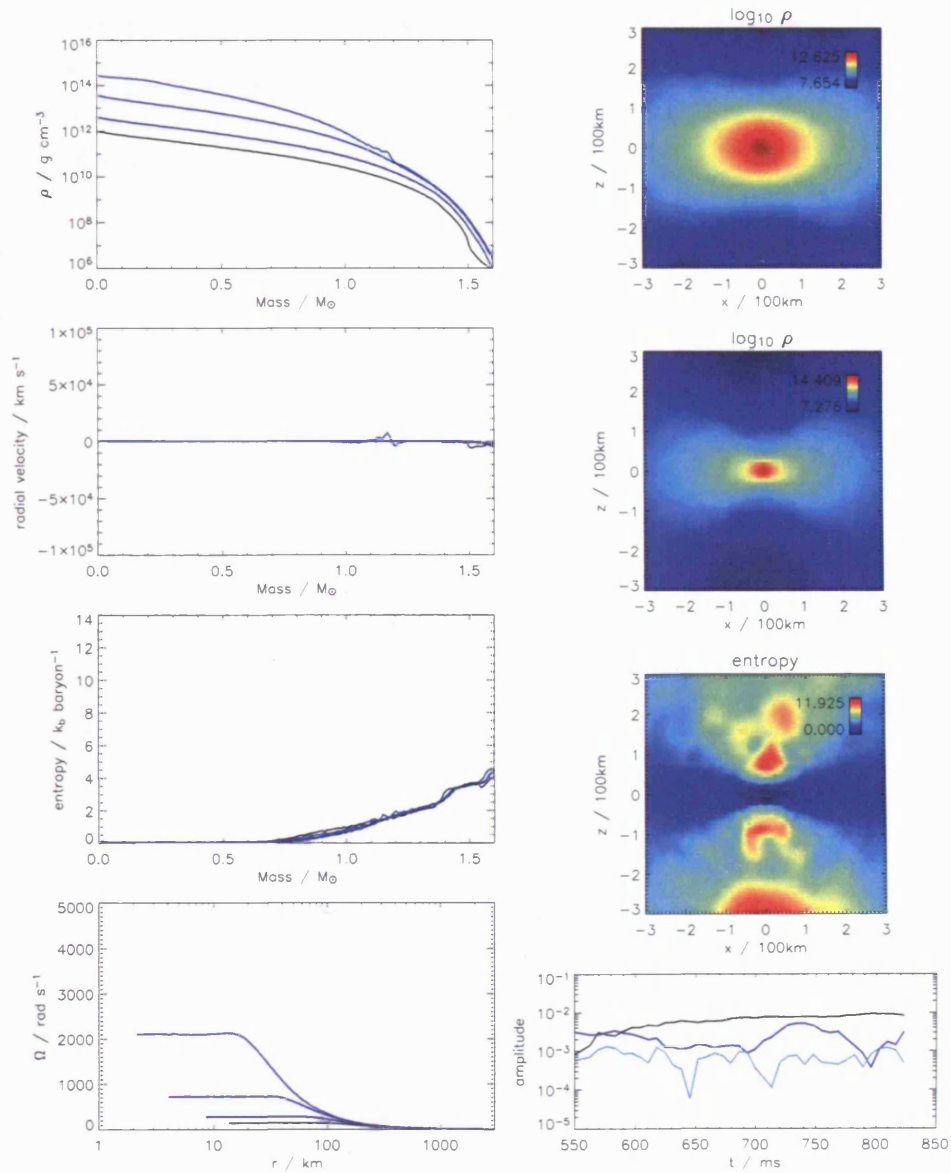


FIGURE 5.38. HEX run of model E15C. Density, radial velocity and entropy versus enclosed mass and angular velocity versus radius at  $t = 548.9, 761.5, 912.5$  and  $946.8$  ms are shown. Nuclear densities are reached by 760 ms. Snapshots show the density at 946.8 ms and the entropy at 761.5 and 946.8 ms. The graph at the bottom right shows the displacement of the centre of mass (black) and the amplitudes of the dipole (blue) and quadrupole (cyan) moments.

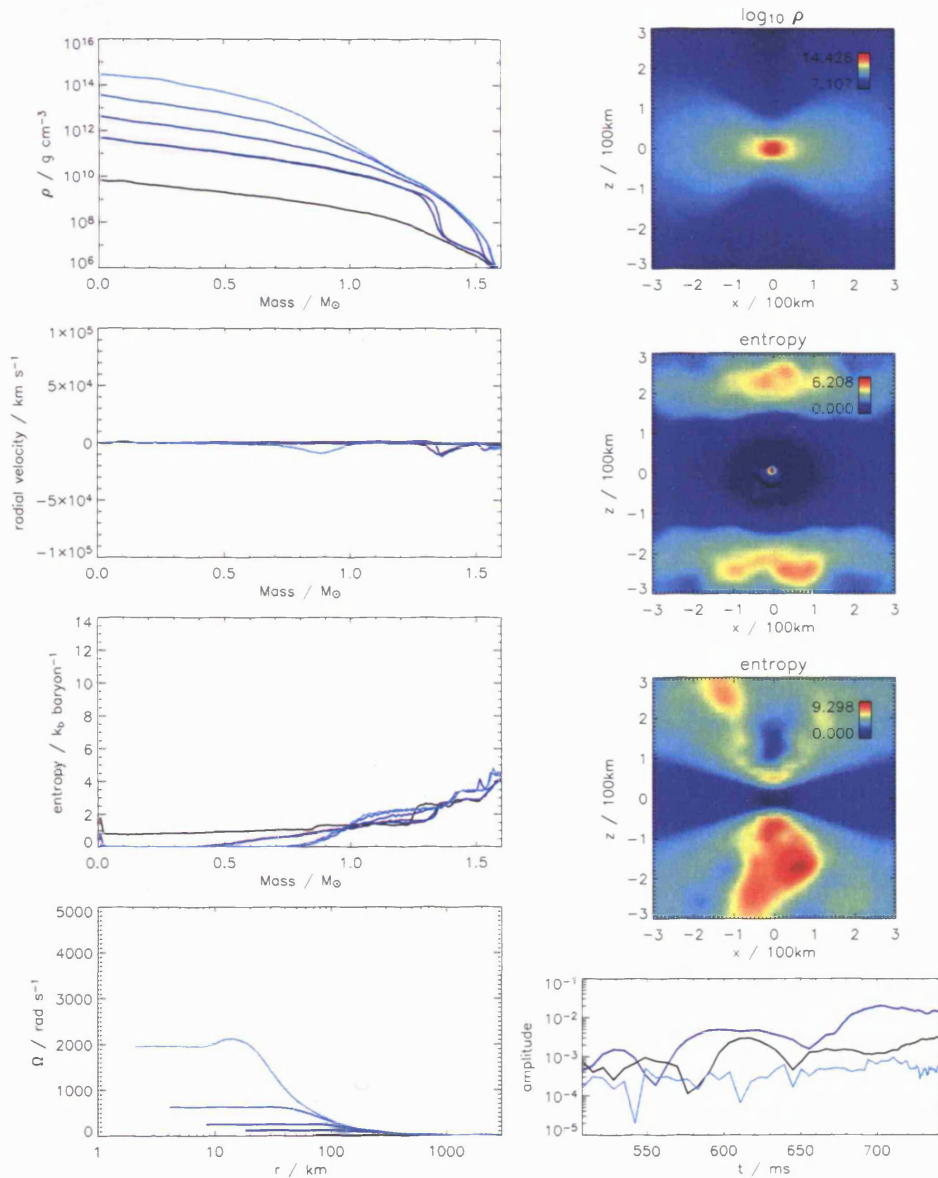


FIGURE 5.39. HEX run of model E15Cvisc, which had viscosity included with  $\alpha_{sph} = 5.0$ . Density, radial velocity and entropy versus enclosed mass and angular velocity versus radius at  $t = 13.72, 288.2, 301.9, 555.7, 661.4,$  and  $683.3$  ms are shown. A centrifugal bounce occurs at around 288 ms and nuclear densities are reached at around 665 ms. Snapshots show the density at 683.3 ms and the entropy at 288.2 and 683.3 ms. The graph at the bottom right shows the displacement of the centre of mass (black) and the amplitudes of the dipole (blue) and quadrupole (cyan) moments.

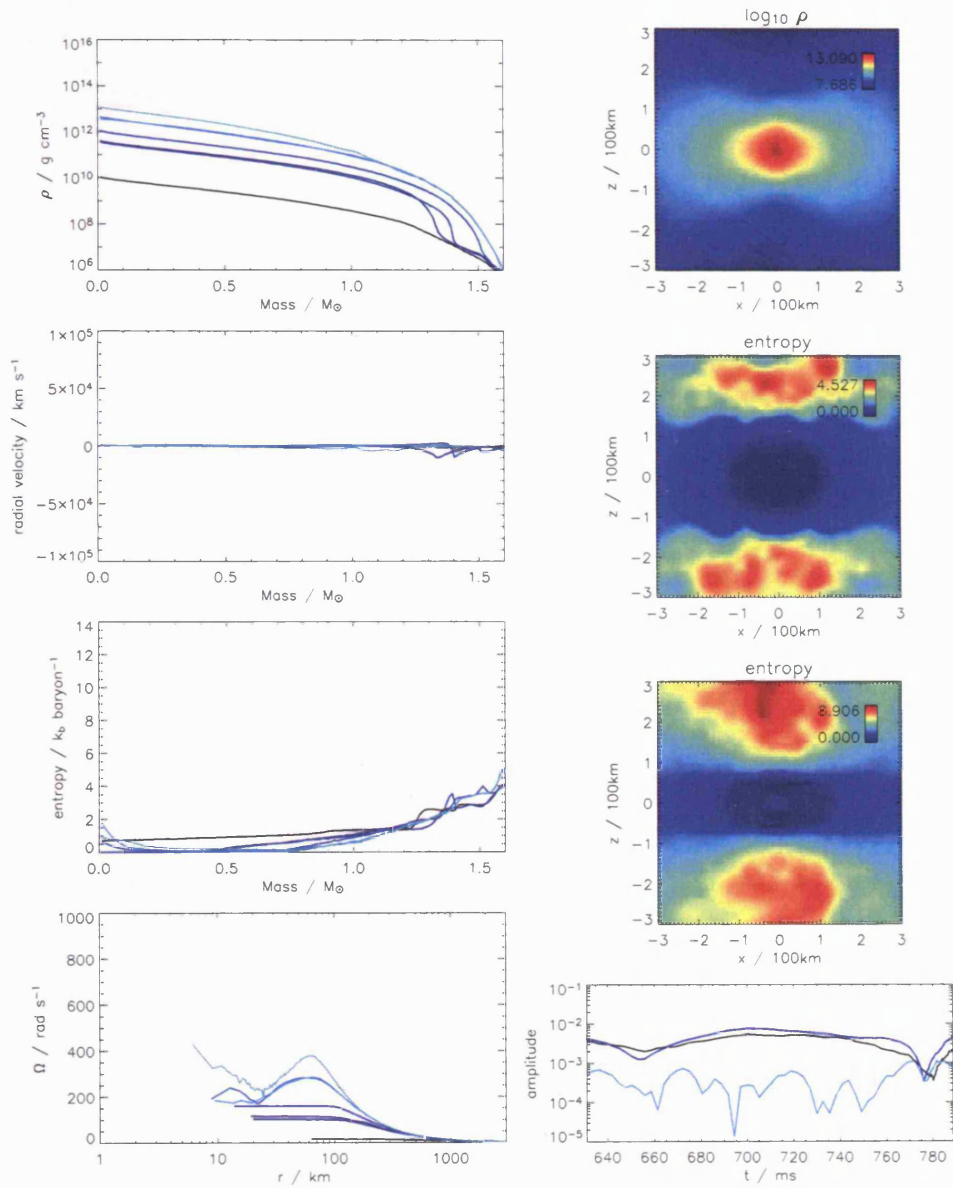


FIGURE 5.40. SRIF2 run of model E15C. Density, radial velocity and entropy versus enclosed mass and angular velocity versus radius at  $t = 54.89, 274.4, 329.3, 548.9, 775.0, 777.7,$  and  $788.7$  ms are shown. Centrifugal bounces occur at around 274 and 775 ms. Snapshots show the density at 777.7 ms, when the simulation was ended, and the entropy at 274.4 and 775.0 ms. The graph at the bottom right shows the displacement of the centre of mass (black) and the amplitudes of the dipole (blue) and quadrupole (cyan) moments.

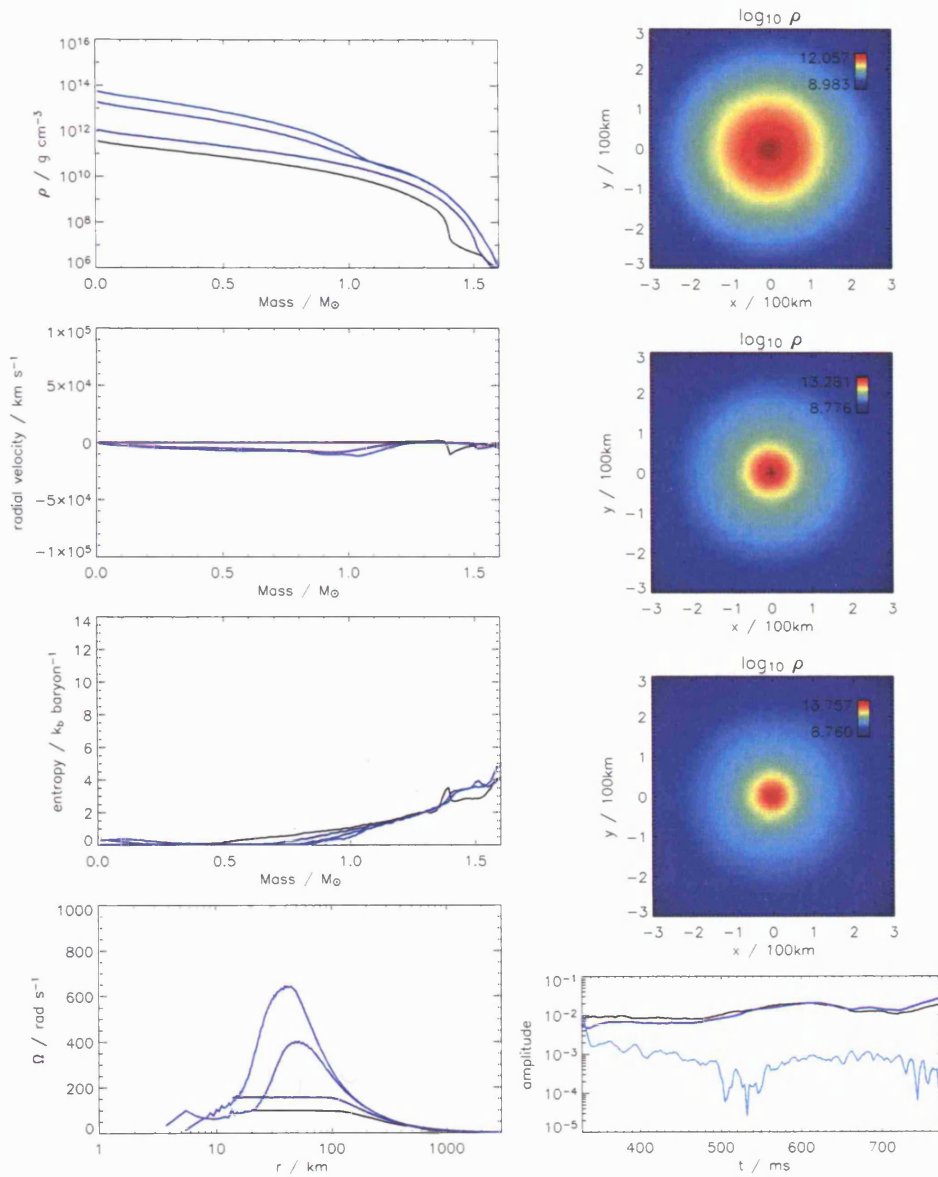


FIGURE 5.41. SRIF2 run of model E15C\_p, which had density perturbations added at 329.3 ms. Density, radial velocity and entropy versus enclosed mass and angular velocity versus radius at  $t = 329.3, 548.9, 776.6$  and  $778.6$  ms are shown. The model does not undergo a second centrifugal bounce or reach nuclear density by the end of the simulation. Snapshots show the density in the  $x$ - $y$  plane at 548.9, 776.6 and 778.6 ms. The graph at the bottom right shows the displacement of the centre of mass (black) and the amplitudes of the dipole (blue) and quadrupole (cyan) moments.

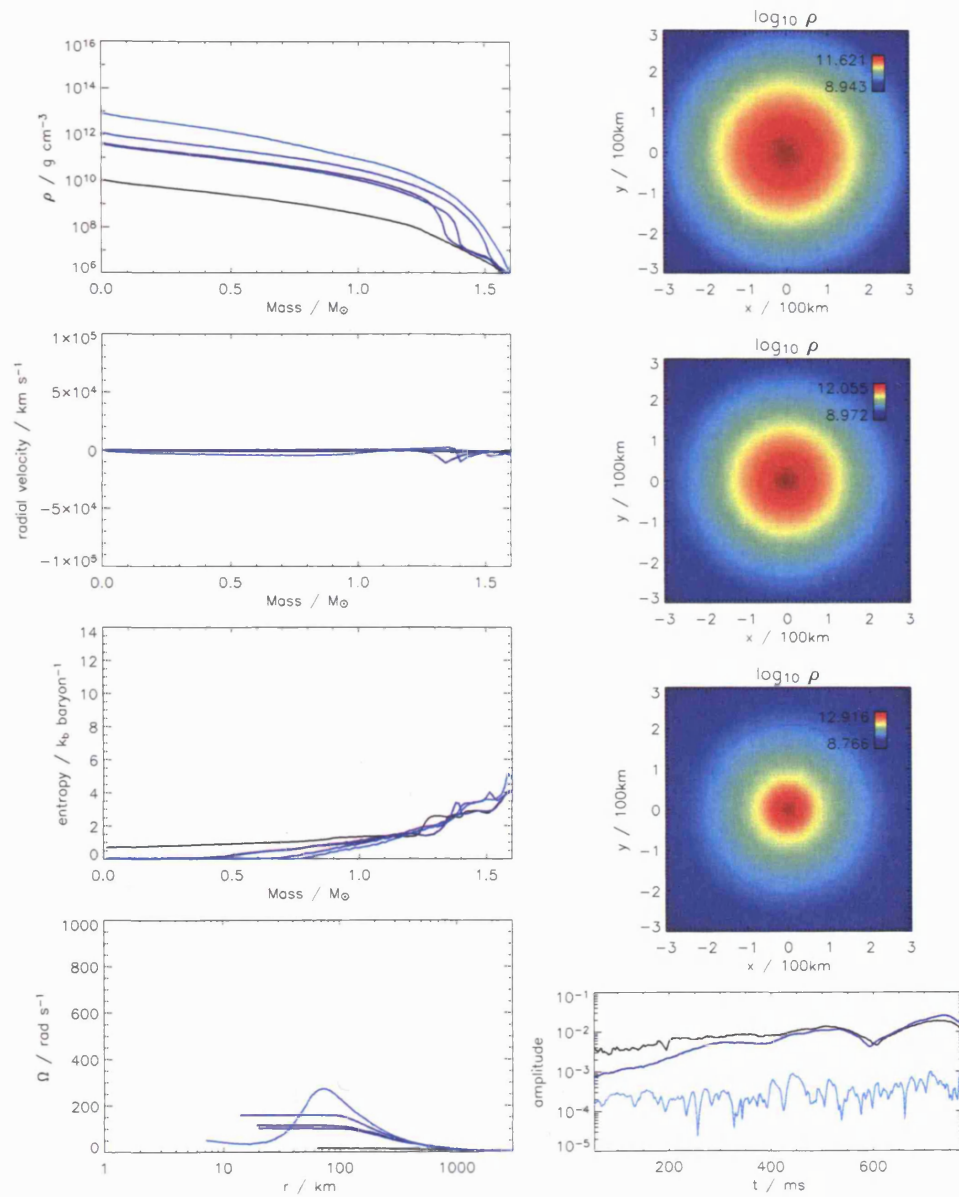


FIGURE 5.42. SRIF2 run of model pE15C, which had density perturbations added from the start. Density, radial velocity and entropy versus enclosed mass and angular velocity versus radius at  $t = 54.89, 279.9, 326.6, 548.9$  and  $776.1$  ms are shown. A centrifugal bounce occurs at around 280 ms. Snapshots show the density in the  $x$ - $y$  plane at 279.9, 548.9 and 776.1 ms. The graph at the bottom right shows the displacement of the centre of mass (black) and the amplitudes of the dipole (blue) and quadrupole (cyan) moments.

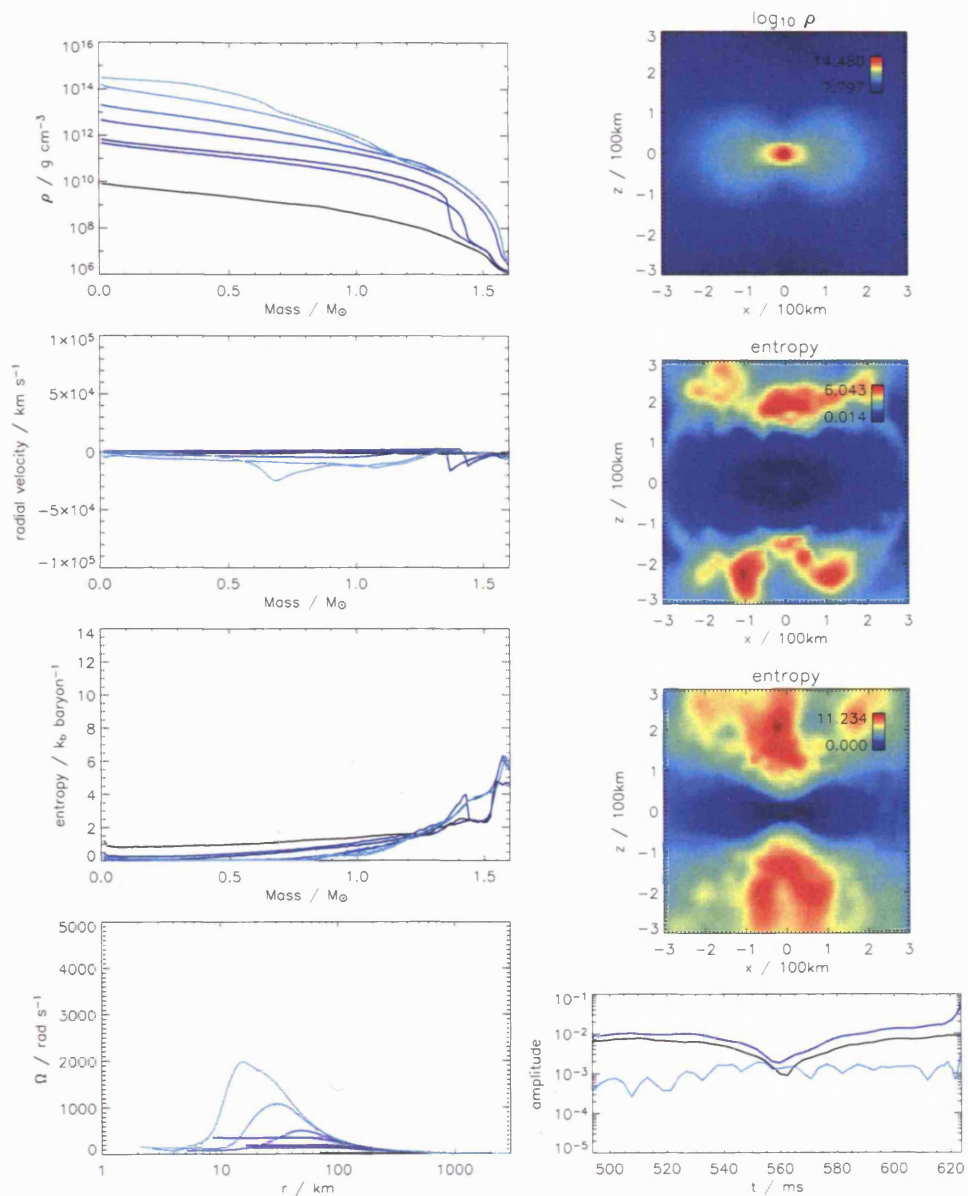


FIGURE 5.43. SRIF2 run of model E20C. Density, radial velocity and entropy versus enclosed mass and angular velocity versus radius at  $t = 54.89, 247.0, 274.4, 548.9, 620.8, 623.2$  and  $623.8$  ms are shown. Centrifugal bounces occur at around 247 and 616 ms and nuclear density is reached at around 623 ms. Snapshots show the density at 623.8 ms and the entropy at 247.0 and 623.8 ms. The graph at the bottom right shows the displacement of the centre of mass (black) and the amplitudes of the dipole (blue) and quadrupole (cyan) moments. Model E20C run on SRIF2

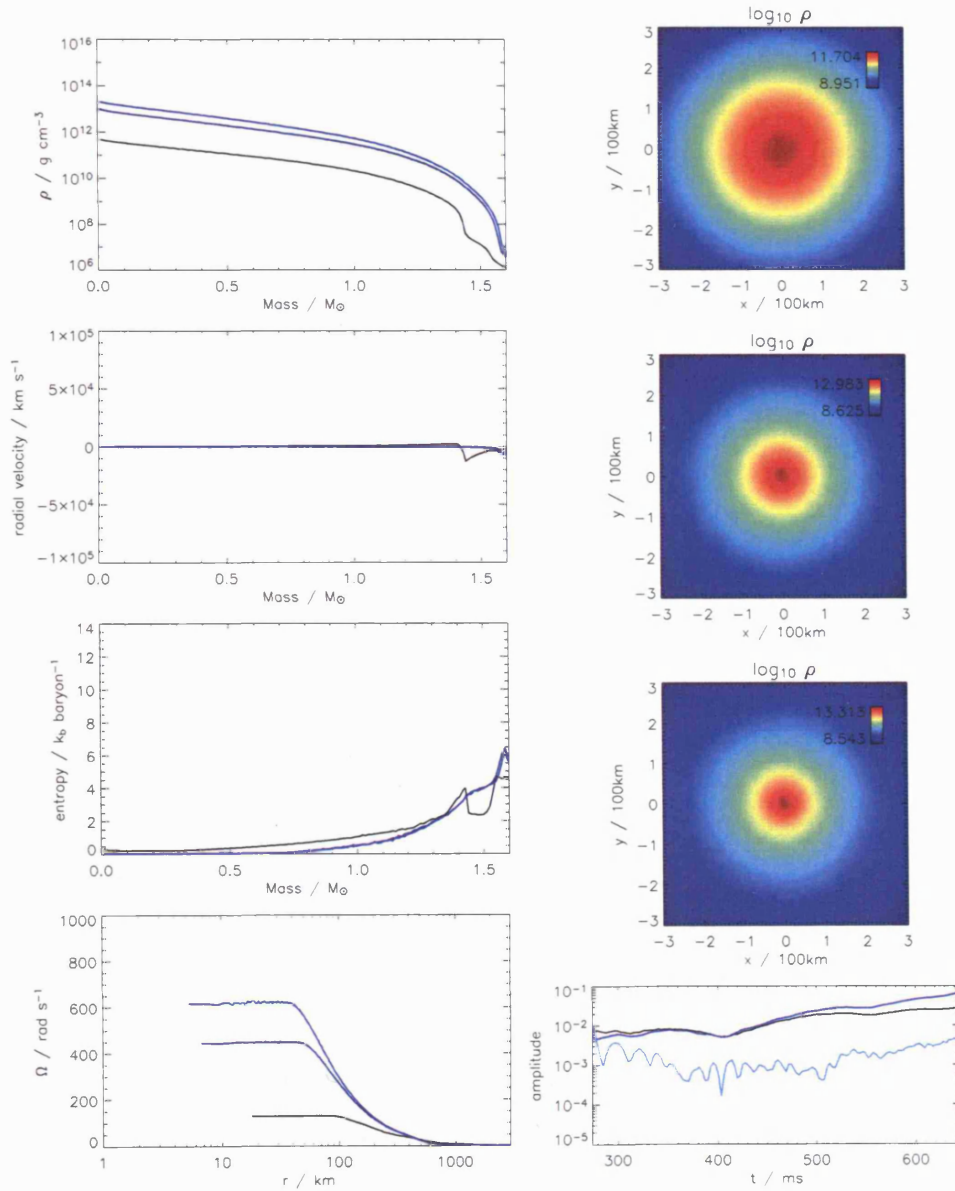


FIGURE 5.44. SRIF2 run of model E20C\_p, which had density perturbations added at 274.4 ms. Density, radial velocity and entropy versus enclosed mass and angular velocity versus radius at  $t = 274.4$ , 603.7 and 647.7 ms are shown. Snapshots show the density in the  $x$ - $y$  plane at these times. The model reaches a peak in  $\beta$  at 603.7 ms but does not undergo a second centrifugal bounce or reach nuclear density by the end of the simulation. The graph at the bottom right shows the displacement of the centre of mass (black) and the amplitudes of the dipole (blue) and quadrupole (cyan) moments.

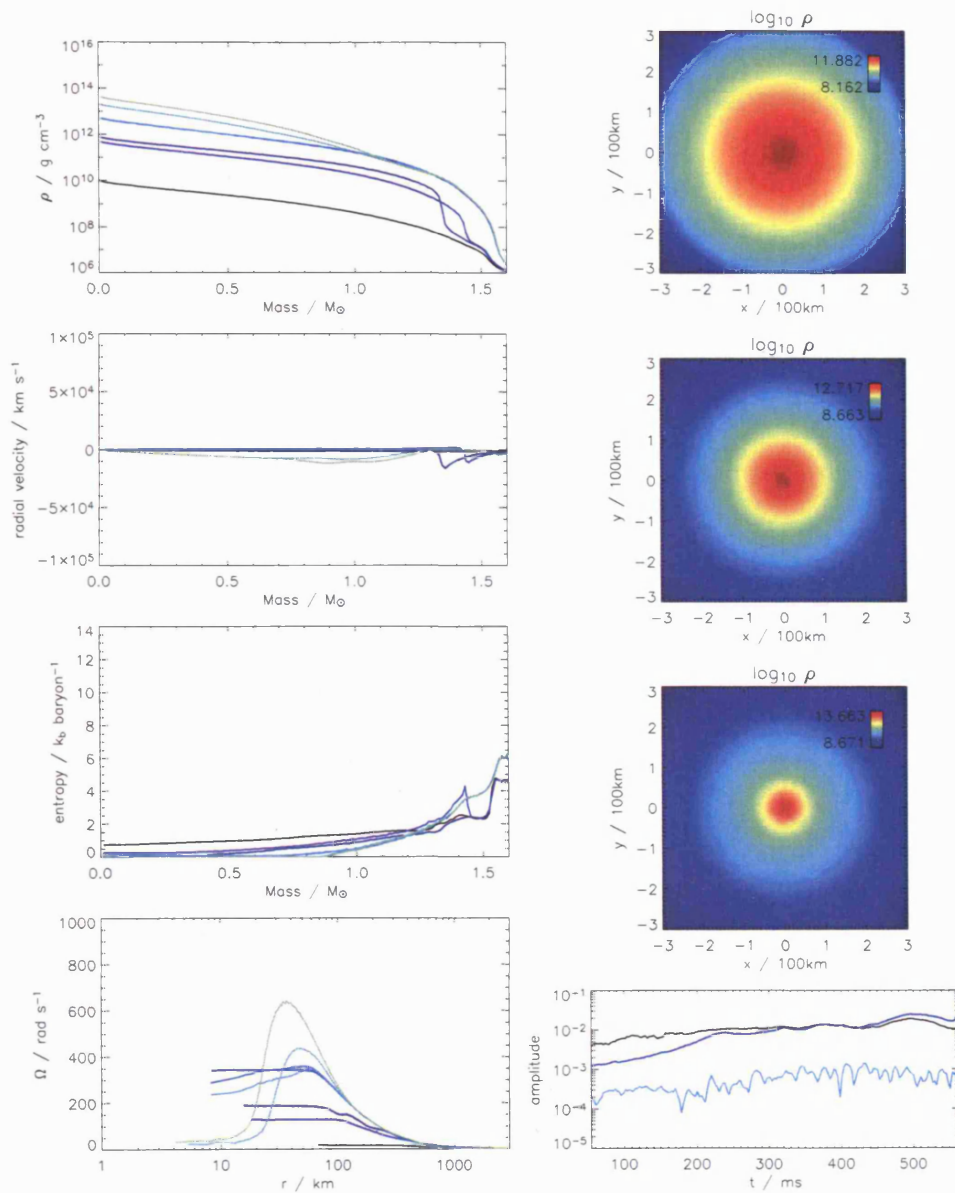


FIGURE 5.45. SRIF2 run of model pE20C, which had density perturbations added from the start. Density, radial velocity and entropy versus enclosed mass and angular velocity versus radius at  $t = 54.89, 233.3, 271.7, 548.9, 554.3, 556.3, 562.9$  and  $564.0$  ms are shown. Centrifugal bounces occur at around 233 and 554 ms. Snapshots show the density in the  $x$ - $y$  plane at 233.3, 554.3 and 564.0 ms. The graph at the bottom right shows the displacement of the centre of mass (black) and the amplitudes of the dipole (blue) and quadrupole (cyan) moments.

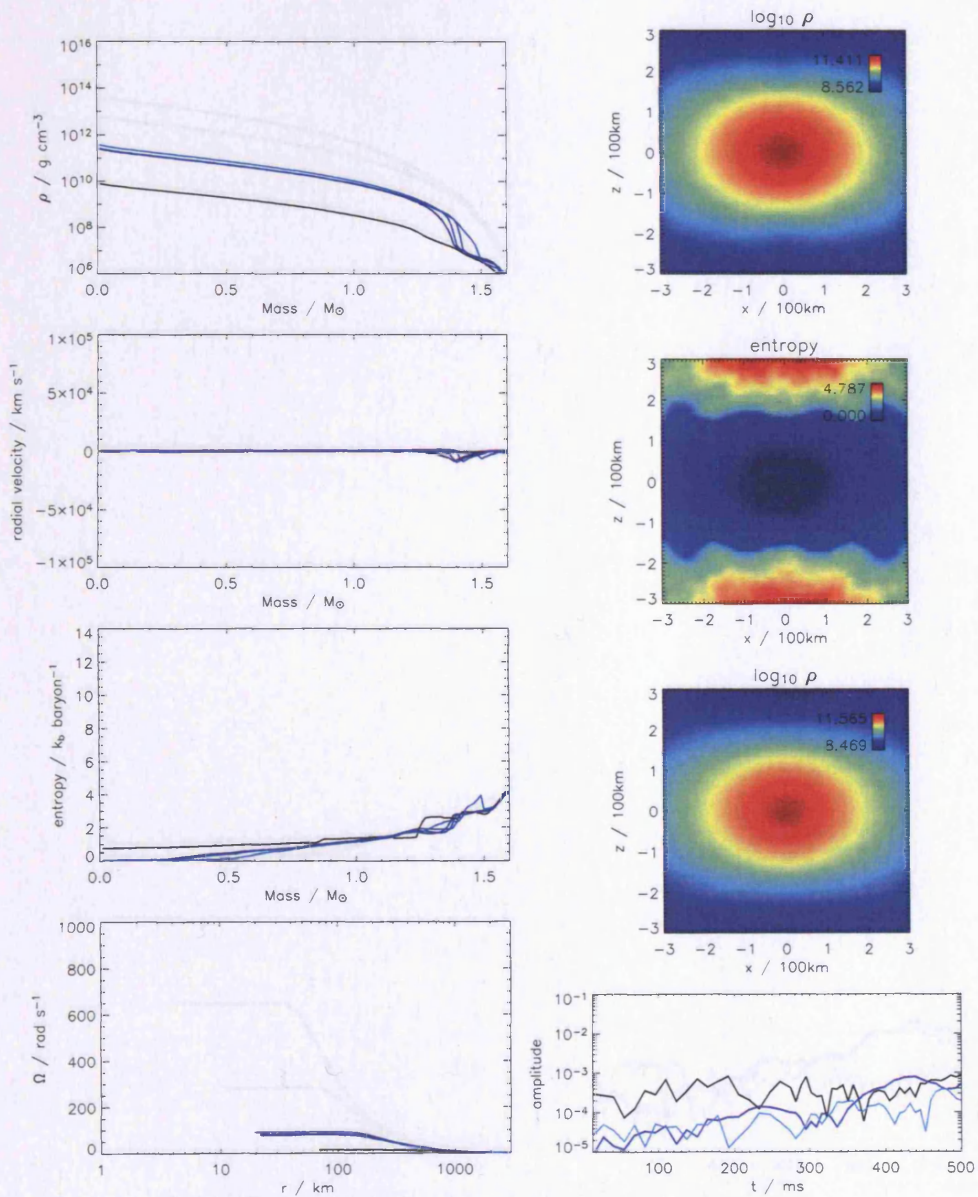


FIGURE 5.46. UKAFF run of model E15D. Density, radial velocity and entropy versus enclosed mass and angular velocity versus radius at  $t = 13.72, 343.0, 363.6, 391.0$  and  $500.8$  ms are shown. A centrifugal bounce occurs at around 364 ms. Snapshots show the density at 363.6 and 500.8 ms and the entropy at 363.6 ms. The graph at the bottom right shows the displacement of the centre of mass (black) and the amplitudes of the dipole (blue) and quadrupole (cyan) moments.

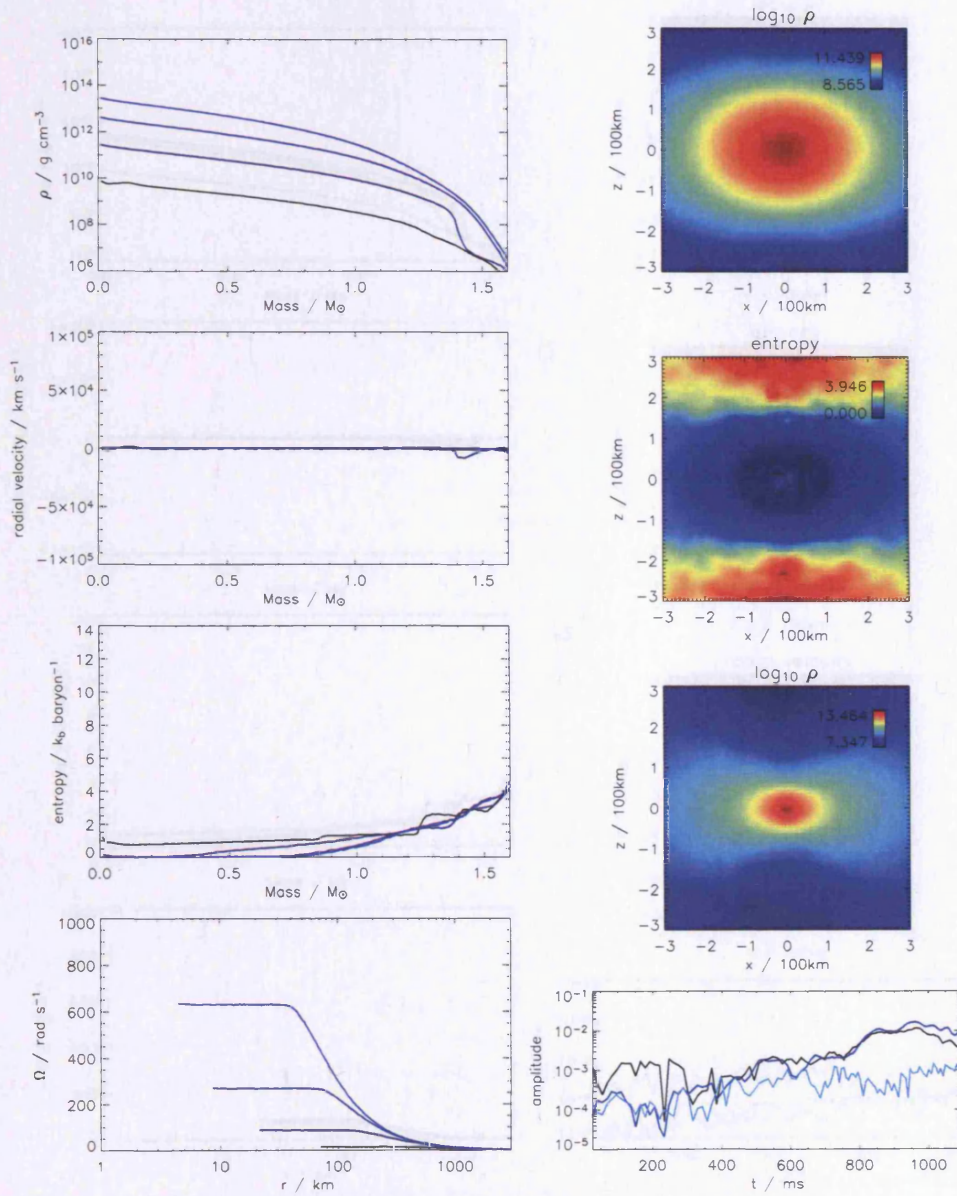


FIGURE 5.47. HEX run of model E15D. Density, radial velocity and entropy versus enclosed mass and angular velocity versus radius at  $t = 13.72, 411.6, 953.6, 391.0$  and  $1098$  ms are shown. A centrifugal bounce occurs at around  $412$  ms. Snapshots show the density at  $411.6$  and  $1097$  ms and the entropy at  $411.6$  ms. The graph at the bottom right shows the displacement of the centre of mass (black) and the amplitudes of the dipole (blue) and quadrupole (cyan) moments.

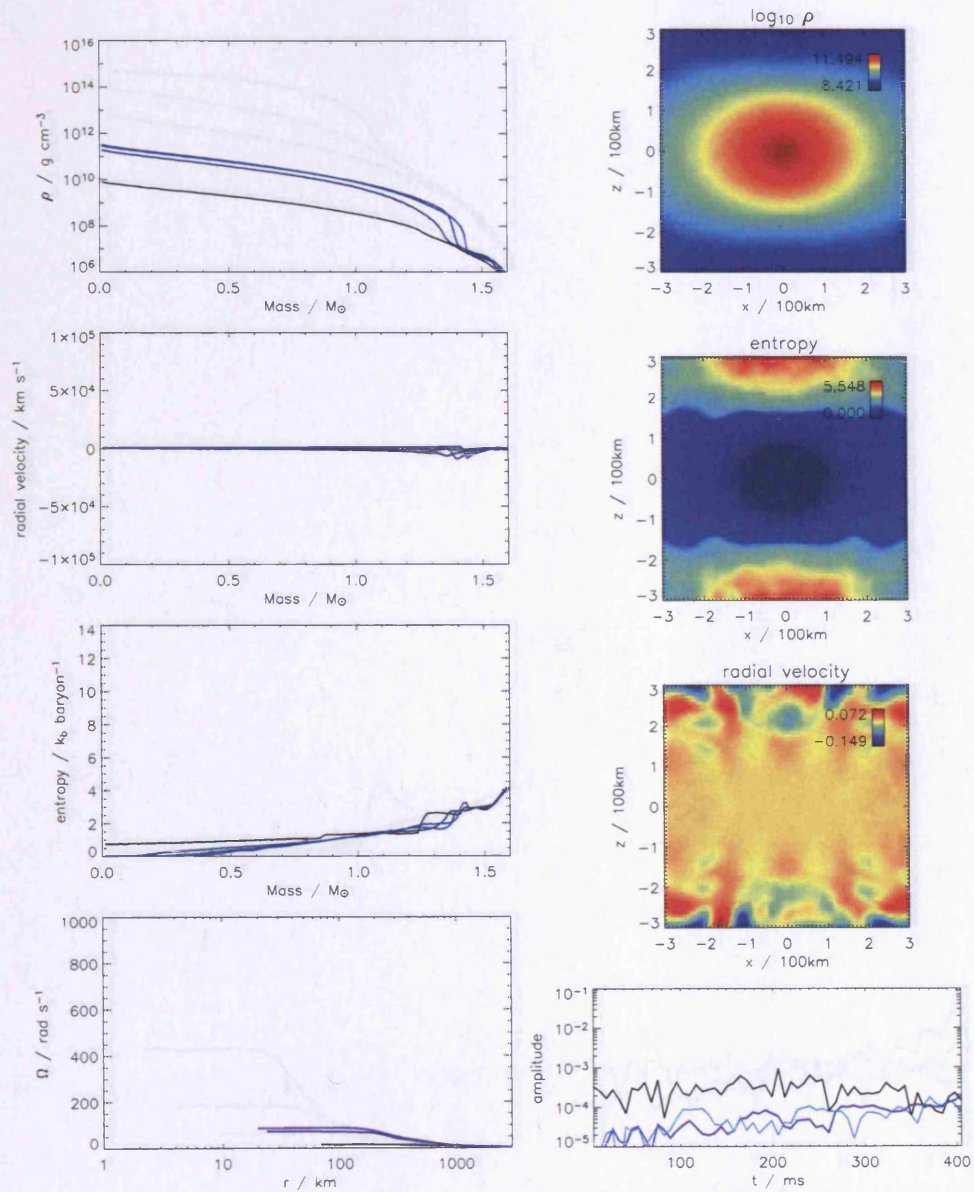


FIGURE 5.48. UKAFF run of model E15Dvisc, which had viscosity included with  $\alpha_{sph} = 2.0$ . Density, radial velocity and entropy versus enclosed mass and angular velocity versus radius at  $t = 13.72, 295.0, 356.8$  and  $404.8$  ms are shown. A centrifugal bounce occurs at around  $357$  ms. Snapshots show the density, entropy and radial velocity at  $356.8$  ms. The graph at the bottom right shows the displacement of the centre of mass (black) and the amplitudes of the dipole (blue) and quadrupole (cyan) moments.

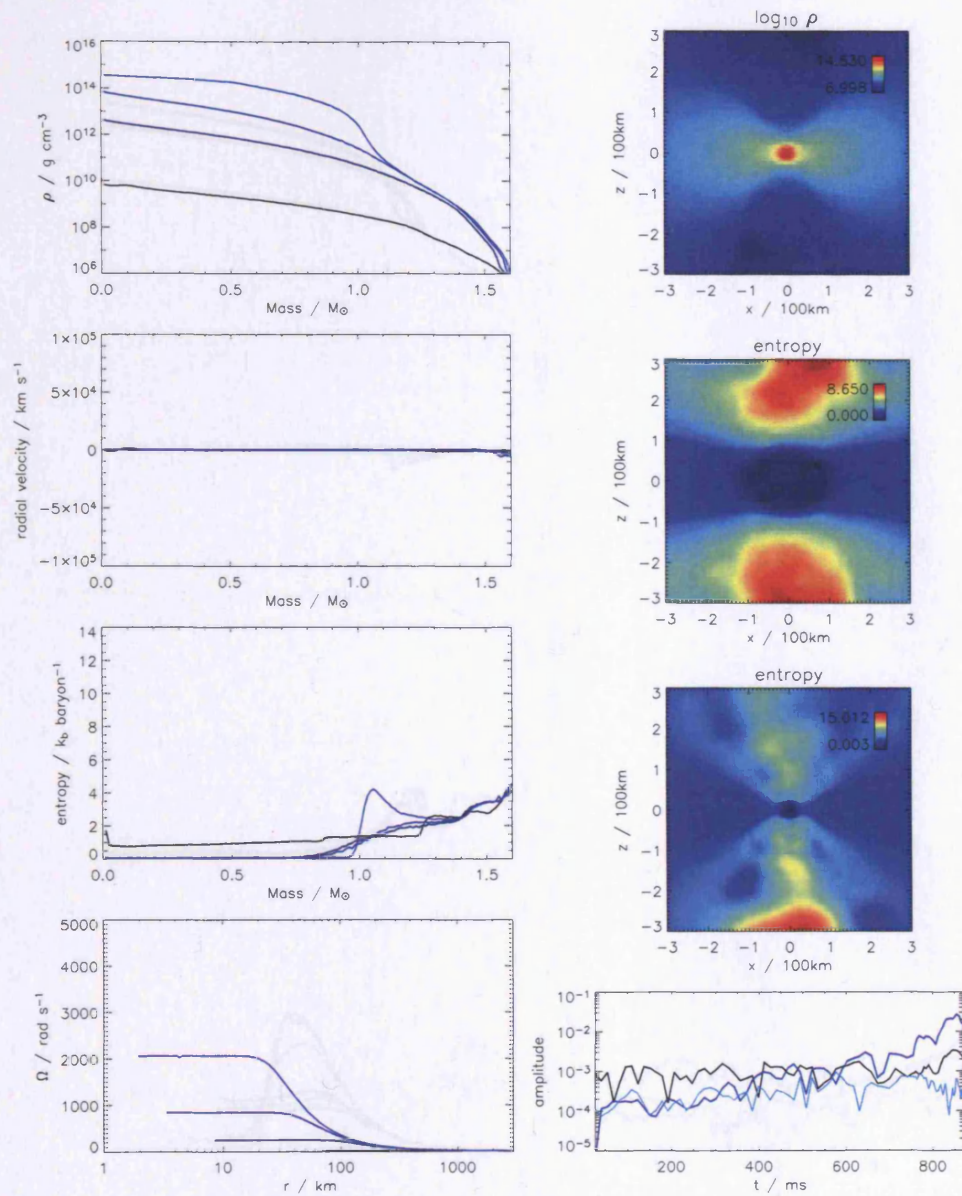


FIGURE 5.49. HEX run of model E15Dvisc, which had viscosity included with  $\alpha_{sph} = 5.0$ . Density, radial velocity and entropy versus enclosed mass and angular velocity versus radius at  $t = 13.72, 686.1, 801.3$  and  $869.9$  ms are shown. The model does not undergo centrifugal bounce, but the collapse plateaus off briefly at around 360 ms. Snapshots show the density at 869.9 ms and the entropy at 686.1 and 869.9 ms. The graph at the bottom right shows the displacement of the centre of mass (black) and the amplitudes of the dipole (blue) and quadrupole (cyan) moments.

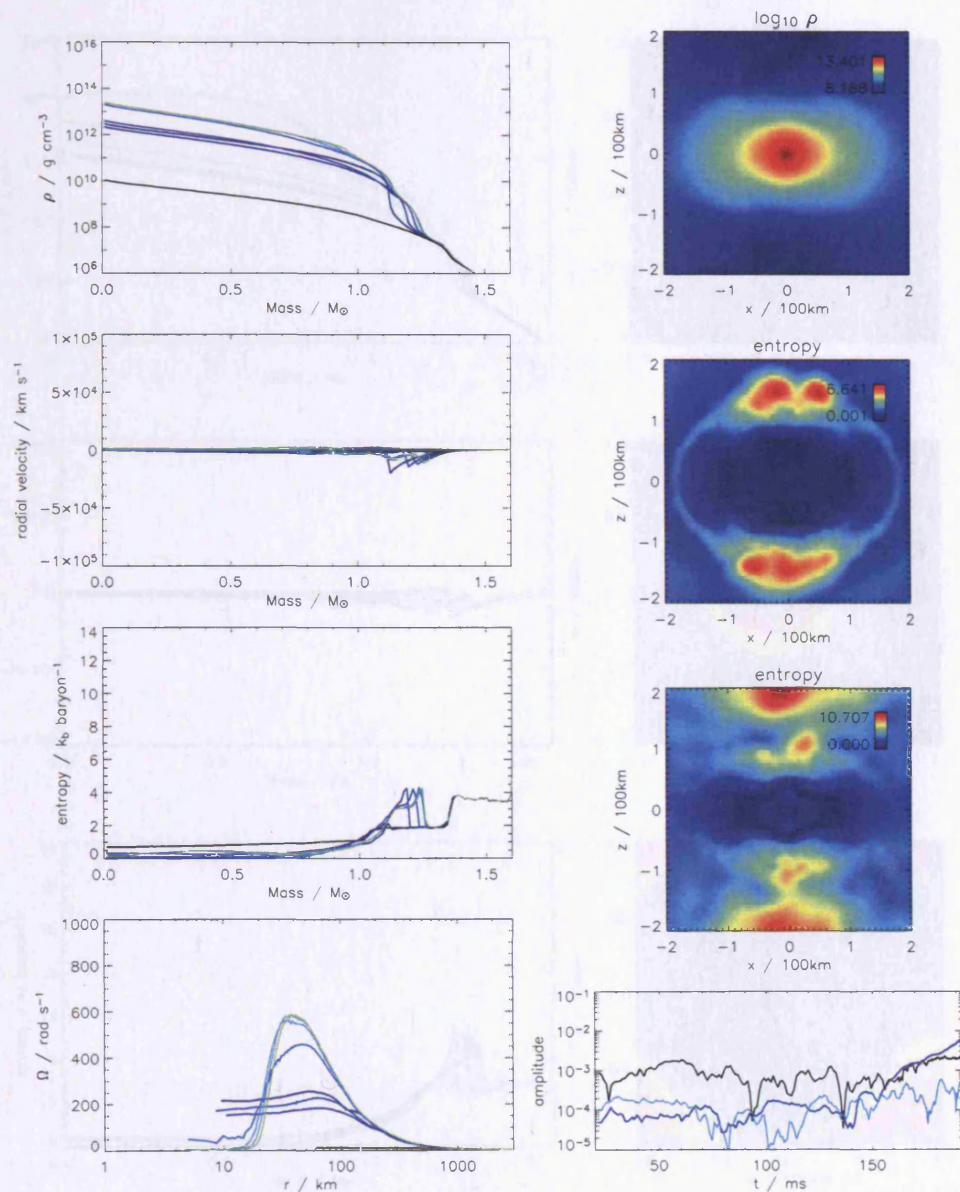


FIGURE 5.50. SRIF2 run of model DE15B, which was made to rotate with a smooth rotation law approximating that of model E15B. Density, radial velocity and entropy versus enclosed mass and angular velocity versus radius at  $t = 19.76, 151.5, 167.7, 179.4, 190.1, 191.6, 192.2$  and  $192.6$  ms. Centrifugal bounces occur at around 151 and 192 ms. Snapshots show the density at 192.2 ms and the entropy at 151.5 and 192.2 ms. The graph at the bottom right shows the displacement of the centre of mass (black) and the amplitudes of the dipole (blue) and quadrupole (cyan) moments.

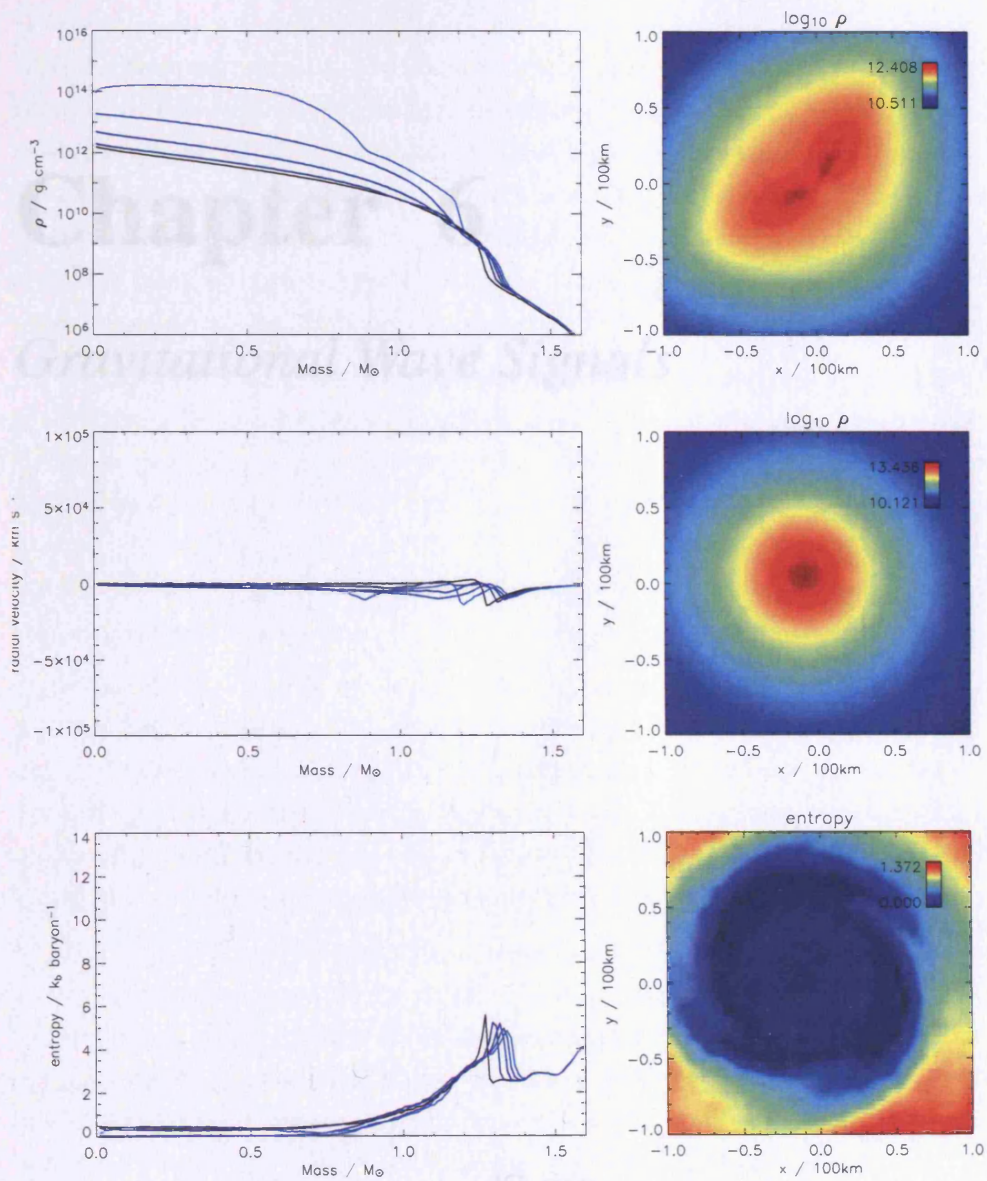


FIGURE 5.51. SRIF2 run of model Bumps, which had extremely large density perturbations added at 183.9 ms. Density, radial velocity and entropy versus enclosed mass at  $t = 183.9, 194.0, 202.5, 208.8$  and  $215.7$  ms are shown. The lumps quickly recombine and the density distribution returns to spheroidal and continues to contract. Snapshots show the density in the  $x$ - $y$  plane at 183.9 and 208.8 ms and the entropy at 208.8 ms.

# Chapter 6

## *Gravitational Wave Signals*

“Gravity  
You just hold me down so quietly”

*Super Furry Animals*

## 6.1 Gravitational Wave Production

Perhaps the most tantalising possibility for astronomy in the near future is that of the detection of gravitational waves. Enormous effort is going into pushing the current generation of gravitational wave detectors towards higher and higher sensitivities. With the launch of the Laser Interferometer Space Antenna (LISA) planned for 2015 it seems inevitable that within my lifetime gravitational wave astronomy will have uncovered a wealth of previously unobserved phenomena in much the same way as X-ray and radio observations did in the 1960s (presuming I don't get run over by a bus or anything).

The attraction of gravitational waves comes with the fact that they are produced with great power only in the strongest of gravitational fields and propagate in spacetime virtually unattenuated. This means that their detection would allow observations of the most catastrophic events in the Universe, such as mergers of compact objects and core collapse supernovae. For supernovae, the strongest gravitational wave signals produced would come from the core at bounce, impossible to observe in electromagnetic radiation due to the intervening material.

General relativity tells us that the shape, or metric, of spacetime is determined by the distribution of matter. Therefore a change in the distribution of matter can cause a change in the shape of spacetime with the disturbance propagating far from the source. By analogy with two rubber ducks floating in the sea, whose relative positions will be changed by a passing wave, a passing gravitational wave can be detected by observing a change in the relative positions of a number of test masses.

This is the principle of gravitational wave detectors. Presently the favoured method for the detection of gravitational radiation makes use of laser interferometry. Mirrors are mounted on large masses which are suspended at the ends of two arms extending at right angles to each other, like the letter L. A laser beam is split and sent along the arms, is reflected from the masses and recombined, producing an interference pattern (in actual fact, such large distances are required that the laser beams are reflected between the several-kilometre long arms a number of times). Changes in the lengths of the arms caused by the passage of a gravitational wave will produce changes in the interference pattern. The important quantity to measure is the strain  $h$ , the fractional change in length of the arms. Detectors currently on line are GEO 600, with 600m long arms, TAMA300, with arms of 300m, VIRGO, which has arms of 3km and two LIGO detectors, each with arms of 4km, from which the highest sensitivity is expected. Both VIRGO and LIGO are now approaching their design sensitivity limits, but so far no signals have been detected.

The launch of the Laser Interferometer Space Antenna (LISA) is planned for 2015.

Three spacecraft will trail  $20^\circ$  behind Earth in its orbit, each marking a vertex of an equilateral triangle with sides of 5 million km. Away from the rumblings of seismic disturbances it will detect gravitational radiation from numerous sources, including binaries thousands of years before they merge and merging supermassive black holes in distant galaxies.

In contrast to electromagnetism, where electric-dipole radiation dominates, gravitational radiation is quadrupolar (or higher order). A system with a constant quadrupole moment (and higher) will not radiate. This means that anything spherical or axially symmetric with constant radius will not be a source of gravitational radiation. In general, large or rapidly varying asphericities are required (Misner, Thorne & Wheeler 1973).

The collapse of the cores of rotating stars is an obvious case in which the asphericity of a very dense object changes rapidly (at its gravitational radius). Two dimensional studies of how the degree of rotation affects the gravitational wave signal around core bounce are numerous (Zwerger & Mueller 1997, Ott et al. 2004, Kotake et al. 2003b, Fryer, Holz & Hughes 2002, Moenchmeyer et al. 1991) and accompanying figures of gravitational wave signals have become almost run-of-the-mill in publications of core collapse simulations (Fryer & Warren 2004, Shibata & Sekiguchi 2005, Fryer & Heger 2005). In general, the signals can be divided into two types: Type I, which are strong at bounce and subsequently “ring down”; and Type II, which show several distinct peaks as the core oscillates after bounce. Which type of signal the core produces depends on the effective adiabatic index given by a combination of the pre-bounce equation of state and the rate of rotation (Zwerger & Mueller 1997). A larger effective  $\Gamma$  (hard equation of state or more rapid rotation) will tend to result in a gravitational wave signal of Type I, and vice versa for Type II. For a set of models run without varying the actual adiabatic index of the equation of state there may be a rotation rate at which a transition takes place between Type I and Type II. Ott et al. (2004) find this transition at an initial rotation parameter  $\beta$  of around 0.3%.

## 6.2 The Weak-Field Quadrupole Approximation

Far away from a source of gravitational waves, where the field is weak, the spacetime metric can be approximated by

$$g_{\mu\nu} = \eta_{\mu\nu} + h_{\mu\nu} , \quad (6.1)$$

where  $\mu, \nu = 0, 1, 2, 3$ ,  $\eta_{\mu\nu}$  is the metric of flat spacetime and  $|h_{\mu\nu}| \ll 1$ .

For “nearly Newtonian” sources (Misner et al. 1973) in SPH, the amplitudes of the gravitational waves can be calculated from the reduced quadrupole moments

$$I_{ij} = \sum_{p=1}^N m_p \left[ x_{ip}x_{jp} - \frac{1}{3}\delta_{ij}r_p^2 \right]. \quad (6.2)$$

Choosing a coordinate frame which results in the simplest description, the amplitudes are given as the transverse-traceless components of  $h_{ij}$  (Centrella & McMillan 1993, Rosswog, Speith & Wynn 2004):

$$h_{xx}^{TT} = \frac{1}{d} \frac{G}{c^4} (\ddot{I}_{xx} - \ddot{I}_{yy}) \quad (6.3)$$

$$h_{xy}^{TT} = \frac{2}{d} \frac{G}{c^4} \ddot{I}_{xy} \quad (6.4)$$

viewed along the  $z$ -axis, where  $h_{xx}^{TT} = -h_{yy}^{TT}$  and  $h_{xy}^{TT} = h_{yx}^{TT}$ . The amplitudes when viewed along the  $x$ - and  $y$ -axes can be obtained by a cyclic permutation of the indices. These are the only two non-zero components of  $h_{\mu\nu}^{TT}$  and the deduction follows that each corresponds to a specific polarization of gravitational waves. Unlike polarized light, which causes an oscillation in one dimension, a polarized gravitational wave will cause an oscillation in two perpendicular directions. The two different polarizations are thus inclined at  $45^\circ$  to each other. Figure 6.1 illustrates this by showing the effect of a passing wave of each polarization on a ring of particles. Hereafter the two polarizations of the gravitational wave signal will be referred to as  $h_+$  and  $h_\times$ .

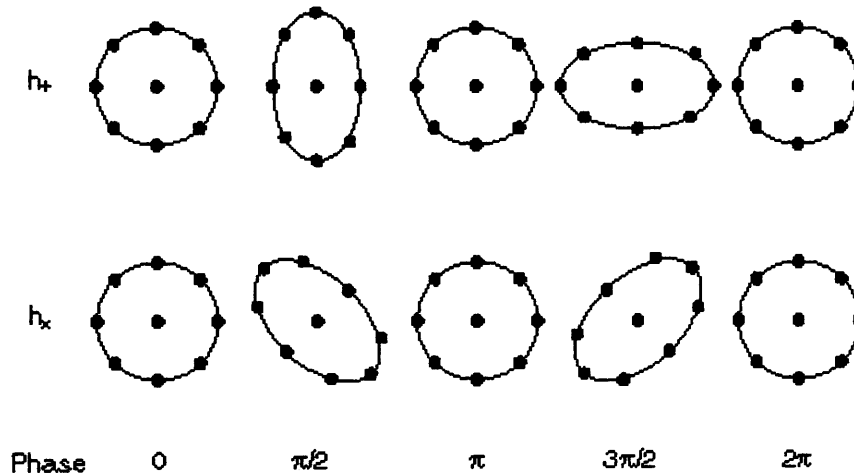


FIGURE 6.1. Effect of the two different polarizations of a gravitational wave on a ring of particles.

The total luminosity emitted as gravitational waves is given by

$$L_{GW} \simeq \frac{G}{5c^5} \dot{I}_{ij}^{(3)} \dot{I}_{ij}^{(3)} \quad (6.5)$$

where  $^{(3)}$  denotes the third derivative with respect to time.

The calculation of the gravitational wave amplitudes was performed by differentiating 6.2 twice with respect to time,

$$\ddot{I}_{ij} = \sum_{p=1}^N m_p \left[ \ddot{x}_{ip} x_{jp} + 2\dot{x}_{ip} \dot{x}_{jp} + x_{ip} \ddot{x}_{jp} - \frac{1}{3} \delta_{ij} (2\ddot{x}_{kp} x_{kp} + 2\dot{x}_{kp} \dot{x}_{kp}) \right], \quad (6.6)$$

meaning that

$$\ddot{I}_{xx} = \frac{2}{3} \sum_{p=1}^N m_p \left[ 2f_{xp} x_p - f_{yp} y_p - f_{zp} z_p + 2v_{xp}^2 - v_{yp}^2 - v_{zp}^2 \right] \quad (6.7)$$

$$\ddot{I}_{xy} = \sum_{p=1}^N m_p \left[ f_{xp} y_p + 2v_{xp} v_{yp} + f_{yp} x_p \right] \quad (6.8)$$

and similarly for  $\ddot{I}_{yy}$ ,  $\ddot{I}_{xy}$  etc..

The third derivatives of the reduced quadrupole moments were found by fitting a cubic spline interpolation to the points  $\dot{I}_{jk}$  and calculating the analytical derivatives (Press et al. 1992).

## 6.3 Results and Discussion

The time evolution of the gravitational amplitudes and the gravitational wave luminosity of the collapsing cores gives a description of the dynamics that is complementary to that derived from the previously-plotted variables. In particular, the amplitudes and luminosities at bounce give a measure of the extremes of density and asphericity in the core. In this section I discuss the signals from all of the models run on the SRIF2 cluster, beginning with the Woosley models.

It has become common practice to quote figures for the gravitational amplitudes  $h_+$  and  $h_\times$  as the strain that would be produced by the source at a distance of 10 Mpc. In the following discussion, all of the amplitudes are expressed in this unit.

### 6.3.1 Woosley Models

The gravitational amplitudes along the  $x$ - and  $z$ -axes and the total gravitational wave luminosity for the Woosley models (Chapter 4) are shown in Figures 6.2-6.6.

In general, there are several points to note:

- The oscillations of  $h_{\times}$  remain smaller than around  $4 \times 10^{-25}$  in all models, and approximately the same size along either axis. This makes sense, since viewed along  $z$ -axis the core is close to symmetrical, whilst viewed along  $x$ -axis  $h_{\times}$  measures the quadrupole moment at 45 degrees to the quadrupole that the core makes. The signal remains at the level of noise created by small deviations from asymmetry.
- The maximum values of  $h_{+}$  are similar in size to those of  $h_{\times}$  when viewed along the  $z$ -axis. This is also as expected, since again the core is symmetrical. Along the  $x$ -axis  $h_{+}$  can be much bigger because the core's oblateness and hence the quadrupole moment change with time.
- In all models, the luminosity grows as the core contracts. The maximum luminosity depends on a combination of the rates of change of the density and the degree of oblateness. There is therefore a balance to be struck between rapid rotation, which gives a large quadrupole that changes fairly slowly and weak rotation, which gives a rapidly changing density but a small quadrupole. The luminosity reaches its highest value between these extremes,  $\sim 10^{52}$  erg s $^{-1}$  for model W30lr.
- The maximum amplitude of  $h_{+}$  changes in a similar fashion, increasing with initial rotation until it reaches approximately  $10^{-23}$  for models W30lr, W30cyl, W40lr and W50lr. The maximum  $h_{+}$  then decreases with rotation for models W60lr and W80lr.

The model with the smallest amount of rotation, W06lr, shows a growth in luminosity as well as gravitational wave amplitudes as it approaches bounce (Figure 6.2). However, the  $h_{+}$  amplitude along the  $x$ -axis does not grow significantly larger than that viewed along the  $z$ -axis. In this case the effect of rotation on the gravitational wave signal is minimal.

For model W80lr, which rotates only slightly faster, a clear peak in both the luminosity and  $h_{+}$  at bounce is visible.  $h_{+}$  peaks at around  $1.4 \times 10^{-24}$ , or three times the value along the  $z$ -axis. After bounce the signals are once again at the level of noise.

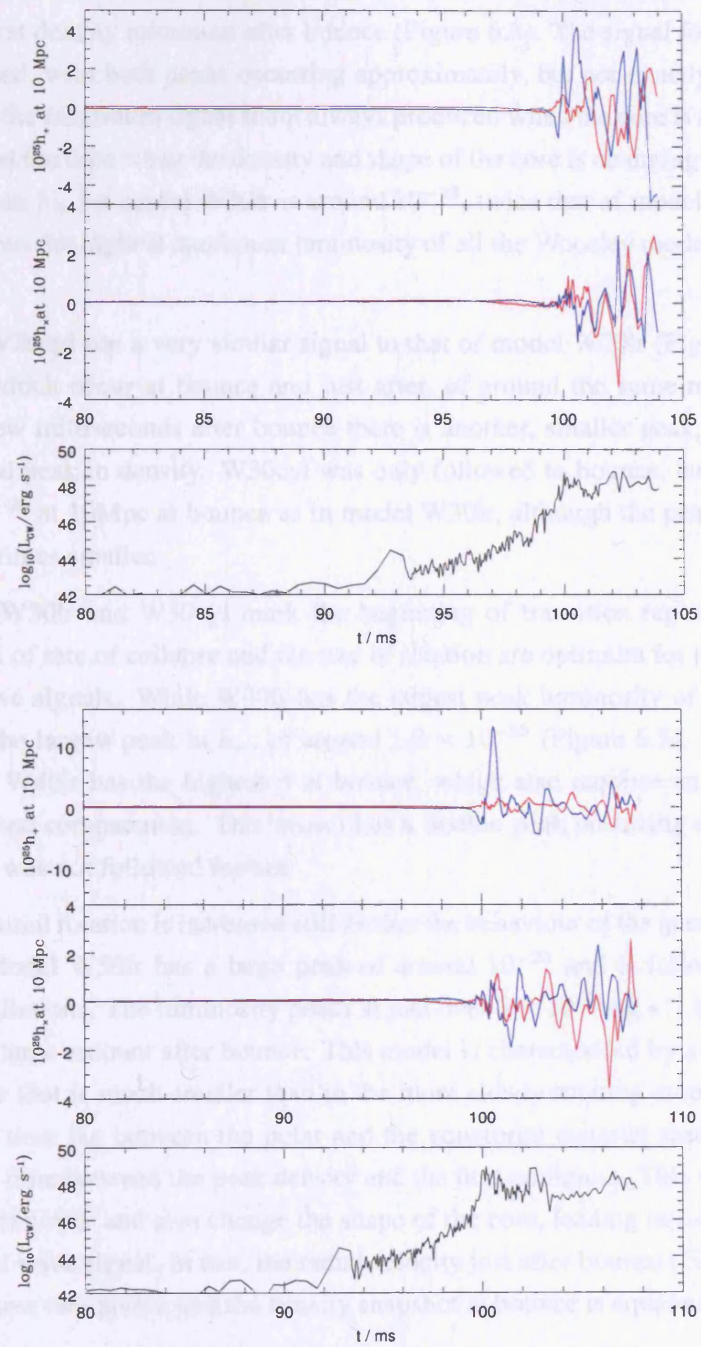


FIGURE 6.2. Time evolution of the gravitational signal amplitudes and total luminosities for models W061r (top) and W081r (bottom). The red lines give the signal when viewed along the  $x$ -axis and the blue lines when viewed along the  $z$ -axis.

W20lr peaks twice in  $h_+$  – the first of these is at the time of bounce and the second just before the first density minimum after bounce (Figure 6.3). The signal for W30lr is also double-peaked, with both peaks occurring approximately, but not exactly, at bounce. It appears that the maximum signal is not always produced when the core is at its maximum density, but at the time when the density and shape of the core is changing most violently. The maximum  $h_+$  for model W30lr is around  $10^{-23}$ , twice that of model W20lr. Model W30lr also has the highest maximum luminosity of all the Woosley models, around  $10^{52}$  erg s<sup>-1</sup>.

Model W20cyl has a very similar signal to that of model W20lr (Figure 6.4). It has two peaks which occur at bounce and just after, of around the same magnitude as in W20lr. A few milliseconds after bounce there is another, smaller peak, corresponding to the second peak in density. W30cyl was only followed to bounce, but shows a peak in  $h_+$  of  $10^{-23}$  at 10Mpc at bounce as in model W30lr, although the peak luminosity is around 100 times smaller.

Models W30lr and W30cyl mark the beginning of transition region in which the combination of rate of collapse and the rate of rotation are optimum for producing gravitational wave signals. While W30lr has the largest peak luminosity of all the models, W40lr has the largest peak in  $h_+$ , of around  $1.3 \times 10^{-23}$  (Figure 6.5). It is interesting to note that W40lr has the highest  $\beta$  at bounce, which also requires an optimum level of rotation and compactness. This model has a double peak occurring at and just after bounce, but was not followed further.

As the initial rotation is increased still further the behaviour of the gravitational waves changes. Model W50lr has a large peak of around  $10^{-23}$  and is followed by several smaller oscillations. The luminosity peaks at just over  $3 \times 10^{50}$  erg s<sup>-1</sup> but does not decrease by a large amount after bounce. This model is characterised by a drop in density after bounce that is much smaller than in the more slowly rotating models. It is possible that the time lag between the polar and the equatorial material reaching bounce is equal to the time between the peak density and the first minimum. This would make the minimum shallower and also change the shape of the core, leading to oscillations in the gravitational wave signal. In fact, the radial velocity just after bounce (Figure 4.16) does appear to show two peaks, and the density snapshot at bounce is equatorially extended.

In model W60lr rotation delays the bounce significantly, and this is seen in the gravitational wave signal (Figure 6.6).  $h_+$  has a dominant peak of around  $6 \times 10^{-24}$  at bounce and several smaller peaks before and after. The largest of these, occurring at around 113 ms, corresponds to a peak in the value of  $\beta$  while the core is still collapsing. Evidently

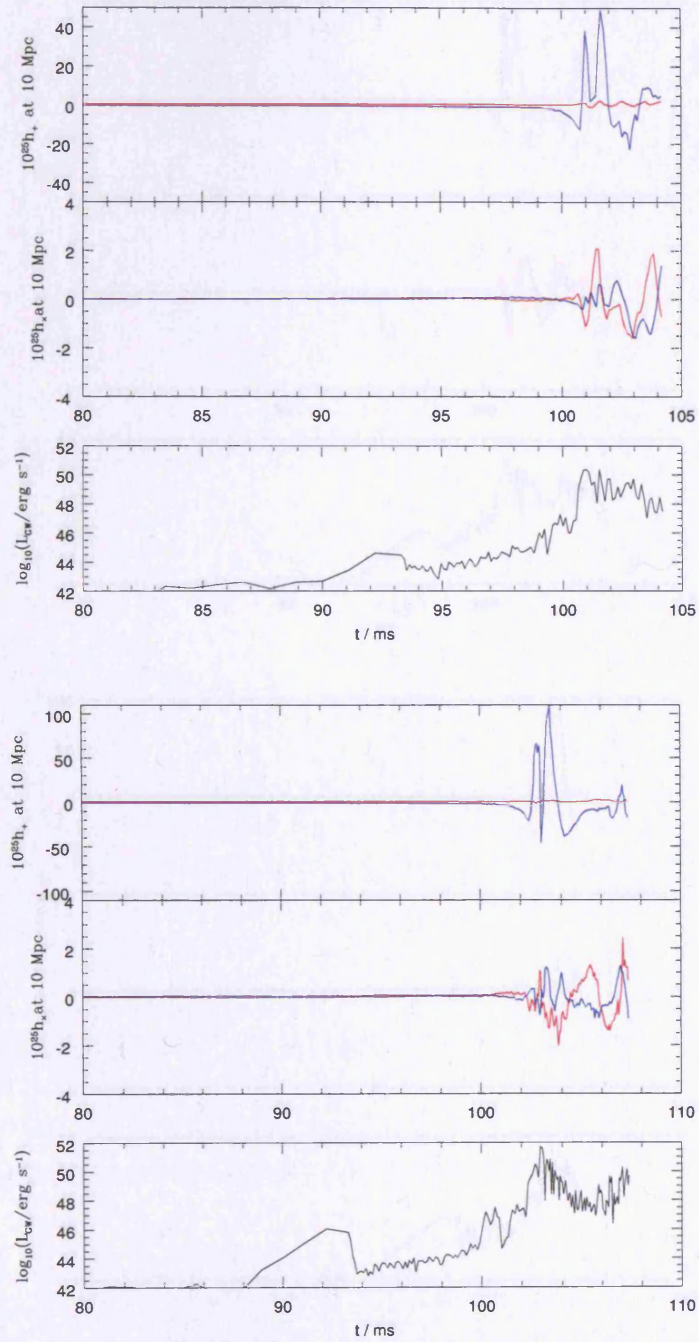


FIGURE 6.3. Time evolution of the gravitational signal amplitudes and total luminosities for models W20lr (top) and W30lr (bottom). The red lines give the signal when viewed along the  $x$ -axis and the blue lines when viewed along the  $z$ -axis.

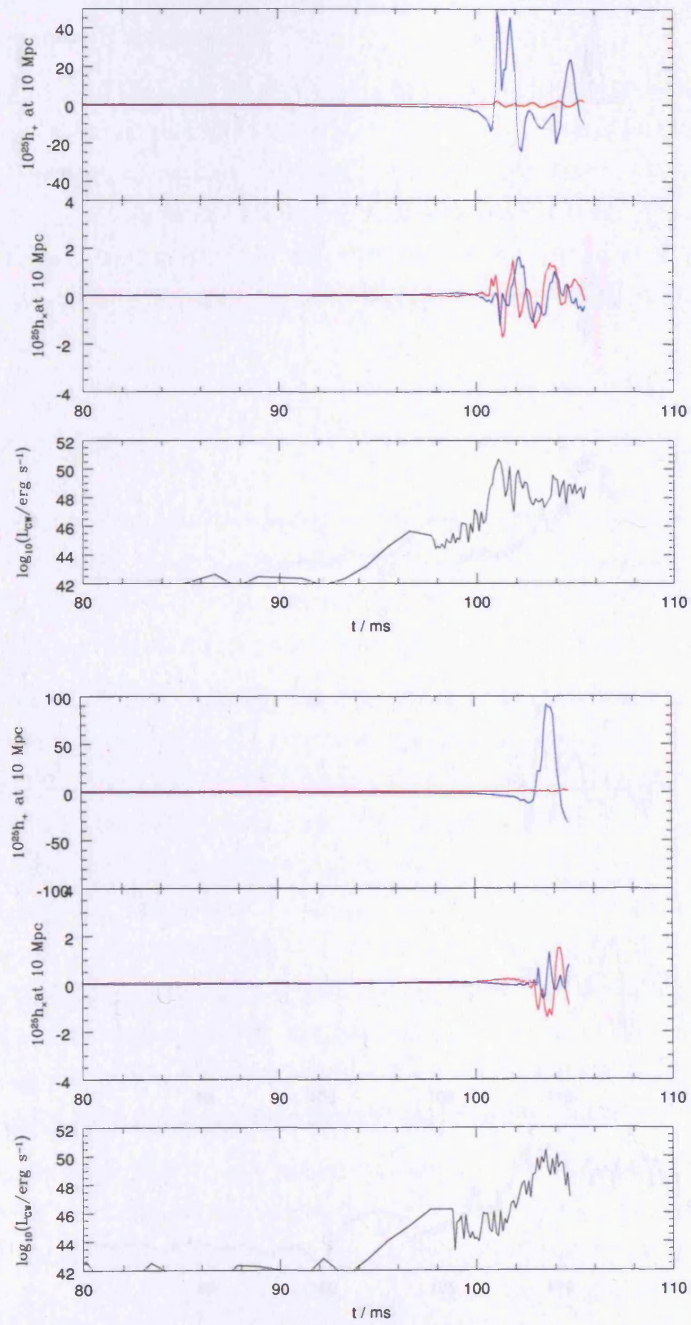


FIGURE 6.4. Time evolution of the gravitational signal amplitudes and total luminosities for models W20cyl (top) and W30cyl (bottom). The red lines give the signal when viewed along the  $x$ -axis and the blue lines when viewed along the  $z$ -axis.

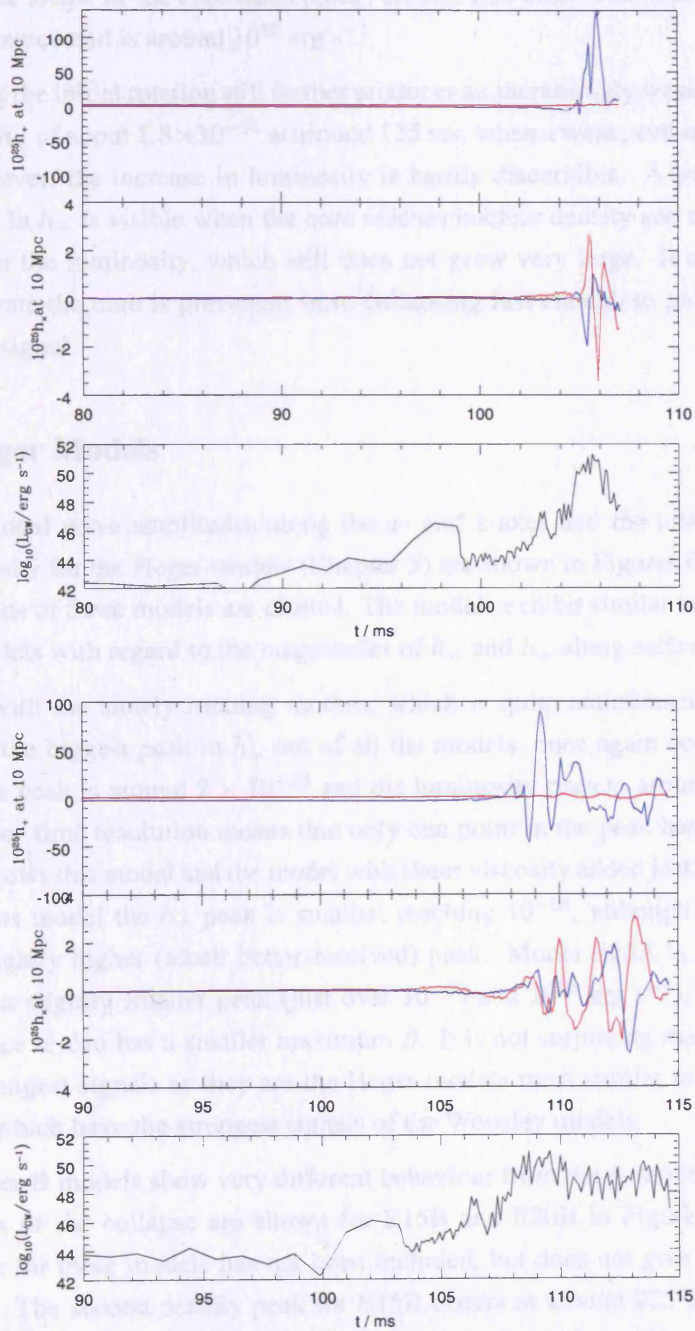


FIGURE 6.5. Time evolution of the gravitational signal amplitudes and total luminosities for models W40lr (top) and W50lr (bottom). The red lines give the signal when viewed along the  $x$ -axis and the blue lines when viewed along the  $z$ -axis.

a change in the shape of the core takes place around this time. The peak luminosity is obtained at bounce and is around  $10^{50}$  erg s<sup>-1</sup>

Increasing the initial rotation still further produces an increasingly weak signal. W80lr has a peak in  $h_+$  of about  $1.8 \times 10^{-24}$  at around 125 ms, when a weak, sub-nuclear bounce occurs. However, the increase in luminosity is hardly discernible. A second, slightly smaller, peak in  $h_+$  is visible when the core reaches nuclear density and corresponds to an increase in the luminosity, which still does not grow very large. It appears that at this rotation rate the core is prevented from collapsing fast enough to produce a strong gravitational signal.

### 6.3.2 Heger Models

The gravitational wave amplitudes along the  $x$ - and  $z$ -axes and the total gravitational wave luminosity for the Heger models (Chapter 5) are shown in Figures 6.7- 6.13. Only the SRIF2 runs of these models are plotted. The models exhibit similar behaviour to the Woosley models with regard to the magnitudes of  $h_x$  and  $h_+$  along each axis.

I begin with the slowly rotating models, which is quite anticlimactic since E15A actually has the biggest peak in  $h_+$  out of all the models, once again occurring around bounce. This peak is around  $2 \times 10^{-23}$  and the luminosity rises to around  $10^{51}$  erg s<sup>-1</sup> (although poor time resolution means that only one point in the peak has been plotted). Figure 6.7 shows this model and the model with shear viscosity added just before bounce. In the viscous model the  $h_+$  peak is smaller, reaching  $10^{-23}$ , although the luminosity reaches a slightly higher (albeit better resolved) peak. Model E20A is very similar to E15A, with a slightly smaller peak (just over  $10^{-23}$  and  $10^{50}$  erg s<sup>-1</sup>), which is to be expected since it also has a smaller maximum  $\beta$ . It is not surprising that the A models have the strongest signals as they are the Heger models most similar to models W30lr and W40lr, which have the strongest signals of the Woosley models.

The Heger B models show very different behaviour from the A models. The highest density parts of the collapse are shown for E15B and E20B in Figure 6.9. The first density peak for these models has not been included, but does not give a large peak in  $h_+$  or  $L_{GW}$ . The second density peak for E15B occurs at around 225-230 ms. This is visible in the gravitational wave signal as a small increase in  $h_+$  and luminosity, spread out over several milliseconds. The luminosity peaks again when the core reaches nuclear densities, but does not much exceed  $10^{49}$  erg s<sup>-1</sup>, with a maximum magnitude of  $h_+$  of around  $3 \times 10^{-24}$ . Model E20B shows similar behaviour, with a small peak in  $h_+$  and  $L_{GW}$  around the second peak in density, which subsides and then grows again as

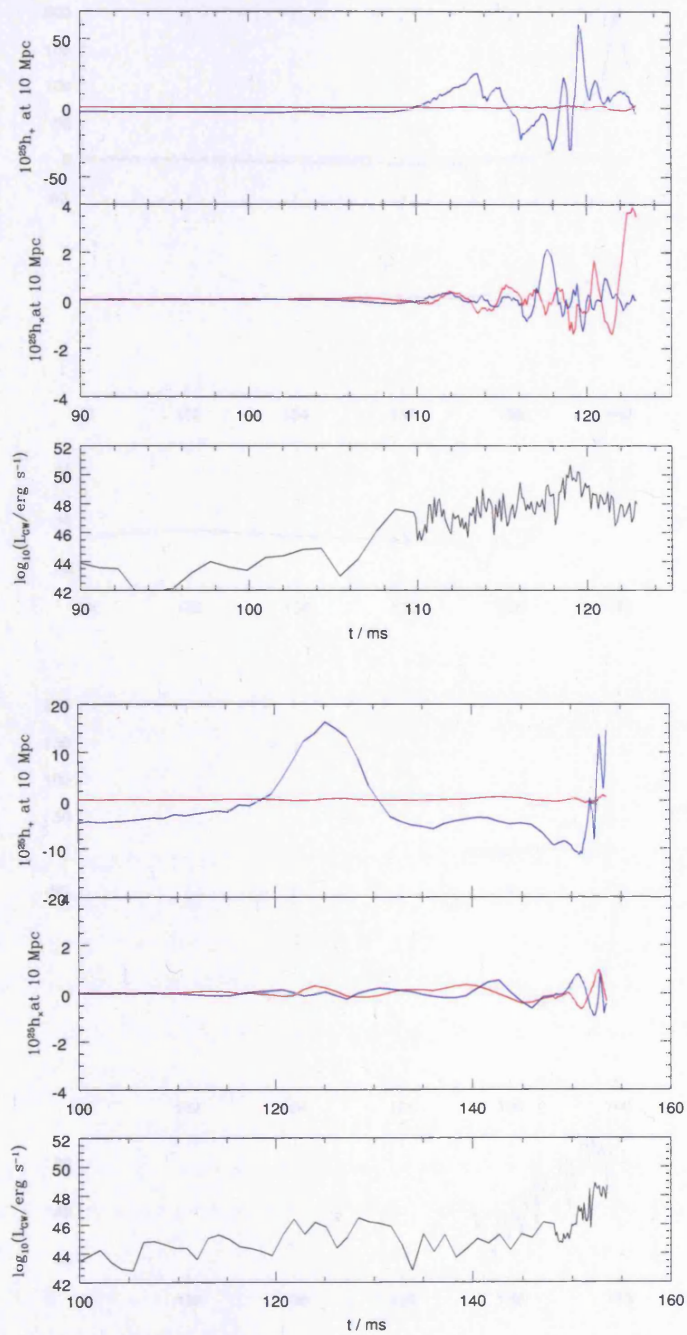


FIGURE 6.6. Time evolution of the gravitational signal amplitudes and total luminosities for models W60lr (top) and W80lr (bottom). The red lines give the signal when viewed along the  $x$ -axis and the blue lines when viewed along the  $z$ -axis.

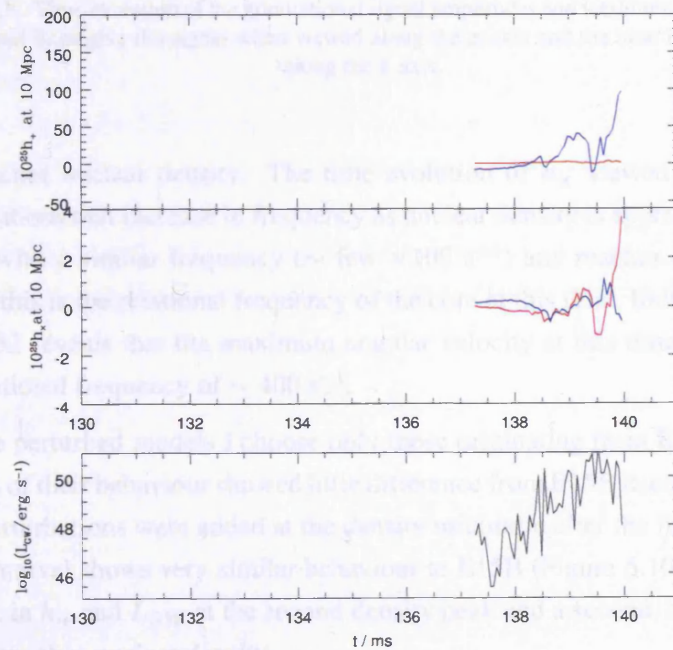
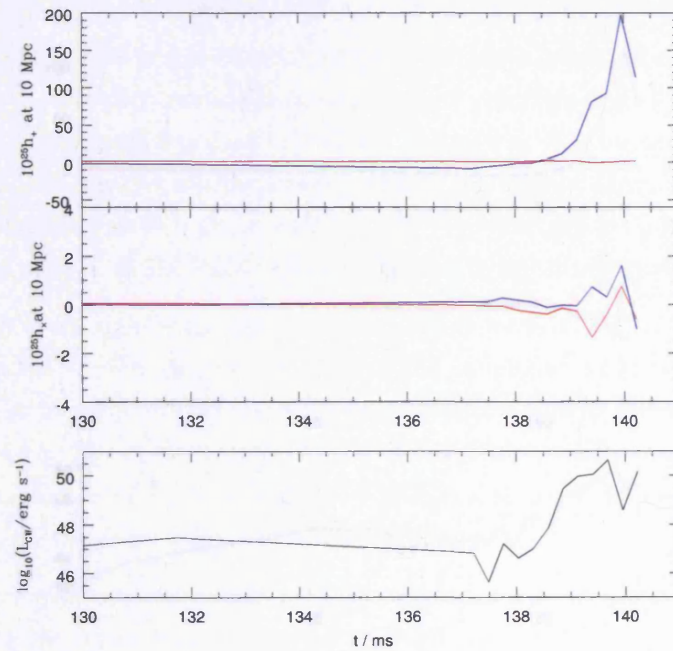


FIGURE 6.7. Time evolution of the gravitational signal amplitudes and total luminosities for models E15A (top) and E15Avisc (bottom). The red lines give the signal when viewed along the  $x$ -axis and the blue lines when viewed along the  $z$ -axis.

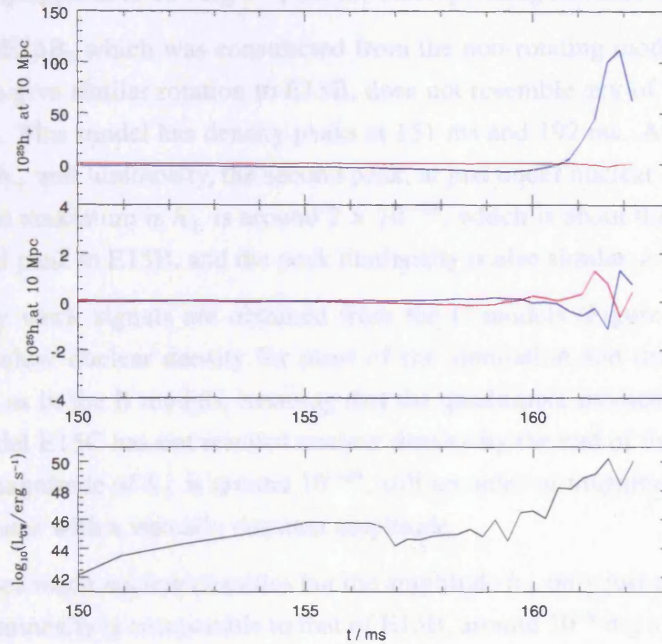


FIGURE 6.8. Time evolution of the gravitational signal amplitudes and total luminosities for model E20A. The red lines give the signal when viewed along the  $x$ -axis and the blue lines when viewed along the  $z$ -axis.

the core reaches nuclear density. The time evolution of  $h_{\times}$  viewed along the  $z$ -axis shows oscillations that increase in frequency as nuclear density is approached.  $h_{+}$  is also oscillatory, with a similar frequency ( $\sim \text{few} \times 100 \text{ s}^{-1}$ ) and reaches about  $5 \times 10^{-24}$ . Presumably this is the rotational frequency of the core at this time. Indeed, looking back at Figure 5.32 reveals that the maximum angular velocity at this time is  $2500 \text{ rad s}^{-1}$ , giving a rotational frequency of  $\sim 400 \text{ s}^{-1}$ .

From the perturbed models I choose only those originating from E15B, since previous analyses of their behaviour showed little difference from E15B itself. Plotting pE15B (in which perturbations were added at the density minimum after the first peak) over the same time interval shows very similar behaviour to E15B (Figure 6.10). Again, there is a slight peak in  $h_{+}$  and  $L_{GW}$  at the second density peak and a second, bigger increase as the core approaches nuclear density.

Model E15B\_p undergoes one more density maximum than E15B, with the second and third bounce at 220 ms and 270 ms. Both are accompanied by an increase in  $h_{+}$  and luminosity, with the second peak similar in magnitude to that of E15B and the third peak having a maximum  $h_{+}$  of around  $3 \times 10^{-24}$ . As the core reaches nuclear density

the luminosity approaches  $10^{50} \text{erg s}^{-1}$ , but the corresponding increase in  $h_+$  is small.

Model DE15B, which was constructed from the non-rotating model with a rotation law added to give similar rotation to E15B, does not resemble any of the E15B models (Figure 6.11). This model has density peaks at 151 ms and 192 ms. At both times there is a peak in  $h_+$  and luminosity, the second peak, at just under nuclear density, being the stronger. The maximum  $h_+$  is around  $2 \times 10^{-24}$ , which is about the same magnitude as the second peak in E15B, and the peak luminosity is also similar, around  $10^{49} \text{erg s}^{-1}$ .

Extremely weak signals are obtained from the C models (Figure 6.12). The core stays well below nuclear density for most of the simulation and the final collapse is not as quick as in the B models, meaning that the quadrupole moment does not change rapidly. Model E15C has not reached nuclear density by the end of the simulation. The maximum magnitude of  $h_+$  is around  $10^{-24}$ , still an order or magnitude larger than  $h_x$ , which oscillates with a virtually constant amplitude.

E20C does reach nuclear densities but the amplitude  $h_+$  only just exceeds  $2 \times 10^{-24}$ . The peak luminosity is comparable to that of E15B, around  $10^{49} \text{erg s}^{-1}$ .

Just for fun, the gravitational amplitudes for the model ‘‘Bumps’’, in which the density was perturbed by 20%, are given in Figure 6.13. Initially both  $h_x$  and  $h_+$  along the  $z$ -axis are of large amplitude –  $h_+$  is actually greater along  $z$ -axis this time because of the large quadrupole moment given to the core. As the density perturbations iron themselves out and the core returns to a spheroidal shape the amplitudes decrease, although  $h_+$  starts to increase again towards the end of the simulation when nuclear densities are reached. The luminosity behaves in a similar way to the amplitudes, falling off to begin with then rising again towards the end, although it never much exceeds  $10^{48} \text{erg s}^{-1}$ .

## 6.4 Summary

It has been shown in this chapter that the production of gravitational waves by a collapsing, rotating stellar core requires sufficient rotation for the mass distribution to become flattened, but not so much that the collapse of the core is slowed significantly. In all models the gravitational wave amplitude  $h_+$  viewed along the  $x$ -axis peaks at times corresponding peaks in the central density and/or the rotation parameter  $\beta$ .

The models for which the largest values of  $h_+$  were obtained were the moderately rotating Woosley models W30lr, W30cyl, W40lr and W50lr, and the Heger models E15A

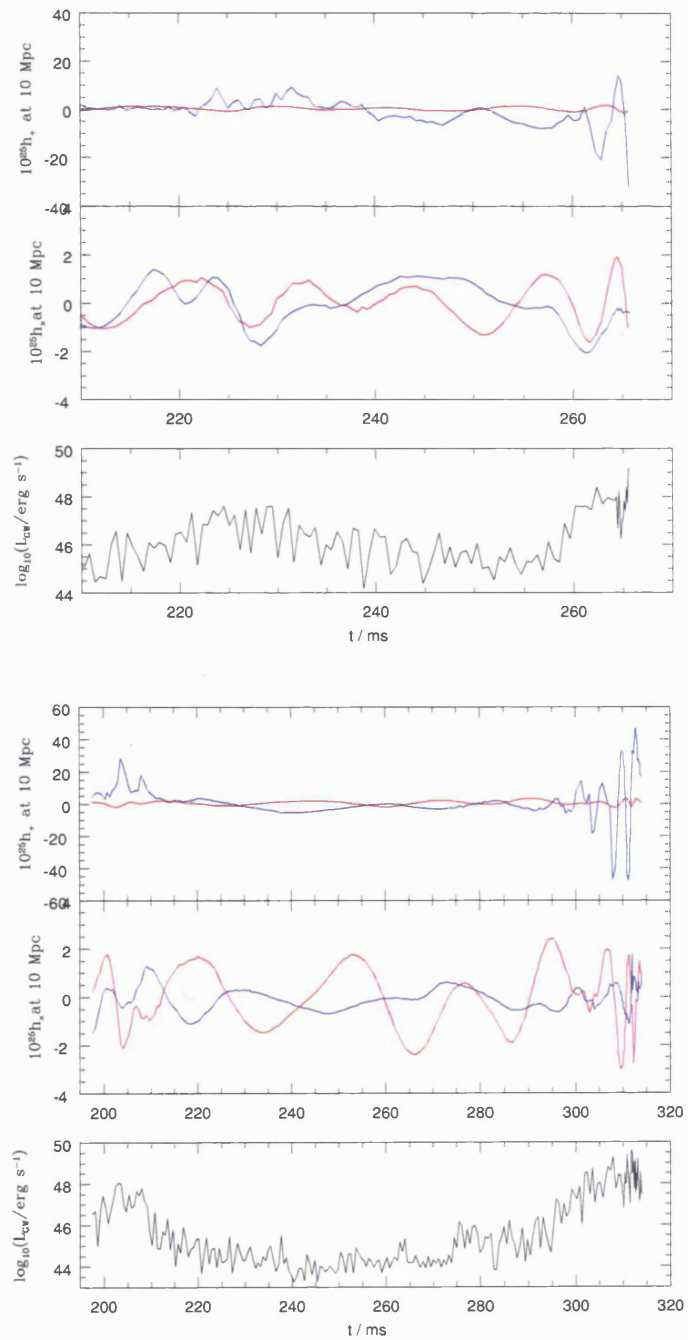


FIGURE 6.9. Time evolution of the gravitational signal amplitudes and total luminosities for models E15B and E20B. The red lines give the signal when viewed along the  $x$ -axis and the blue lines when viewed along the  $z$ -axis.

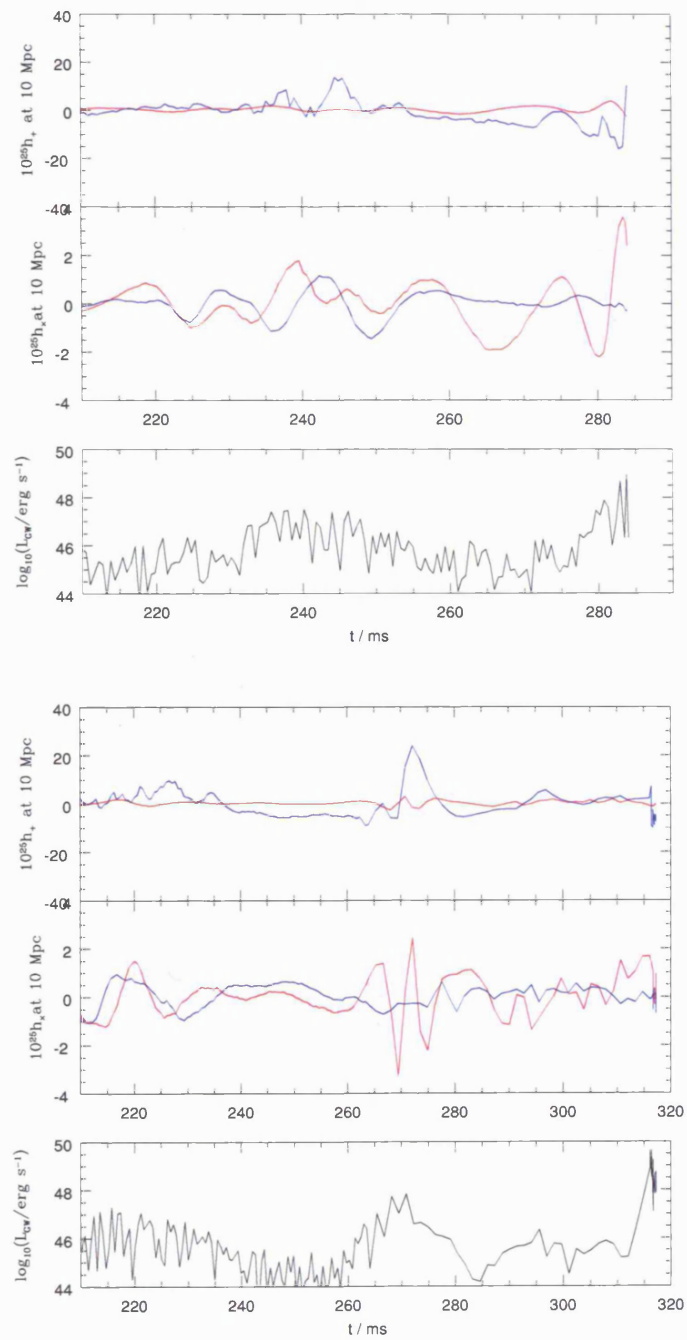


FIGURE 6.10. Time evolution of the gravitational signal amplitudes and total luminosities for models pE15B and E15B\_p. The red lines give the signal when viewed along the  $x$ -axis and the blue lines when viewed along the  $z$ -axis.

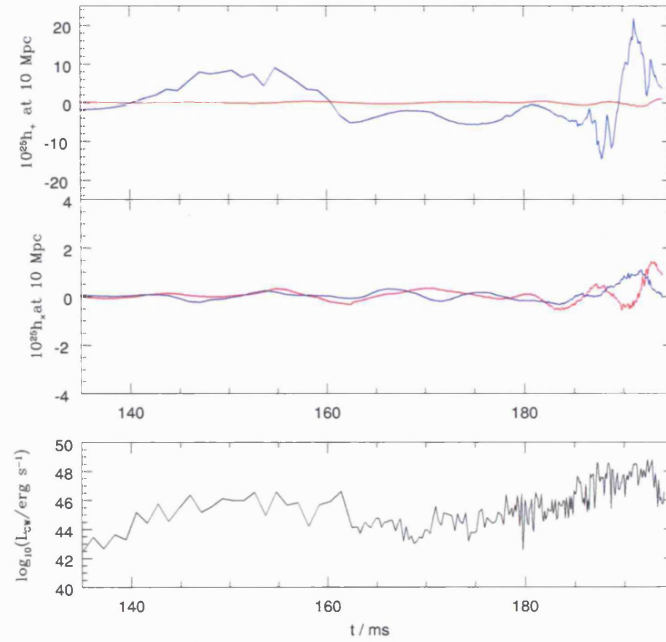


FIGURE 6.11. Time evolution of the gravitational signal amplitudes and total luminosities for model DE15B. The red lines give the signal when viewed along the  $x$ -axis and the blue lines when viewed along the  $z$ -axis.

and E20A. In these models  $h_+$  grew to  $1-2 \times 10^{-23}$  with corresponding luminosities between  $10^{50}-10^{52} \text{ erg s}^{-1}$ . Above and below these rotation rates in the Woosley models, the magnitude of the maximum  $h_+$  and  $L_{GW}$  falls off quite drastically.

The Heger B models, in which collapse is slowed considerably by rotation, have much weaker peak amplitudes and luminosities, with maxima in  $h_+$  of around  $4 \times 10^{-24}$  and  $L_{GW}$  of around  $10^{48}-10^{50} \text{ erg s}^{-1}$ . The signals from the C models are weaker still, as rotation prevents the cores from reaching nuclear densities for a long time.

Overall, even the maximum luminosities obtained are not a sizeable fraction of the total energy liberated by gravitational collapse. Assuming a peak luminosity of  $\sim 10^{51} \text{ erg s}^{-1}$  is obtained for  $\sim 1 \text{ ms}$  during bounce gives an energy of around  $10^{48} \text{ erg}$ , five orders of magnitude less than the binding energy of the core at bounce.

Whilst the gravitational signals obtained in the moderately rotating Woosley and Heger A models have the largest amplitudes, their short lived, non-periodic nature would make them difficult to detect. In contrast, the B models show oscillatory behaviour in the gravitational amplitudes which increases in frequency as the core collapses. In the

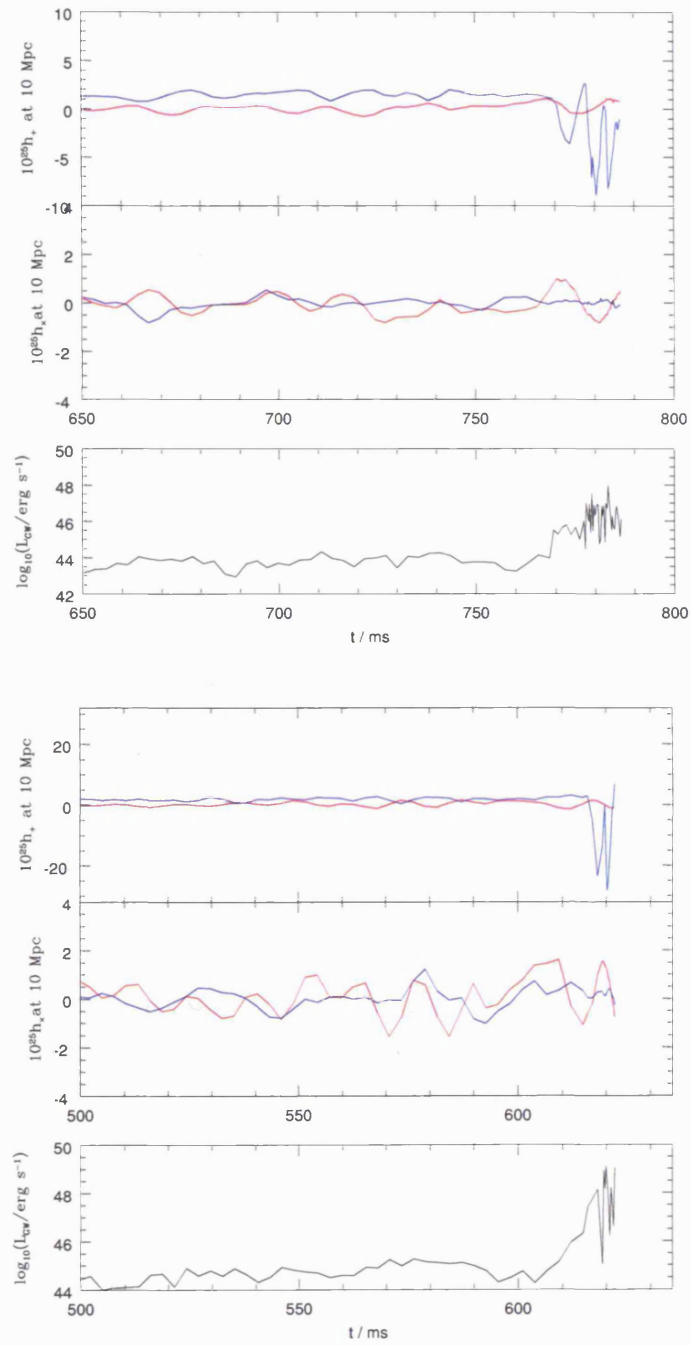


FIGURE 6.12. Time evolution of the gravitational signal amplitudes and total luminosities for models E15C and E20C. The red lines give the signal when viewed along the  $x$ -axis and the blue lines when viewed along the  $z$ -axis.

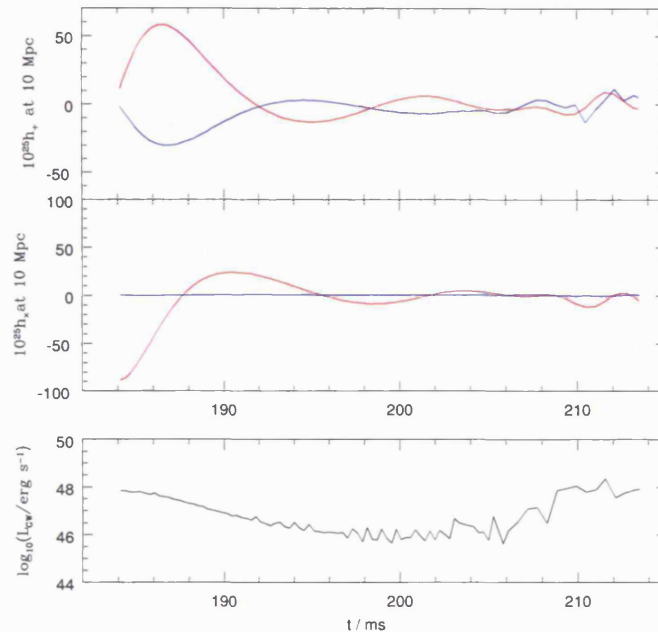


FIGURE 6.13. Time evolution of the gravitational signal amplitudes and total luminosities for model Bumps. The red lines give the signal when viewed along the  $x$ -axis and the blue lines when viewed along the  $z$ -axis.

dominant polarisation the oscillations are sizeable and it was seen above that their frequency corresponds to the rotation rate of the core.

The target sensitivity limit for Initial LIGO is a strain of just under  $3 \times 10^{-23}$  at a frequency of 200 Hz. The maximum  $h_+$  produced by the Heger A models was around  $2 \times 10^{-23}$  at 10 Mpc, and by the Heger “B” models  $5 \times 10^{-24}$  at 10 Mpc. A core collapse event with the same rate of rotation as the A models would therefore be detectable out to  $\sim 7$  Mpc. It is highly unlikely that a supernova in the Virgo cluster ( $\sim 17$  Mpc), the nearest rich cluster to our Galaxy, would be detected.

A recent study of the supernova rate in the local Universe has put the combined rate of Type II and Ib/c in late type spirals at  $2.0 \pm 0.5$  (Cappellaro, Evans & Turatto 1999), where  $1 \text{ SNu} = 1 \text{ SN } (100 \text{ yr})^{-1} (10^{10} L_{B\odot})^{-1}$ . A previous study had estimated the rate of Type II and Type Ib/c supernovae as 0.88 SNu and 0.16 SNu respectively (Cappellaro et al. 1997) for late type spirals. The supernova rate correlates with galaxy luminosity and is much lower in dwarf galaxies.

The number of galaxies within 10 Mpc is  $\sim$  several hundred, around 85% of which

are dwarfs (Karachentsev et al. 2004). We expect most supernovae to be found in spirals, of which there are at most 50-100 within 10 Mpc. The rate of supernovae within our detection radius is therefore  $\lesssim 1 \text{ yr}^{-1}$ , of which a minority would be rotating at the optimum rate for gravitational wave production and viewed along an axis perpendicular to the axis of rotation. One detection every 10 years would be an optimistic estimate for gravitational signals produced by rotating core collapse.

# Chapter 7

## *Concluding Remarks*

“No pessimist ever discovered the secrets of the stars...”

*Helen Keller*

The aim of this thesis has been to investigate the effects of rotation on the core collapse of massive stars. In particular, it was hoped that rotational instabilities such as might lead to fragmentation of the core would be found. This would support the model of gamma ray bursts in which the burst is either delayed or revived after a period of dormancy as the fragments merge. I conclude by summarizing the results of this work and suggesting avenues for further investigation.

## 7.1 Summary and Discussion

The future is bright for supernova research. After forty years, computing capabilities are reaching the stage where three dimensional calculations including detailed descriptions of the dominant physical effects are becoming possible. Modellers are now able to study the consequences of asymmetric effects such as rotation and convection. Future simulations may include magnetic fields that are able to drive jets along the poles of the supernova, thus revealing the likelihood that jets help to power supernova explosions and shedding light on the central engines of GRB.

In Chapters 2 and 3 I described the three dimensional SPH code, formerly used for simulations of neutron star mergers, that was used to simulate core collapse. I explained how alterations were made to the code to adapt it to this problem and how realistic progenitor models were used as initial conditions. I also included a description of how a parametrization of shear “ $\alpha$ ” viscosity was added to the code.

In Chapter 4 the code was tested by simulating the collapse of the “standard” Woosley progenitor S15A and comparing it to published results. Following from other studies, a variety of rotation rates were then added to the model using a simple parametrization of the angular velocity.

It was found that the effect of the slowest rotation rates on collapse was negligible. In contrast with previous studies, at higher rotation rates the maximum density at bounce decreased only slightly with increasing rotation. A second density peak was observed for the models which were followed past bounce and, in agreement with previous studies, the time between the first and second peaks increased with increasing rotation.

The ratio  $\beta$  of rotational to gravitational energy at bounce increases with initial rotation up to an initial angular velocity  $\Omega_0 = 4 \text{ rad s}^{-1}$ . Above this rate, which appears to mark a transition region in which centrifugal effects become important,  $\beta$  at bounce becomes non-monotonic in  $\Omega_0$ . As a result of this,  $\beta$  remains  $< 0.1$  for all models, much lower than the secular instability limit of  $\sim 0.14$ .

In Chapter 5 rotating progenitor models were used to investigate the effects of more rapid rotation. Three types of rotation were used: slow, rapid and enhanced, the latter produced by artificially increasing the angular velocities in the rapid rotators by a constant factor.

The weakly rotating models collapsed in a very similar manner to the optimally rotating Woosley model, obtaining a maximum value of  $\beta = 0.12$ . Centrifugal support prevented the more rapid rotators from having their rotation amplified to the same degree. All of the models with strong and enhanced rotation underwent several peaks and troughs in the central density before nuclear density was reached. At the end of the simulations the distribution of material in these models was centrally peaked and surrounded by an extended torus in the equatorial plane. The maximum  $\beta$  obtained for these models was around 12-13%.

Models were also run with enhanced shear viscosity in an attempt to remove enough angular momentum to make them collapse quickly. Collapse was accelerated a little but the shape of the core remained virtually the same as in the models with low viscosity.

Another set of models was run with  $m = 1$  and  $m = 2$  mode density perturbations added, some from the start of the simulation and others from the density minimum that followed the first density peak. Although the rate of collapse was somewhat affected by these perturbations they had little effect on the shape of the core, which proved resistant to deformation, even when the density was perturbed significantly.

No sign of fragmentation or significant growth of the  $m = 1$  or  $m = 2$  modes was observed for any of the models, even when the seed density perturbations were added to the faster rotators. The most interesting structure observed was the torus of centrifugally supported material surrounding the inner core in the rapidly rotating models.

The conclusion of this thesis is therefore that the core collapse of rotating massive stars, when simulated with up to date progenitor models and a realistic equation of state, does not result in triaxial deformations or fragmentation, at least before it reaches nuclear density. The main reason for this is that the equatorial material, which has high angular momentum, is centrifugally supported in a torus around the compact core.

## 7.2 Future Avenues

The simulations described in this thesis were run to a maximum of  $\sim 10$  ms after core bounce, when the shock formed at bounce had propagated just past the edge of the inner

core. (Defining when core bounce occurred was difficult for the rapidly rotating models, which bounced several times and were thus followed until nuclear densities were obtained in the centre.) Since the rapidly rotating models obtained values for the rotation parameter  $\beta$  approaching the limit for secular instabilities, it would be interesting to continue running these models on a secular timescale. It is possible that instabilities could still arise and lead to core deformation or fragmentation. Indeed, in studies where core fragmentation or spiral mode ( $m = 1$ ) instabilities have been found, these have occurred on a secular timescale after bounce (Rampp et al. 1998, Ott et al. 2004).

Up to bounce, the inclusion of neutrino transport is not crucial because neutrino trapping in the core maintains a high lepton abundance in the central regions. The inclusion of neutrino transport would cause a slight decrease in pressure in the core due to the reduced abundance of electrons. It would be interesting to see how much further this would enable the rapidly rotating cores to collapse before they became centrifugally supported.

If the simulations were to be continued past bounce a treatment for neutrinos would be vital since neutrinos diffuse out of the core on a secular timescale and the energy they transport becomes important. If only the core was of interest, a parametrization of the neutrino emission might be sufficient as the next step in improving the model. If the evolution of the shock was also to be followed the inclusion of a full treatment of neutrino emission, absorption and scattering would be required. Neutrino transport at this level of sophistication is way beyond the scope of this PhD.

It has been suggested that collapsars should be associated with “failed supernovae”, in which the shock formed by sub-nuclear bounce is not strong enough to eject the outer layers of the star. (In some of these cases enough power might eventually be leeched from the GRB jet to cause an explosion.) In the simulations in which rotation caused the core to bounce at sub-nuclear densities only a weak shock formed. At the same time a torus-like structure was visible around the compact inner core. These simulations are therefore consistent with the collapsar model of GRB. It would be interesting to follow the evolution of this torus after bounce to see whether it would go on to form an accretion disc and if so, how long it would persist and even whether instabilities would arise that would enable it to fragment.

## *Bibliography*

- Adams, D. (1979), *The Hitchhiker's Guide To The Galaxy*, Pan Macmillan.
- Akiyama, S. & Wheeler, J. C. (2005), 'The Nonmonotonic Dependence of Supernova and Compact Remnant Formation on Progenitor Rotation', *ApJ* **629**, 414–421.
- Akiyama, S., Wheeler, J. C., Meier, D. L. & Lichtenstadt, I. (2003), 'The Magnetorotational Instability in Core-Collapse Supernova Explosions', *ApJ* **584**, 954–970.
- Antonelli, L. A., Piro, L., Vietri, M., Costa, E., Soffitta, P., Feroci, M., Amati, L., Frontera, F., Pian, E., Zand, J. J. M. i., Heise, J., Kuulkers, E., Nicastro, L., Butler, R. C., Stella, L. & Perola, G. C. (2000), 'Discovery of a Redshifted Iron K Line in the X-Ray Afterglow of GRB 000214', *ApJL* **545**, L39–L42.
- Arzoumanian, Z., Chernoff, D. F. & Cordes, J. M. (2002), 'The Velocity Distribution of Isolated Radio Pulsars', *ApJ* **568**, 289–301.
- Atkinson, K. E. (1989), *An Introduction to Numerical Analysis*, John Wiley & Sons, Inc, —c1989, 2nd ed.
- Baade, W. & Zwicky, F. (1934a), 'Cosmic Rays from Super-novae', *Proceedings of the National Academy of Science* **20**, 259–263.
- Baade, W. & Zwicky, F. (1934b), 'On Super-novae', *Proceedings of the National Academy of Science* **20**, 254–+.
- Balbus, S. A. & Hawley, J. F. (1991), 'A powerful local shear instability in weakly magnetized disks. I - Linear analysis. II - Nonlinear evolution', *ApJ* **376**, 214–233.
- Balsara, D. S. (1995), 'von Neumann stability analysis of smooth particle hydrodynamics—suggestions for optimal algorithms', *Journal of Computational Physics* **121**, 357–372.
- Baron, E. & Cooperstein, J. (1990), 'The effect of iron core structure on supernovae', *ApJ* **353**, 597–611.

- Baron, E., Cooperstein, J. & Kahana, S. (1985), 'Type-II supernovae in 12-solar-mass and 15-solar-mass stars The equation of state and general relativity', *Physical Review Letters* **55**, 126–129.
- Barthelmy, S. D. e. a. (2005), 'Unravelling the origin of short gamma-ray bursts'.
- Benz, W. (1990), Smooth Particle Hydrodynamics - a Review, in 'Numerical Modelling of Nonlinear Stellar Pulsations Problems and Prospects', pp. 269–+.
- Benz, W., Cameron, A. G. W., Press, W. H. & Bowers, R. L. (1990), 'Dynamic mass exchange in doubly degenerate binaries. I - 0.9 and 1.2 solar mass stars', *ApJ* **348**, 647–667.
- Berger, E., Kulkarni, S. R., Frail, D. A. & Soderberg, A. M. (2003), 'A Radio Survey of Type Ib and Ic Supernovae: Searching for Engine-driven Supernovae', *ApJ* **599**, 408–418.
- Bethe, H. A. (1990), 'Supernova mechanisms', *Reviews of Modern Physics* **62**, 801–866.
- Blondin, J. M. & Mezzacappa, A. (2005), 'The spherical accretion shock instability in the linear regime'.
- Blondin, J. M., Mezzacappa, A. & DeMarino, C. (2003), 'Stability of Standing Accretion Shocks, with an Eye toward Core-Collapse Supernovae', *ApJ* **584**, 971–980.
- Bloom, J. S., Kulkarni, S. R. & Djorgovski, S. G. (2002), 'The Observed Offset Distribution of Gamma-Ray Bursts from Their Host Galaxies: A Robust Clue to the Nature of the Progenitors', *Aj* **123**, 1111–1148.
- Bloom, J. S., Kulkarni, S. R., Djorgovski, S. G., Eichelberger, A. C., Cote, P., Blakeslee, J. P., Odewahn, S. C., Harrison, F. A., Frail, D. A., Filippenko, A. V., Leonard, D. C., Riess, A. G., Spinrad, H., Stern, D., Bunker, A., Dey, A., Grossan, B., Perlmutter, S., Knop, R. A., Hook, I. M. & Feroci, M. (1999), 'The unusual afterglow of the gamma-ray burst of 26 March 1998 as evidence for a supernova connection.', *nature* **401**, 453–456.
- Bonnell, I. A. & Pringle, J. E. (1995), 'Gravitational radiation from supernovae', *MNRAS* **273**, L12–L14.
- Bowers, R. L. & Wilson, J. R. (1982), 'A numerical model for stellar core collapse calculations', *ApJS* **50**, 115–159.
- Bruenn, S. W. (1988), 'The physics of stellar core collapse', *Ap&SS* **143**, 15–44.
- Bruenn, S. W. (1989a), 'The prompt-shock supernova mechanism. I - The effect of the free-proton mass fraction and the neutrino transport algorithm', *ApJ* **340**, 955–965.
- Bruenn, S. W. (1989b), 'The prompt-shock supernova mechanism. II - Supranuclear EOS behavior and the precollapse model', *ApJ* **341**, 385–400.

- Buras, R., Rampp, M., Janka, H.-T. & Kifonidis, K. (2003), 'Improved Models of Stellar Core Collapse and Still No Explosions: What Is Missing?', *Physical Review Letters* **90**(24), 241101–+.
- Burrows, A., Hayes, J. & Fryxell, B. A. (1995), 'On the Nature of Core-Collapse Supernova Explosions', *ApJ* **450**, 830–+.
- Burrows, A., Walder, R., Ott, C. D. & Livne, E. (2005), Rotating Core Collapse and Bipolar Supernova Explosions, in 'Astronomical Society of the Pacific Conference Series', pp. 358–+.
- Cappellaro, E., Evans, R. & Turatto, M. (1999), 'A new determination of supernova rates and a comparison with indicators for galactic star formation', *A&A* **351**, 459–466.
- Cappellaro, E., Turatto, M., Tsvetkov, D. Y., Bartunov, O. S., Pollas, C., Evans, R. & Hamuy, M. (1997), 'The rate of supernovae from the combined sample of five searches.', *A&A* **322**, 431–441.
- Centrella, J. M. & McMillan, S. L. W. (1993), 'Gravitational Radiation from Nonaxisymmetric Collisions of Neutron Stars', *ApJ* **416**, 719–+.
- Christensen, L., Hjorth, J. & Gorosabel, J. (2004), 'UV star-formation rates of GRB host galaxies', *A&A* **425**, 913–926.
- Colgate, S. A. & White, R. H. (1966), 'The Hydrodynamic Behavior of Supernovae Explosions', *ApJ* **143**, 626–+.
- Cooperstein, J. (1988), 'Neutrinos in supernovae.', *Phys. Rep.* **163**, 95–126.
- Costa, E., Frontera, F., Heise, J., Feroci, M., in 't Zand, J., Fiore, F., Cinti, M. N., dal Fiume, D., Nicastro, L., Orlandini, M., Palazzi, E., Rapisarda, M., Zavattini, G., Jager, R., Parmar, A., Owens, A., Molendi, S., Cusumano, G., Maccarone, M. C., Giarrusso, S., Coletta, A., Antonelli, L. A., Giommi, P., Muller, J. M., Piro, L. & Butler, R. C. (1997), 'Discovery of an X-ray afterglow associated with the gamma-ray burst of 28 February 1997.', *nature* **387**, 783–785.
- Davies, M. B., King, A., Rosswog, S. & Wynn, G. (2002), 'Gamma-Ray Bursts, Supernova Kicks, and Gravitational Radiation', *ApJL* **579**, L63–L66.
- Della Valle, M. (2004), Supernovae Shedding Light on Gamma Ray Bursts, in '4th Workshop on Gamma-Ray Bursts in the Afterglow Era'.
- Dimmelmeier, H., Font, J. A. & Müller, E. (2002), 'Relativistic simulations of rotational core collapse I. Methods, initial models, and code tests', *A&A* **388**, 917–935.
- Doggett, J. B. & Branch, D. (1985), 'A comparative study of supernova light curves', *Aj* **90**, 2303–2311.
- Endal, A. S. & Sofia, S. (1978), 'The evolution of rotating stars. II - Calculations with time-dependent redistribution of angular momentum for 7- and 10-solar-mass stars', *ApJ* **220**, 279–290.

- Frail, D. A., Kulkarni, S. R., Nicastro, S. R., Feroci, M. & Taylor, G. B. (1997), 'The radio afterglow from the gamma-ray burst of 8 May 1997.', *nature* **389**, 261–263.
- Frank, J., King, A. & Raine, D. J. (2002), *Accretion Power in Astrophysics: Third Edition*, Accretion Power in Astrophysics, by Juhan Frank and Andrew King and Derek Raine, pp. 398. ISBN 0521620538. Cambridge, UK: Cambridge University Press, February 2002.
- Freedman, D. Z. (1974), 'Coherent effects of a weak neutral current', *Physical Review D* **9**, 1389–1392.
- Fryer, C. L. (1999), 'Mass Limits For Black Hole Formation', *ApJ* **522**, 413–418.
- Fryer, C. L. & Heger, A. (2000), 'Core-Collapse Simulations of Rotating Stars', *ApJ* **541**, 1033–1050.
- Fryer, C. L. & Heger, A. (2005), 'Binary Merger Progenitors for Gamma-Ray Bursts and Hypernovae', *ApJ* **623**, 302–313.
- Fryer, C. L., Holz, D. E. & Hughes, S. A. (2002), 'Gravitational Wave Emission from Core Collapse of Massive Stars', *ApJ* **565**, 430–446.
- Fryer, C. L. & Warren, M. S. (2004), 'The Collapse of Rotating Massive Stars in Three Dimensions', *ApJ* **601**, 391–404.
- Fryer, C. L., Woosley, S. E. & Hartmann, D. H. (1999), 'Formation Rates of Black Hole Accretion Disk Gamma-Ray Bursts', *ApJ* **526**, 152–177.
- Fukuda, I. (1982), 'A statistical study of rotational velocities of the stars', *PASP* **94**, 271–284.
- Galama, T. J., Vreeswijk, P. M., van Paradijs, J., Kouveliotou, C., Augusteijn, T., Bohnhardt, H., Brewer, J. P., Doublier, V., Gonzalez, J.-F., Leibundgut, B., Lidman, C., Hainaut, O. R., Patat, F., Heise, J., in 't Zand, J., Hurley, K., Groot, P. J., Strom, R. G., Mazzali, P. A., Iwamoto, K., Nomoto, K., Umeda, H., Nakamura, T., Young, T. R., Suzuki, T., Shigeyama, T., Koshut, T., Kippen, M., Robinson, C., de Wildt, P., Wijers, R. A. M. J., Tanvir, N., Greiner, J., Pian, E., Palazzi, E., Frontera, F., Masetti, N., Nicastro, L., Feroci, M., Costa, E., Piro, L., Peterson, B. A., Tinney, C., Boyle, B., Cannon, R., Stathakis, R., Sadler, E., Begam, M. C. & Ianna, P. (1998), 'An unusual supernova in the error box of the gamma-ray burst of 25 April 1998.', *nature* **395**, 670–672.
- Gehrels, N. e. a. (2005), 'The first localization of a short gamma-ray burst by swift'.
- Höflich, P., Wheeler, J. C. & Wang, L. (1999), 'Aspherical Explosion Models for SN 1998BW/GRB-980425', *ApJ* **521**, 179–189.
- Halbedel, E. M. (1996), 'Rotational Velocity Determinations for 164 Be and B Stars', *PASP* **108**, 833–+.

- Heger, A., Fryer, C. L., Woosley, S. E., Langer, N. & Hartmann, D. H. (2003), ‘How Massive Single Stars End Their Life’, *ApJ* **591**, 288–300.
- Heger, A., Langer, N. & Woosley, S. E. (2000), ‘Presupernova Evolution of Rotating Massive Stars. I. Numerical Method and Evolution of the Internal Stellar Structure’, *ApJ* **528**, 368–396.
- Herant, M., Benz, W., Hix, W. R., Fryer, C. L. & Colgate, S. A. (1994), ‘Inside the supernova: A powerful convective engine’, *ApJ* **435**, 339–361.
- Hernquist, L. (1993), ‘Some cautionary remarks about smoothed particle hydrodynamics’, *ApJ* **404**, 717–722.
- Horowitz, C. J., Pérez-García, M. A. & Piekarewicz, J. (2004), ‘Neutrino-“pasta” scattering: The opacity of nonuniform neutron-rich matter’, *Physical Review C* **69**(4), 045804–+.
- Houck, J. C. & Chevalier, R. A. (1992), ‘Linear stability analysis of spherical accretion flows onto compact objects’, *ApJ* **395**, 592–603.
- Janka, H.-T., Buras, R., Kifonidis, K., Marek, A. & Rampp, M. (2005a), Core Collapse Supernovae at the Threshold, in ‘Cosmic Explosions, On the 10th Anniversary of SN1993J. Proceedings of IAU Colloquium 192. Edited by J.M. Marcaide and Kurt W. Weiler. Springer Proceedings in Physics, vol. 99. Berlin: Springer, 2005., p.253’, pp. 253–+.
- Janka, H.-T., Scheck, L., Kifonidis, K., Müller, E. & Plewa, T. (2005b), Supernova Asymmetries and Pulsar Kicks — Views on Controversial Issues, in ‘Astronomical Society of the Pacific Conference Series’, pp. 372–+.
- Karachentsev, I. D., Karachentseva, V. E., Huchtmeier, W. K. & Makarov, D. I. (2004), ‘Catalog of Nearby Galaxies and the Local Cosmic Web’, *ArXiv Astrophysics e-prints* .
- King, A. et al. (2005), ‘Gamma-ray bursts: Restarting the engine’.
- Klebesadel, R. W., Strong, I. B. & Olson, R. A. (1973), ‘Observations of Gamma-Ray Bursts of Cosmic Origin’, *ApJL* **182**, L85+.
- Kotake, K., Yamada, S. & Sato, K. (2003a), ‘Anisotropic Neutrino Radiation in Rotational Core Collapse’, *ApJ* **595**, 304–316.
- Kotake, K., Yamada, S. & Sato, K. (2003b), ‘Gravitational radiation from axisymmetric rotational core collapse’, *Physical Review D* **68**(4), 044023–+.
- Kouveliotou, C., Meegan, C. A., Fishman, G. J., Bhat, N. P., Briggs, M. S., Koshat, T. M., Paciesas, W. S. & Pendleton, G. N. (1993), ‘Identification of two classes of gamma-ray bursts’, *ApJL* **413**, L101–L104.
- Lai, D. (2003), Core-collapse Supernovae and Neutron Star Kicks, in ‘ASP Conf. Ser. 302: Radio Pulsars’, pp. 307–+.

- Landau, L. D. & Lifshitz, E. M. (1959), *Fluid mechanics*, Course of theoretical physics, Oxford: Pergamon Press, 1959.
- Langer, N., Kiriakidis, M., El Eid, M. F., Fricke, K. J. & Weiss, A. (1988), ‘The surface temperature of C/O-rich Wolf-Rayet stars’, *A&A* **192**, 177–181.
- Lattimer, J. M. & Swesty, F. D. (1991), ‘A generalized equation of state for hot, dense matter’, *Nuclear Physics A* **535**, 331–376.
- Leonard, D. C., Filippenko, A. V., Ardila, D. R. & Brotherton, M. S. (2001), ‘Is It Round? Spectropolarimetry of the Type II-p Supernova 1999EM’, *ApJ* **553**, 861–885.
- Leonard, D. C., Filippenko, A. V., Barth, A. J. & Matheson, T. (2000), ‘Evidence for Asphericity in the Type IIN Supernova SN 1998S’, *ApJ* **536**, 239–254.
- Leonard, D. C., Filippenko, A. V., Chornock, R. & Foley, R. J. (2002), ‘Photospheric-Phase Spectropolarimetry and Nebular-Phase Spectroscopy of the Peculiar Type Ic Supernova 2002ap’, *PASP* **114**, 1333–1348.
- Lieboldörfer, M., Messer, O. E. B., Mezzacappa, A., Bruenn, S. W., Cardall, C. Y. & Thielemann, F.-K. (2004), ‘A Finite Difference Representation of Neutrino Radiation Hydrodynamics in Spherically Symmetric General Relativistic Spacetime’, *ApJS* **150**, 263–316.
- Lieboldörfer, M., Rampp, M., Janka, H.-T. & Mezzacappa, A. (2005), ‘Supernova Simulations with Boltzmann Neutrino Transport: A Comparison of Methods’, *ApJ* **620**, 840–860.
- Livne, E., Burrows, A., Walder, R., Lichtenstadt, I. & Thompson, T. A. (2004), ‘Two-dimensional, Time-dependent, Multigroup, Multiangle Radiation Hydrodynamics Test Simulation in the Core-Collapse Supernova Context’, *ApJ* **609**, 277–287.
- Lucy, L. B. (1977), ‘A numerical approach to the testing of the fission hypothesis’, *ApJ* **82**, 1013–1024.
- MacFadyen, A. I. & Woosley, S. E. (1999), ‘Collapsars: Gamma-Ray Bursts and Explosions in “Failed Supernovae”’, *ApJ* **524**, 262–289.
- Madokoro, H. & Shimizu, T. M. Y. (2004), ‘Importance of Prolate Neutrino Radiation in Core-Collapse Supernovae: The Reason for the Prolate Geometry of SN1987A?’, *PASJ* **56**, 663–669.
- Mazurek, T. J. (1975), ‘Chemical potential effects on neutrino diffusion in supernovae’, *Ap&SS* **35**, 117–135.
- Metzger, M. R., Djorgovski, S. G., Kulkarni, S. R., Steidel, C. C., Adelberger, K. L., Frail, D. A., Costa, E. & Frontera, F. (1997), ‘Spectral constraints on the redshift of the optical counterpart to the gamma-ray burst of 8 May 1997.’, *nature* **387**, 879–+.
- Misner, C. W., Thorne, K. S. & Wheeler, J. A. (1973), *Gravitation*, San Francisco: W.H. Freeman and Co., 1973.

- Moenchmeyer, R., Schaefer, G., Mueller, E. & Kates, R. E. (1991), 'Gravitational waves from the collapse of rotating stellar cores', *A&A* **246**, 417–440.
- Monaghan, J. J. (1992), 'Smoothed particle hydrodynamics', *ARA&A* **30**, 543–574.
- Monaghan, J. J. (2002), 'SPH compressible turbulence', *MNRAS* **335**, 843–852.
- Morris, J. P. & Monaghan, J. J. (1997), 'A Switch to Reduce SPH Viscosity', *Journal of Computational Physics* **136**, 41–50.
- Murray, J. R. (1996), 'SPH simulations of tidally unstable accretion discs in cataclysmic variables', *MNRAS* **279**, 402–414.
- Myra, E. S. & Bludman, S. A. (1989), 'Neutrino transport and the prompt mechanism for type II supernovae', *ApJ* **340**, 384–395.
- Nelson, R. P. & Papaloizou, J. C. B. (1994), 'Variable Smoothing Lengths and Energy Conservation in Smoothed Particle Hydrodynamics', *MNRAS* **270**, 1–+.
- Nice, D. J. et al. (2005), 'A 2.1 solar mass pulsar measured by relativistic orbital decay'.
- Odrzywolek, A., Kutschera, M., Misiaszek, M. & Grotowski, K. (2003), 'Core-collapse supernova mechanism - importance of rotation'.
- Ott, C. D., Burrows, A., Livne, E. & Walder, R. (2004), 'Gravitational Waves from Axisymmetric, Rotating Stellar Core Collapse', *ApJ* **600**, 834–864.
- Ott, C. D., Ou, S., Tohline, J. E. & Burrows, A. (2005), 'One-armed Spiral Instability in a Low-T/—W— Postbounce Supernova Core', *ApJL* **625**, L119–L122.
- Paczynski, B. (1998), 'Are Gamma-Ray Bursts in Star-Forming Regions?', *ApJL* **494**, L45+.
- Penny, L. R. (1996), 'Projected Rotational Velocities of O-Type Stars', *ApJ* **463**, 737–+.
- Petrovic, J., Langer, N., Yoon, S.-C. & Heger, A. (2005), 'Which massive stars are gamma-ray burst progenitors?', *A&A* **435**, 247–259.
- Pfahl, E., Rappaport, S., Podsiadlowski, P. & Spruit, H. (2002), 'A New Class of High-Mass X-Ray Binaries: Implications for Core Collapse and Neutron Star Recoil', *ApJ* **574**, 364–376.
- Piro, L., Costa, E., Feroci, M., Frontera, F., Amati, L., dal Fiume, D., Antonelli, L. A., Heise, J., in 't Zand, J., Owens, A., Parmar, A. N., Cusumano, G., Vietri, M. & Perola, G. C. (1999), 'The X-Ray Afterglow of the Gamma-Ray Burst of 1997 May 8: Spectral Variability and Possible Evidence of an Iron Line', *ApJL* **514**, L73–L77.
- Podsiadlowski, P. (1992), 'The progenitor of SN 1987 A', *PASP* **104**, 717–729.
- Podsiadlowski, P., Mazzali, P. A., Nomoto, K., Lazzati, D. & Cappellaro, E. (2004), 'The Rates of Hypernovae and Gamma-Ray Bursts: Implications for Their Progenitors', *ApJL* **607**, L17–L20.

- Press, W. H., Teukolsky, S. A., Vetterling, W. T. & Flannery, B. P. (1992), *Numerical recipes in FORTRAN. The art of scientific computing*, Cambridge: University Press, —c1992, 2nd ed.
- Prialnik, D. (2000), *An Introduction to the Theory of Stellar Structure and Evolution*, An Introduction to the Theory of Stellar Structure and Evolution, by D. Prialnik. ISBN 052165937X. <http://www.cambridge.org/us/catalogue/catalogue.asp?isbn=052165937X>. Cambridge, UK: Cambridge University Press, 2000.
- Price, D. J. (2004), Magnetic Fields in Astrophysics, PhD thesis, Institute of Astronomy, Cambridge University.
- Price, D. J. & Monaghan, J. J. (2004), ‘Smoothed Particle Magnetohydrodynamics - II. Variational principles and variable smoothing-length terms’, *MNRAS* **348**, 139–152.
- Rampp, M. & Janka, H.-T. (2002), ‘Radiation hydrodynamics with neutrinos. Variable Eddington factor method for core-collapse supernova simulations’, *A&A* **396**, 361–392.
- Rampp, M., Mueller, E. & Ruffert, M. (1998), ‘Simulations of non-axisymmetric rotational core collapse’, *A&A* **332**, 969–983.
- Ravenhall, D. G., Pethick, C. J. & Wilson, J. R. (1983), ‘Structure of Matter below Nuclear Saturation Density’, *Physical Review Letters* **50**, 2066–2069.
- Reeves, J. N., Watson, D., Osborne, J. P., Pounds, K. A., O’Brien, P. T., Short, A. D. T., Turner, M. J. L., Watson, M. G., Mason, K. O., Ehle, M. & Schartel, N. (2002), ‘The signature of supernova ejecta in the X-ray afterglow of the  $\gamma$ -ray burst 011211’, *nature* **416**, 512–515.
- Rosswog, S. & Davies, M. B. (2002), ‘High-resolution calculations of merging neutron stars - I. Model description and hydrodynamic evolution’, *MNRAS* **334**, 481–497.
- Rosswog, S., Davies, M. B., Thielemann, F.-K. & Piran, T. (2000), ‘Merging neutron stars: asymmetric systems’, *A&A* **360**, 171–184.
- Rosswog, S., Speith, R. & Wynn, G. A. (2004), ‘Accretion dynamics in neutron star-black hole binaries’, *MNRAS* **351**, 1121–1133.
- Saijo, M., Baumgarte, T. W. & Shapiro, S. L. (2003), ‘One-armed Spiral Instability in Differentially Rotating Stars’, *ApJ* **595**, 352–364.
- Sato, K. (1975), ‘Supernova explosion and neutral currents of weak interaction’, *Progress of Theoretical Physics* **54**, 1325–1338.
- Shakura, N. I. & Sunyaev, R. A. (1973), ‘Black holes in binary systems. Observational appearance.’, *A&A* **24**, 337–355.

- Shapiro, S. L. & Teukolsky, S. A. (1983), *Black holes, white dwarfs, and neutron stars: The physics of compact objects*, Research supported by the National Science Foundation. New York, Wiley-Interscience, 1983, 663 p.
- Shen, H., Toki, H., Oyamatsu, K. & Sumiyoshi, K. (1998a), 'Relativistic equation of state of nuclear matter for supernova and neutron star', *Nuclear Physics A* **637**, 435–450.
- Shen, H., Toki, H., Oyamatsu, K. & Sumiyoshi, K. (1998b), 'Relativistic Equation of State of Nuclear Matter for Supernova Explosion', *Progress of Theoretical Physics* **100**, 1013–1031.
- Shibata, M. & Sekiguchi, Y. (2005), 'Three-dimensional simulations of stellar core collapse in full general relativity: Nonaxisymmetric dynamical instabilities', *Physical Review* **71**(2), 024014–+.
- Shimizu, T. M., Ebisuzaki, T., Sato, K. & Yamada, S. (2001), 'Effect of Anisotropic Neutrino Radiation on Supernova Explosion Energy', *ApJ* **552**, 756–781.
- Springel, V. & Hernquist, L. (2002), 'Cosmological smoothed particle hydrodynamics simulations: the entropy equation', *MNRAS* **333**, 649–664.
- Stanek, K. Z., Matheson, T., Garnavich, P. M., Martini, P., Berlind, P., Caldwell, N., Challis, P., Brown, W. R., Schild, R., Krisciunas, K., Calkins, M. L., Lee, J. C., Hathi, N., Jansen, R. A., Windhorst, R., Echevarria, L., Eisenstein, D. J., Pindor, B., Olszewski, E. W., Harding, P., Holland, S. T. & Bersier, D. (2003), 'Spectroscopic Discovery of the Supernova 2003dh Associated with GRB 030329', *ApJL* **591**, L17–L20.
- Sumiyoshi, K. et al. (2005), 'Postbounce evolution of core-collapse supernovae: Long-term effects of equation of state'.
- Swesty, F. D., Lattimer, J. M. & Myra, E. S. (1994), 'The role of the equation of state in the 'prompt' phase of type II supernovae', *ApJ* **425**, 195–204.
- Takahara, M. & Sato, K. (1988), 'Supernova explosions and the soft equation of state', *ApJ* **335**, 301–305.
- Thorstensen, J. R., Fesen, R. A. & van den Bergh, S. (2001), 'The Expansion Center and Dynamical Age of the Galactic Supernova Remnant Cassiopeia A', *Aj* **122**, 297–307.
- Tubbs, D. L. & Schramm, D. N. (1975), 'Neutrino Opacities at High Temperatures and Densities', *ApJ* **201**, 467–488.
- van Paradijs, J., Groot, P. J., Galama, T., Kouveliotou, C., Strom, R. G., Telting, J., Rutten, R. G. M., Fishman, G. J., Meegan, C. A., Pettini, M., Tanvir, N., Bloom, J., Pedersen, H., Nordgaard-Nielsen, H. U., Linden-Vornle, M., Melnick, J., van der Steene, G., Bremer, M., Naber, R., Heise, J., in 't Zand, J., Costa, E., Feroci, M.,

- Piro, L., Frontera, F., Zavattini, G., Nicastro, L., Palazzi, E., Bennet, K., Hanlon, L. & Parmar, A. (1997), 'Transient optical emission from the error box of the gamma-ray burst of 28 February 1997.', *nature* **386**, 686–689.
- Vietri, M. & Stella, L. (1998), 'A Gamma-Ray Burst Model with Small Baryon Contamination', *ApJL* **507**, L45–L48.
- Wang, L., Baade, D., Höflich, P. & Wheeler, J. C. (2003), 'Spectropolarimetry of the Type Ic Supernova SN 2002ap in M74: More Evidence for Asymmetric Core Collapse', *ApJ* **592**, 457–466.
- Wang, L., Howell, D. A., Höflich, P. & Wheeler, J. C. (2001), 'Bipolar Supernova Explosions', *ApJ* **550**, 1030–1035.
- Wang, L., Wheeler, J. C., Li, Z. & Clocchiatti, A. (1996), 'Broadband Polarimetry of Supernovae: SN 1994D, SN 1994Y, SN 1994ae, SN 1995D, and SN 1995H', *ApJ* **467**, 435–+.
- Watanabe, G., Maruyama, T., Sato, K., Yasuoka, K. & Ebisuzaki, T. (2005), 'Simulation of Transitions between “Pasta” Phases in Dense Matter', *Physical Review Letters* **94**(3), 031101–+.
- Weaver, T. A., Zimmerman, G. B. & Woosley, S. E. (1978), 'Presupernova evolution of massive stars', *ApJ* **225**, 1021–1029.
- Wilson, J. R. (1985), Supernovae and Post-Collapse Behavior, in 'Numerical Astrophysics', pp. 422–+.
- Woosley, S. E. (1993), 'Gamma-ray bursts from stellar mass accretion disks around black holes', *ApJ* **405**, 273–277.
- Woosley, S. E. & Weaver, T. A. (1988), 'Presupernova models: Sensitivity to convective algorithm and coulomb corrections', *Phys. Rep.* **163**, 79–94.
- Woosley, S. E. & Weaver, T. A. (1995), 'The Evolution and Explosion of Massive Stars. II. Explosive Hydrodynamics and Nucleosynthesis', *ApJS* **101**, 181–+.
- Zeh, A., Klose, S. & Hartmann, D. H. (2004), 'A Systematic Analysis of Supernova Light in Gamma-Ray Burst Afterglows', *ApJ* **609**, 952–961.
- Zhang, W., Woosley, S. E. & Heger, A. (2004), 'The Propagation and Eruption of Relativistic Jets from the Stellar Progenitors of Gamma-Ray Bursts', *ApJ* **608**, 365–377.
- Zwinger, T. & Mueller, E. (1997), 'Dynamics and gravitational wave signature of axisymmetric rotational core collapse.', *A&A* **320**, 209–227.